Numerical Modelling Techniques for Fretting Fatigue Crack Initiation and Propagation

Numerieke modelleringstechnieken voor scheurinitiatie en -propagatie in frettingvermoeiing

Reza Hojjati Talemi

Promotoren: prof. dr. ir. M. Abdel Wahab, prof. dr. ir. P. De Baets
Proefschrift ingediend tot het behalen van de graad van
Doctor in de Ingenieurswetenschappen: Werktuigkunde-Elektrotechniek

Vakgroep Mechanische Constructie en Productie
Voorzitter: prof. dr. ir. P. De Baets
Faculteit Ingenieurswetenschappen en Architectuur
Academiejaar 2013 - 2014

UNIVERSITEIT GENT

ISBN 978-90-8578-693-1
NUR 978
Wettelijk depot: D/2014/10.500/39

Promoters

prof. dr. ir. M.A. Wahab
prof. dr. ir. P. De Baets

Ghent University
Faculty of Engineering and Architecture
Department of Mechanical Construction and Production

Examination Committee

prof. R. Van De Walle (Chair)
prof. M.A. Wahab
prof. P. De Baets
prof. W. De Waele
prof. G. De Roeck
prof. B. Verhegghe
prof. R. Petrov
dr. J. Van Wittenberghe

Research Institute

Ghent University
Department of Mechanical Construction and Production
Laboratory Soete
Technologiepark 903
B-9052 Zwijnaarde
Belgium

Tel. +32 9 331 04 70
Fax. +32 9 331 04 90
Reza.HojjatiTalemi@UGent.be

www.frettingfatigue.ugent.be

"The greatest challenge to any thinker is stating the problem in a way that will allow a solution"
Bertrand Russell

Acknowledgements

It is a great pleasure for me to express my gratitude to the many people who have helped me or have been an important part of my life the last three and a half years.

First of all, I would like to express my special appreciation and thanks to my first promoter Prof. Wahab for giving me the opportunity to start my PhD. I would like to thank you for encouraging my research and for trusting me to grow as an independent researcher. Moreover, I would like to thank my second promoter Prof. De Baets, you have been a tremendous mentor for me and your advices on both research as well as on my career have been invaluable. I would also like to thank my committee members, Prof. Van de Walle, R., Prof. De Roeck, G., Prof. Verhegghe, B., Prof. Petrov R. and Dr. Van Wittenberghe, J. for spending time to read my thesis.

I would like to acknowledge Ghent University for the academic, technical and financial support received by the special funding, BOF (Bijzonder Onderzoeksfonds), in the framework of project no. BOF 01N02410.

My sincere thanks also go beyond Ghent University to some colleagues, who helped me to stand at this point. I would like to express my spacial gratitude to:

- *Prof. Martin Olsson, from KTH Royal Institute of Technology, Sweden, who introduced this position to me and recommended me. Thank you for giving me this opportunity.*
- *Prof. Eugenio Giner, from Polytechnic University of Valencia, Spain, for*

all useful discussions on eXtened Finite Element Method (XFEM), providing experimental results for conformal contact configuration reported in Chapter 7 and fruitful cooperation. Thank you for all your invaluable and inspiring comments.

Dozens of people have helped and taught me immensely at the Soete Laboratory, Ghent University. The experimental parts of this study would have been impossible without the technical support of some people. I would like to thank Chris Bonne, Rudy Desmet, Jonathan Vancoillie, Wouter Ost, Tony Lefevre, Michel De Waele and Hans Van Severen.

When asked what a great work environment is, most people would mention a good relationship with colleagues. I would like to thank all of my present and former colleagues at the Soete Laboratory, Ghent University: Jan De Pauw, thank you for all of technical discussions regarding fretting fatigue and for sharing the office with me for three and half years, Yue Tongyan, Stijn Hertele, Matthias Verstraete, Jeroen Van Wittenberghe, Koen Van Minnebruggen, Nahuel Micone, Timothy Galle, Hanan Al Ali, Diego Belato Rosado, Gusztav Fekete, Yeczain Perez, Jacob Sukumaran, Matyas Ando, Vanessa Rodriguez, Patric Neis, Tan Dat Nguyen, Zamaan Sadeghi, Mohsen Safaei, Behnam Sobhani, Georgette D'Hondt, Josiane Yde, Rudi Denys and Dirk Vanderschueren.

Finally, my special gratitude goes to my family; my parents Farideh and Ahmad, for supporting and facilitating my studies during all these years unconditionally; my brothers Arsalan and Emad; my parents in law Mitra And Shamsedin; my brother and sister in law Salar and Samra and the last but not the least my beloved wife. Soad, thank you for your faith in me. Thank you for bearing with me when I worked those long late hours, when everybody else was home with his/her family. Thank you for letting me work during holidays and even weekends, when other people were on vacation. My whole research was not possible if it was not for your love, understanding, patience, and compassion.

Reza Hojjati

Ghent, January 2014

Summary

Despite the great steps that have been made in technology, mechanical failures continue to occur, often accompanied by great human and economic loss. Mechanical failure analysis can be an absorbing subject to those involved in investigating the cause of an accident. The capable investigator must have a thorough understanding of the mode of operation of the components of the system involved, as well as, a knowledge of the possible mechanical failure modes, if a correct conclusion is to be reached.

Fretting fatigue damage occurs in contacting components while they are subjected to fluctuating loads and relatively small movement at the same time. There are many practical applications that are subjected to fretting fatigue, such as bolted and riveted connections, bearing shafts, blade-disk attachment in gas and steam turbines and aero-engine splined couplings. Fretting fatigue failure evolution is caused by combination of several parameters, which can be related to different mechanical response of material. These parameters can be divided into two sets of primary and secondary variables, which have more and less influence on fretting fatigue total lifetime. Fretting fatigue failure process can be divided into two portions of crack initiation and propagation. The primary variables have also different effects on each of these fractions of total lifetime. The number of cycles at which the macro-crack nucleates is called damage threshold.

It is very difficult, to separate the crack initiation and propagation portions of the total life experimentally. On the other hand since tracking of crack under fretting fatigue condition is a very challenging task, finding the damage threshold is very difficult. Therefore, in order to better understand each portion

and estimate fretting fatigue total lifetime, a numerical approach is a useful technique to model fretting fatigue crack initiation and propagation lifetime separately.

The main objectives of this investigation is to estimate response of materials subjected to fretting fatigue loading condition by means of Finite Element (FE) modelling approach. In the first step, the fretting fatigue lab scale experimental set-up is introduced, which consists of two different set-ups namely, single clamp and practical applications tests. The practical applications tests are Single and Double Bolted Lap Joints along with the shock absorber valve test configurations. Moreover, Digital Image Correlation (DIC) technique is proposed to characterize fretting fatigue frictional behaviour.

Next, based on experimental test configurations, three different categories of fretting fatigue FE contact models are highlighted in different groups, namely, Finite Element Analysis (FEA) of fretting contact, fretting fatigue contact and practical applications. Effects of different loading conditions on fretting relative slip amplitude at contact interface are presented for single clamp flat and cylindrical contact configurations by means of developed FE models. In addition, using the developed models, a parametric study is carried out in order to find the interaction effects of two primary variables namely, axial stress and contact force, on fretting fatigue FE slip amplitude. Finally, to characterize fretting fatigue characteristics, SBLJ, DBLJ and washer-disc contact configuration are modelled using FE approach.

In terms of crack initiation lifetime prediction, Continuum Damage Mechanics (CDM) approach is introduced. An uncoupled damage evolution law is derived for HCF using the principle of thermodynamics to predict fretting fatigue crack initiation lifetime for both elastic and elasto-plastic behaviour of material. Furthermore, stress and energy based methodologies are discussed in order to predict fretting fatigue initial crack site. For validating the proposed approach, the damage evolution law is implemented to fretting fatigue problem form literature. Damage parameters, which are material dependent constants, are calibrated using regression analysis to calculate the best least square fit between the experimental results and the predicted cycles to crack initiation. In addition, a parametric study is performed to study the effect of different primary variables, e.g. contacts geometry, axial stress and COF on localized plasticity. Subsequently, the relation between location of maximum localized plasticity and crack initiation site predicted by different criteria is discussed.

For modelling crack propagation, a general 2-D crack propagation model is developed using both conventional Finite Element Method (FEM) and eXtend Finite Element Method (XFEM) approaches. The developed model is verified by two different benchmark studies, namely, Double Edge Notch Tension (DENT) specimen and Double Cantilever Beam (DCB) specimen. Following, the developed codes are implemented to 2-D fretting fatigue crack propagation problem. The crack propagation path is modelled based on experimental observations and compared with three different criteria, which are usually used for proportional loading condition, available in literature.

Eventually, to predict fretting fatigue total lifetime, the developed FE models for crack initiation and propagation are combined. The developed models are implemented to two different experimental set-ups, namely, single clamp cylindrical and flat contact configurations. The predicted fretting fatigue life using CDM+XFEM approach is compared with the variable crack initiation method (McDiarmid+XFEM), which is based on critical plane approach, and validated against observed experimental results.

The effect of phase difference between axial and tangential load on fretting fatigue behaviour is investigated. in addition, by applying cyclic contact load instead of constant contact load, its effect on fretting fatigue response and crack initiation lifetime is investigated. Furthermore, by adding different types of surface and sub-surface geometrical inhomogeneities using the CDM combined with FE modelling approaches, the sensitivity of fretting fatigue parameters and crack initiation lifetime are investigated. Furthermore, effect of geometrical impurities on fretting fatigue parameters and crack initiation life are discussed.

At the end, proposed methodologies used in this study to investigate fretting fatigue crack initiation and propagation behaviour and the main conclusions are summarized. Finally, to extend the proposed methodologies in both experimental and numerical approaches some recommendations are put forward for future work.

Samenvatting

(Dutch summary)

Ondanks het feit dat de moderne technologie enorme progressie heeft gemaakt, blijft mechanisch falen toch optreden wat dan dikwijls leidt tot grote verliezen voor mens en economie. Mensen die betrokken zijn bij het zoeken naar de oorzaken van dat falen moeten alle mogelijke facetten bekijken tijdens de analyse van dergelijk mechanisch falen. Een bekwame onderzoeker moet niet alleen een grondige kennis hebben van de manier van werken van alle onderdelen in het systeem in kwestie, maar ook van de mogelijke mechanische fouten die kunnen optreden, om tot een correcte conclusie te komen.

Schade aangericht door passingroest komt voor wanneer onderdelen onderworpen worden aan een schommelende belasting, met elkaar in contact komen en ten opzichte van elkaar relatief kleine bewegingen uitvoeren. Er bestaan heel veel practische toepassingen die onderworpen worden aan passingroest, zoals verbindingen met schroeven of klinknagels, lagerassen, mes-schijf verbindingen in gas- en stoomturbines en getande koppelingen in vliegtuigmotoren. De evolutie van passingroest wordt veroorzaakt door een combinatie van verscheidene parameters, die te maken kan hebben met de verschillende mechanische reacties van de materialen. Deze parameters kunnen onderverdeeld worden in primaire en secundaire variabelen die meer of minder invloed hebben op de totale levensduur van passingroest. Het proces van passingroest kan op zijn beurt onderverdeeld worden in het starten van de scheur en de verspreiding ervan. De primaire variabelen hebben ook een verschillende invloed op elk van deze fracties van de totale levensduur. Het aantal cycli waarna de macro-scheur

een kern vormt, wordt de schadedrempel genoemd.

Het is zeer moeilijk om experimenteel het starten van de scheur en de verspreiding ervan te onderscheiden binnen de gehele levensduur. Daaruit volgt dus dat aangezien het opvolgen van de scheur onder passingroest een zeer moeilijke karwei is, het dan ook zeer moeilijk wordt om de schadedrempel te vinden. Om daarom elk onderdeel beter te begrijpen en de totale levensduur van passingroest te kunnen schatten, is een numerieke aanpak een handige techniek om een afzonderlijk model te maken van de start van de scheur en de levensduur van de verspreiding.

Het voornaamste doeleind van deze studie is om de reactie te schatten van materialen die onderworpen worden aan de laadcondities van passingroest door gebruik te maken van een FE-model. In een eerste fase wordt de experimentele opstelling van de passingroest op laboratoriumniveau opgesteld. Die bestaat uit twee opstellingen, namelijk de Single Clamp techniek en de praktische toepassingstesten. De praktische toepassingstesten zijn de Single en Double Bolted Lap Joints en de configuratie van de kleptest van de schokbreker. Bovendien wordt ook de Digital Image Correlation (DIC) techniek voorgesteld om het frictiegedrag van passingroest te karakteriseren.

Dan, gebaseerd op experimentele testconfiguraties, worden drie verschillende categorin van FE-contactmodellen van passingroest ondergebracht in verschillende groepen, namelijk de Finite Element Analysis (FEA) van passingroestcontact, passingroestcontact en praktische toepassingen. De gevolgen van verschillende belastingconditities op de omvang van de passingroestslip op de contactoppervlakte worden voorgesteld voor Single Clamp vlakke en cylindrische contactconfiguraties gebruik makend van vergevorderde FE-modellen. Daarenboven wordt ook een parameterstudie uitgevoerd, met gebruik van deze vergevorderde modellen, om de interactiegevolgen van twee primaire variabelen te weten te komen, namelijk de contackracht en de axiale spanning op de FE-slipgrootte van passingroest. Tenslotte, om passingroest te karakteriseren, wordt een model gemaakt van de SBLJ, DBLJ en sluitring-schijf contactconfiguraties, gebruik makend van de FE-modellen.

Voor de voorspelling van de levensduur van de start van een scheur wordt de Continuum Damage Mechanics (CDM)-methode gentroduceerd. Een ongerelateerde schade-evolutiewet werd afgeleid voor HCF soor gebruik te maken van het principe van thermodynamica om de levensduur van de start van de scheur

van passingroest te voorspellen voor zowel elastisch als elasto-plastisch gedrag van materiaal. Verder worden ook methodologien gebaseerd op spanning en energie besproken om de initile scheurplaats van passingroest te voorspellen. Om nu die voorgestelde aanpak te valideren wordt de schade-evolutiewet toegepast op de literatuur rondom de vorm van het probleem van passingroest. Schade-parameters, die constante elementen zijn afhankelijk van het materiaal, worden gecalibreerd met gebruik van regressie-analyse om de beste minst goede overeenkomst te berekenen tussen de resultaten van de experimenten en de voorspelde cycli tot het begin van de scheur. Daarenboven wordt een parameterstudie voorgevormd om de gevolgen te bestuderen van verscheidene primaire variabelen, zoals bijvoorbeeld contactgeometrie, axiale spanning en COF op gelokaliseerde kneedbaarheid. Daarna wordt de relatie besproken tussen de lokatie van maximum gelokaliseerde kneedbaarheid en de plaats van de start van de scheur zoals die voorspeld werd door verschillende criteria.

Om een model te maken van de verspreiding van de scheur, wordt een algemeen 2-D model van scheurverspreiding ontwikkeld gebruik makend van zowel de conventionele Finite Element Method (FEM) en de eXtend Finite Element Method (XFEM). Het resulterende model wordt dan geverifieerd door twee mijlpaalstudies, de Double Edge Notch Tension (DENT) test en de Double Cantilever Beam (DCB) test. De resulterende codes worden dan gemplementeerd op het probleem van de 2-D passingroest scheurverspreiding. Van het pad van de scheurverspreiding wordt een model gemaakt gebaseerd op experimentele observaties en vergeleken met drie verschillende criteria die normaal gebruikt worden voor proportionele laadvoorwaarden en die gemakkelijk in literatuur terug te vinden zijn.

Tenslotte worden de zo ontwikkelde FE-modellen voor de start van de scheur en de verspreiding ervan gecombineerd om de totale levensduur van de passingroest te voorspellen. De resulterende modellen worden toegepast op twee experimentele opstellingen, namelijk de Single Clamp cylindrische en vlakke contactconfiguraties. De voorspelde levensduur van de passingroest met de CDM + XFEM aanpak wordt vergeleken met de variabele scheurstartmethode (McDiarmid + XFEM) die gebaseerd is op de kritieke oppervlaktemethode, en gevalideerd tegen de geobserveerde experimentele resultaten.

De gevolgen van het verschil in verschillende fasen tussen de axiale en tangentile lading op het gedrag van passingroest wordt onderzocht. Daarenboven wordt ook het effecrt op de passingroestreactie en de levensduur van

de scheurstart onderzocht door cyclische contactbelasting toe te passen in plaats van een constante contactbelasting. Bovendien worden geometrische inhomogeniteiten van verschillende soorten oppervlakten en sub-oppervlakten toegevoegd door gebruik te maken van de CDM gecombineerd met FE-modellen om de gevoeligheid van de passingroestparameters en de levensduur van de startscheur te onderzoeken. Ook worden de gevolgen van geometrische onzuiverheden op de passingroestparameters en levensduur van de startscheur besproken.

Uiteindelijk worden de voorgestelde methodologien die in deze studie gebruikt worden om het gedrag van de startscheur van passingroest en de verspreiding ervan en de voornaamste conclusies samengevat. Ook worden een paar aanbevelingen aangebracht naar de toekomst toe om de voorgestelde methodologien uit te breiden in zowel een experimentele als een numerieke aanpak.

Contents

Nomenclature

Abbreviations

2-D	two dimensional
3-D	three dimensional
AD	airworthiness directive
AL	augmented Lagrange
AOI	area of interest
APDL	ANSYS parametric design language
ASTM	American society for testing and materials
CDM	continuum damage mechanics
COF	coefficient of friction
CP	cylindrical pad
DBLJ	double bolted lap joint
DENT	double edge notch tension
DIC	digital image correlation
DOF	degree of freedom
FAA	federal aviation administration

FEM	finite element method
FF	fretting fatigue
FP	flat pad
FS	Fatemi-Soice parameter
GSR	gross slip regime
LSM	level set method
MERR	maximum energy release rate
MPC	multi-point constraint
MPS	maximum principal strain
MSD	multiple-site damage
MSR	mixed slip regime
MSSR	modified shear stress range
NDE	non-destructive examination
NTSB	national transportation safety board
PD	phase difference
PEEQ	equivalent plastic strain
PL	pure Lagrange
PSR	partial slip regime
RRSE	root relative squared error
RVE	representative volume element
SBLJ	single bolted lap joint
SENT	single edge notch tension
SI	surface inclusion
SIF	stress intensity factor
SMV	surface micro void

SSD	sum of squared difference
SSI	sub-surface inclusion
SSMV	sub-surface micro void
SSR	shear stress range
SWT	Smith-Watson-Toppar parameter
XFEM	extended finite element method

Symbols

α_p	orientation of principal axis with respect to loading axis
ΔK_{th}	long crack stress intensity factor threshold
Δl	crack propagation increment
δS	area of resistance
δS_D	total area of defects
Δ	global slip amplitude
δ	local slip amplitude
$\Delta\epsilon_1$	maximum range of principal strain
$\Delta\epsilon_{p,max}$	maximum value of principal strain range
$\delta\gamma_{max}$	maximum range of shear strain
$\Delta\sigma$	stress range
$\Delta\tau$	shear stress range
$\Delta\tau_{crit}$	critical shear stress range
$\Delta\tau_{max}$	maximum shear stress range
$\delta\widetilde{S}$	effective area of resistance
δ_{ij}	kronecker delta
δ_{max}	maximum local slip amplitude
$\dot{\pi}$	accumulated micro-plastic strain

$\dot{D}$	damage rate
$\dot{P}$	rate of plastic strain
$\dot{Y}$	damage strain energy release rate
ϵ_c	compressive strain
$\epsilon_{e,H}$	hydrostatic elastic strain
ϵ_e	deviatoric elastic strain
ϵ_e	elastic strain
ϵ'_f	fatigue ductillity coffecient
ϵ_p	plastic strain
ϵ_{total}	total strain
Γ	closed counter-clockwise contour
Γ_L	crack
μ	coefficient of friction
μ_{gs}	coefficient of friction at onset of gross sliding
μ_n	coefficient of friction after n cycle
μ_{slip}	coefficient of friction in slip region
ν	Poisson's ratio
ψ	thermodynamic potential
$\Psi(x), \Phi(x)$	level set distance functions
ρ	density
σ^*	equivalent multiaxial damage stress
σ'	deviatoric stress
σ'_f	fatigue strength coefficient
σ_0	plain fatigue strength
$\sigma_{1,2}$	principal stresses

$\sigma_{\theta\theta}, \sigma_{r\theta}$	orthogonal stresses at crack tip
σ_{axial}	maximum applied axial fatigue stress
σ_a	alternating stress
σ_{eq}	equivalent stress
σ_{eq}^{MD}	McDiarmid equivalent stress
σ_H	hydrostatic stress
σ_{max}	maximum stress
σ_{min}	minimum stress
σ_m	mean stress
σ_n^{max}	maximum normal stress to critical plane
σ_{range}	stress range
$\sigma_{reaction}, \sigma_r$	reaction stress
σ_{ult}	ultimate stress
σ_x	tangential stress distribution
σ_{yield}	yield stress
σ_y	normal contact stress distribution
$\tau_{average}$	average shear stress
τ_f	fatigue limit in torsion
$\tau_{xy}, q(x)$	frictional shear stress distribution
θ_p	crack propagation angle
φ	dissipated potential function
φ_π	micro-plastic dissipated potential function
φ_D	damage dissipated potential function
φ_p	plastic dissipated potential function
$\vec{n}$	normal vector

$\vec{q}$	heat flux
$\widetilde{\mu}$	average coefficient of friction
$\widetilde{\sigma}$	effective stress
$\widetilde{E}$	modulus of elasticity of damage material
a	semi contact width
A, β	damage parameters
A_{bush}	bush cross section
a_{ijkl}	fourth order elastic tensor
A_k	any associated thermodynamic variable
A_s	cross section area of specimen
b	width of fatigue specimen
b'	fatigue strength exponent
C	fatigue durability exponent
c	size of stick zone
c_n	size of stick zone after n cycle
C_p	Paris law coefficient
D	damage variable
d	contact diameter
d_{bolt}	bolt nominal diameter
D_c	critical damage variable
E	modulus of elasticity
E^*	effective modulus of elasticity
$e^{\mu p}$	micro plastic strain
E_d	dissipated energy
E_d^*	dissipated energy over contact area after one cycle

E_t	total energy
F	contact, normal force
F_{axial}	axial force
F_{cl}	clamping force
F_r	reaction force
g	overlap of two connected bodies in tangential direction
G^k	energy release rate
h	overlap of two connected bodies in normal direction
$H(x)$	discontinuous jump function
J	J-integral
$J_{2,a}$	amplitude of second invariant of deviatoric stress
k_1	Ruiz fretting wear parameter
k_2	Ruiz fretting fatigue parameter
K_{eq}	equivalent stress intensity factor
K_{IC}	mode I critical stress intensity factor
K_I, K_{II}, K_{III}	mode I, II and III stress intensity factors
K_I^k, K_{II}^k	stress intensity factor at tip of the putative crack
K_I^{WF}	weight function stress intensity factor
K_{max}	maximum stress intensity factor
L	specimen length
l	crack length
l_0	initial crack length
L_c	critical distance
N_f	total failure lifetime
$N_{I,J,K}$	shape function at node i,j,k

N_i	crack initiation lifetime
N_p	crack propagation lifetime
n_p	Paris law exponent
P	accumulated plastic strain
$p(x)$	contact pressure
P_{cl}	clamping pressure
p_{max}	maximum contact pressure
P_{oil}	oil pressure
Q	tangential, shear load
q_K^0, q_K^α	nodes surrounding the crack tip
Q_{max}	maximum tangential load
Q_{slip}	tangential load at onset of sliding
R	contact radius
R^*	effective contact radius
R_τ	shear stress ratio
R_A	amplitude ratio
R_n	isotropic hardening scalar
R_q	tangential load ratio
R_s	stress ratio
R_v	triaxiality function
S	entropy
S_A	all nodes in a domain
S_C	nodes surrounding the crack tip
S_H	nodes whose supports are cut by the crack
T	temperature

T_{cl}	clamping torque
T_i	traction vector
T_x	triaxiality ratio
$u^h(x)$	finite element displacement approximation
U_i	displacement vector
V_k	any internal thermodynamic variable
$W(y)$	weight function
W_e	density of elastic strain energy
W'_e	density of deviatoric elastic strain energy
W_e^H	density of hydrostatic elastic strain energy
Y	damage strain energy release

Chapter 1

Introduction

"The first chapter presents a brief introduction of fretting fatigue mechanical failure mechanism"

1.1 Mechanical failure

Despite the great steps that have been made in technology, mechanical failures continue to occur, often accompanied by great human and economic loss. In this section an introduction to the subject of mechanical failure is presented in form of some real case studies. Mechanical failure analysis can be an absorbing subject to those involved in investigating the cause of an accident. The capable investigator must have a thorough understanding of the mode of operation of the components of the system involved, as well as a knowledge of the possible mechanical failure modes, if a correct conclusion is to be reached. There is a growing interest in on-line monitoring of various infrastructures. The importance of managing ageing infrastructures has gained publics interest in light of catastrophic incidents such as the Aloha airlines flight accident as shown in Figure 1.1 [NSTB, 1989].

Figure 1.1: Aloha airline flight 243 accident [NSTB, 1989].

In 1988, a Boeing 737-200 operated by Aloha Airlines, during flight experienced an explosive decompression and mechanical structural failure as the plane levelled at seven Km. Approximately 5.5 m of the cabin skin and structure of the cabin entrance door and above the passenger floor had separated from the air-plane. There were 89 passengers and 6 crew-members on board. One flight attendant was swept overboard and seven passengers and one flight attendant received serious injuries. An emergency landing was made on the island of Maui. As a result of the accident the air-plane was damaged beyond repair and was dismantled and sold for scrap.

The B-737 involved had been manufactured in 1969. At the time of the accident it had acquired 35,496 flight hours and 89,680 flight cycles (landings), the second highest number of cycles in the worldwide 737 fleet. Due to the short distance between destinations on some Aloha Airlines routes, the full pressurization of 52 kPa was not reached on every flight. Therefore, the number of full pressure cycles was significantly less than 89 680. The plane had also been exposed to warm, humid, maritime air, which promoted corrosion.

Failure was found to have initiated along a fuselage skin longitudinal lap joint that had been cold bonded. In addition, the joint contained three rows of countersunk rivets. Fuselage hoop loads were intended to be transferred through the joint, rather than through the rivets, allowing for thinner skin with no degradation in fatigue life. However, early service history with production B-737 air-planes revealed that difficulties were encountered with the bonding process, and it was discontinued after 1972. In order to safeguard those B-737 planes that had been connected using riveted joints, Boeing issued a number of service bulletins over a period of time directing the attention of operators to the problem and providing information on how to check for potential cracked sites using the eddy current non-destructive examination (NDE) technique. In 1987, the Federal Aviation Administration (FAA) issued an airworthiness directive (AD) requiring that eddy current inspections of the bonds and repairs, if needed, be carried out in compliance with the Boeing service bulletins. Some areas of the lap joints did not bond at all, and moisture and corrosion could contribute to further dis-bonding. When dis-bonding did occur, the hoop load transfer though the joint was borne by the three rows of countersunk rivets. However, the countersinking extended through the entire thickness of the sheet, which resulted in a knife edge being created at the bottom of the hole, which concentrated stress and promoted fatigue crack nucleation, Figure 1.2. For this reason, fatigue cracking would be expected to begin in the outer layer of the skin along the lap joint along the upper, more highly stressed, row of rivet holes.

The National Transportation Safety Board (NTSB) believed that the top rivet row was cracked at the critical lap joint before the accident flight take-off. They determined that the probable cause of the accident was the failure of the Aloha Airlines maintenance program to detect the presence of the significant dis-bonding and fatigue damage that ultimately led to the failure of the lap joint and the separation of the fuselage upper lobe. This accident was significant in

that it brought attention to some of the corrosion and fatigue problems that could develop in ageing aircraft. It also focused attention on the problem of multiple-site damage (MSD), that is, the formation and possible linking up of fatigue cracks formed at adjacent rivet holes.

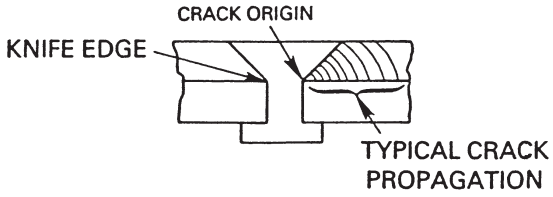

Figure 1.2: Schematic view of a countersunk rivet and an associated fatigue crack observed in Aloha Airlines 737 [NSTB, 1989].

More recently, a plane carrying parachutists planning to celebrate a birthday with a skydive crashed in Belgium on Saturday October 19, 2013, resulting in the death of all 11 people aboard, Figure 1.3. Minutes after the aircraft took off from a small airfield near the city of Namur, witnesses saw part of a wing break off, sending the plane into a spiraling nosedive and crash in a field. The plane was probably about 3 kilometers high when it suddenly went down. Such plane crashes in Belgium, a small country of 11 million people, are fairly rare. However, this dramatic incident reminds us the importance of design and maintenance of structures to avoid having such a catastrophic mechanical failure.

Figure 1.3: Namur flight accident [AP, 2013].

1.2 Fretting fatigue phenomenon

There is a growing interest in predicting of various mechanical failure modes of infrastructures. The importance of managing ageing infrastructures has gained publics interest in light of catastrophic incidents such as the Aloha airlines flight accident as elaborated earlier. Fretting fatigue phenomenon is one of the complex mechanical failure mode, which occurs in combination of different failure modes. Literally, it can be defined as combination of tribological and fatigue behaviour of materials, which are in contact together. Fretting occurs due to oscillatory relative displacement between two components, which results in damage at contact interface. Once these components face cyclic fatigue load at the same time, fretting fatigue phenomenon occurs. Due to fretting, fatigue lifetime is significantly reduced as compared to plane fatigue. There are many practical applications that are subjected to fretting fatigue, such as bolted and riveted connections, bearing shafts, blade-disk attachment in gas and steam turbines and aero-engine splined couplings [Hills and Nowell, 1994].

After 23 years of Aloha airline accident, on April 1, 2011, a Boeing 737, operating as Southwest Airlines flight 812 experienced a rapid decompression while climbing through flight level 340. The flight crew conducted an emergency descent and diverted to Yuma International Airport (NYL), Yuma, Arizona. Of the 5 crew-members and 117 passengers on board, one crew-member and one non-revenue off-duty airline employee passenger sustained minor injuries. The air-plane sustained substantial damage; post-accident inspection revealed that a section of fuselage skin had fractured and flapped open on the upper left side above the wing, Figure 1.4 (a). The entire section of skin remained attached along the lower edge and was deformed outward as shown in Figure 1.4 (b). The fracture along the upper edge was through the lower rivet row of the lap joint. There was no visible damage to the surrounding frames, stringers, and stringer clips. At the NTSB materials laboratory, microscope examination of the fracture surfaces of the ruptured skin revealed fatigue cracks emanating from at least 42 out of the 58 rivet holes by the fracture. Non-destructive eddy current inspections conducted around intact rivets on the removed skin section forward of the rupture revealed crack indications at nine rivet holes in the lower rivet row of the lap joint [NSTB, 2013].

(a)

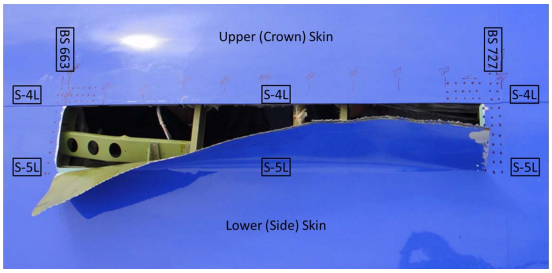

(b)

Figure 1.4: (a) Photograph of Southwest airline air-plain with the hole in upper left fuselage, (b) Close-up view of hole in fuselage side skin [NSTB, 2013].

Figure 1.5 shows two connected fuselage plates in air-plane structure, which are subjected to oscillatory motion due to cyclic loads. The load transfer to the structure takes place on a local scale at the rivet/plate interface. The remote load that is produced from vibration causes shear loading (Q) and normal force (F) due to squeezing of the rivet. By looking closer at the critical regions, i.e. rivet/plate interface, it can be seen that the crack nucleates at the contact interface between rivet's shank and the plate's hole due to fretting condition and propagates up to sudden failure as depicted in Figure 1.6. The figure represents the side profile view of rivet with its corresponding rivet hole. According to NTSB technical report, at the inner surface of the lap joint, the rivet holes in the upper and lower skins were found to be slightly offset relative to each other, and many of the rivet holes on the lower skin were not circular but slightly oval. The fracture (fatigue cracks) intersected the lower portion of a majority of the lower-row rivet holes. The corresponding area located at the underside of the expanded portion of the rivets also showed fretting damage

consistent with the underside of the expanded portion of the shank rubbing against the plate.

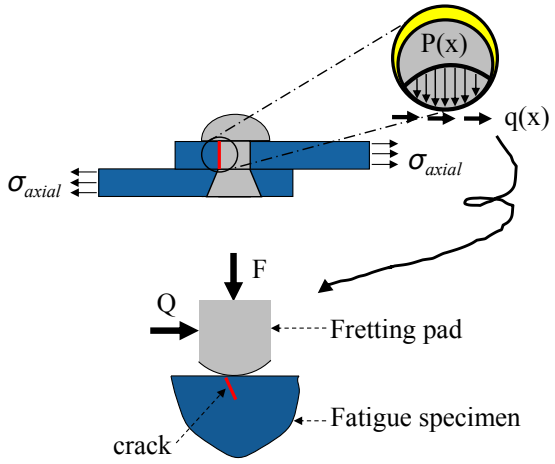

Figure 1.5: Fretting fatigue phenomena in lap-joint connections.

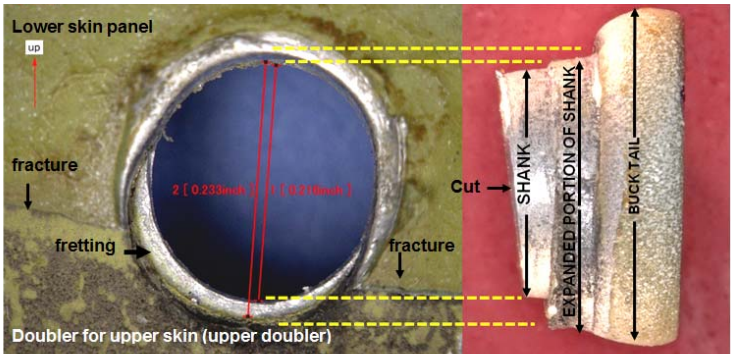

Figure 1.6: Rivet hole when viewed from inner face of the skin panel (left side) and side view of corresponding rivet that was removed from the rivet hole (right side) [NSTB, 2013].

1.3 New application of fretting fatigue

After obtaining my master thesis, during working as head of R&D department in an automotive shock absorber producer company. It was interesting to find

that hydraulic shock absorber is one of the most complex components in the suspension system, which plays a crucial role during the vehicle running. It can efficiently prevent the relative motion of the sprung and unsprung mass. What makes it even more complicated is the traditional design methods, which are according to experience to determine the design parameter before test modified and the samples with different structural parameters are used to equip to an automobile, then the test evaluations are given by the commissioning members. This method must adjust the inter parameters and needs trial-manufacture and tests a lot of times. It does not only need a long period and high cost, but also has difficulty to get the optimal characteristics.

During my work at automotive industry I have accidentally faced a failure in one of the components of shock absorbers during regular durability lab test. As a researcher, who had been working on fretting fatigue failure mechanism since his final bachelor and master project, it was really interesting to understand the failure process. Literally, all of available evidences showed that the failure phenomenon is due to fretting fatigue problem, as there are a lot of connected components inside shock absorber that are subjected to oscillatory loading condition. After disassembling the failed shock absorber sample, it was found that the fracture occurred at one component of piston value. Figure 1.7 illustrates 2-D assembly drawing of automotive twin-tube shock absorber with shim disc valve design. As the name implies, in a twin-tube shock absorber, there are two tubes. One forms the outer body of the shock absorber and the other is a cylinder inside which the piston moves. Orifices in the piston valve as well as special valve between the inner and outer tubes, which is called body valve, restrict the flow of oil to control wheel motion. Rather than actually absorbing shocks, the real purpose of the shock absorber is to keep the wheels of the car in contact with the road, and damp the spring movement. This is accomplished by the scientific principle of transference. The energy created by the spring is transferred to a piston valve in a chamber that is filled with oil and the energy gets dissipated into heat form.

The twin-tube system represents the basic design of a modern shock absorber. The piston rod and protective tube are fixed via the mounting flange to the car body. The cylinder is fixed to the wheel suspension. The inner tube contains the working chamber in which the piston moves up and down. The compensating tube, between the inner and the outer tube (cylinder), is partially filled with oil and contains the extruded oil volume caused by the piston

rod when moving downwards. Valves, fitted in the piston, control the oil flow at different rates. Figure 1.8 (a) to (c) depict the detailed view of piston valve with shim disc valve design, schematic view of oil pressure along with tightening nut force and fretting fatigue failure loading and boundary conditions, respectively.

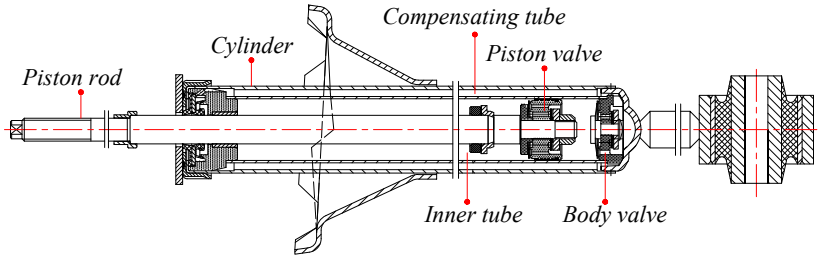

Figure 1.7: 2D assembly drawing of automotive twin-tube shock absorber with shim disc valve design.

As the piston moves upwards, oil is suck back out of the compensating tube through the body valve. The pressure difference among each chamber is related to the deflection of the damper valves. When the piston and piston rod move upward, the oil flows from rebound chamber into compression chamber via the leak restriction and the rebound valve of the piston assembly. Due to the volume of the piston rod, the oil which flows from rebound chamber into compression chamber is not enough to compensate the change of the compression chamber's volume. A part of the oil will flow from the reserve chamber into the compression chamber through the equivalent valve and the leak restriction in the body valve. As the piston and piston rod move downward, the oil flows from compression chamber into rebound chamber via the leak restriction and the flow valve of the piston assembly. Due to the volume of the piston rod, the oil which flows from compression chamber into rebound chamber is bigger than the change of the compression chamber's volume. A part of the oil will flow from compression chamber into reserve chamber through the compression valve and the leak restriction in the base valve [Dixon, 2007].

Figure 1.8 (c) illustrates the oil pressure (P_{oil}) distribution over the valve disc based on the above mentioned cyclic loading sequences. The contact force between washer and the valve disc comes from the tightening of the nut with constant force. At presence of these two loads fretting occurs at contact inter-

face, which leads to formation of micro-crack and at further steps propagation of the micro-crack under fatigue loading condition to final rupture of the valve disc.

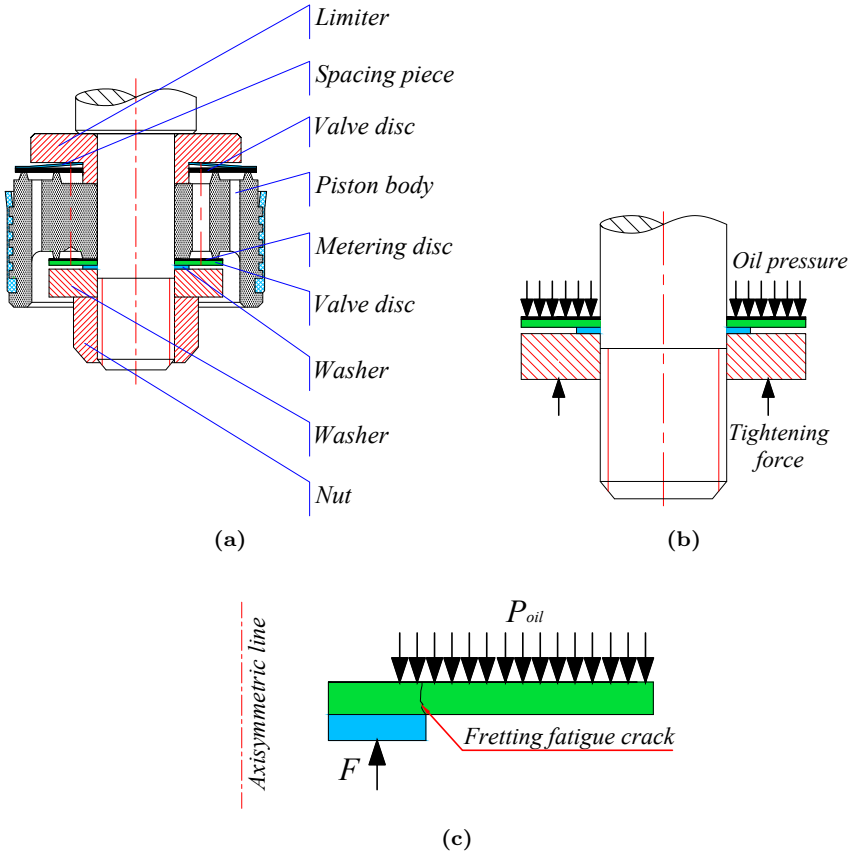

Figure 1.8: (a) detailed view of piston valve, (b) schematic view of oil pressure over valve disc and (c) schematic view of fretting fatigue failure loading and boundary conditions.

Figure 1.9 illustrates the fretting fatigue failure at automotive shock absorber valve disc. From the figure, the fretting trace of washer on top of valve disc can be seen clearly, this fretting scars leads to fretting fatigue crack initiation and propagation till sudden fracture of valve disc as depicted in Figure 1.9. More information about its failure mechanisms with more detailed fractography images are elaborated in chapter 2.

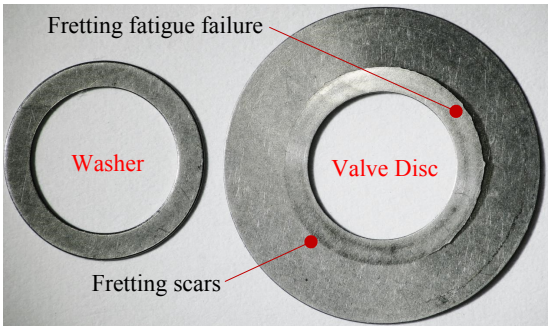

Figure 1.9: Fretting fatigue failure at automotive shock absorber valve disc.

1.4 Experimental Set-up

By a short literature review, it can be seen that there are a lot of fretting fatigue experimental set-ups that can scale down a practical application to lab scale test. All of them have some common features such as aiming to control fretting fatigue variables e.g. the slip regime, applied axial stress, tangential and contact loads and so on. However, recently thanks to ASTM E2789-10 standard guide for fretting fatigue testing [ASTM E2789-10, 2011], some of these tests can be carried out based on the standard.

First difference of different fretting fatigue rigs is based on the specimens scale, full scale or coupon scale. Full scale test rigs are directly related to a practical applications, for instance, dovetail connection [Golden and Nicholas, 2005, Golden and Calcaterra, 2006, Kermanpur et al., 2008a], wire rope connections [Azevedo et al., 2009], bolted or riveted lap connection [Wagle and Kato, 2009, Wagle and Kato, 2011, Szolwinski and Farris, 2000], Press-fit connections [Kubota et al., 2003], splined coupling [Leen et al., 2002, Ding et al., 2007a, Ratsimba et al., 2004], [Santus, 2008, Bertini et al., 2008] and Leaf spring [Aggarwal et al., 2005, Aggarwal et al., 2006]. Further classification has been done for the coupon scale test rigs. Based on their capability to apply a fretting slip amplitude, three categories are made.

The first type. One actuator test rig, is not designed to control or influence the fretting slip. In this type of test rigs the fretting fatigue test is commonly carried out on dynamic servo hydraulic machines. The pressure required to produce fretting is transmitted to the contact area between the fatigue specimen and two fretting pads via a calibrated proving ring, Figure 1.10. Each pad has

two bases (contacting surfaces) through which the contact load is exerted on the fatigue specimen.

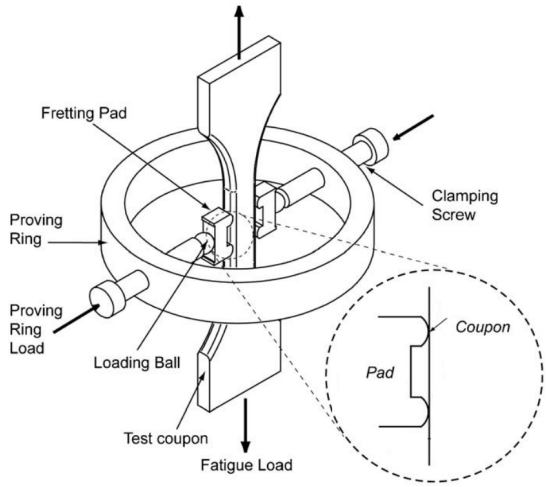

Figure 1.10: Illustration of the fretting fatigue proving ring test ring [Liu and Hill, 2009].

The second type. One actuator test rig with adjustable compliance can influence the slip in advance, but is not able to control the slip during the experiments. The schematic view of the single clamp test is shown in Fig 1.11. In contrast to the first type fretting fatigue test rig, there is a single fretting contact at each side of fatigue specimen. In this type of tests, the fretting rig is mounted on fretting fatigue apparatus pushed against fatigue specimen. Thus, the displacement amplitude at contact interface depends on the compliance of both fretting rig as well as fatigue specimen. As depicted in Figure 1.11, two fretting pads are pushed against the fatigue specimen by a contact load, F and then, the fatigue specimen is subjected to cyclic axial fatigue stress σ_{axial}. The tension at either end of the fatigue specimen is unequal due to the tangential loads Q induced by attached complaint spring to the fretting pads. This geometry is representative of a number of common fretting fatigue experiments [Cortez et al., 1999, Iyer and Mall, 2001, Lee et al., 2005, Jin et al., 2007]. In both first and second types, the slip is in phase with the fatigue force.

The third type. A modification of second type set-up involves the use of a second servo-hydraulic actuator attached to the fretting fixture, which then

applies tangential force or relative slip to pad through the fretting fixture. This modified test set-up provides a better method to control the relative fretting slip independent of other loads, i.e. bulk load on specimen and normal contact load on fretting pad. However, when no load or displacement is applied through the second actuator, a tangential force on the pad is developed through the compliance of fretting fixture. Schematic and general view of this type of fretting fatigue test rig is illustrated in Figure 1.12.

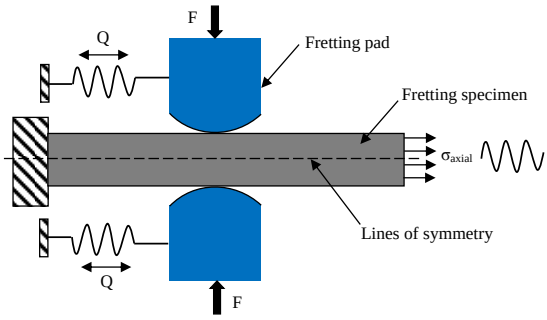

Figure 1.11: Schematic view of second type fretting fatigue test rig.

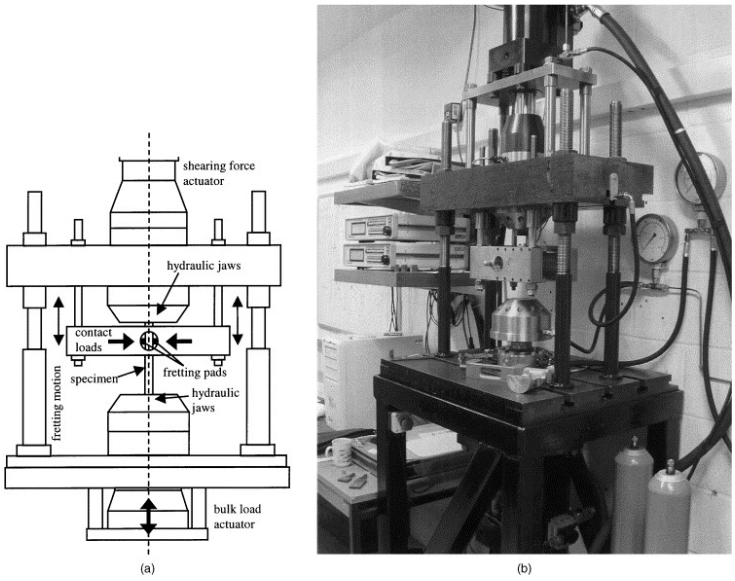

Figure 1.12: (a) Schematic view and (b) picture of third type fretting fatigue test rig [Mugadu et al., 2002].

The above represented fretting fatigue test rigs is a brief categorising of available test rigs. More detailed information about the performed experimental test is elaborated in chapter 3.

1.5 Objectives

Fretting fatigue failure evolution is caused by combination of several parameters, which can be related to different mechanical response of material. These parameters can be divided into two sets of primary and secondary variables, which have more and less influence on fretting fatigue total lifetime [Dobromirski, 1992]. In general, fretting fatigue failure process is divided into two main phases, namely crack initiation and crack propagation. The fraction of fretting fatigue lifetime spent in crack initiation and in crack propagation depends on many factors, e.g. contact stresses, amount of slip, frequency, environmental conditions, etc., and varies from one practical application to another. Therefore, both crack initiation and propagation phases are important in analysing fretting fatigue. Although several studies on fretting fatigue have been reported in literature, most of the works were of experimental nature with a simple Finite Element (FE) model to calculate contact stresses and strains. However, in fretting fatigue experiments, it is very difficult to detect the crack initiation phase; the onset of crack growth and the crack growth rate because damage and cracks are always hidden between the two contact surfaces. Therefore, numerical modelling techniques for analysing fretting fatigue crack initiation and propagation phases are very desirable. Furthermore, these numerical models could be used to predict the fatigue lifetime of components subjected to fretting conditions.

The main objective of this thesis is to develop generic numerical modelling techniques in order to predict the response of materials and the damage initiation and propagation under fatigue loading in fretting conditions. The individual objectives are summarised as follows:

- Developing FE models for crack initiation, which take into account the accumulation of damage due to cyclic loading, the triaxiality nature of stress in the damaged materials and the oscillatory slip between the two contact surfaces.
- Developing FE models for crack propagation, which take into account the effect of cyclic loading, the mode mixity and its effect on crack growth

direction, fretting conditions and contact stresses.

- Combining the FE models for crack initiation and propagation to produce a fretting fatigue lifetime prediction tool.

1.6 Thesis scopes and methodology

Following the above mentioned objectives, in this study fretting fatigue crack initiation is explained by accumulation of damage, which leads to formation of initial micro-cracks at the contact interface surface. Fretting fatigue crack propagation is defined as the advance of micro-cracks to final rupture of bulk material. Therefore, as illustrated schematically in Figure 1.13, damage and fracture mechanics approaches are used in order to model fretting fatigue crack initiation and propagation, respectively. For this purpose this thesis is organized as follows:

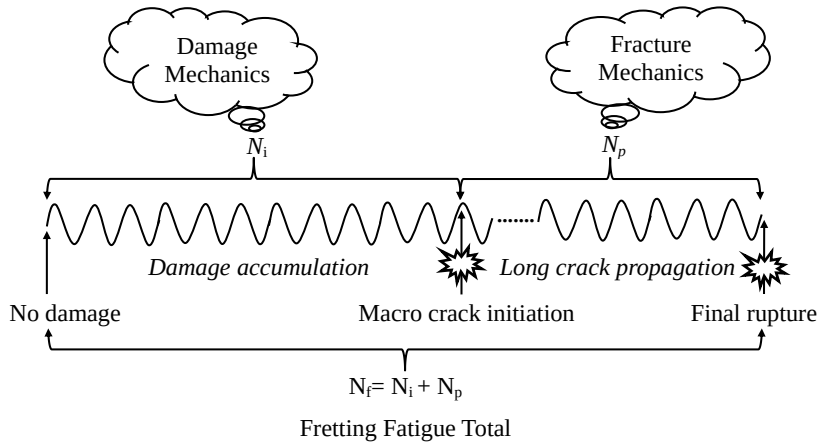

Figure 1.13: Schematic view of fretting fatigue crack initiation and propagation modelling approaches.

Chapter 2 presents a literature review on relevant works, discussing *the state of art* in the fields according to scope of this thesis. It consists of contact and failure mechanics i.e. damage mechanics, fatigue of material and fracture mechanics, followed by a comprehensive literature review on different available fretting fatigue FE approaches.

Chapter 3 describes the experimental tests that are performed to find some input parameters for FE models such as Coefficient Of Friction (COF) using Digital Image Correlation (DIC) technique. This chapter consists of different experimental set-ups i.e. fretting fatigue, Single Bolted Lap Joint (SBLJ), Double Bolted Lap Joint (DBLJ) and shock absorber practical application test. The fretted and fractured surfaces of the failed specimens are analysed in order to characterise fretting fatigue failure mode.

Chapter 4 elaborates Finite Element Analysis (FEA) of 2-D fretting and fretting fatigue contact configurations including fretting cylindrical contact model, fretting fatigue models for bridge type and single clamp types configurations, and 3-D modelling of single and double bolted lap joints along with shock absorber washer-disc contact configuration, to characterize different fretting fatigue parameters i.e. location of initial crack, slip distribution and stress distribution at contact interface.

Chapter 5 develops two uncoupled damage models based on thermodynamics potential function under elastic and elasto-plastic conditions. Eventually, the developed damage model is applied to fretting fatigue cylindrical contact configuration in order to predict crack initiation lifetime.

Chapter 6 represents two different approaches to model fretting fatigue crack propagation i.e. conventional FEM and Extended Finite Element Method (XFEM) techniques. Conventional FEM and XFEM techniques are validated by implementing some benchmark examples. Eventually, the developed FE models are implemented to fretting fatigue cylindrical contact configuration in order to find the crack propagation lifetime. Moreover, different fretting fatigue crack propagation criteria are used to find the proper crack propagation trajectory.

Chapter 7 combines the predicted fretting fatigue crack initiation and propagation lifetimes to predict fretting fatigue total lifetime for flat and cylindrical contact configurations.

Chapter 8 studies effects of different fretting fatigue variables such as phase difference and material geometrical impurities on fretting fatigue crack initiation lifetime by means of developed numerical prediction tool.

Chapter 9 outlines the conclusions from this dissertation and makes recommendations for future work.

Chapter 2

Background and literature survey

"The main idea of this chapter is about background of different approaches that are used in case of fretting fatigue problem"

2.1 Overview

The main aim of this chapter is to review *the state of art* of classical contact problem, different crack initiation and propagation FE modelling approaches and its extension to fretting and fretting fatigue cases. Therefore, first basic contact mechanics and analytical solutions associated with different fretting fatigue contact configurations are discussed in detail. Next, the tribological fretting contact characteristics are monitored aiming to distinguish between fretting fatigue and fretting wear along with review of available analytical model for frictional behaviour of contact under fretting condition. Then, the basic concept of failure mechanisms including fatigue of material, fracture and damage mechanics are reviewed. Finally, a comprehensive literature survey of available FE models of fretting fatigue contact, crack initiation and propagation is presented.

2.2 Contact mechanics

Contact problems are one of the challenging issues of Solid Mechanics, because contact is the main method of applying loads to a deformable body, which results in stress concentration in the most critical point in the body. More complexity of the contact problem appears when friction laws are taken into account, which leads to non-linear behaviour of connected bodies. These complex situation can lead to problems with existence and uniqueness of quasi-static solution and to lack of convergence of numerical algorithms. In frictional problems, there can also be lack of stability, leading to stick-slip (partial slip) regimes and frictional vibrations.

By a short literature review of the practical engineering applications in field of *solid mechanics*, it can be noticed that the vast majority of solid components are in contact to each other. These connected components are subjected to stress concentration and are therefore potential sites for mechanical failure. As mentioned by [Barber and Ciavarella, 2000], "*it is not surprising that Contact Mechanics has occupied a central place in the development of Solid Mechanics over the years and continues to do so today*".

2.2.1 Hertzian contact

Historically, the first development of analytical solution for contact for the frictionless contact of two elastic bodies, goes back to 1881 from the paper of Heinrich Hertz [Hertz, 1881]. Hertz developed a theory to calculate the contact area and pressure between the two surfaces and predict the resulting compression and stress induced in the objects. This section addresses the basics of Hertzian contact stress theory and its relation to certain aspects of fretting fatigue contact problem.

Contact between two continuous, non-conforming solids is initially a point or a line. Under the action of a load the solids deform and a contact area is formed as shown in Figure 2.1. Hertz contact stress theory allows for the prediction of the resulting contact area, contact pressure, compression of the bodies, and the induced stress in the bodies. Hertz developed his theory for contact stress after studying Newtons rings with two glass lenses. He became concerned about the effect of contact pressure between the two lenses and set out to analyse the effects. The result was the first satisfactory theory for contact mechanics and is still in use today. Hertz for developing his theory made some simplifying assumptions, which are summarized as follows:

- Surfaces are continuous and non-conforming (i.e. initial contact is a point or a line)
- Induced strains due to contact load are small
- The material behaves elastically
- The contact is frictionless

With the exception of the last hypothesis, these assumptions imply that the semi contact width is extremely smaller than the effective radius of curvature of the two connected bodies (i.e. $a << R$).

The effective radius of curvature (R^*) is defined by the radii of curvature of the two connected bodies as:

$$\frac{1}{R^*} = \frac{1}{R_1} + \frac{1}{R_2} \tag{2.1}$$

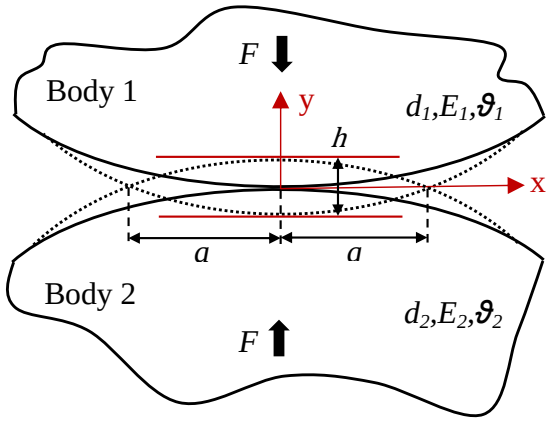

Figure 2.1: Schematic view of Hertzian contact.

In a same way the effective modulus of elasticity can also be defined by the modulus of elasticity and Poisson's ratio of the individual connected bodies as:

$$\frac{1}{E^*} = \frac{1-\nu_1^2}{E_1} + \frac{1-\nu_1^2}{E_2} \tag{2.2}$$

A normal load applied to two bodies in contact will give rise to a rectangular contact area due to the deformation of the two bodies. The force, F, applied over the area gives rise to a pressure distribution in the materials with a maximum (P_{max}) along a line at the centre of the area. By considering two solid elastic cylinders held in contact by forces F uniformly distributed along the cylinder length l. The maximum pressure and the semi contact width (a) are given as:

$$p_{max} = \frac{2F}{\pi a l} \tag{2.3}$$

$$a = \left[\frac{2F}{\pi l} \times \frac{\left(1-\nu_1^2/E_1\right) + \left(1-\nu_2^2/E_2\right)}{1/d_1 + 1/d_2}\right]^{1/2} \tag{2.4}$$

The dashed line in Figure 2.1 indicates overlap of the two surfaces if deformation did not occur depicting the geometry necessary for these calculations. The total compression between the two bodies is given by:

$$h = \frac{a^2}{R^*} \tag{2.5}$$

The contact pressure distribution at contact interface (x is the horizontal distance from the centre of contact) can be calculated as:

$$p(x) = -p_{max}\sqrt{a^2 - x^2} \tag{2.6}$$

Under plain strain conditions (ϵ_z=0), the third stress component σ_z is found to be dependent on Poisson's ratio; $\sigma_z = \nu(\sigma_x + \sigma_y)$. Hence, for typical materials (ν= 0.3) the condition $\sigma_z \approx \sigma_x = \sigma_y = -p_{max}$ creates a near hydrostatic stress state at the contact interface. The subsurface stresses along the centreline of the contact can be now obtained and written as:

$$\sigma_x(y) = -p_{max}\left[\left(\frac{1 + 2(\frac{y}{a})^2}{\sqrt{1 + (\frac{y}{a})^2}}\right) - 2\left|\frac{y}{a}\right|\right] \tag{2.7}$$

$$\sigma_y(y) = -p_{max}\frac{1}{\sqrt{1 + \left(\frac{y}{a}\right)^2}} \tag{2.8}$$

$$\sigma_z(y) = -2\nu p_{max}\left[\sqrt{1 + 2\left(\frac{y}{a}\right)^2} - \left|\frac{y}{a}\right|\right] \tag{2.9}$$

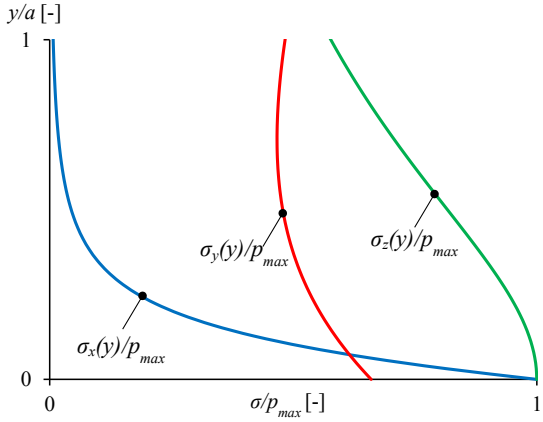

Figure 2.2: Magnitude of stress components below the surface as a function of maximum pressure for contacting cylinders (p_{max}= 254 MPa, d= 50 mm, L= 4 mm, a= 0.31 mm).

When these equations are plotted as a function of maximum contact pressure up to a distance a below the surface contact point at x= 0, the plot of

Figure 2.2 is generated, based on a Poisson's ratio of 0.3, elasticity modulus of 71 GPa, contact load F= 500 N and R= 25 mm for both in contact cylinders.

Another type of contact configuration, which is used in this study, is flat on flat contact. This type of contact is called conforming contact, where the contact width is dependent of the applied contact load [Hills and Nowell, 1994]. As depicted in Figure 2.3, this type of contact configuration is distinguished by its sharp corners, which act as stress riser in contact with other components. By assuming the plane elastic half-space hypothesis, the analytical solution for flat on flat contact configuration gives rise to an asymptotic pressure distribution at contact edges [Johnson and Johnson, 1987]. The analytical solution for contact pressure distribution can be written as:

$$p(x) = \frac{F}{\pi\sqrt{a^2 - x^2}} \tag{2.10}$$

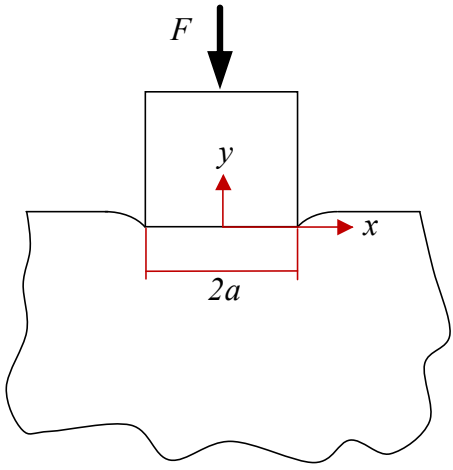

Figure 2.3: Flat on flat contact configuration.

Figure 2.4 illustrates the variation of normalised contact pressure over contact interface. As it can be seen from the figure, at contact edges i.e. x= $\pm a$, the pressure distribution shows singular behaviour.

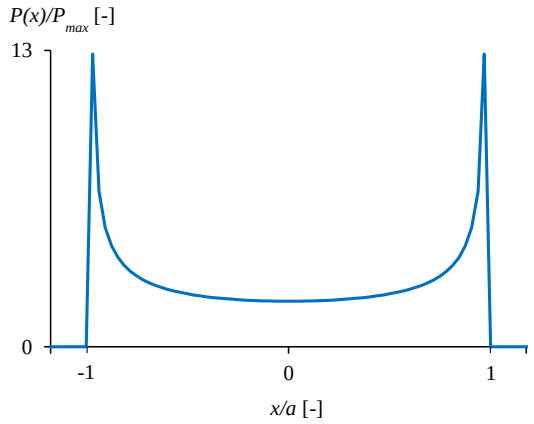

Figure 2.4: Contact pressure distribution for flat on flat contact configuration (p_{max}= 254 MPa).

2.2.2 Fretting contact

Cattaneo [Cattaneo, 1938] and Mindelin & Deresiewicz [Mindlin and Deresiewica, 1953] independently have extended the Hertz' original theory to cover the application of tangential load and at the presence of friction at the interface. Under this condition the the contact will be divided into distinguished slip and stick zones as depicted in Figure 2.5. The Coulomb friction model was employed as:

$$q(x) \leq \mu p(x) \tag{2.11}$$

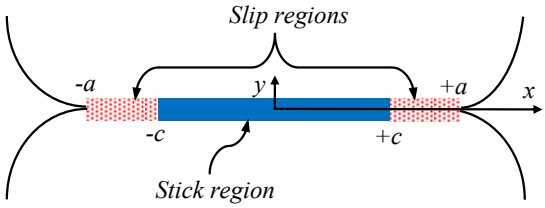

Figure 2.5: By applying tangential load the contact area is divided into slip and stick zones.

Where *q(x)* is the shear traction at point x, and μ is the coefficient of friction.

If the applied tangential load Q is less than μF, partial slip occurs and a central stick zone of half-width c can be developed with a partial slip zone occurring at the edge, c$\leq|\ x\ |\leq$ a. Therefore, the shear traction distributions are provided by the following equation:

$$q(x) = \begin{cases} -\mu p_{max}\sqrt{1-(x/a)^2} & c \leq |\ x\ | \leq a \\ -\mu p_{max}\left[\sqrt{1-(x/a)^2} - 2\dfrac{c}{a}\sqrt{1-(x/c)^2}\right] & |\ x\ | < c \end{cases} \tag{2.12}$$

where c is a function of Q:

$$\frac{c}{a} = \sqrt{1-\frac{Q}{2\mu F}} \tag{2.13}$$

Maouche et al. [Maouche et al., 1997] investigated a detailed variation of the shear traction within one fretting cycle. Figure 2.6 illustrates the distribution of normalised frictional shear stress versus the normalized contact area.

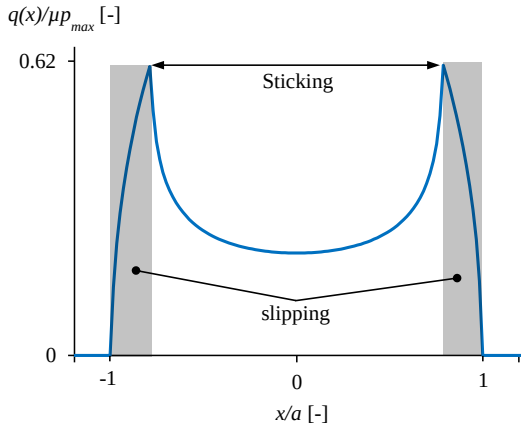

Figure 2.6: Normalised frictional shear stress distribution versus normalised contact distance for F= 200 N, Q= 50 N, $Q/\mu F$= 0.5 .

2.2.3 Fretting fatigue contact

Hills and Nowell [Hills and Nowell, 1994] recognized the application of an axial stress causing a shift in the stick zone and in turn a change in the distribution

of the frictional shear stress in the contact zone and modifies the solutions of Cattaneo and Mindlin [Cattaneo, 1938, Mindlin and Deresiewica, 1953]. They began with a plane strain assumption and the corresponding strain induced by the axial tensile stress. They continue by assuming that for two similar elastic bodies the applied axial stress results in relative tangential displacement as:

$$\frac{1}{A}\frac{\partial g}{\partial x} = \frac{1}{\pi}\int_{-a}^{a}\frac{q(\xi)}{(x-\xi)}d\xi \tag{2.14}$$

where ∂g is relative tangential displacement at contact interface, $q(\xi)$, is the shear stress distribution and A can be written as:

$$A = 2\left\{\frac{1-\nu_1^2}{E_1} + \frac{1-\nu_2^2}{E_2}\right\} \tag{2.15}$$

Hills and Nowell [Hills and Nowell, 1994] assumed that the axial tensile stress to be applied under plain strain condition, therefore, the corresponding strain in x-direction can be written as:

$$\epsilon_x = \frac{\sigma(1-\nu^2)}{E} \tag{2.16}$$

The difference in relative displacement gradients $\left(\frac{\partial g}{\partial x}\right)$ in the stick zone was written as:

$$\frac{\partial g}{\partial x} = \frac{\partial u_1}{\partial x} - \frac{\partial u_2}{\partial x} = -\frac{\sigma(1-\nu^2)}{E} \tag{2.17}$$

Therefore, the Equation 2.14 can be written as:

$$\frac{-\sigma}{4} = \frac{1}{\pi}\int_{-a}^{a}\frac{q(\xi)}{(x-\xi)}d\xi \tag{2.18}$$

The applied axial stress produces a shift in the stick zone, e. This means that the centre of contact can lie anywhere from x=e-c to x=e+c. Thus, the solution can be assumed to be a perturbation of the full sliding condition, so that:

$$q(x) = -\mu p_{max}\sqrt{1-(x/a)^2} + q'(x) \tag{2.19}$$

where q'(x)= 0 is satisfied in the slip zones. By substituting Equation 2.19

into Equation 2.14 and normalizing yields to:

$$\int_{-1}^{1} \frac{q'(x)}{s-t} dt = \frac{\mu p_{max} \pi c}{a} \left[s + \frac{e}{c} + \frac{b}{c} \right] \tag{2.20}$$

where s=(x-e)/c, t=(ξ-e)/c and b=σa/(4μp_{max}). Solving Equation 2.20 for e using the following additional consistency equation is obtained:

$$\int_{-1}^{1} \frac{\xi + (e/c) - (b/c)}{\sqrt{1-\xi^2}} d\xi = 0 \tag{2.21}$$

which yields

$$e = b = \frac{\sigma a}{4\mu p_{max}} \tag{2.22}$$

and q'(x) can be written as:

$$q'(x) = -\mu p_{max} \frac{c}{a\sqrt{1-\left(\frac{x-e}{c}\right)^2}} \tag{2.23}$$

Figure 2.7 depicts the variation of normalised frictional shear stress versus the normalized contact area under fretting fatigue loading condition.

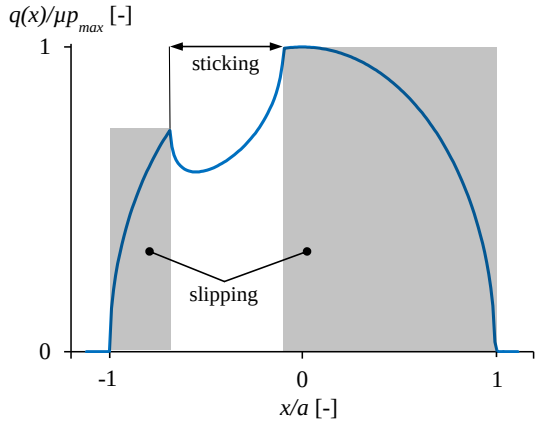

Figure 2.7: Normalised frictional shear stress distribution versus normalised contact distance for $Q/\mu F$= 0.91 and $\sigma_{axial}/\mu p_{max}$= 1.56.

The above analytical solution is valid as long as the applied axial load is

low compared with the tangential load. By applying larger value of axial load, one edge of the stick zone approaches the edge of contact. Therefore, according to Hills and Nowell [Hills and Nowell, 1994] the current solution is valid if $e+c \leq a$ i.e.

$$\frac{\sigma}{\mu p_{max}} \leq 4\left(1-\sqrt{1-Q/\mu F}\right) \tag{2.24}$$

At presence of larger applied axial load, reverse slip occurs at one edge of the contact as illustrated in Figure 2.8. This variation of frictional shear stress distribution at contact interface is an important piece of evidence for showing that the axial bulk load applied to the fatigue specimen has significant effect on shear stress distribution at contact interface.

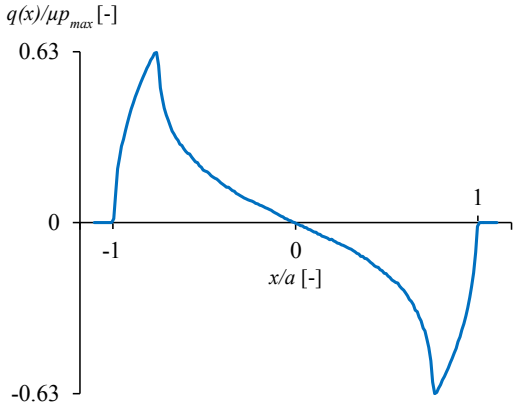

Figure 2.8: Normalised frictional shear stress distribution versus normalised contact distance for $Q/\mu F = 0$ and $\sigma_{axial}/\mu p_{max} = 1$.

The σ_x distribution or the total stress along the contact interface in the x-direction can be expressed as follows [Hills and Nowell, 1994]:

$$\sigma_x = \sigma_{x,normal} + \sigma_{x,tangential} + \sigma_{x,axial} \tag{2.25}$$

where $\sigma_{x,normal}$, $\sigma_{x,tangential}$ and $\sigma_{x,axial}$ are the fraction of tangential stress which are generated by contact, tangential load and axial stress, which can be written as:

$$\sigma_{x,normal} = -P_{max}\frac{\sqrt{a^2+x^2}}{a} \tag{2.26}$$

$$\sigma_{x,tangential} = 2\mu P_{max} - \frac{2}{\pi}\int_{-a}^{a}\frac{q'(x)}{x+a}dx \tag{2.27}$$

2.2.4 Tribological behaviour of contact

Tribology is defined as a study that deals with the design, friction, wear, and lubrication of interacting surfaces in relative motion. In this section, some basic concepts of tribological behaviour of fretting fatigue contact are reviewed.

Fretting mechanism

Fretting is a complex tribological problem, which depends on different parameters having influence on response of connected surfaces e.g. Coefficient of Friction (COF), roughness, slip amplitude, environmental conditions and so on. Each of the these parameters has significant impact on fretting and fretting fatigue response of material. As mentioned above fretting occurs under relatively small slip amplitude between connected surfaces. In *state of art* work, Vinsgsbo and Soderberg [Vingsbo and Söderberg, 1988] defined fretting damage as *"the damage inflicted to tribosurfaces due to oscillatory displacements at low amplitude"*. However, they stated that there is no general definition for *"low amplitude"*. Although they mentioned that it is obvious that a transition to reciprocating sliding must occur, historically fretting has been categorized as occurring at relative slip amplitude up to around 300 μm. By exceeding the slip amplitude above this limit, the relative moment is known as "reciprocating sliding" [Vingsbo and Söderberg, 1988]. They measured the global slip amplitude by means of experimental approach. They have tried to distinguish different regimes of fretting under dynamic tangential load and displacement measurements as:

- *Stick regime*; Very limited surface damage by oxidation and wear. No fatigue crack formation observed up to one million cycles. *Low damage fretting.*
- *Mixed stick-slip regime*; Wear and oxidation effects are small. Accelerated crack growth may result in strongly reduced fatigue life. *Fretting fatigue.*
- *Gross slip regime*; Severe surface damage by wear, assisted by oxidation. Crack formation limited. *Fretting wear.*

- *Reciprocating sliding regime*; Wear rates become identical to those in unidirectional sliding.

There is a significant amount of evidence that the most damaging scenario is when a large portion of the contact interface sees no relative displacement (sticking) and the edges of contact experience small amplitudes of relative displacement (slipping) i.e. partial slip condition. Figure 2.9 shows that sticking contact and gross sliding are not as damaging as the partial slip (mixed stick and slip) regime. From Figure 2.9, it can be seen that as expected by changing the contact status from sticking to gross sliding the amount of wear increases significantly. By transition from partial slip to gross sliding regime, even a minor rise in fretting slip amplitude results in a large effect on wear rate. Fretting fatigue life is a minimum at the transition between partial slip and gross sliding condition.

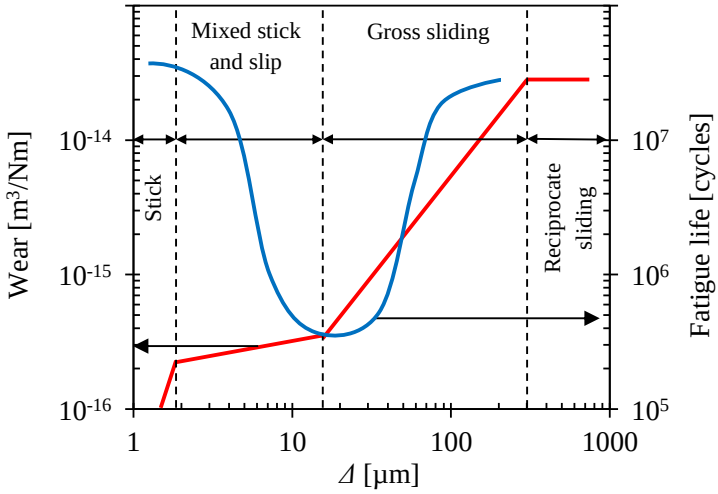

Figure 2.9: Schematic view of the variation in fretting fatigue life and fretting wear rate with experimentally measured global displacement amplitude [Vingsbo and Söderberg, 1988].

There are always two failure mechanisms involved in fretting problems, which are competing to each other and are called wear damage and fatigue cracking. By increasing the fretting slip amplitude and transferring from sticking to partial slip regime, the damage experienced by the material increases

leading to reduced life. The motion of the fretting contact is causing damage, so the more the contact moves, the more the surface damages. On the other hand under partial slip regime condition fretting fatigue cracks nucleate at the surface somewhere in the slip zone at/near the edge of contact. As the wear rate increases, the probability of a fatigue crack being removed by the advancing wear. If a crack is less likely to propagate, the fatigue life will increase.

The contact condition during fretting is described by hysteresis loops; i.e tangential force Q is plotted versus displacement δ. The area inside the loop describes the amount of energy dissipated by frictional work. Figure 2.10 depicts two different types of contact conditions with their corresponding characteristics hysteresis loops for spherical contact configuration taken from [Fouvry et al., 2003]. The amount of slip at the edge of contact increases as the tangential force increases and the hysteresis loop widens. When the ratio of tangential force to normal force rises above the COF, the entire interface experiences slip.

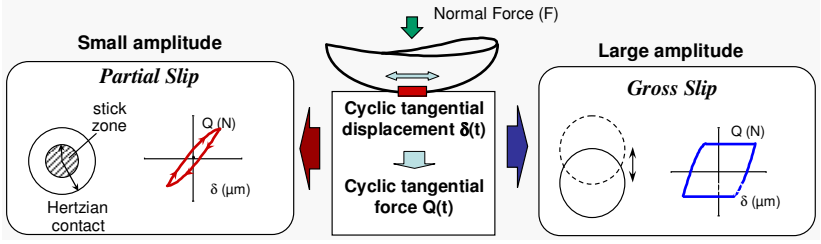

Figure 2.10: Illustration of partial slip and gross slip contact conditions showing the corresponding characteristic hysteresis loop [Fouvry et al., 2003].

During on going fretting and fretting fatigue tests, the contact conditions change. A three dimensional plot of friction force versus displacement as a function of cycles, called a *friction log*, describes the change in contact condition as a function of cycles [Colombie et al., 1984]. During fretting procedure, the running condition is divided into three different regimes: as mentioned above, the Partial Slip Regime (PSR), Mixed Slip Regime (MSR) and Gross Slip Regime (GSR). Figure 2.11 shows the evolution of these three regimes with the corresponding characteristic friction logs. The partial slip regime is distinguished by a partial slip contact condition for all cycles. The friction log for partial slip shows hysteresis loops that stay closed for all cycles. The mixed slip regime is characterized by gross slip initially and a transition to partial slip as cycling continues as illustrated in the friction log as open loops

that transition to closed loops over the duration of cycling. As fretting damage is induced at contact interface, friction is increasing with cycles. Finally, the gross slip regime is defined by gross slip conditions for all cycles.

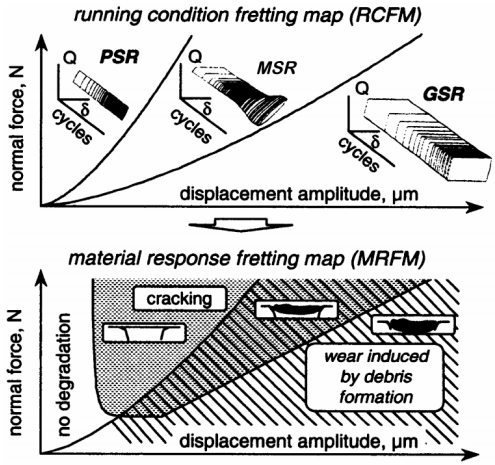

Figure 2.11: Running condition fretting map showing corresponding friction logs and material response fretting map showing corresponding damage mechanisms [Fouvry et al., 2003].

Friction

Frictional resistance to the relative motion of two solid objects is usually proportional to the force which presses the surfaces together, as well as, the roughness of the surfaces. The frictional force is also presumed to be proportional to the coefficient of friction . However, the amount of force required to move an object starting from rest is usually greater than the force required to keep it moving at constant velocity once it is started. Therefore, in general two coefficients of friction are sometimes quoted for a given pair of surfaces namely, a static and kinetic COF.

Fretting is a challenging phenomenon, which is induced by combination of different sciences i.e. tribology, contact mechanics, fatigue and fracture behaviour of material. Dobromirski [Dobromirski, 1992] counted fifty different variables, which have effect on fretting response of connected materials. He classified the fretting fatigue variables to two sets of primary and secondary variables, which have direct and indirect effects on fretting fatigue behaviour,

respectively. He considered normal contact load, COF and relative slip amplitude as primary variables. Between the primary variables, COF is an important parameter, which can be affected by other primary variables. For instance it has been proven that COF is affected by slip amplitude distribution over contact interface [Hills et al., 1988a, Jin and Mall, 2002]. It has been also shown that COF changes by increasing the number of cycles [Hills et al., 1988a, Szolwinski et al., 1997, McColl et al., 2004]. COF is also required to compute the stress and strain field in the contact zone, which affects the crack nucleation and growth in fretting [Milestone and Janeczko, 1971, Nix and Lindley, 1985, Nix and Lindley, 1988, Venkatesh et al., 2001].

In fretting contact problems, there are also two categories; Static [Hills et al., 1988b] and dynamic [Jin and Mall, 2004b]. The static COF is measured either before a fretting fatigue test or after carrying out the fretting test for a certain number of cycles as carried out in [Jin and Mall, 2004b]. The dynamic COF is easy to be confused with the kinetic one, which is defined as the friction during gross sliding [Endo et al., 1974]. When the fretting pads are in gross sliding mode, the dynamic COF is equal to kinetic COF. However, when the contact condition is in the state of partial slip ($Q < \mu F$), the dynamic COF is smaller than the kinetic one.

Figure 2.12 indicates the variation of COF versus the number of fretting cycles under different contact loads. As it can be noted, COF increases rapidly in the initial stages of testing, when the number of fretting cycles exceeds 2000 cycles, COF reaches a plateau [McColl et al., 2004]. From this figure, it also can be found that the stable COF is reduced with an increase in normal load. The same behaviour has been reported by Hills et al. and Szolwinski et al. [Hills et al., 1988a, Szolwinski et al., 1997].

Generally, under partial slip condition, the COF is often assumed to be constant along the contact surface. There are different ways to calculate the COF under partial slip and gross sliding conditions. Measuring COF for fretting fatigue case under partial slip condition goes back to late 70's by work of Endo et al. [Endo et al., 1974]. They found that during fretting tests between two steel components, the dynamic COF increased initially and then stabilized to an almost constant value for the duration of the test after 50,000 cycles. They also reported that in gross sliding, the kinetic COF remained constant, which was almost independent of contact pressure and contact geometry. Switek [Jin and Mall, 2000] studied the effect of relative slip and clamping pressure on the

COF between SAE 1045 steels. He realized that the COF increased with the relative slip up to δ = 15-20 μm and then attained a steady value for the higher slip amplitude. At slip amplitudes smaller than the critical ones, the COF attained a higher value at the lower contact pressure. Lee and Mall [Lee and Mall, 2004] also studied the effects of several fretting variables on COF. These variables included contact pressure, relative slip, temperature, cyclic frequency, etc. They found that an increase in slip amplitude results in an increase of the COF, while an increase in contact pressure, cyclic frequency, and temperature decreases the COF, which is similar to the observations made by the previous researchers [Endo et al., 1974, Jin and Mall, 2000].

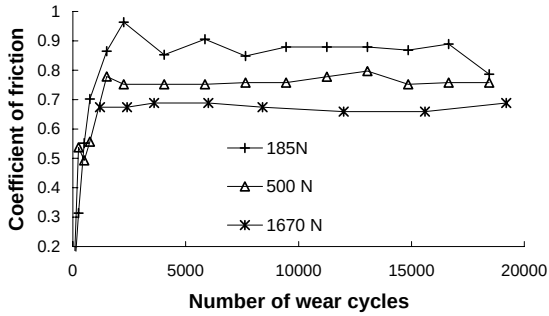

Figure 2.12: Coefficient of friction versus number of fretting cycles [McColl et al., 2004].

Jin and Mall [Jin and Mall, 2004b] investigated the relationship between the dynamic COF and relative slip under independent pad displacement condition for Ti-6Al-4V alloy. They noted that the COF increased linearly from 0.33 to 1.0 with slip amplitude until δ = 50-60 μm and after that it became constant. As this trend found by other researchers [Nix and Lindley, 1988] it can be concluded that the COF increases linearly with the slip amplitude in partial slip condition and reaches to a steady value in gross sliding condition.

Fouvry et al. [Fouvry et al., 2004] tried to define the transition from partial to gross slip condition using an energy discontinuity analysis. For this purpose they used incremental displacement method introduced by Voisin et al. [Voisin et al., 1995]. As depicted in Figure 2.13 this method consists in successive increase of displacement amplitude from very small in partial slip regime to large displacement in gross sliding condition.

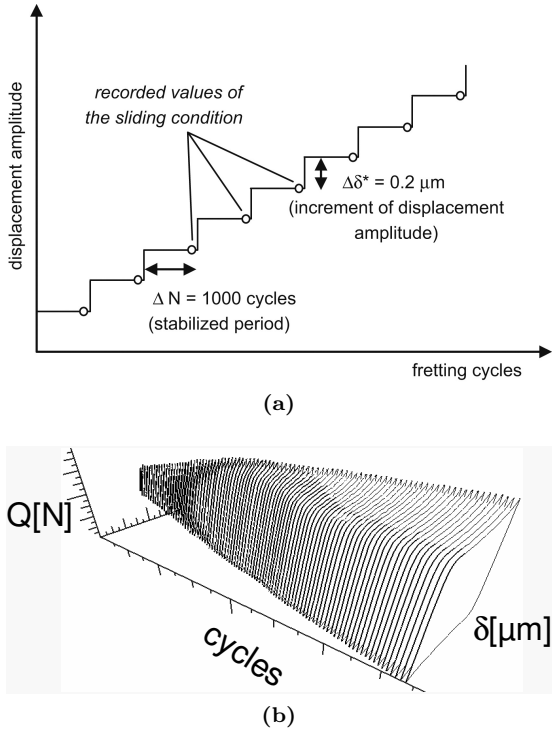

Figure 2.13: Illustration of the methodology to define the sliding transition between partial and gross slip condition (a) Displacement increments versus fretting cycles and (b) fretting loop [Kubiak et al., 2010].

Slip amplitude and dissipated energy at contact interface, which is represented by hysteresis on fretting loop are relatively low under partial slip condition. Fretting damage in the partial slip regime is usually limited to the slip bands at leading and trailing edges of contact. By transferring to gross sliding condition, slip amplitude and therefore energy dissipated at the contact are much higher. Therefore, the wear rate is higher at contact interface due to having full sliding all over the contact interface. For a given normal load, if the imposed slip amplitude increases, the contact condition transfers from the partial to gross sliding. Fouvry et al. [Fouvry et al., 1995] quantified this transition by following the evolution of the normalised tangential force amplitude (Q/F) and a non-dimensional sliding criterion defined as the ratio between the dissipated energy (E_d) and the total energy of the cycle (E_t) as depicted in Figure 2.14. Therefore, for each transition condition the corresponding COF

can be determined.

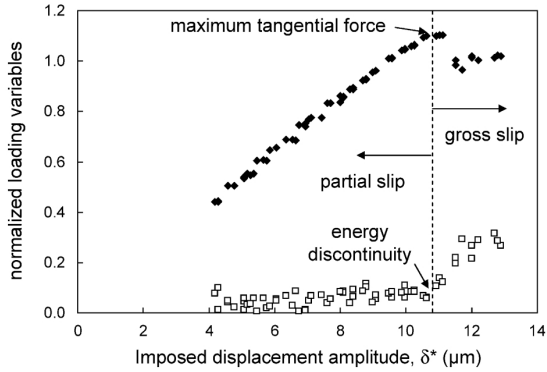

Figure 2.14: Illustration of the methodology to define the sliding transition between partial and gross slip conditions. [Fouvry et al., 2004].

Hills et al. [Hills et al., 1988b] determined the effect of number of cycles on the dynamic COF for Ti-6Al-4V. They have performed two sets of tests to investigate the increase in friction experimentally. They used the first type test rig as schematically shown in Chapter 1 in Figure 1.11. In the fist set, the springs were adjusted to be stiff and the shear force developed was sufficient to cause sliding. They found that the tangential load saturated at a constant value after certain amount of cycles. However, they realised that after almost 50 of cycles, the average COF had risen to the point where the normal load was able to resist relative motion without sliding, where in that regime it was impossible to determine the COF. In the second set of tests, a more compliant spring setting has been chosen so that partial slip existed from an early stage test. After 10^4 cycles they stopped the test and a large value of Q was applied monotonically so that sliding occurred. The initial value of average COF $\overline{\mu}$, which is defined as the ratio Q/F during sliding was found 0.4. They have also revealed that the surface modification occurs under partial slip since the measured value for $\overline{\mu}$ was higher than the applied ratio Q/F= 0.24.

Hills et al. [Hills et al., 1988b] have tried to relate $\overline{\mu}$ to the true coefficient of friction in the slip zones after n cycles, μ_n. They assumed that the COF in the slip zone was a function of fretting cycles and reached to a value μ_n after n cycles. They divided the contact zone in three portions and derived an analytical equation relating the stick and slip zone COFs with the average

COF, $\overline{\mu}$. The COF in the stick zone was considered to be constant during fretting at the initial value of μ_0. The ratio of Q_{slip}/F provides the average COF, $\overline{\mu}$, which is the static COF as introduced above. Once $\overline{\mu}$ is measured, μ_n could be calculated according to following procedure. The $\overline{\mu}$ can be written as:

$$\overline{\mu} = \frac{Q_{slip}}{F} = \frac{\int_{-a}^{a} q(x)dx}{\int_{-a}^{a} p(x)dx} \tag{2.28}$$

They have assumed that the initial COF is uniformly μ_n and the application of the tangential load, Q, results in Mindlin-type contact, which leads to having a central stick zone (i.e. $-c_0 \leq \mathrm{x} \leq +c_0$) bordered by slip zones. Hills et al. [Hills et al., 1988b] have shown that during a fretting test after n cycles the size of stick zone increases and the COF in the slip zone being μ_n. The size of new stick zone c_n can be written as:

$$\left(\frac{c_n}{a}\right)^2 = 1 - \frac{Q}{\mu_n F} \tag{2.29}$$

and the frictional shear stress distribution at contact interface can be written as:

$$q(x) = -\mu_n \left[p(x) - p_{max} \frac{c_n}{a} \left(1 - \left(\frac{x}{c_n} \right)^2 \right)^{1/2} \right] \tag{2.30}$$

Eventually, by substituting Equations 2.6 and 2.30 into 2.28 and carrying out the integration they came up to an expression, which was derived in the final correct form in [Araujo and Nowell, 2002] and can be written as:

$$\overline{\mu} = \mu_n + \left\{ \frac{4Q}{\pi F} \left[\frac{\pi}{2} - \cot\theta_s - \theta_s \right] - \frac{\pi}{2} \left[\mu_n \phi_s - \frac{Q}{F} \tan\phi_s \right] \right\} \tag{2.31}$$

where

$$\theta_s = \sin^{-1} \sqrt{\frac{Q}{\mu_n}} \tag{2.32}$$

and

$$\phi s = \cos^{-1} \sqrt{\frac{Q}{\mu_n}} \tag{2.33}$$

This equation has been extended to flat and rounded geometries in [Dini and Nowell, 2003]. Szolwinski et al. [Szolwinski et al., 1997] have also used the increasing amplitude waveform, rather than the monotonic introduced by Hills [Hills et al., 1988b], in order to detect the onset of sliding during condition of cyclic fretting loading for AL 2024-T351. Following the same experimental approach they could measure the $\overline{\mu}$= 0.50, then by implementing Equation 2.31 the COF at slip zone was found as $\mu_n \approx 0.65$.

Fretting wear VS fretting fatigue

Wear and fatigue are the two primary modes of failure in fretting contacts. In order to characterise the failure process, it is necessary to determine whether the component subjected to fretting condition fails due to either fretting wear or fretting fatigue. The principles for making this decision are straight forward, however for each practical application, more in depth investigation is needed. In first instance, the main difference is that for fretting fatigue case the component under fretting condition is subjected to alternating tensile bulk stress. The fretting contact serves as a stress concentration, which initiates a crack and reduces the fatigue life of the part. These fretting cracks appears at contact interface due to accumulation of damage and propagates the initial crack up to final rupture of bulk material. At presence of the bulk stress, the contact may fail from fretting wear or fretting fatigue; this depends upon the fretting slip amplitude. At absence of bulk stress, the component is highly unlikely to experience fretting fatigue failure. If a fatigue crack initiates at the fretting contact, it is likely to grow a short distance from the contact and will be arrested.

When fretting fatigue phenomenon occurs under partial slip regime, it is known that fretting wear amount is negligible compared to gross sliding regime. In fretting fatigue, fretting damage initiation or cracking governed by fretting and wear appears after transition to gross sliding as illustrated schematically in Figure 2.15.

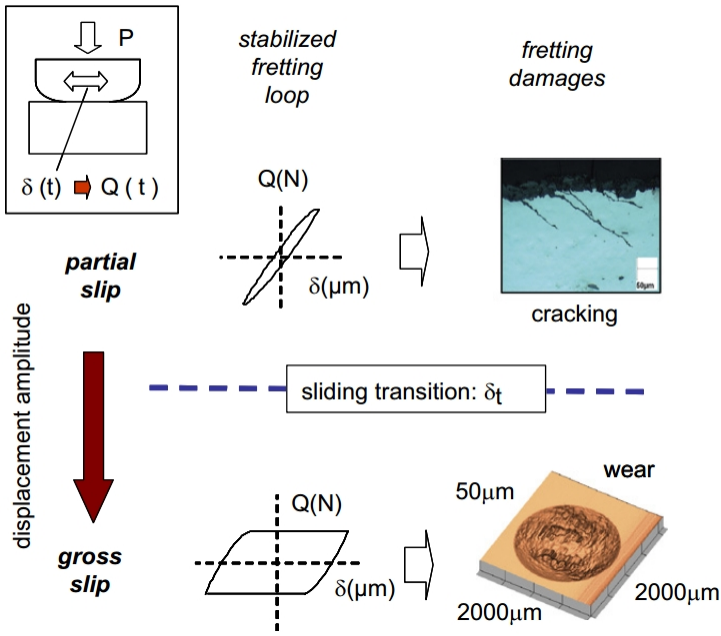

Figure 2.15: Illustration of the fretting damage versus the imposed sliding condition [Meriaux et al., 2010].

2.3 Basic concept of failure mechanisms

Two main steps in the journey of failure analysis are: a) identification of failure mode and b) failure mechanisms. By definition, failure mode is the manner whereby the failure is observed. Generally, it describes the way in which the failure happens and its impact on equipment operation. Failure modes must be determined according to the performance different components. Since it is possible to have several causes for the same failure mode, all the probable and independent causes for each failure mode must be identified and described. Depending on how one looks at it, a failure mode could also cause the failure of another element in the system.

Failure mechanism is the actual physical defect or condition that causes the failure mode to occur. For instance physical, chemical, mechanical or other processes that lead to failure is called failure mechanisms. It is essential to distinguish between failure modes and failure mechanisms. For instance, wear and fatigue are not failure modes, they are failure mechanisms. As mentioned

above fretting fatigue failure mechanism is a complex process, which is a combination of different failure mechanisms. In this study damage and fracture mechanics approaches is used to deal with fretting fatigue crack initiation and propagation, respectively. Therefore, in this section the basic concept of fatigue of material, damage and fracture mechanics are reviewed.

2.3.1 Fatigue of materials

Fatigue is one of the failure modes of a structural element, which are subjected to a repetitive load application. As a simple example of life, we are not able to break a simple clip by applying a constant force, but if we apply a repetitive force, sooner or later the clip will break. This repetitive force even smaller than the ultimate load of material will cause material failure by the phenomenon called fatigue. It has been estimated that fatigue contributes to approximately 90% of all mechanical service failures [Campbell, 2008]. Fatigue is a problem that can affect any part or component that moves. Auto-mobiles on roads, aircraft wings and fuselages, ships at sea, nuclear reactors, jet engines, and land-based turbines are all subject to fatigue failures. Fatigue was initially recognized as a problem in the early 1800s, when investigators in Europe observed that bridge and rail-road components were cracking when subjected to repeated loading [Campbell, 2008]. As the century progressed and the use of metals expanded with the increasing use of machines, more and more failures of components subjected to repeated load were recorded. Nowadays, structural fatigue has assumed an even greater importance as a result of the ever-increasing use of high-strength materials and the desire for higher performance from these materials. Fatigue depends on several factors. For instance an air-plane structural components fatigue life depends of the following points:

- The material properties against fatigue.
- Stress concentration factors applied to the structural component.
- Amplitude of the load applied to structure.
- Frequency of application of the load.
- The relation between the minimum and maximum applied load.

There are three basic factors necessary to cause fatigue: (a) a maximum tensile stress of sufficiently high value, (b) a large enough variation or fluctuation in the applied stress, and (c) a sufficiently large number of cycles of the

applied stress. There are many types of fluctuating stresses. A fully reversed stress cycle, where the maximum and minimum stresses are equal, is commonly used in testing. Another common stress cycle is the repeated stress cycle, in which there is a mean stress (σ_m) applied in addition to the maximum and minimum stresses i.e. positive stress ratio. The last type of loading cycle is the random or irregular stress cycle, in which the part is subjected to random loads during service. A fluctuating stress is made up of two components: a mean or steady stress, σ_m, and an alternating or variable stress, σ_a. The stress range, σ_{range}, is the difference between the maximum and minimum stress in a cycle:

$$\sigma_{range} = \sigma_{max} - \sigma_{min} \tag{2.34}$$

The alternating stress is one-half the stress range:

$$\sigma_a = \frac{\sigma_{range}}{2} = \frac{\sigma_{max} - \sigma_{min}}{2} \tag{2.35}$$

The mean stress is the algebraic average of the maximum and minimum stress in the cycle:

$$\sigma_m = \frac{\sigma_{max} + \sigma_{min}}{2} \tag{2.36}$$

Two ratios frequently used in presenting fatigue data are:

$$R_s = \frac{\sigma_{max}}{\sigma_{min}}, \quad \text{Stress ratio} \tag{2.37}$$

$$R_A = \frac{\sigma_a}{\sigma_m} = \frac{1 - R_s}{1 + R_s}, \quad \text{Amplitude ratio} \tag{2.38}$$

High and low cycle fatigue

High-cycle fatigue consists a large number of cycles ($N \geq 10^5$ cycles) and an elastically applied stress. High-cycle fatigue tests are usually carried out for 10^7 cycles and sometimes 5×10^8 cycles for non-ferrous metals [Campbell, 2008]. Although the applied stress is low enough to be elastic, plastic deformation can take place at the crack tip. High-cycle fatigue data are usually presented as a plot of stress, S, versus the number of cycles to failure, N (known as S-N curve). A log scale is used for the number of cycles. The value of stress, S, can be the maximum stress, σ_{max}, the minimum stress, σ_{min}, or the stress amplitude, σ_a. The S-N relationship is usually determined for a specified value of the mean stress, σ_m, or one of the two ratios, R_s or R_A. The fatigue life

is the number of cycles to failure at a specified stress level, while the fatigue strength (also known as the endurance limit) is the stress below which failure does not occur. As the applied stress level is declined, the number of cycles to failure rises. Fatigue cracking can occur quite early in the service life of the component by the formation of a small crack, generally at some point on the external surface. The crack then propagates slowly through the material in a direction roughly perpendicular to the main tensile axis as depicted in Figure 2.16 [Smallman and Bishop, 1999]. Figure 2.17 [Campbell, 2008] illustrates the typical fracture surface of a fatigued high strength steel component.

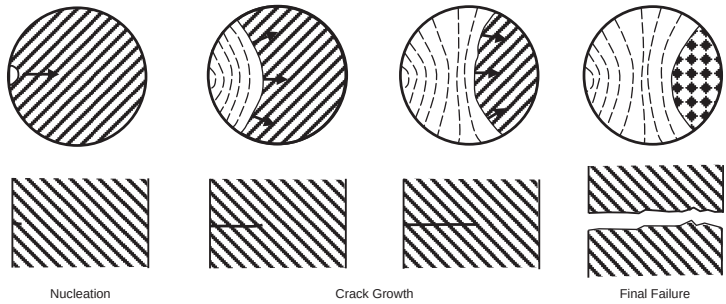

Figure 2.16: Typical fatigue crack propagation [Smallman and Bishop, 1999].

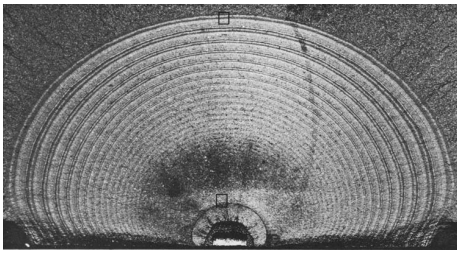

Figure 2.17: Fatigue crack growth in a high-strength steel component [Campbell, 2008].

The first systematic study into the relationship between stress and life was conducted by the German railway engineer August Wöhler [Wöhler, 1870], observing that fatigue life was a stronger function of stress range than of peak stress. The ensuing S-N curve approach is still popular. The stress-life approach was developed by Basquin [Basquin, 1910] with the observation of a

log-log relationship between stress amplitude and life in high-cycle fatigue.

$$\frac{\Delta\sigma}{2} = \frac{\sigma'_f}{E}(2N_f)^{b'} \tag{2.39}$$

where $\Delta\sigma$ is the stress range, σ'_f is the fatigue strength coefficient, b' is the fatigue strength exponent.

During cyclic loading within the elastic regime, stress and strain are directly related through the elastic modulus. Nonetheless, for cyclic loading that produces plastic strains, the responses are more complex and form a hysteresis loop. Low-cycle fatigue failure has the following characteristics: the structure suffers high load; lives are relatively short; and significant plastic straining takes place. The failure caused by a low-cycle fatigue load takes place in structures subjected to a heavy load. This load induces irreversible strain at a micro-scale or macro-scale level. The damage accumulated in a structure will reach the point of initiation and propagation of cracks. A cycle is usually defined as the interval between two service times. The number of cycles leading to failure (N_f) is relatively small. Lemaitre and Desmorat [Lemaitre and Desmorat, 2005] have categorized the classification of low cycle fatigue as follows

- The value of N_f lies between 10-10^2 for aerospace rockets or metal formed by forging.
- The value of N_f lies between 10^2-10^3 for thermal or nuclear power plants or chemical plants.
- The value of N_f lies between 10^3-10^4 for aircraft engines or car engines where stresses induce plastic strain with magnitudes approaching $\epsilon_p \approx \sigma_{yield}/E$, where ϵ_p is the plastic strain and E is Young's modulus.

The basic characteristic of low cycle fatigue is based on the Coffin-Manson equation as described in [Radhakrishnan, 1992]. Figure 2.18 shows a typical CoffinManson Curve. The total strain, $\Delta\epsilon_t$, consists of both elastic and plastic components:

$$\Delta\epsilon_t = \Delta\epsilon_e + \Delta\epsilon_p \tag{2.40}$$

Therefore, based on Coffin-Mansons equation the total strain amplitude can

be calculated as follows:

$$\frac{\Delta\epsilon_t}{2} = \frac{\Delta\epsilon_e}{2} + \frac{\Delta\epsilon_p}{2} = \frac{\sigma'_f}{E}\left(2N_f\right)^{b'} + \epsilon'_f\left(2N_f\right)^{c} \tag{2.41}$$

where $\Delta\epsilon_e/2$ is the elastic strain amplitude, $\Delta\epsilon_p/2$ is the plastic strain amplitude, σ'_f the fatigue strength coefficient, defined by the stress intercept at one load reversal (see Figure 2.18), ϵ'_f is the fatigue ductility coefficient, defined by the strain intercept at one load reversal, $2N_f$ is the total number of reversals to failure and b and c are the fatigue ductility exponents (empirical material properties).

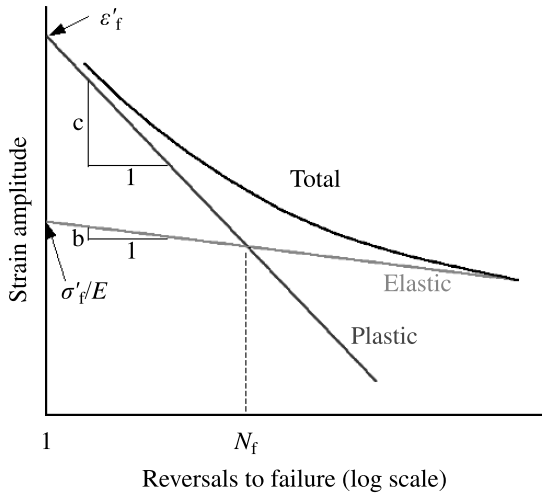

Figure 2.18: Typical joint lifetime according to Coffin-Mansons equation [Lemaitre, 1994].

Fatigue crack initiation and propagation

Fatigue cracks in most cases nucleates at free surfaces, usually external surfaces, but also can be initiated at sub-surfaces in presence of defects such as voids and inclusions. Common surface defects include geometric notches and surface roughness. Fatigue crack nucleation and growth occurs in the following stages [Campbell, 2008]:

- *Stage I*: Crack initiation usually starts at surface discontinuity such as a notch, which acts as a stress riser. In the absence of a surface defect,

crack initiation will eventually occur due to the formation of persistent slip bands. Slip bands are result of the systematic build up of fine slip movements on the order of approximately one nano meter. Therefore, the relative movement of the slip bands over each other results to the formation of intrusions and extrusions at the surface, which possibly lead to the formation of a crack. The initial crack propagates parallel to the slip bands. The crack propagation rate during stage *I* is very low. The crack initially follows the slip bands at approximately 45° to the principal stress direction as illustrated schematically in Figure 2.19.

- *Stage II*: When the crack length becomes sufficient for the stress field at the tip to become dominant, the overall crack plane changes and becomes perpendicular to the principal stress, and the crack enters stage *II*. Fatigue crack growth proceeds by a continual process of crack sharpening followed by blunting, as shown in Figure 2.20.

- *Stage III*: Eventually, sudden failure occurs when the fatigue crack becomes long enough that the remaining cross section can no longer support the applied load, which is also called tensile fracture.

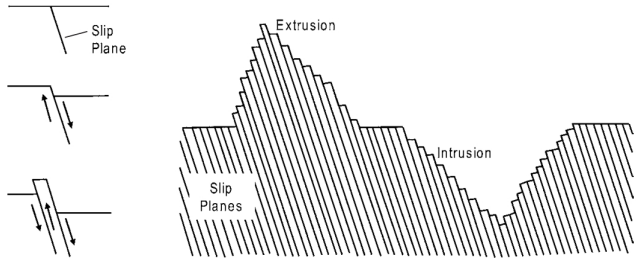

Figure 2.19: Fatigue crack initiation [Smallman and Bishop, 1999].

Fatigue crack growth rate

The rate of fatigue crack propagation is determined by subjecting fatigue-cracked specimens to constant-amplitude cyclic loading. The incremental increase in crack length is recorded along with the corresponding number of elapsed load cycles acquire stress intensity (K), crack length (l), and cycle count (N) data during the test. The data is presented in an l-N curve. Various l versus N curves can be generated by varying the magnitude of the cyclic

loading and/or the size of the initial crack. The data can be reduced to a single curve by presenting the data in terms of crack growth rate per cycle of loading (dl/dN) versus the fluctuation of the Stress Intensity Factor (SIF) at the tip of the crack (ΔK). ΔK is representative of the mechanical driving force, and it incorporates the effect of changing crack length and the magnitude of the cyclic loading. The most common form of presenting fatigue crack growth data is a log-log plot of dl/dN versus ΔK as schematically illustrated in Figure 2.21.

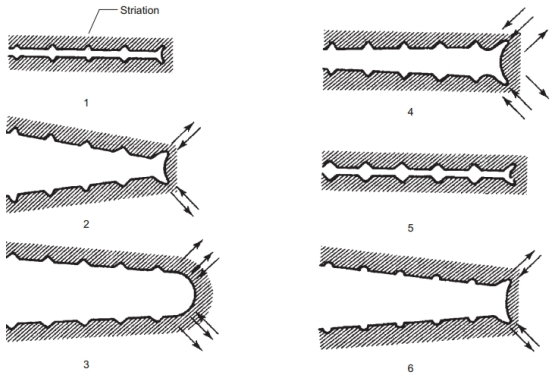

Figure 2.20: Fatigue crack growth mechanisms (1) no load (2) loaded (3) maximum load (4) load reduced (5) no load (6) again loaded [Campbell, 2008].

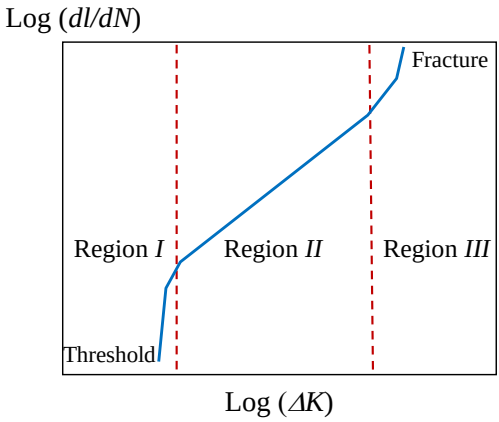

Figure 2.21: Schematic view of fatigue crack growth rate .

The fatigue crack propagation behaviour of many materials can be divided

into three regions as shown in the Figure 2.21. *Region I*, is the fatigue threshold region where the ΔK is too low to propagate a crack. *Region II*, encompasses data where the rate of crack growth changes roughly linearly with a change in stress intensity fluctuation. In *region III*, small increases in the stress intensity amplitude, produce relatively large increases in crack growth rate since the material is nearing the point of unstable fracture.

2.3.2 Continuum Damage Mechanics (CDM)

Basic concept

Damage in materials is mainly the process of the initiation and propagation of micro-cracks and cavities. At that scale the damage phenomenon is discontinuous. It was first introduced by Kachanov [Kachanov, 1958] in late 50s by using a continuous variable related to the density of such a defect. It is possible to divide the damage to three main categories: fatigue damage, ductile damage and creep damage. The introduced variable by Kachanov [Kachanov, 1958] has constitutive equation for evolution, written in terms of stress and strain, which may be used in structural calculations in order to predict the initiation of macro-cracks. These constitutive equations have been formulated in the framework of thermodynamics and identified for many phenomena such as dissipation and low cycle fatigue in metals, coupling between damage and creep, high cycle fatigue, creep-fatigue interaction, ductile plastic damage.

Therefore the theory of Continuum Damage Mechanics (CDM) is based on introducing a damage variable, which is defined as the effective surface of micro-cracks that intersects with plane. This damage variable is used to describe the evolution of stress as damage progress, using the concept of effective stress. The initiation of macro-cracks will take place once the accumulated damage reaches a critical value. In CDM, failure does not mean fracture, but is a point at which material has sufficiently degraded and continuity of material is lost due to formation of micro-cracks, micro-voids or cavities. From a physical point of view, damage is always related to plastic or irreversible strains and more generally to a strain dissipation either on the meso-scale, the scale of the Representative Volume Element (RVE), or on the micro-scale, the scale of the discontinuities. Damage mechanics has some elements, which are briefly described below.

Damage variables

With considering a damaged solid in which an element of finite volume has been isolated, of a sufficiently large size with respect to the in-homogeneities of the medium, and the element size has been grossly enlarged as depicted in Figure 2.22.

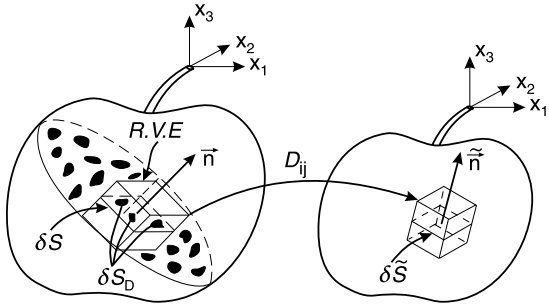

Figure 2.22: Physical damage and mathematical continuous damage [Lemaitre and Desmorat, 2005].

In Figure 2.22, δS is the area of a section of volume element identified by its normal $\vec{n}$. On the section shown in Figure 2.22, micro-cracks and cavities, which constitute the damage, leave traces of different forms. By considering $\delta\widetilde{S}$ as the effective area of resistance, $\delta\widetilde{S} < \delta S$, the stress concentration is in the vicinity of geometric discontinuities between the defects such as micro-cracks and cavities. The effective area can be considered as:

$$\delta S_D = \delta S - \delta\widetilde{S} \tag{2.42}$$

Where δS_D, is the total area of defects. Later on, it will be explained that using other elements of damage mechanics help to avoid the calculation of total area of defects, which would be extremity difficult to measure due to lack of knowledge of precise geometry of the defects. By definition, the damage variable D associated with the direction of the normal $\vec{n}$ is:

$$D = \frac{\delta S - \delta\widetilde{S}}{\delta S} \tag{2.43}$$

Where D= 0 corresponding to the undamaged state, D= D_c, where D_c is a critical value, corresponding to the rapture of element in two parts ($0.2 \leq D_c \leq 0.8$ for metals) [Lemaitre, 1985]. Isotropic damage consists of micro-cracks and

cavities with an orientation distributed uniformly in all directions. In this case, the variable does not depend on the orientation of $\vec{n}$ and the damaged state is completely characterized by the scalar D.

Effective stress

The introduction of a damage variable, which represents a surface density of discontinuities in the material leads directly to the concept of effective stress. The effective stress is the calculated stress over the section, which effectively resists the forces. Figure 2.23 illustrates the uniaxial case, in which the F is the applied force on a section of the representative volume element, $\sigma = F/\delta S$ in the usual stress satisfying the equilibrium equation. In the presence of isotropic damage, D, the effective area of resistance can be calculated as:

$$\delta\widetilde{S} = \delta S - \delta S_D = \delta S\,(1 - D) \tag{2.44}$$

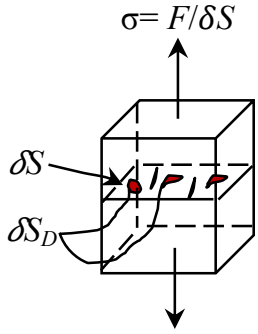

Figure 2.23: Schematic view of concept of effective stress.

According to the definition of the effective stress $\widetilde{\sigma}$, it can be calculated as:

$$\widetilde{\sigma} = \frac{F}{\delta\widetilde{S}} = \frac{F}{\delta S - \delta S_D} = \frac{F}{\delta S(1 - D)} \tag{2.45}$$

Evidently, $\widetilde{\sigma} \geq \sigma$, $\widetilde{\sigma} = \sigma$ for undamaged material and $\widetilde{\sigma} \to \infty$ at the moment of fully damaged material i.e. onset of macro crack initiation.

Principle of strain-equivalence

As mentioned above measuring the effective resisting area is a challenging task. This area can be calculated through mathematical homogenization techniques but the shape and the size of defects must be known, which is somewhat difficult, even with a good electron microscope. To avoid these difficulties, the principle of strain equivalence can be used. It is stated that any strain constitutive for a damaged material is divided from the same potential as the undamaged material except that all the stress variables are replaced by effective stresses (Figure 2.24). In case of one-dimensional linear elasticity:

$$\epsilon_e = \frac{\sigma}{E}, \quad \text{Undamaged material} \tag{2.46}$$

$$\epsilon_e = \frac{\widetilde{\sigma}}{E} = \frac{\sigma}{(1-D)E} = \frac{\sigma}{\widetilde{E}}, \quad \text{Damaged material} \tag{2.47}$$

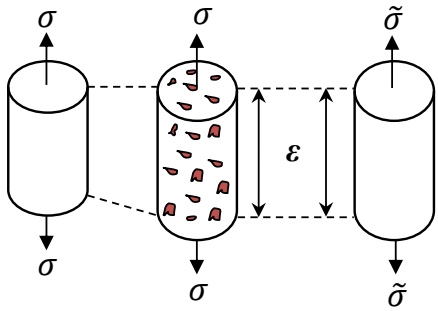

Figure 2.24: Schematic view of equivalence strain concept.

Where ϵ_e is the elastic strain and E the Young's modulus. Defining $\widetilde{E}$ as the elastic modulus of the damaged material, $\widetilde{E} = (1-D)E$, the reduction in elastic modulus with the increase in fatigue cycles is shown in Figure 2.25. The damage variable is thus given by D= 1-$\widetilde{E}$/E which can be used to indirectly measure the damage variable D in a process known as the method of variation of elasticity modulus.

Thermodynamic approach

In order to model the isotropic phenomena of elasticity, thermal effects, plasticity and damage within the framework of the thermodynamics of irreversible

processes, Lemaitre [Lemaitre, 1985] has introduced the state variables as: the total strain ϵ_{total}, the elastic strain ϵ_e, the plastic strain $\epsilon_p = \epsilon_{total} - \epsilon_e$. If thermal effects are involved in the damage process, the temperature T is introduced as an *observable state* variable with its *associated variable*, entropy S. The state variables can be defined as observed and internal variables. All these state and associated variables are tabulated in Table 2.1.

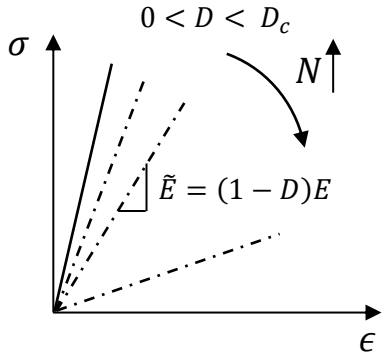

Figure 2.25: Stiffness degradation with increase in fatigue cycles.

Table 2.1: Thermodynamics variables

State variables		
Observable variables	Internal variables	Associated variables
ϵ_e Elastic strain		σ Stress
T Temperature		S Entropy
	P Accumulated plastic strain	R_h Isotropic hardening scalar
	D Damage	$-Y$ Damage strain energy release rate
	V_k	A_k

The state variables, observable and internal, are chosen in accordance with the physical mechanisms of deformation and degradation of the material. Ac-

cording to Table 2.1, V_k and A_k can be any internal and associated variables, respectively.

Thermodynamic potential function

The free energy ψ, taken as the thermodynamic potential, in which elasticity and plasticity are uncoupled, given the law of thermo-elasticity coupled with damage and the definition of the associated variables related to internal variables. Taking small deformations into consideration, the total strain is split into a thermo-elastic part ϵ_e and a plastic part ϵ_p and can be written as:

$$\epsilon_{total} = \epsilon_e + \epsilon_p \tag{2.48}$$

The potential function is a convex function of all the state variables and can be written as:

$$\psi = \psi_e\left(\epsilon_e, T, D\right) + \psi_p\left(T, P\right) \tag{2.49}$$

In case of elasticity, the total strain $\epsilon_{total} = \epsilon_e$, and ψ becomes:

$$\psi = \psi_e\left(\epsilon_e, T, D\right) \tag{2.50}$$

For an isothermal case, expression of free energy ψ can be chosen as

$$\psi = \frac{1}{\rho}\left[\frac{1}{2}a_{ijkl}\epsilon_{ij}\epsilon_{kl}(1-D)\right] \tag{2.51}$$

Where, a_{ijkl} is the fourth order elasticity stiffness tensor and ρ is the density. By using *Clausius-Duhem* inequality:

$$\dot{\psi} = \frac{\partial\psi}{\partial\epsilon_e} : \dot{\epsilon_e} + \frac{\partial\psi}{\partial T}\dot{T} + \frac{\partial\psi}{\partial V_k}\dot{V_k} \tag{2.52}$$

The following expression is obtained:

$$\left(\sigma - \rho\frac{\partial\psi}{\partial\epsilon_e}\right) : \dot{\epsilon_e} + \sigma : \epsilon_p - \rho\left(S - \frac{\partial\psi}{\partial T}\right)\dot{T} - \rho\frac{\partial\psi}{\partial V_k}\dot{V_k} - \frac{\vec{q}}{T}\ \vec{grad}\ T \geq 0 \tag{2.53}$$

According to Lemaitre [Lemaitre, 1985] a classical assumption permits to cancel some terms in this inequality independently. An elastic deformation takes place at constant and uniform temperature ($\dot{T}$=0 and $\vec{grad}\ T$=0) which changes neither the plastic strain ($\dot{\epsilon_e}$=0) nor the internal variables ($\dot{V_k}$=0). To

satisfy the above inequality it is necessary to consider that the elastic deformations can occur at a time scale higher that those which would question the validity of the hypothesis of the local state, and lower than those of dissipative phenomena. Since the *Clausius-Duhem* inequality holds regardless of any particular $\dot{\epsilon_e}$, it necessarily follows that:

$$\sigma - \rho \left(\frac{\partial \psi}{\partial \epsilon_e} \right) = 0 \tag{2.54}$$

Therefore the second principle of thermodynamics gives the elasticity law coupled with damage variable:

$$\sigma_{ij} = \rho \frac{\partial \psi}{\partial \epsilon_{e,ij}} = \frac{1}{2} a_{ijkl} \epsilon_{kl} (1 - D) \tag{2.55}$$

where

$$\epsilon_{ij} = \frac{1+\nu}{E} \frac{\sigma ij}{1-D} - \frac{\nu}{E} \frac{\sigma_{kk}}{1-D} \delta_{ij} \tag{2.56}$$

Where, ν is poissons ratio and δ_{ij} is Kronecker delta. As shown in Table 2.1, the damage strain energy release rate variable Y associated with D can be defined as:

$$Y = -\rho \frac{\partial \psi}{\partial D} = \frac{1}{2} a_{ijkl} \epsilon_{ij} \epsilon_{kl} \tag{2.57}$$

Considering W_e as density of elastic strain energy, gives:

$$W_e = \int dW_e = \int \sigma_{ij} d\epsilon_{ij} = \frac{1}{2} a_{ijkl} \epsilon_{ij} \epsilon_{ij} (1 - D) \tag{2.58}$$

Furthermore, the mechanism of damage is governed by the total elastic strain energy:

$$\underbrace{W_e = W'_e + W^H_e}_{\text{Total energy=Distortion+Volumetric}} \tag{2.59}$$

$$W_e = \int_0^{\epsilon_e} \sigma : d\epsilon_e = \underbrace{\int_0^{\epsilon'_e} \sigma' : d\epsilon'_e}_{Deviatoric} + \underbrace{3 \int_0^{\epsilon_{e,H}} \sigma_H : d\epsilon_H}_{Hydrostatic} \tag{2.60}$$

where σ' and ϵ'_e are the deviators of σ and ϵ_e. σ_H and $\epsilon_{e,H}$ are the hydrostatic stress and strain respectively. By introducing elastic law with damage

through the concept of effective stress:

$$\epsilon'_e = \frac{1+\nu}{E}\frac{\sigma'}{(1-D)}, \quad \text{Deviatoric elastic strain} \tag{2.61}$$

$$\epsilon_{e,H} = \frac{1-2\nu}{E}\frac{\sigma_H}{(1-D)}, \quad \text{Hydrostatic strain} \tag{2.62}$$

By assuming that the damage does not vary within the elastic domain and substituting Equations 2.61 and 2.62 into the Equation 2.60:

$$W_e = \frac{1}{2}\left[\frac{1+\nu}{E}\frac{\sigma' : \sigma'}{(1-D)} + 3\frac{1-2\nu}{E}\frac{\sigma_H}{(1-D)}\right] \tag{2.63}$$

Considering equivalent von-Mises stress gives:

$$\sigma_{eq} = \left(\frac{2}{3}\sigma' : \sigma'\right)^{1/2} \tag{2.64}$$

Substituting Equation 2.64 into Equation 2.63 yields:

$$W_e = \frac{1}{2E(1-D)}\left(\frac{2}{3}(1+\nu)\sigma_{eq}^2 + 3(1-2\nu)\sigma_H^2\right) \tag{2.65}$$

By defining equivalent multi-axial damage stress σ^* by stating that this energy in a multi-axial state is equal to that in an equivalent uni-axial state defined by σ^*, for which (σ_{eq}=σ^*,σ_H=$\sigma^*/3$), Equation 2.65 becomes:

$$W_e = \frac{{\sigma^*}^2}{2E(1-D)} \tag{2.66}$$

therefore:

$$\frac{{\sigma^*}^2}{2E(1-D)} = \frac{1}{2E(1-D)}\left(\frac{2}{3}(1+\nu)\sigma_{eq}^2 + 3(1-2\nu)\sigma_H^2\right) \tag{2.67}$$

or

$$\sigma^* = \sigma_{eq}\left(\frac{2}{3}(1+\nu) + 3(1-2\nu)\left(\frac{\sigma_H}{\sigma_{eq}}\right)^2\right)^{1/2} \tag{2.68}$$

The ratio T_x=σ_H/σ_{eq} in this relation expresses the tiaxiality ratio of the state of stress. The second term in Equation 2.68 known as triaxiality function

and can be written as:

$$R_v = \frac{2}{3}(1+\nu) + 3(1-2\nu)\left(\frac{\sigma_H}{\sigma_{eq}}\right)^2 \tag{2.69}$$

Putting triaxiality function in Equation 2.68 gives:

$$\sigma^* = \sigma_{eq}\sqrt{R_v} \tag{2.70}$$

Moreover, according to Lamitre [Lemaitre, 1985] the threshold *fatigue limit* can be represented as an initial condition on effective stress. σ^*, in the differential equation D=0 if $\sigma^* \leq \sigma_0$, where, σ_0 is the fatigue limit in tension. The variable Y associated with the damage variable D may be used in order to define the equivalent multi-axial damage stress, σ^* derived above. From Equations 2.57 and 2.58:

$$Y = \frac{W_e}{(1-D)} = \frac{1}{2}\frac{dW_e}{dD} \tag{2.71}$$

Substituting Equation 2.63 into Equation 2.71:

$$Y = \frac{W_e}{(1-D)} = \frac{\sigma_{eq}^2}{2E(1-D)^2}R_v \tag{2.72}$$

Dissipated potential function and fatigue damage evolution law

As explained earlier, the thermodynamic potential allows writing relations between observable state variables and associated variables. However, for internal variables it just allows the definition of their associated variables. To describe the dissipation process, mainly the evolution of the internal variables, a complementary formalism is needed. This can be formulated with dissipation potential function. After selecting the appropriate variables, the most important step in the determination of strain and stress and damage constitutive equations is the selection of analytical expression for the potential of dissipation used to write the kinetic law (related fluxes and their associated dual variables). Concentrating on damage, the below assumption should be taken into account:

- Irreversible nature of damage regarding to second principle of thermodynamics Y$\geq$0.
- Non-linearities of damage with regard to stress and number of cycle in fatigue.

- Effect of triaxiality on rapture.
- Effect of mean stress or difference in the behaviour of damaged material in tension and compression.
- Existence of damage thresholds.
- Non linear accumulation of damage due to different loading.

There are many possible choices for the analytical form of the dissipation potential function, depending on the knowledge of experimental results, the purpose of use and the ability of the model developer. The best is the simplest with the required domain of validity, where simplest means the smallest possible number of material parameters. Taking into account the state laws, the *Clausius-Duhem* inequality, which defines the second law of thermodynamics that is used in continuum mechanics, can be reduced to express the fact that dissipation is necessarily positive:

$$\varphi = \underbrace{\sigma : \dot{\epsilon_p} - A_k \dot{V_k}}_{\text{Mechanical dissipation}} - \underbrace{\frac{\vec{q}}{T} \vec{grad}\, T}_{\text{Thermal dissipation}} \geq 0 \tag{2.73}$$

Where φ is the dissipation potential function, which is a sum of the products of the force variables or dual variables. As it is shown in Equation 2.73, the first term is:

$$\varphi_1 = \sigma : \dot{\epsilon_p} - A_k \dot{V_k} \tag{2.74}$$

This is called mechanical dissipation (intrinsic dissipation) which consists of plastic dissipation and the dissipation associated with the evolution of the other internal variables. And the second term is:

$$\varphi_2 = \frac{\vec{q}}{T} \vec{grad}\, T \geq 0 \tag{2.75}$$

This is the thermal dissipation due to conduction of heat, which is not taken into account in this study. Therefore, by assuming that plastic deformation and micro-plastic deformation to cause damage and internal energy dissipation, the dissipation potential function can be expressed as:

$$\varphi = \varphi_p + \varphi_D + \varphi_\pi \tag{2.76}$$

Where, φ_p is plastic dissipated potential function, φ_D is damage dissipated potential function and φ_π is micro-plastic dissipation function. There is little information about micro-plastic dissipation function, which is not considered in this study and out of scope of the present work. Furthermore the plastic dissipation function disappears due to absence of macro plastic deformation. Therefore, the dissipation potential function can be considered as damage dissipated potential function ($\varphi = \varphi_D$).

According to [Lemaitre, 1985], it is proven that a damage potential function can be written as function of three variables $\dot{Y}$, $\dot{P}$ and $\dot{\pi}$, which are damage energy release rate, rate of plastic strain and accumulated micro-plastic strain, respectively. Two parameters, temperature (T) and damage variable (D), are sufficient to model all the main properties, within the hypothesis of isotropy. Furthermore, it is sufficient to consider the following simple analytical form function of two material coefficients C and β. Moreover, many experimental results show also that φ must be a non-linear function of Y [Lemaitre, 1987].

$$\varphi = \frac{C}{\frac{\beta}{2}+1}\left(\frac{-Y}{C}\right)^{\frac{\beta}{2}+1}\left(\dot{P}+\dot{\pi}+\dot{Y}\right) \tag{2.77}$$

2.3.3 Fracture mechanics

Introduction

The mechanics of fracture progressed from being a scientific curiosity to an engineering discipline primarily because of the major failures that occurred in the *Liberty ships* during World War *II*. The Liberty ships had an all-welded hull, as opposed to the riveted construction of traditional ship designs. Fracture mechanics is a field of solid mechanics that deals with the mechanical behaviour of cracked bodies. The wide range of the Engineering Fracture Mechanics disciplines for different practical applications is schematically illustrated in Figure 2.26. Historically, the first major step in the direction of quantification of the effects of crack like defects was taken by Inglis [Inglis, 1963] in early 1900s. He published a stress analysis for an elliptical hole in an infinite linear elastic plate loaded at its outer boundaries.

Griffith [Griffith, 1921] carried out tests on cracked glass spheres and showed that the simple elastic analysis could be applied to describe the propagation of different size cracks at different stress levels. He transformed the Inglis analysis

by calculating the effect of the crack on the strain energy stored in an infinite cracked plate. He also proposed that this energy, which is a finite quantity, should be taken as a measure of the tendency of the crack to propagate. After World War *II*, the fracture mechanics research group at the Naval Research Laboratory was led by Irwin [Irwin, 1958]. Having studied the early work of Inglis, Griffith, and others, Irwin found out that the basic tools needed to analyse fracture were already available. Irwins first major contribution was to extend the Griffith approach to metals by including the energy dissipated by local plastic flow.

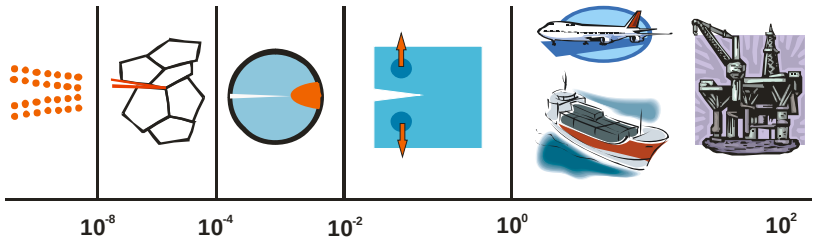

Figure 2.26: Fracture mechanics at different scales after [Mirzaei, 2010].

Modes of fracture

Considering a cracked plate, it can be distinguished in several manners in which a force may be applied to the plate, which might enable the crack to propagate. Irwin [Irwin, 1958] proposed a classification corresponding to the three situations represented in Figure 2.27. In the mode *I*, or opening mode, the body is loaded by tensile forces, such that the crack surfaces are pulled apart in the y direction. In the mode *II*, or sliding mode, the body is loaded by shear forces parallel to the crack surfaces, which slide over each other in the x direction. The deformations are then symmetric with respect to the plane perpendicular to the z axis. Finally, in the mode *III*, or tearing mode, the body is loaded by shear forces parallel to the crack surfaces, and the crack surfaces slide over each other in the z direction.

For each of these modes, crack extension may only take place in the direction of the x axis, the original orientation of the crack. In a more general situation, typically a mixed mode situation can be observed, where there is a superposition of the modes. In a linear elastic mixed mode problem, the prin-

ciple of stress superposition states that the individual contributions to a given stress component are additive and can be written as:

$$\sigma_{ij} = \sigma_{ij}^{I} + \sigma_{ij}^{II} + \sigma_{ij}^{III}, \text{i,j} = \text{x,y} \tag{2.78}$$

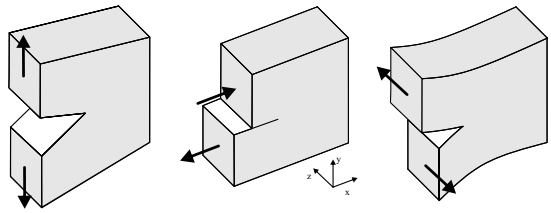

Figure 2.27: Fracture modes, from right to left mode *I*, mode *II* and mode *III*, respectively.

Within the scope of the theory of linear elasticity, a crack introduces a discontinuity in the elastic body such that the stresses tend to infinity as one approaches the crack tip. Irwin [Irwin, 1958] related the singular behaviour of the stress components to the distance to the crack tip r. The relation he obtained can be written in a simplified form as:

$$\sigma = \frac{K}{\sqrt{2\pi r}} \tag{2.79}$$

The parameter K, called *stress intensity factor*, plays a fundamental role in fracture mechanics, as it characterizes the stress field in this region. Equation 2.79 is only valid near the crack tip, where the $1/\sqrt{r}$ singularity dominates the stress field. Stresses far from the crack tip are governed by the remote boundary conditions. For example, if the cracked structure is subjected to a uniform remote tensile stress, σ approaches a constant value, σ^{∞}.

Crack tip stress and displacement fields

Considering a 2-D static crack in a plate which is in a plane stress situation. Assuming that the crack surfaces are free of stress and that the crack is positioned along the negative x-axis, as shown in Figure 2.28. Then the distribution of the stresses in the region near the crack tip may be derived as an interior

asymptotic expansion [Anderson, 2005]:

$$\sigma_{ij}(r,\theta) = \frac{K_I}{\sqrt{2\pi r}} f_{ij}^{I}(\theta) + \frac{K_{II}}{\sqrt{2\pi r}} f_{ij}^{II}(\theta) + \sigma_{ij}^{0} \tag{2.80}$$

for $r \to 0$, $i,j=x,y$, and σ_{ij}^{0} indicates the finite stresses at the crack tip. The constants of the stress field K_I and K_{II} represent the stress intensity factors (SIFs) for the corresponding modes I and II, respectively, and are defined as:

$$K_I = \lim_{r \to 0} \sqrt{2\pi r}\sigma_{yy}(r,0) \tag{2.81}$$

$$K_{II} = \lim_{r \to 0} \sqrt{2\pi r}\sigma_{xy}(r,0) \tag{2.82}$$

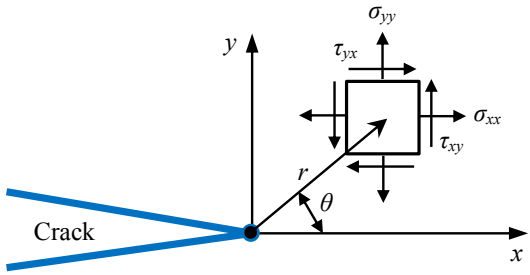

Figure 2.28: Crack tip stress field.

By considering a 2-D mixed-mode Linear Elastic Fracture Mechanics (LEFM) problem assumption, the size of the plastic zone around crack tip is very small as compared to the structure size. For an element near crack tip as illustrated in Figure 2.28, the 2-D mixed mode stress and displacement filed according to

Anderson [Anderson, 2005] are given by:

$$\begin{Bmatrix} \sigma_{xx} \\ \\ \sigma_{yy} \\ \\ \sigma_{xy} \end{Bmatrix} = \frac{K_I}{\sqrt{2\pi r}} \cos\frac{\theta}{2} \begin{Bmatrix} 1 - \sin\frac{\theta}{2}\sin\frac{3\theta}{2} \\ \\ 1 + \sin\frac{\theta}{2}\sin\frac{3\theta}{2} \\ \\ \sin\frac{\theta}{2}\cos\frac{\theta}{2}\cos\frac{3\theta}{2} \end{Bmatrix} + \frac{K_{II}}{\sqrt{2\pi r}} \begin{Bmatrix} \sin\frac{\theta}{2}\left[2 + \cos\frac{\theta}{2}\cos\frac{3\theta}{2}\right] \\ \\ \sin\frac{\theta}{2}\cos\frac{\theta}{2}\cos\frac{3\theta}{2} \\ \\ \cos\frac{\theta}{2}\left[1 - \sin\frac{\theta}{2}\sin\frac{3\theta}{2}\right] \end{Bmatrix} \tag{2.83}$$

and

$$\begin{Bmatrix} u_x \\ \\ u_y \end{Bmatrix} = \frac{K_I}{2G_s}\sqrt{\frac{r}{2\pi}} \begin{Bmatrix} \cos\frac{\theta}{2}\left[k - 1 + 2\sin^2\frac{\theta}{2}\right] \\ \\ \sin\frac{\theta}{2}\left[k + 1 - 2\cos^2\frac{\theta}{2}\right] \end{Bmatrix} + \frac{K_{II}}{2G_s}\sqrt{\frac{r}{2\pi}} \begin{Bmatrix} \sin\frac{\theta}{2}\left[k + 1 + 2\cos^2\frac{\theta}{2}\right] \\ \\ \cos\frac{\theta}{2}\left[k - 1 - 2\sin^2\frac{\theta}{2}\right] \end{Bmatrix} \tag{2.84}$$

where G_s is the shear modulus and the small differences in formulas for plane stress and plane strain are handled by k, where

$$k = \begin{cases} 3 - 4\nu & \text{Plane strain} \\ \\ \dfrac{3-\nu}{1+\nu} & \text{Plane stress} \end{cases} \tag{2.85}$$

2.3.4 *J*-integral

Rice and Rosengren [Rice and Rosengren, 1968] noticed the importance of the J-integral as a criterion for crack propagation in fracture mechanics. Path independency of J-integral allows for evaluation of linear and non linear elastic

energy release rates and elasto-plastic work far from the crack tip. Figure 2.29 indicates an elastic body containing a crack, for which the J-integral can be written for a crack in the (x, y)-plane as:

$$J = \oint_{\Gamma} \left(W_s n_x - T_i \frac{\partial u_i}{\partial x} \right) ds \tag{2.86}$$

where W_e is the strain energy density, which can be written as:

$$W_e = \int_0^{\epsilon} \sigma_{ij} d\epsilon_{ij} \tag{2.87}$$

in which ϵ_{ij} is the strain tensor. Moreover, Γ is a closed counter-clockwise contour, ds is the differential element of the arc along the path Γ, u is the displacement vector and T_i is the traction vector on a plane defined by the outward normal vector $\vec{n}$, which can be written as:

$$T_i = \sigma_{ij} n_j \tag{2.88}$$

therefore, Equation 2.86 can be written as:

$$J = \int_0^{\epsilon} \sigma_{ij} d\epsilon_{ij} - \oint_{\Gamma} \left((\sigma_x n_x + \sigma_{xy} n_y) \frac{\partial u_x}{\partial x} + (\sigma_y n_y + \sigma_{xy} n_x) \frac{\partial u_y}{\partial x} \right) ds \tag{2.89}$$

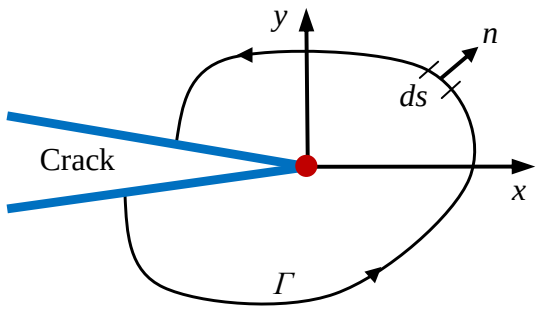

Figure 2.29: Definition of J integral around the crack tip

2.4 Numerical modelling of fretting fatigue

2.4.1 Introduction

Fretting fatigue is a combination of two complex phenomena which can be related to two different mechanical responses of material, namely damage mechanics that is related to tribological behaviour of two contacted surfaces (fretting) and at further step fracture mechanics which is more related to fatigue response of materials. Once these two complex phenomena are combined together, fretting fatigue occurs. As counted above there are a lot of practical applications that are subjected to fretting fatigue. Based on contact conditions, e.g. surface finish, coefficient of friction, etc, and mechanical variables, e.g. axial stress, contact stress and slip amplitude, fretting damage at contact interface can cause crack initiation and growth leading to catastrophic and sudden fracture. Fretting fatigue experiments have been studied by using different types of test rigs and apparatus in different laboratories [Hills and Nowell, 1994, Szolwinski et al., 1997, Jin and Mall, 2004b, Arora et al., 2007, Majzoobi et al., 2010]. As mentioned above numerical modelling techniques such as FEA technique for analysing fretting fatigue behaviour are very popular and useful.

FEA method gives opportunity to quantify quantities such as non-linearity of contact problem along with non-proportionality and multi-axial stress state and deformation patterns due to applied external loads and different boundary conditions. One of the advantages of FEA method is that it provides information, which cannot be obtained through experimental testing or analytical solutions. FEA enables to determine local parameters at contact interface between fretting pad and fatigue specimen in fretting fatigue problem from the applied global boundary and loading conditions. Moreover, determination of these local parameters allows predictive parameters to be developed based on local rather than applied global stresses. FEA has been widely used in the last few decades to understand and predict fretting and fretting fatigue phenomena, some of them can be found here [Szolwinski et al., 1997, Tsai and Mall, 2000, Mutoh and Xu, 2003, Lanoue et al., 2009, Chan et al., 2010]. Applications of FEA were expanded to simulate fretting and fretting fatigue behaviour for more than three decades. Early study of the application of FEA in fretting contact problem dates back to mid 1980s by Stover et al. and Ruiz et al. [Ruiz et al., 1984, Stover et al., 1985]. Current researches implementing FEA to support studies in 3-D modelling of more complex practical applications

subjected to fretting or fretting fatigue such as design optimisation of turbine blade fir-tree root using intelligent CAD and FEA approaches by Song et al. [Song et al., 2002] or FEA simulation of fretting wear-fatigue interaction in spline couplings by Ding et al. [Ding et al., 2008].

Studies incorporating FEA in fretting and fretting fatigue research areas are around 380 publications, since 1991 till 2013 (the total number of published work available on *Web of Knowledge* for the search strings "finite element" and "fretting"; searched in http://wokinfo.com/). Figures 2.31 and 2.30 show that the number of papers that have been published and cited using FEA in case of fretting and fretting fatigue appears to be increasing over two last decades considerably. All of these informations reveals the importance of FEA modelling of fretting and fretting fatigue phenomena.

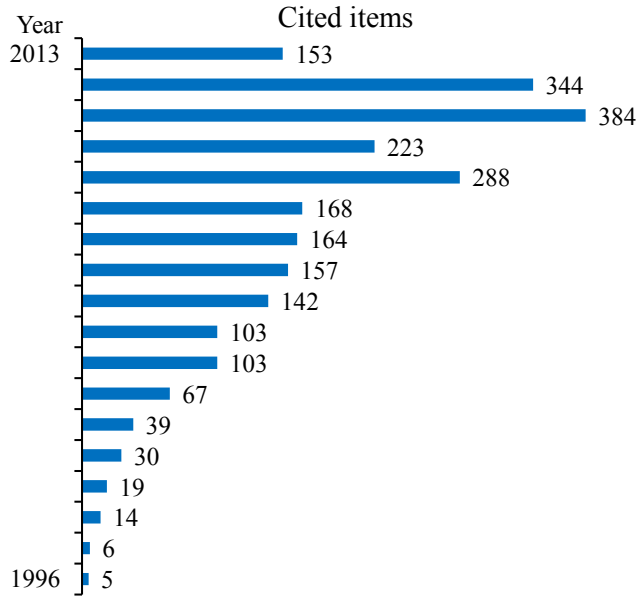

Figure 2.30: Cited FEA based ISI papers in field of fretting and fretting fatigue since 1996 till 2013 (up to june).

Simulation approaches that are used for modelling fretting and fretting fatigue are highly multidisciplinary, involving non-skilled and skilled developers in all aspects of mechanical and bio-mechanical engineering research. Despite enormous FEA investigations concerned with monitoring stress state at and

near contact surfaces of fretting and fretting fatigue contact problem, there is no standard or kind of guideline for FEA modelling of fretting and fretting fatigue phenomena. Therefore, questions arise on the reliability of FEA based models used for fretting and fretting fatigue models in different scales i.e. coupon (lab) scale tests and practical applications.

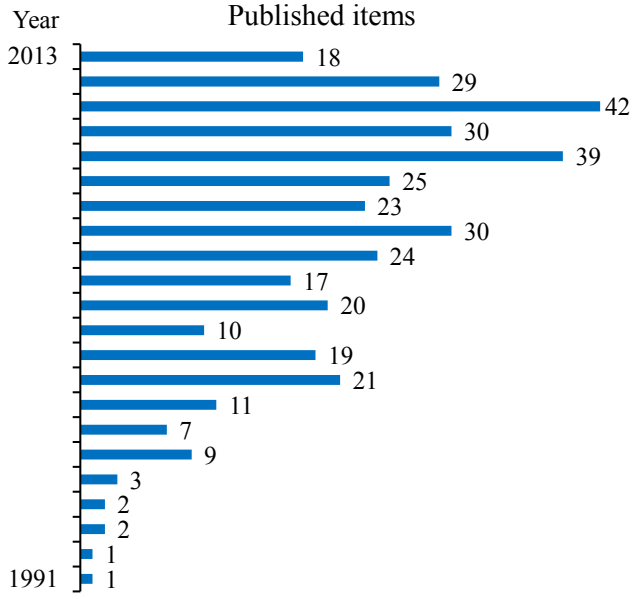

Figure 2.31: Published FEA based ISI papers in field of fretting and fretting fatigue since 1991 till 2013 (up to june)

Establishing standards for FEA of fretting problems is a challenging task, particularly when combined with the complexity of fretting and fretting fatigue issues such as non-linear contact problem, non-proportional loading condition, multi-axial state of stress at and near contact interface and a lot of primary and secondary variables. However, by establishing some sort of guideline the perspective use of FEA modelling of fretting and fretting fatigue phenomena may lead to transparency and increase in reproducibility and reliability of the models. The main objective of this section is in the same direction by reviewing some of available models and categorize them in different groups. To this end, in Appendix A some recommendations are made to establish easy to follow, adaptive, and expandable guideline for FEA studies of fretting and fretting fatigue phenomena.

2.4.2 Contact model

In this section in order to model fretting and fretting fatigue contact problem, four major categories are highlighted in different groups based on recent ASTM standard for fretting fatigue experimental tests [ASTM E2789-10, 2011] as illustrated in Figure 2.32 and listed as FEA of fretting contact, fretting fatigue and practical applications.

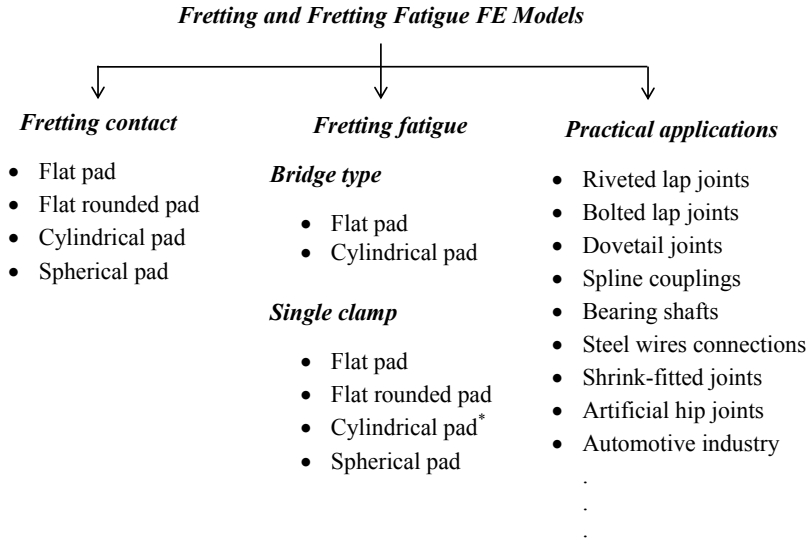

Figure 2.32: Fretting and fretting fatigue FE models.

Fretting contact

Fouvry et al. [Fouvry et al., 2003] presented the first FEA model of wear process of fretting contact problem. They have modelled metallic materials involving plastic strain deformation. Their model was validated against experimental results. They have found that less than 10 % of the energy is consumed by the plastic dissipation.

McColl et al. [McColl et al., 2004] have used FEA method to simulate both fretting wear and the evolution of fretting variables with number of wear cycles in a cylinder-on-flat fretting configuration. In their model, they have simulated wear incrementally and the total simulation time has been minimised via mesh and increment size optimisation. McColl et al. [McColl et al., 2004] have

also compared the predicted wear profiles with profilometer measurements of fretting test scars. Hyde et al. [Hyde et al., 2005] have offered a methodology for the experimental simulation of fretting conditions in complex shaft couplings, using a simple representative specimen/test rig. The geometry and loading conditions of the representative specimen were designed to model the stress and slip amplitude at contact interface, as predicted by detailed 3-D FEA of the coupling. They have used an iterative FEA process with feedback from preliminary measurements to design representative specimen/test rig.

Ding et al. [Ding et al., 2007a] presented the FEA model of the third body as a thin layer of elements with differing material properties which formed the top row of elements on the lower body. The third body properties were calibrated by matching the models behaviour with experimentally recorded fretting loops. They have calculated the local wear as a function of local contact pressure and local slip, and incrementally updated the contact geometry with material removal. Fouvry et al. [Fouvry et al., 2007] have performed a FEA investigation in order to rationalize the fretting wear response of adhesive wear and non-adhesive wear interfaces and predict interface durability under fretting wear. They have shown that the wear depth kinetics can be predicted by considering the accumulated energy density. Mary and Fouvry [Mary and Fouvry, 2007] have optimized the same FEA model by proposing a criterion of the maximum wear depth per computation step.

More recently, Basseville et al. [Basseville et al., 2011] have investigated the computation of realistic stress and strain fields at a local scale in fretting contact problem. They have proposed models to improve surface and volume modelling, by taking into account the heterogeneity of stress fields due to the irregular interface. Zhang et al. [Zhang et al., 2011] have implement FEA based energy wear simulation to fretting contact. They have combined the method with a critical-plane multi-axial fatigue prediction method for crack nucleation using the Smith-Watson-Topper (SWT) fatigue parameter and non-linear kinematic hardening model for cyclic plasticity. They have also developed a detailed FEA model for further study on the effect of contact geometry on fretting wear, fatigue and cyclic plasticity (ratchetting) performance of two round on flat fretting configurations and a rounded punch on flat geometry [Zhang et al., 2011]. Leonard et al. [Leonard et al., 2011, Leonard et al., 2012] have proposed new approach for modelling fretting wear problem using combined Finite Discrete Element Model (FDEM) to study the effects of different fretting parameters

on fretting wear process. They have validated the FDEM by comparing the pressure and frictional shear stress results to the continuum mechanics solution for a Hertzian fretting contact.

Fretting fatigue contact

Bridge type contact:

Based on ASTM standard for fretting fatigue testing, these type of fretting fatigue tests typically involve two bridge-shaped fretting pads pushing against the gage section of fatigue specimen as illustrated in Figure 1.10 [ASTM E2789-10, 2011].

Sato [Sato, 1992] calculated the contact stress pressure distribution by using a boundary element method. He investigated the effect of different shapes of fretting pad on contact pressure distribution. Neu et al. [Neu and Pape, 1998] used FEA approach to estimate the local state stress at and near contact interface in order to predict fretting fatigue crack nucleation lifetime. For this purpose they have used multiaxial fatigue criteria based on critical plane approach. Swalla and Neu [Swalla and Neu, 2001] used the same FEA model as developed in [Neu and Pape, 1998] to study the influence of COF on fretting fatigue crack nucleation prediction. They concluded that prescribing a higher coefficient of friction in an elastic/plastic FEA of fretting fatigue gives results that more closely approximate experimental observations. They have revealed that the fretting fatigue contact parameters such as, the stick/slip behaviour, local cyclic stress/strain, and cumulative plastic strain are all better described using FEA approach.

Mutoh and Xu [Jayaprakash et al., 2010] proposed a new FEA approach based on a singular stress field near the contact edge and on fracture mechanics to predict fretting fatigue crack propagation lifetime. Modelling bridge type contact using the FEA approach has to adequately represent the proper loading and boundary conditions. An example of a bridge type contact model was studied by Mutoh and Xu [Mutoh and Xu, 2003] where structural steel JIS SM430A was used for both pad and specimen. The bulk axial loading was conducted at R_s= -1. The corresponding stress distributions obtained by FEA are shown in Fig 2.33 (a-b) for tension and compression, respectively. They distinguished that in general there are three regions on the contact interface: sticking, slipping, and gapping (separation of fretting pad and specimen). In

their case, the singularity appears at the external contact edge under compression loading and at the internal contact edge under tension.

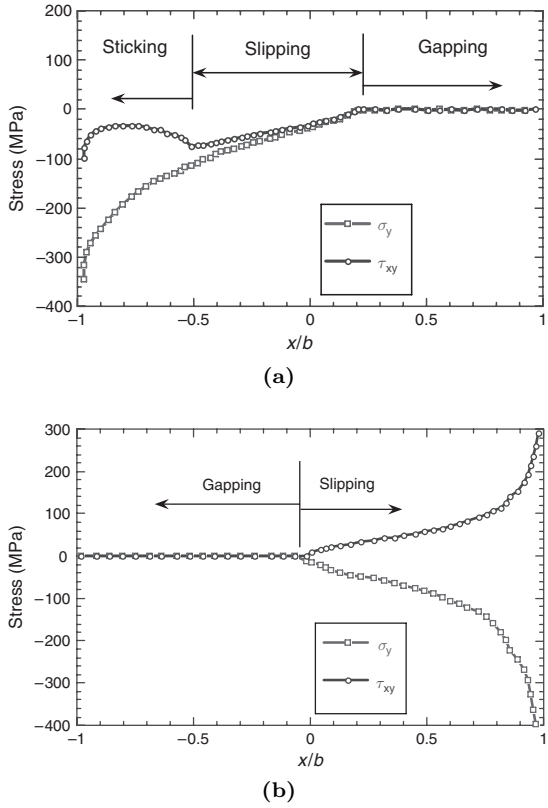

Figure 2.33: The corresponding shear and contact stress distributions obtained by FEA for (a) tension and (b) compression [Mutoh and Xu, 2003].

Jayaprakash et al. [Jayaprakash et al., 2010] carried out FEA to evaluate the stress distribution near the contact edge for studying the effect of contact pad rigidity on fretting fatigue behaviour. In another work [Mutoh and Jayaprakash, 2011] they used the same FEA model to predict fretting fatigue strength by means of a tangential stress range-compressive stress range diagram, which was extracted using the stress distribution at the contact interface.

Single clamp contact:

The schematic view of the single clamp test is shown in Figure 1.11. In

contrast to the bridge type fretting fatigue test, there is a single fretting contact at each side of fatigue specimen. In this type of tests, the fretting pads are mounted on fretting fatigue apparatus and pushed against a fatigue specimen. Thus, the displacement amplitude at contact interface depends on the compliance of both fretting rig as well as fatigue specimen. In this section some of the available FEA models of this type of test configuration are reviewed.

Giannakopoulos and Suresh [Giannakopoulos and Suresh, 1998] modelled a 3-D FEA of fretting fatigue contact between a spherical pad and a flat specimen of the same material. They have used the FEA results later to capture the evolution of surface and sub-surface fields for different levels of partial slip, interfacial friction and externally imposed mean stress values. Farris et al. [Farris et al., 2000] combined FEA modelling and experimental observations, which leaded to thermography/FEM approach to understand the influence of fretting on fatigue failure of riveted aircraft structures. An elasto-plastic analysis of fretting stresses in a pre-stressed strip in contact with a cylindrical pad has been studied by Tsai et al. [Tsai and Mall, 2000]. They investigated the effect of plastic deformation of different fretting fatigue parameters. Iyer and Mall [Iyer and Mall, 2001] advanced the same FEA model to analyse the effects of contact pressure and stress amplitude on fretting fatigue lifetime. By comparison with experimental results, they have revealed that the local stress range computed from FEA may be sufficient for predicting fretting fatigue life. Kim and Mall [Kim and Mall, 2005] have extended the same FEA model to investigate three-dimensional effects of finite contact width on fretting fatigue using two quite different pad geometries i.e. cylinder and flat with rounded edge. They used sub-modelling technique to obtain an accurate stress and displacement state in the contact region. They have also concluded that a two-dimensional plane strain formulation can be used to analyse fretting fatigue crack initiation behaviour in most of fretting fatigue tests involving finite width. Sabelkin and Mall [Sabelkin and Mall, 2005] modified the previous FEA models to include the compliance of fretting fixture as well as to allow the application of bending moment on the pad. For this purpose they added a set of springs on the top of the fretting pad. Using their FEA modelling approach, they computed local relative slip from the measured global relative slip. Massingham and Irving [Massingham and Irving, 2006] used FEA modelling approach to study variation of frictional shear stress distributions at the contact interface subjected to variable amplitude fretting fatigue loading condition.

Bernardo et al. [Bernardo et al., 2006] proposed a FEA based method in order to estimate the effects of fretting pad size on fretting fatigue lifetime. They claimed that their proposed modelling approach has two advantages, when compared with the conventional FEA. First, the proposed model provides a direct evaluation of the fatigue strength at nodal points along with the stress/strain distribution results. Second, they showed that for fretting fatigue problem the stress state should be extracted using a process zone approach rather than in a single point. They have also revealed that selecting of an appropriate mesh size at contact interface is capable of estimating the critical contact size effect successfully. Madge et al. [Madge et al., 2007] developed a FEA based method to predict the wear depth of material subjected to fretting fatigue loading condition. Their model was capable of monitoring the evolution of contact geometry, contact stresses and a multi-axial fatigue damage parameter with cumulative damage effects, as a function of slip amplitude. Wang et al. [Wang et al., 2007] used FEA modelling approach to simulate a non-uniform friction distribution model in the fretting contact zone. They determined the size of stick/slip regions by means of a closed-form solution. A FEA sub-modelling method was used to estimate the crack propagation lifetime for two contact geometries, cylinder-on-flat and flat-on-flat by Fadag et al. [Fadag et al., 2008].

Hirsch and Neu [Hirsch and Neu, 2011] developed a FEA model in order to determine the cyclic stress-strain response of material subjected to fretting loading condition. Rammohan and Murthy [Rammohan and Murthy, 2012] employed 3-D FEA to study the effects of edge fillet and bulk stress on fretting specimen. Nesládek et al. [Nesládek et al., 2012] have combined Digital Image Correlation (DIC) technique and FEA modelling technique to calibrate the friction coefficient of fretting fatigue contact. They have used the detailed model of the fretting-fatigue experimental set-up for computing the stress field. They also used FEA results as input for the multi-axial fatigue criteria and verified the prediction quality of the criteria.

Practical application

Some researchers have directly modelling the 2-D/3-D simplified geometry of real applications such as dovetail-attachment joints, spline couplings, bearing shafts, steel wires connections, shrink-fitted joints, artificial hip joints, automotive industry, bolted and riveted connections, etc. In this section some of these practical applications are reviewed.

Dovetail joints:

Boddington et al. [Boddington et al., 1985] presented a technique for the FEA of dovetail joints, which was capable of modelling relative motion at the interface of the assembly. They have used the FEA results to study the interface motion in contacting assemblies along with the stress distribution at contact interface. Papanikos et al. [Papanikos et al., 1998] developed a 3-D non-linear FEA of the dovetail region in aero-engine compressor disc assemblies in order to evaluate the effect of the critical geometric features and frictional interface conditions in the dovetail region. They validated the FEA results using three-dimensional photoelastic stress freezing technique.

Meguid et al. [Meguid et al., 2000] carried out a comprehensive 2-D and 3-D FEA of the fir-tree region in aero-engine turbine disc assemblies. They have investigated the effect of the critical geometrical features, such as the number of teeth, flank length and flank angle upon stress field in the disc. They have also extended the model to study the effect of of the skew angle and the interfacial friction between the disc and attached blades. They have found that 2-D and 3-D results correlated well. However, the 2D results showed the stress values by a maximum error of 10%. Figure 2.34 illustrates the 3D FE model of typical dovetail joint's assembly view along with the stress distribution in disc and blade taken from [Rao et al., 2008].

Sinclair et al. [Sinclair et al., 2002] represented a sub-modelling procedure which captures the peak stresses near contact edges in dovetail attachments. Song et al. [Song et al., 2002] used combination of intelligent computer-aided design system (ICAD) and FEA in order to optimize the design of a turbine blade fir-tree root. They have used a feature-based geometry modelling tool and the optimisation techniques to examine the effects of critical geometric features on the stress distribution at the interface between the blade and disk connection.

Arrieta et al. [Arrieta et al., 2004] have modelled a two-dimensional FEA of blade-disk attachment contact to quantify the influence of the key factors on mechanical quantities (stress and strain). To balance computational effort with results accuracy, they have paid special attention to material models and surface interaction (friction coefficient and contact conditions). Kermanpur et al. [Kermanpur et al., 2008b] constructed a 2D FEA of the blade root. They have used the FEA results to provide accurate estimates of stress field in the dovetail blade root in order to determine the crack initiation site in the dovetail

joint.

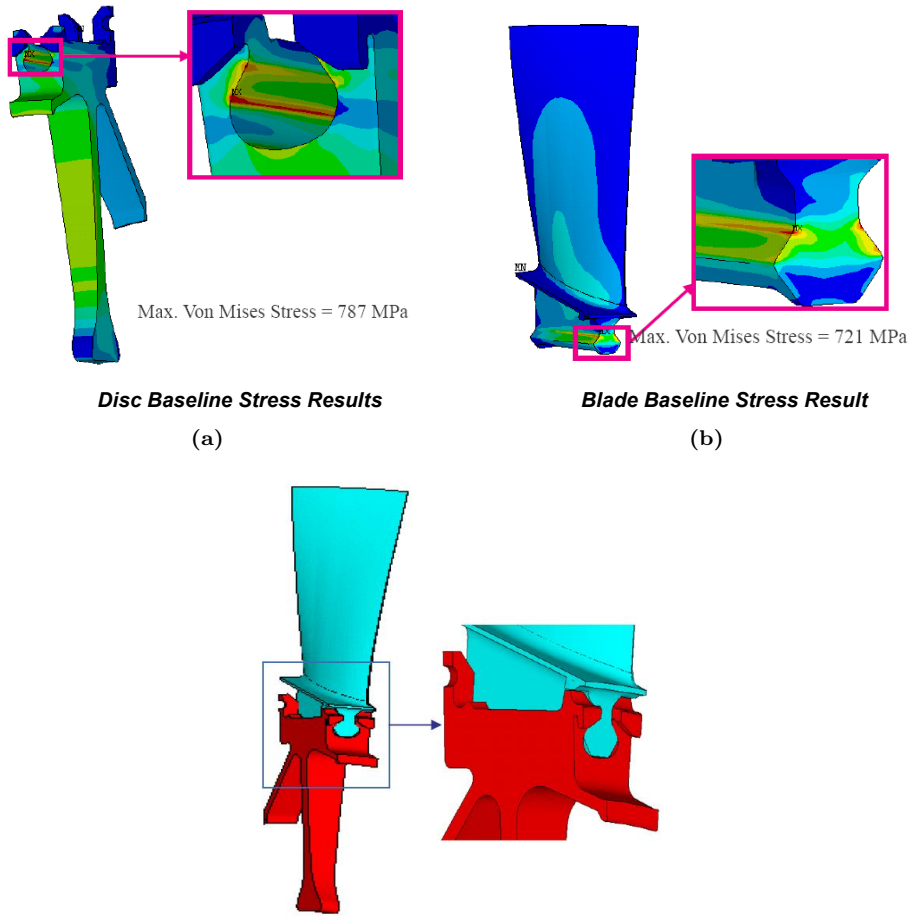

Figure 2.34: Assembly view dovetail joint along with the von-Mises stress distribution in disc and blade. The maximum stress appears at edge of contact between disc and blade attachment [Rao et al., 2008].

Chan et al. [Chan et al., 2010] have performed a global FEA of the disk blade assembly. Using FEA stress distribution results, they have evaluated the effectiveness of residual stresses on stress state in a blade/disk assembly subjected to fretting fatigue loading condition. Wackers et al. [Wackers et al.,

2010] used 3-D FEA to identify relevant parameters such as friction coefficient, slip conditions and machine compliance in blade-disk attachment. They have used the FEA results to predict life in a real compressor practical application.

Spline couplings:

Ding et al. [Ding et al., 2007b] have used FEA approach in order to predict fretting contact stress status, particularly multiaxial frictional contact stresses and slips, for a complex spline coupling assembly subjected to non-symmetrical and variable amplitude loading as depicted in Figure 2.35. The fretting damage appears at contact interface between the mail and female part of internal and external spline coupling. Houghton et al. [Houghton et al., 2009] have combined experimental and a 3-D FEA approach for fretting fatigue life prediction of aero-engine splined couplings.

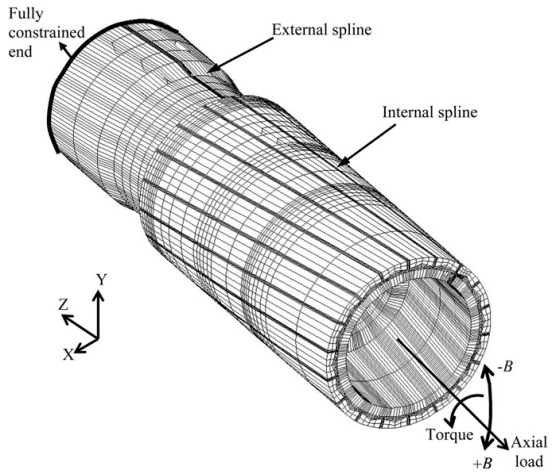

Figure 2.35: FE model of the spline coupling illustrating the constraints boundary conditions on the external spline and the applied loads to the internal spline [Ding et al., 2007b].

Shrink fitted joints:

Gutkin and Alfredsson [Gutkin and Alfredsson, 2008] investigated the influence of friction on lame pressure and slip zone at shrink-fit assembly subjected to rotating bending. They have also implemented numerical routine and 3D FEA model to assess the contribution of the fretting load and to compute the crack growth lifetime.

Lanoue et al. [Lanoue et al., 2009] have developed a 3D FEA study of an interference fit assembly subjected to bending as shown in Figure 2.36. They focused their study on mesh convergence, sub-modelling and different contact algorithms to obtain accurate displacement and stress results near the contact edge where fretting fatigue failure occurs. They have tested four contact algorithms: Penalty function, Augmented Lagrangian, Normal Lagrange and Pure Lagrange. They have concluded their study with some valuable recommendations for FEA modelling of fitted joints.

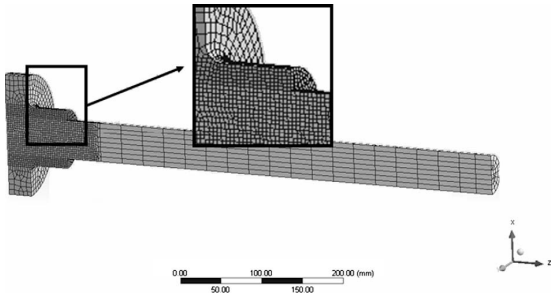

Figure 2.36: FE mesh of shrink fitted joints [Lanoue et al., 2009].

Steel wires connections:

More recently, 3-D modelling of fretting fatigue phenomena in wire connections become more popular [Cruzado et al., 2012, Cruzado et al., 2013, Wang et al., 2013b, Wang et al., 2013a]. Cruzado et al. [Cruzado et al., 2013] simulated a 3D FEA model of cylinder on cylinder contact configuration to study the effect of fretting on fatigue life reduction of thin steel wires. For this purpose they extracted multi-axial contact stresses from a FEA wear model from their previous work [Cruzado et al., 2013]. A full scale FEA model plus sub-modelling approach to model hoisting rope and three-layered strand has been developed by Wang et al. [Wang et al., 2013b] as shown in Figure 2.37. They have studied stress distributions and fretting damages including wear profiles on the the contact surfaces, which were subjected to fretting fatigue loading conditions.

Artificial hip joints:

FEA modelling of fretting in hip joints are very limited in the literature. Hornbach et al. [Hornbach et al., 2006] used 3D FEA modelling approach to apply compressive residual stress field of the hip stem. They have used their

model to estimate both the in-service applied stresses and the low plasticity burnishing (LPB) residual stresses in the neck stem segment. Zhang et al. [Zhang et al., 2013] developed an 2-D/3-D FEA based methodology for fretting wear-fatigue prediction in a prosthetic hip implant. They simulated 3-D FEA model to model the global stem-head contact and a 2-D axi-symmetric model of the realistic commercially available stem-head joint (see Figure 2.38) for fretting wear and fatigue computation.

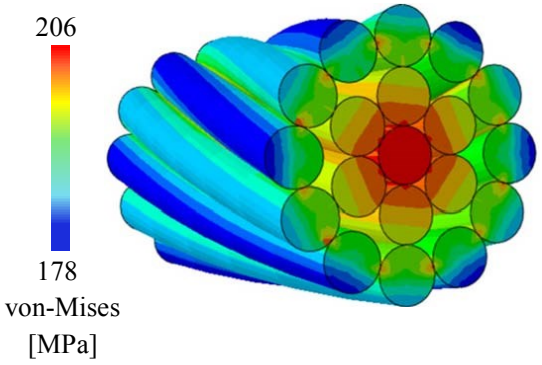

Figure 2.37: von-Mises stress distribution in steel wire connection. Fretting damage appears at contact interface between two wires [Wang et al., 2013b].

Automotive industry:

Buciumeanu et al. [Buciumeanu et al., 2007] implemented FEA modelling approach for improving design of car's suspension component, which was subjected to fretting fatigue as shown in Figure 2.39. For this purpose they used 2D/3D FEA model to determine the stress state along the component. They have used topology optimization method in combination with FEA in order to modify shape of connected components to enhance this fretting fatigue total lifetime. Jayaprakash et al. [Jayaprakash et al., 2011] carried out FE analysis to discuss effect of groove on fretting fatigue strength of the bolted joints of SAPH400 automotive steel plates. They used stress distribution as well as tangential stress range and compressive stress range at the contact edge of bolted joints to investigate the strength of the joint.

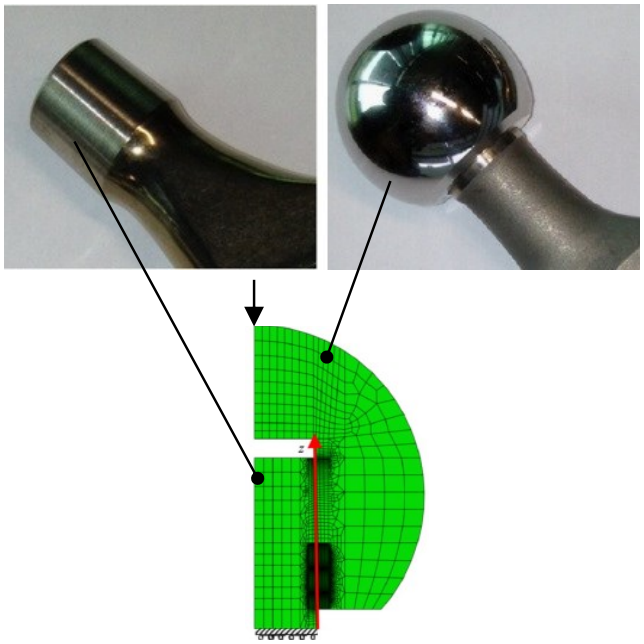

Figure 2.38: 2D axisymmetric FE model of stemhead contact. Fretting damage occurs at contact interface (the red line) [Zhang et al., 2013].

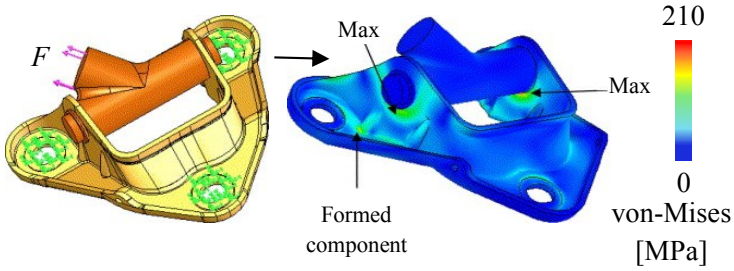

Figure 2.39: von-Mises stress distribution in car suspension component. Fretting damage occurs at contact interface between the bolt washer and the formed component (as named in the reference paper) [Buciumeanu et al., 2007].

Bolted and riveted joints:

The early FEA study of riveted joints dates back to mid 90's reported by Hoeppner et al. [Heoppner et al., 1996]. When a FEA based methodology was used to determine the stress state at rivet locations, where the fretting fatigue

crack initiates. They used the FEA results as a valid baseline condition to apply the method for prediction of COF during fretting process to a riveted joint. Szolwinski et al. [Farris et al., 2000] targeted at characterizing the conditions at/around the rivet/hole interface by means of FEA approach. They modelled both mechanics of load transfer in riveted joints and the residual stress field. A 3-D FEA of riveted joint was modelled by Guo et al. [Guo et al., 2008]. They have tried to study the mechanism of fretting fatigue crack formation in aluminium alloys, and the determination of the characteristic crack initiation sites by means of both experimental and numerical methods. Moreover, they investigated the influence of the contact COF and fastening forces on the initiation of cracks by means of the comparison of the different numerical results. Benhamena et al. [Benhamena et al., 2010] used 3-D FEA approach to analyse the effect of tightening torque on single bolted lap joint under fretting fatigue loading condition. In their work they also tried to monitor the contact status along with the potential location of fretting fatigue crack under different loading conditions. Chakherlou et al. [Chakherlou and Abazadeh, 2012] performed FE modelling of double shear lap joints subjected to cyclic load and compared with the experimental results under static loading condition in order to study the joints performance.

2.4.3 Crack initiation

Determining the exact failure mechanism of fretting fatigue crack initiation is a challenging task, as many conditions are present which could result in the formation of the initial crack. There are several possible mechanisms that can lead to fretting fatigue crack formation. Some researchers [Kovalevskii, 1981, Hills et al., 1988a, Reeves and Hoeppner, 1976] proposed that failure occurs due to adhesively contacting asperities. Investigators have sorted through the effects of increased stress due to contact, fretting wear damage, environment, etc. and have determined that most fretting fatigue failures are not the result of a single variable, but a combination of variables [Hoeppner et al., 1994]. However, there is a disagreement as to the relative importance of each effect. The mechanism of fretting fatigue occurs in four stages [Hoeppner et al., 1994]. First, the crack initiates from fretting damage. Then, there is a period of crack propagation (short crack propagation) caused by contact stresses, which is faster than would be attributable to bulk stress alone. Once the crack has grown beyond the influence of the contact stress state, normally two times the semi-contact width, the crack propagation is governed by the axial bulk stress

alone. Eventually, fast fracture may occur as the crack grows.

Fretting fatigue crack initiation scenario can be explained by accumulation of damage, which leads to formation of initial micro-cracks at the contact interface. The number of cycles at which the micro-cracks form is called damage threshold [Hoeppner et al., 1994]. The damage threshold is thought to be the point at which a crack has formed and has begun propagating [Hoeppner, 1981]. Therefore, the *'damage threshold'* is not only dependent on the initiation stage of fretting, but also on the contact stress state. The stress state determines how large an initiated crack has to be in order to propagate. According to literature there is no criterion to define the initial crack length that can be considered as crack initiation or onset of crack propagation. Waterhouse [Waterhouse, 1981] observed that fretting fatigue crack initiating in aluminium alloy after only a few thousand cycles when the cycles to failure is 10^7 cycles. He suggested that the average lifetime taken in initiation plus the slow growth cycle (damage threshold) is about 10 percent of total life. Edwards [Edwards, 1981] showed that after 25 percent of total life, crack growth was independent of fretting or friction. A contradictory view holds that fretting fatigue is an initiation controlled process and that even in fretting fatigue, the majority of life occurs during crack initiation [Hills et al., 1988a]. These investigations clearly show that the fretting fatigue crack initiation is depending on different parameters such as loading conditions and material behaviour and varies from one application to another.

Following the work of Hills et al. [Hills et al., 1988a], by assuming that the majority of the total lifetime is consumed in the initiation portion, has led to use of maximum value of a parameter at or near the edge of contact interface between fretting pad and fatigue specimen. There are many researches concerned with predicting fretting fatigue crack initiation lifetime. Many of them have dealt with stress or strain at a point, the value of parameter at a point or the stress or parameter at some distance beneath the contact surface (critical distance approach) or an average value over some surface area or volume. In fretting fatigue case, due to steep stress gradients that are present in the contact area, the parameters that were used for notch fatigue have been used to predict the initiation lifetime. Since, the nature of stress is multi-axial at the contact interface between fretting pad and fatigue specimen, many researchers have used critical plane based predictive parameters and criteria, which were based on the stresses found on the critical plane. Some of the most used crack

initiation criteria in case of fretting fatigue are mentioned below.

Multiaxial fatigue criteria

One of the predictive parameters are the stresses occurring at the critical plane. The critical plane models are based on the fact that crack initiates on a particular plane, called the critical plane. It has been assumed that on that plane, normal stress opens cracks that reduces the friction between the crack surfaces and shear stress inducing dislocation movement along slip bands, and causing crack initiation. In general, the application of the method requires the consideration of the stress field not only on the surface, but also in a zone within the proximities of the point with the highest stress level. The fatigue strength is analysed as a function of the value of the damage parameter of the multi-axial criterion evaluated for that zone, which can be a *distance*, an *area*, or a *critical volume* [Fouvry et al., 2002, Navarro and Domínguez, 2004]. Some of the most used multi-axial criteria are reviewed, based on calculation of stresses, strains, or a combination of both.

Smith-Watson-Topper (SWT) parameter:

The criterion defined by Smith et al.[Smith et al., 1970] is applied to materials in which cracks grow practically from the beginning in mode *I*. In this case the fatigue parameter, usually called Smith-Watson-Topper (SWT), is expressed as:

$$SWT = \sigma_n^{max} \frac{\Delta\epsilon_1}{2} \tag{2.90}$$

where $\Delta\epsilon_1$ is the maximum range of principal strain and σ_n^{max} is the maximum normal stress in the plane where the maximum range of principal strain is produced. The parameter is applied according to the following equation:

$$SWT = \frac{\sigma_f'^2}{E} \left(2N_f\right)^{2b'} \tag{2.91}$$

When the load cycle is not proportional, as occurs in fretting fatigue case, it is more complicated to apply this parameter as a result of the rotation of the principal directions. For this purpose there are other proposed developments of the SWT approach for shear fracture mode, which is the case in fretting fatigue problem. This criterion has the ability to account for the effect of cyclic hardening because both σ_1 and ϵ_1 are presented in its equation [Smith et al., 1970, Dowling, 1971]. Thus, it is possible to use the maximum value of

the product, $(\sigma_1 \Delta\epsilon_1)/2$ at contact interface between fretting pad and fatigue specimen, in which σ_1 is the first principal stress and $\Delta\epsilon_1$ first principal strain range. Consequently, the final form of SWT parameter can be written as [Socie, 1987, Yan et al., 2006, Navarro et al., 2008]:

$$SWT = \left(\sigma_1 \frac{\Delta\epsilon_1}{2}\right)_{max} \tag{2.92}$$

In this way there is greater simplicity and the results turn out to be the same as those obtained with the first definition of this parameter i.e. Equation 2.90. The SWT parameter has been implemented to fretting fatigue problem in order to estimate crack initiation lifetime by researchers; some of them can be found here [Szolwinski et al., 1997, Lykins et al., 2001b, Navarro et al., 2008, Sabsabi et al., 2011, Giner et al., 2011a].

Fatemi-Soice (FS) parameter:

This criterion is based on strains and on the maximum normal stress to the critical plane. The critical plane in this criterion is the plane where the shear strain range is maximum [Fatemi and Socie, 1988]. The Fatemi-Socie parameter is defined as:

$$FS = \frac{\Delta\gamma_{max}}{2}\left(1 + k\frac{\sigma_n^{max}}{\sigma_{yield}}\right) \tag{2.93}$$

where $\Delta\gamma_{max}$ is the maximum range of shear strain, σ_n^{max} is the maximum normal stress perpendicular to the critical plane, σ_{yield} is the yield strength and k is a constant that is fitted from the uni-axial and torsion fatigue test data. The ratio σ_{yield}/k is often very close to the value σ'_f [Araujo and Nowell, 2002, Neu and Pape, 1998]. By considering a simple case of plain fatigue with reverse cycle σ, the number of cycles to initiation N_i as a function of the FS parameter can be written as:

$$FS = \frac{1+\nu}{E}\sigma'_f(2N_i)^{b'}\left(1 + \frac{1}{2}(2N_i)^{b'}\right) \tag{2.94}$$

This criterion has also been used for fretting fatigue problem by some researchers in literature [Navarro et al., 2008, Sabsabi et al., 2011, Giner et al., 2011a].

McDiarmid parameter:

This criterion is one of the multi-axial fatigue criteria based on stresses. The critical plane in this criterion is the plane where the shear stress range is

maximum [McDiarmid, 1991]. McDiarmid parameter criterion has been implemented to fretting fatigue problem by some researchers [Navarro et al., 2008, Sabsabi et al., 2011, Giner et al., 2011a]. The McDiarmid equivalent stress is defined as:

$$\sigma_{eq}^{MD} = \frac{\Delta\tau_{max}}{2} + \left(\frac{\tau_f}{2\sigma_u}\right)\sigma_n^{max} \tag{2.95}$$

where $\Delta\tau_{max}$ the maximum shear stress range, σ_n^{max} is the maximum normal stress in the direction perpendicular to the plane of $\Delta\tau_{max}$, τ_f is the fatigue limit in torsion and σ_u is ultimate stress. Therefore, the number of initiation cycles N_i as a function of the McDiarmid equivalent stress can be provided:

$$\sigma_{eq}^{MD} = \frac{1}{2}\left(1 + \frac{\tau_f}{2\sigma_u}\right)\sigma_f'\left(2N_i\right)^{b'} \tag{2.96}$$

Findley parameter (FP):

This criterion takes into account both the shear stress amplitude and the maximum stress normal to the orientation of the maximum shear plane. Findley [Findley, 1956] suggested the use of a multi-axial fatigue parameter to predict fretting fatigue behaviour in the following form:

$$FP = \tau_{average} + k\sigma_{max} \tag{2.97}$$

where $\tau_{average}$ is the average shear stress, σ_{max} is the maximum stress normal to the orientation of maximum shear plane and k is an influence factor (normally k=0.35) found from plain fatigue data. The critical plane is such that crack initiation is assumed to occur on the plane with the maximum Findley Parameter value. The parameter is determined, on all planes from $-90°$ to $90°$ on increments of $0.1°$. It has been investigated by Namjoshi et al. [Namjoshi et al., 2002] that, FP parameter could not discern between plain and fretting fatigue when determining fatigue life, which is obviously an error. Thus, despite this parameter has been used by some researchers [Murthy et al., 2009, Lee et al., 2004], it is probably not the best choice of a predictive fretting fatigue parameter.

Shear Stress Rang (SSR) parameter:

Another parameter considered by Namjoshi et al. [Namjoshi et al., 2002] included the Shear Stress Range parameter, (SSR), developed by Lykins et al.

[Lykins et al., 2001a] which is defined as follows:

$$\Delta\tau = \tau_{max} - \tau_{min} \tag{2.98}$$

where $\Delta\tau$ is the shear stress range and τ_{max} and τ_{min} are the shear stress values due to the maximum and minimum globally applied loading, respectively. Thus, the critical plane is the plane where the shear stress range is at a maximum. The shear stress range parameter was slightly modified to account for the effects of mean axial/shear stress since it has been shown that the mean stress also affects fatigue behaviour. Using a technique proposed by Walker [Walker, 1970] to account for mean shear stress ratio effect on the critical plane, the shear stress range parameter was then rewritten as:

$$SSR = \Delta\tau_{crit} = \tau_{max}\,(1 - R_\tau)^\eta \tag{2.99}$$

where τ_{max} is the maximum shear stress on the critical plane, R_τ is the shear stress ratio on the critical plane defined as τ_{min}/τ_{max}, and η is fitting parameter determined to be 0.45 from plane fatigue data [Lykins et al., 2001a].

Modified Shear Stress Rang (MSSR) parameter:

Namjoshi et al. [Namjoshi et al., 2002] observed that the SSR parameter successfully predicts the location and orientation of crack initiation, however, not for all pad geometries used in their study. Therefore, they proposed a new parameter called the Modified Shear Stress Range (MSSR) with the goal of combining the positive qualities of the Findley and SSR parameters. The MSSR parameter is stated as:

$$MSSR = A\Delta\tau_{crit}^{B} + C\sigma_{max}^{D} \tag{2.100}$$

Where $\Delta\tau_{crit} = \tau_{max}\,(1 - R_\tau)^\eta$, τ_{max} is the maximum shear stress on the critical plane, R_τ is the shear stress ratio on the critical plane, and η, A, B, C, D are curve fitting parameters. Using this approach the critical plane is determined by the maximum value of the shear stress range, $\Delta\tau$, and not by the maximum value of the MSSR parameter.

Crossland parameter:

The Crossland criterion [Crossland, 1956] is different from the previous ones in the sense that it is no longer a critical plane criterion, but a global one, based on the values of an invariant of the stresses. While previous criteria require a maximum value among all directions projecting the stresses (or strains), in

the Crossland criterion the calculation of stresses can be done in any direction, and it only requires the calculation of an invariant. This criterion has the obvious advantage of a much shorter computation time, with the inconvenience of the loss of a physical sense of the problem. The stress, or equivalent stress parameter, is

$$Cross = \sqrt{J_{2,a}} + \frac{I_{1,max}}{3}\left(\frac{3t}{b'} - \sqrt{3}\right) \tag{2.101}$$

where $J_{2,a}$ is the amplitude of the second invariant of the deviatoric stress tensor and $I_{1,max}$ is the maximum of the first invariant of the stress tensor,t is the shear fatigue limit and b' is the bending fatigue limit. The application of this parameter to the case of a uni-axial fatigue test provides the necessary expression for its application to any case in the calculation of the number of cycles:

$$Cross.\frac{b'}{t} = \sigma'_f \left(2N_f\right)^{b'} \tag{2.102}$$

Almost all mentioned above studies used FEA modelling approach to extract stress and strain states at contact interface in order to use one the mentioned criteria to deal with fretting fatigue problem. For instance, Ding et al. [Ding et al., 2011] implemented FEA modelling to present two empirical parameters for the prediction of fretting. These parameters combined a multi-axial fatigue parameter and a surface damage parameter, which represents the surface damaging effect of fretting, extracted from FEA of fretting wear and fatigue models. Hirsch and Neu [Hirsch and Neu, 2011] developed a FEA model in order to determine the cyclic stress-strain response of material subjected to fretting loading condition. They have extracted the FEA results to evaluate the Smith-Watson-Topper (SWT) and Fatemi-Socie (FS) critical-plane-based multi-axial fatigue damage parameters. In their model, fretting specimen consisted of three layers: the moving specimen with a rigid layer at the top, the stationary specimen with a compliant layer at each end, and the bottom body, which includes a Teflon (PTFE) layer, backing plate, and a compliant layer at each side of the backing plate [Hirsch and Neu, 2011]. Therefore, as mentioned earlier, choosing a proper FEA modelling technique of fretting and fretting fatigue contact may have large influence on the estimated results.

Continuum Damage Mechanics (CDM) approach

Recently Continuum Damage Mechanics (CDM) became more popular for modelling fretting fatigue damage [Quraishi et al., 2005, Zhang et al., 2012, Aghdam et al., 2012]. Nevertheless, FEA modelling of fretting fatigue using CDM approach is very limited in the literature. The main advantage of CDM approach is that the damage model is obtained from the law of thermodynamics and uses the bulk material properties to predict the cycles to crack initiation.

Quraishi [Quraishi et al., 2005] developed a simple engineering model based on the thermodynamics framework for damage accumulation, which was introduced by Bhattacharya et al. [Bhattacharya and Ellingwood, 1998, Bhattacharya and Ellingwood, 1999, Bhattacharya and Ellingwood, 1999] to predict fretting crack nucleation. They calculated the subsurface stress distribution due to fretting loading conditions to predict the occurrence of fretting fatigue failure. They found that the maximum alternating shear stresses caused fretting cracks. They combined the damage due to stresses in two directions to predict the fretting fatigue life using the maximum shear stress by CDM.

Zhang et al. [Zhang et al., 2012] have developed a FE based method coupled with a non-linear continuum damage model introduced by [Chaboche and Lesne, 1988] and implemented for 2-D fretting fatigue problem for Ti-6Al-4V with comparisons against published data for the effect of slip on lifetime. They have found that incremental damage accumulation (coupled damage model) in combination with with FE analysis predicts longer life compared with the integrated formula (un-coupled damage model). They have realised that the reason for this overestimation is related to load redistribution in the high stress gradient area at and near contact interface. They have also showed that FE analysis of fretting fatigue coupled with the CDM model predicts a similar trend of life versus slip to the critical plane SWT method. From their developed model the predicted cracking positions were across the slip band and, specifically, in the centre of the slip zone.

2.4.4 Crack propagation

In terms of fretting fatigue crack propagation there are numerous studies [Rooke and Jones, 1979, Adibnazari and Hoeppner, 1994, Sheikh et al., 1994, Kondoh and Mutoh, 2000, Hattori et al., 2003, Nicholas et al., 2003, Munoz et al., 2007, Giner et al., 2008, Sabsabi et al., 2011, Giner et al., 2011a, Navarro et al.,

2011] that have used fracture mechanics approach to calculate crack growth lifetime. The propagation stage in a fretting fatigue problem is substantially different from that of plain fatigue during the phase, in which the crack length is less than the characteristic dimension of the contact zone [Hills and Nowell, 1994]. Therefore, it is essential to account for the effect of the contact stress field on the crack and vice versa (crack-contact interaction). It is especially important to estimate realistic values of the stress intensity factors (SIFs) and as a consequence, numerical modelling often becomes a necessity e.g. using the FEM approach. Moreover, FEA method has been used widely to calculate SIFs at the crack tip in pre-cracked specimen [Kondoh and Mutoh, 2000, Giner et al., 2008, Sabsabi et al., 2011, Giner et al., 2011a]. Thus, for prediction of fretting fatigue crack propagation lifetime a fracture mechanics approach is usually considered to be appropriate [Hills and Nowell, 1994].

Due to the intrinsic complexity of modelling fretting fatigue crack propagation, simplifications are often introduced. Several authors have studied the propagation stage in two dimensions. Rooke and Jones [Rooke and Jones, 1979] used Green's function, which is a purely analytical formula for calculating SIFs at the crack tip. Some researchers used combination of FE method and analytical formula such as Weight functions [Nicholas et al., 2003, Munoz et al., 2007, Navarro et al., 2011] to calculate SIFs for the cracks normal to the contact line or an arbitrary path of crack inside the un-cracked fatigue specimen. Kimura and Sato [Kimura and Sato, 2003] calculated K_I analytically by applying equivalent contact tractions and Greens functions for inclined mixed-mode cracks. Sheikh et al. [Sheikh et al., 1994] used a FE model of the classic fretting bridge type contact configuration and studied the SIFs for several crack lengths and different crack angles with respect to the contact surface. Mutoh et al. [Mutoh and Xu, 2003] presented one of the most comprehensive experimental and numerical studies on crack propagation for a fretting bridge type contact configuration. Their FE model included the contact influence, with the crack located at the end of the contact zone. They considered several crack propagation increments to simulate the crack growth path and applied the estimated values of the SIFs to compute the fretting fatigue life.

Fadag et al. [Fadag et al., 2008] have used a conventional FE sub-modelling technique to estimate the fretting fatigue crack propagation life using FE code, which is called FRANC2D/L®[FRANC2D/L, 2010]. For this purpose, they extracted the loading and boundary conditions on the sub-model region from the

analysis conducted on the full test configuration by ABAQUS®[Hibbitt et al., 2011] software. Then an edge crack was inserted in the sub-model to perform the crack growth analysis by FRANC2D/L®code, which has capability for incremental crack growth using fracture mechanics principles as elaborated later. More recently, Mohd et al. [Mohd Tobi et al., 2012] implemented both steps i.e. performing fretting fatigue contact and crack propagation in ABAQUS®in order to address coating fracture in hard brittle coatings subjected to combined normal and tangential loads.

Despite the conventional FEM is a popular approach for 2-D crack propagation, when it turns to 3-D modelling, it is really challenging and time consuming. However, there are some researchers that implemented conventional FEM approach to model 3-D fretting fatigue crack propagation [Alfredsson and Olsson, 2000, Cadario and Alfredsson, 2005, Gutkin and Alfredsson, 2008, Carter et al., 2012]. Gutkin [Gutkin and Alfredsson, 2008] studied the 3-D crack growth in a shrink-fit assembly subjected to rotating bending, by means of two FE models and a numerical routine to evaluate the contribution of the fretting load and to compute the crack growth. They have tried to determine the component life reduction due to the fretting crack propagation as compared to crack growth at the corresponding pure bending load. However, in their 3-D model they did not consider the effect of crack-contact interaction during crack propagation increments. Carter [Carter et al., 2012] used a 3-D FEA to compute the fretting fatigue life for metallic components. For this purpose they used standard FEA capabilities of ANSYS®[Kohnke, 2010] and FRANC3D®[Wawrzynek et al., 2012]. They have computed the propagation lifetime using discrete 3-D crack growth simulations based on conventional FE approach.

Fundamentals of the XFEM

Modelling stationary discontinuities, such as cracks, with the conventional FE method requires that the mesh conforms to the geometric discontinuities. Therefore, considerable mesh refinement is needed in the neighbourhood of the crack tip to capture the singular asymptotic fields adequately. Modelling a growing crack is even more cumbersome because the mesh must be updated continuously to match the geometry of the discontinuity as the crack progresses.

The eXtended Finite Element Method (XFEM) alleviates the shortcomings associated with meshing crack surfaces. The XFEM was first introduced by

Belytschko and Black [Belytschko and Black, 1999]. It is an extension of the conventional FE method based on the concept of partition of unity by Melenk and Babuska [Melenk and Babuška, 1996], which allows local enrichment functions to be easily incorporated into a FE approximation. The presence of discontinuities is ensured by the special enriched functions in conjunction with additional degrees of freedom. However, the finite element framework and its properties such as sparsity and symmetry are retained. In comparison to the standard conventional FEM, the XFEM provides significant benefits in the numerical modelling of crack propagation. The main advantages are that the FE mesh needs not to conform to the crack boundaries (crack faces) to account for the geometric discontinuity. Furthermore, mesh regeneration is not needed in crack propagation simulations. Therefore, only a single mesh, which is often easily generated, can be used for any crack length and orientation. Because of all of these capabilities it seems to be a prefect solution for complex fretting fatigue crack propagation simulation. In a simple definition, XFEM is based on the introduction of additional degrees of freedom (DOFs), which are associated with the nodes of the elements intersected by the crack geometry. These extra DOFs in combination with special functions enable the accurate modelling of the crack.

Discontinuous jump function

For the purpose of fracture mechanics analysis, the enrichment functions typically consist of the near-tip asymptotic function that captures the singularity around the crack tip and a discontinuous function (also called jump, heaviside or step function) that represents the jump in displacement across the crack line (in case of 2-D crack). Using the *partition of unity* concept, XFEM adds a priori knowledge about the solution in the FE area and makes it possible to model discontinuities and singularities independently of the mesh. To explain how the discontinuous functions are added to the FE approximation, a simple two-dimensional crack is studied [Moës et al., 1999].

By Considering the case of a crack in a mesh with four elements, where the crack is placed on the element boundary, in Figure 2.40, the finite element approximation for the mesh is:

$$u^h(x) = \sum_{i=1}^{10} N_i(x) u_i \tag{2.103}$$

where N_i is the shape function for node i, u_i is the displacement vector at

node i and x is the position vector. Defining ξ and ζ as:

$$\xi = \frac{u_9 + u_{10}}{2}, \quad \zeta = \frac{u_9 - u_{10}}{2} \tag{2.104}$$

where ξ lie in between u_9 and u_{10} and ζ is half the distance between u_9 and u_{10}. u_9 and u_{10} can be expressed in terms ξ and ζ.

$$u_9 = \xi + \zeta, \quad u_{10} = \xi - \zeta \tag{2.105}$$

The FE approximation Equation 2.103 can then be written as:

$$u^h(x) = \sum_{i=1}^{8} N_i(x)u_i + \xi(N_9 + N_{10}) + \zeta(N_9 + N_{10})H(x) \tag{2.106}$$

where the discontinuous sign/jump function $H(x)$ is written as:

$$H(x) = \begin{cases} 1 & y > 0 \\ -1 & y < 0 \end{cases} \tag{2.107}$$

By replacing $N_9 + N_{10}$ by N_{11} and ξ by u_{11} and the FE approximation can be expressed as

$$u^h(x) = \sum_{i=1}^{8} N_i(x)u_i + N_{11}u_{11} + \zeta N_{11}H(x) \tag{2.108}$$

The first two parts on the right-hand side of the equation ($\sum_{i=1}^{8} N_i(x)u_i + N_{11}u_{11}$) are the standard FE approximation, and the third part ($\zeta N_{11}H(x)$) is the additional discontinuous jump enrichment. Equation 2.108 indicates that the FE approximation of a crack in a mesh, as schematically illustrated in Figure 2.40 (a), may be interpreted as a mesh without a crack, as in Figure 2.40 (b), and an additional discontinuous enrichment. The extension to a crack that is not placed on the element boundary can be described in a similar manner [Moës et al., 1999].

To be able to capture the singularity at the crack tip, discontinuous asymptotic crack tip functions are added to the nodes that surround the crack tip [Moës et al., 1999], as illustrated in Figure 2.41. If the tip does not end at an element boundary, the crack tip functions also describe the discontinuity over the crack surfaces in the element containing the crack tip. Thus, in total, there

are two types of enrichments; the asymptotic crack tip functions to describe the crack tip and the jump function to describe the rest of the crack. The nodes are enriched with the jump function when their supports are fully intersected by a crack whereas the element nodes surrounding the crack tip are enriched with the crack tip functions. As indicated in Figure 2.41, the triangular nodes are enriched with the jump function and the squared ones are enriched with the crack tip functions.

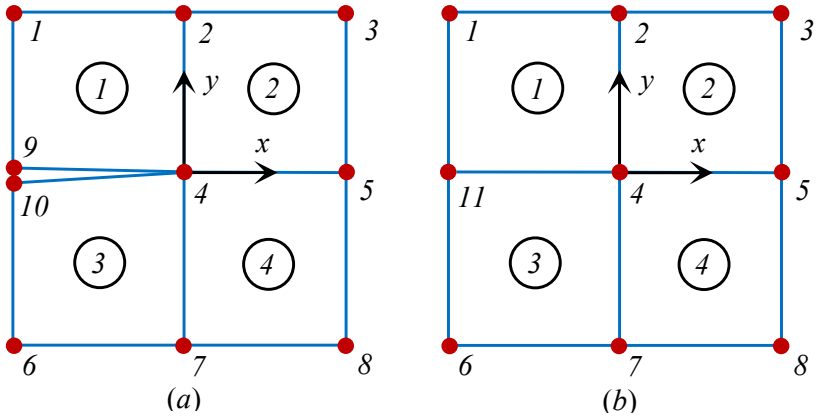

Figure 2.40: Mesh with a crack, (a) and a mesh without a crack, (b). The circled numbers are element numbers.

The total formulation of XFEM can now be derived. By defining all the nodes in the mesh by the set S_A, the nodes surrounding the crack tip by the set S_c and the nodes whose supports are cut by the crack (excluding the nodes in S_c) be defined by S_H . The finite element approximation can be written as:

$$u^h(x) = \sum_{I \in S_A} N_I(x) u_I + \sum_{J \in S_H} N_J(x) H(x) q_J^0 + \sum_{K \in S_c} \sum_{\alpha=1}^{4} N_K(x) F_\alpha(x) q_K^\alpha \tag{2.109}$$

Where, $N_I(x)$ is the usual nodal shape functions for conventional FE formulation. u_I, is the usual nodal displacement vector associated with the continuous part of the FE solution. The second term is the product of the nodal enriched degree of freedom vector, q_J^0, and the associated discontinuous jump function $H(x)$ across the crack line. The third term is the product of the nodal

enriched degree of freedom vector, q_K^α, and the related elastic asymptotic crack-tip functions, $F_\alpha(x)$. The usual nodal displacement vector, u_I, is implemented to all the nodes in the FEA model. The second term, $N_J(x)H(x)q_J^0$, is valid for nodes whose shape function support is cut by the crack. The third term i.e. $N_K(x)F_\alpha(x)q_K^\alpha$, is used only for nodes whose support is cut by the crack tip. Figure 2.41 shows the discontinuous jump function across the crack surfaces, which is defined by:

$$H(x) = \begin{cases} 1 & for, (x - x^*)n \geq 0 \\ -1 & else, \end{cases} \tag{2.110}$$

Where x is a sample integration (Gauss) point, x^* is the point on the crack closest to x, and n is the unit outward normal to the crack at x^*.

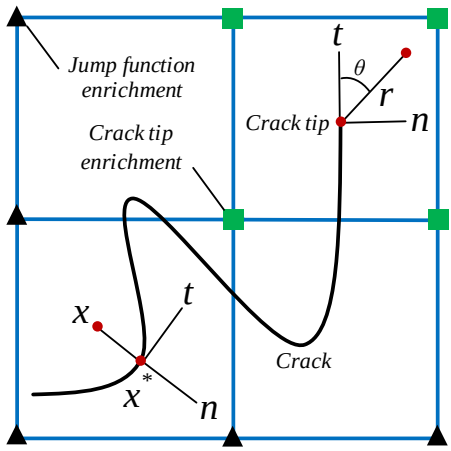

Figure 2.41: Normal and tangential coordinates for a smooth crack.

Crack tip enrichment function

The discontinuous jump function is good when the element is totally cut by the crack, such that it divides the element into two. In case the element contains the crack tip, then part of the element is cut and part of it not as can be seen in Figure 2.41. Hence in such cases, the discontinuous jump function cannot be used to enrich the domain. In Linear elastic fracture mechanics (LEFM), the exact solution of the stress and displacement field is available. Where the displacement field around the crack tip is given in Equation 2.84. Flemming et al. [Fleming et al., 1997] have shown that asymptotic crack tip

functions in an isotropic elastic material contained within the span of following four functions:

$$\{F_\alpha(r,\theta)\}_{\alpha=1}^{4} = \left\{\sqrt{r}\cos\left(\frac{\theta}{2}\right), \sqrt{r}\sin\left(\frac{\theta}{2}\right), \sqrt{r}\sin\left(\frac{\theta}{2}\right)\sin\theta, \sqrt{r}\cos\left(\frac{\theta}{2}\right)\sin\theta\right\} \tag{2.111}$$

Where (r,θ), is a polar coordinate system with its origin at the crack tip and $\theta = 0$ is tangent to the crack faces. These functions forms the basis of the asymptotic field around the crack tip. These four functions are used for enriching the field near the crack tip, thus giving rise to four additional degrees of freedom in each direction at a node, in addition to standard degrees of freedom. It should be noted here that among the four the second function $\sqrt{r}\sin\left(\frac{\theta}{2}\right)$ is discontinuous along the crack surfaces, thus giving the effect of required discontinuity in the approximation along the crack. The rest of the three functions are used for improving the solution near the crack tip. The inclusion of $\sqrt{r}$ term in the enrichment function gives the required singularity in the stress field. It is important to note that, with the use of the above mentioned near tip enrichment functions an element partially cut by the crack could be modelled.

Level set method:

A key development that facilitates treatment of cracks in an XFEM analysis is the description of crack geometry, because the mesh is not required to conform to the crack geometry. The level set method (also called level surface or iso-surface), which is a powerful numerical technique for analysing and computing interface motion, fits naturally with the XFEM and makes it possible to model arbitrary crack growth without re-meshing. In other word Level Set Method (LSM) can be defined as a numerical technique used to track motion of interfaces [Stolarska et al., 2001]. In LSM, the crack Γ_L is considered as a one dimensional curve evolving in a two-dimensional domain as depicted in Figure 2.42. Therefore, the crack geometry can be defined by two orthogonal level-set functions. The first, Φ, describes the crack surface, while the second, Ψ, is used to construct an orthogonal surface. The crack is represented by a set of points:

$$\Gamma_L = \left\{x \in \mathbb{R}^2 | \quad \Psi(x) = 0 \quad \text{and} \quad \Phi(x) \leq 0\right\} \tag{2.112}$$

For a crack that lies completely inside a structure, two tangential level sets, Φ and Ψ, are used. In case of 2D models, the crack tip is located at the intersection of zero level sets of the two orthogonal signed level-set functions. XFEM and LSM work together naturally for crack growth modelling. Level sets contain all the necessary information for modelling crack and facilitate selection of nodes for enrichment. To determine whether a node lies above or below the crack, one simply needs to retrieve sign of Ψ at that point. If the crack cuts through an element, then $\Phi \leq 0$ and $\Psi_{min}\Psi_{max} \leq 0$, where Ψ_{min} and Ψ_{max} are the minimum and maximum values of Ψ at that point. Nodes of this element are enriched with discontinuous jump function. If crack tip lies inside an element, then, $\Phi_{min}\Phi_{max} \leq 0$ and $\Psi_{min}\Psi_{max} \leq 0$, and nodes of the element are enriched with crack tip enrichment function.

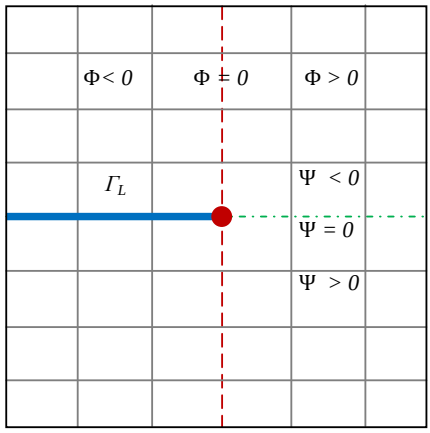

Figure 2.42: Representation of a 2-D crack by two level set functions, the crack tip is shown by intersection of $\Phi = 0$ and $\Psi = 0$.

Application to fretting fatigue problem:

For the first time XFEM has been implemented to fretting fatigue 2-D crack propagation problem by Giner et al. [Giner et al., 2008]. They have studied the the crack-contact interaction effects in an efficient way for fretting fatigue crack propagation problem. There are also some other studies that used XFEM for 2-D fretting fatigue crack propagation simulation [Baietto et al., 2010, Giner et al., 2011a, Sabsabi et al., 2011, Giner et al., 2011b, Giner et al., 2013].

Pierres et al. [Pierres et al., 2011] have developed a 3-D two-scale fric-

tional contact fatigue crack model within the XFEM framework. They have implemented their model to a 3-D ball/plate fretting fatigue test with running conditions inducing crack nucleation and propagation. They have defined 3-D crack shapes from actual experimental ones by considering the fretting loading cycle. Baietto et al. [Baietto et al., 2013] have combined experimental and numerical approaches in order to predict fretting crack propagation by means of a 3-D XFEM modelling approach.

2.5 Summary and conclusions

This chapter has shown the basic concept of fretting and fretting fatigue problem, starting with the *state of art* background of Hertzian contact problem and its extension to fretting and fretting fatigue contact formulations. Following an overview of tribological behaviour of fretting and fretting fatigue contact problems under different contact conditions i.e. sicking, partial slip and gross sliding regimes. Besides, frictional behaviour of fretting contact has been reviewed and an analytical modelling approach for calculating COF at slip zone is introduced along with the comparison between fretting wear and fretting fatigue problems.

As mentioned in Chapter 1, the damage and fracture mechanics approaches have been used to deal with fretting fatigue crack initiation and propagation lifetime estimation, respectively, which is the primary objective of this study. Therefore, after discussing the basics of engineering failure mechanisms and an overview of fatigue of material, a basic review is given on damage and fracture mechanics principles.

By a comprehensive literature review, it can be concluded that in case of fretting fatigue problem, FE approach is an effective tool-kit for more understanding of its complexity. However, by a broad range of literature review, which covers from lab scale tests to practical applications such as spline couplings, shrink fitted joints, steel wires connections, artificial hip joints, automotive industry, it can be noted that there is no standard or kind of guideline for FEA modelling of fretting and fretting fatigue phenomena. To this end, the secondary objective of this study is to establish an easy to follow, adaptive, and expandable guideline for FEA studies of fretting and fretting fatigue phenomena.

Chapter 3

Fretting fatigue experiments

"This chapter is about the experimental methods that are used to study fretting fatigue behaviour"

3.1 Overview

In this chapter, different experimental set-ups that are used in this study for fretting fatigue tests are introduced. These test set-ups consist of fretting fatigue bridge and single clamp contact configurations along with the Single and Double Bolted Lap Joints (SBLJ and DBLJ) experiments. The Digital Image Correlation (DIC) technique is introduced to measure fretting fatigue frictional contact properties. Finally, a new fretting fatigue practical application, i.e. shock absorber test set-up, is elaborated.

3.2 Experimental set-up

Different fretting fatigue set-ups have been reviewed in Chapter 1. In this study, three different experimental set-ups were used to investigate fretting fatigue crack initiation and propagation. According to classification introduced in Chapter 1, bridge type fretting fatigue test set-up belongs to *first type* configuration and single clamp type fretting fatigue test which is under the category of *second type* test are elaborated. Eventually, two practical application test set-ups including SBLJ and DBLJ are explained along with the automotive shock observer's durability test.

3.2.1 Bridge type contact

Material and specimen

Aluminum alloy 7075-T6 was used in this investigation because of its low-specific weight and high strength to weight ratio and also its high electrical and thermal conductance. This alloy is widely used in industry and in particular in aircraft structure and pressure vessels. From a number of tensile tests (three tests) carried out on a universal tensile testing machine at a velocity of 0.05 mm/s, ultimate strength and yield stress of the material were obtained as σ_{ult}= 590 MPa and σ_{yield}= 503 MPa, respectively. The material's composition is given in Table 3.1. The specimens used in this work are prepared in accordance with the ASTM standard [ASTM-E8, 1997]. The dog-bone fatigue specimen illustrated in Figure 3.1, had a width of 14.1 mm, a thickness of 4.5 mm and a gauge length of 70 mm. For this type of test configurations, the fretting pads were made of stainless steel 410 with σ_{ult}= 700 MPa and σ_{yield}= 420 MPa. Figure 3.2 illustrates the different pad geometries that were used in this study.

Table 3.1: The chemical composition of AL7075T6 (wt%) [Hojjati Talemi, 2010].

Al	Others	Ti	Zn	Cr	Fe	Si	Mn	Mg	Cu
Base	0.05	0.06	5.37	0.17	0.14	0.38	0.06	2.38	1.48

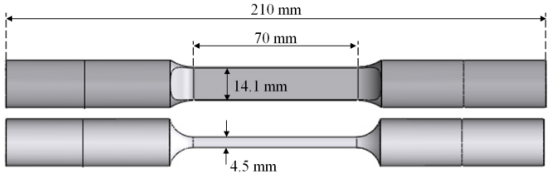

Figure 3.1: Dog-bone shape specimen used for fretting fatigue tests.

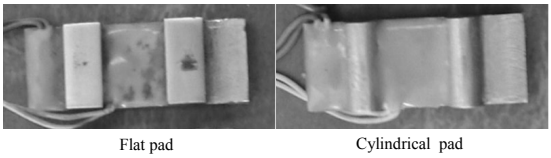

(a)

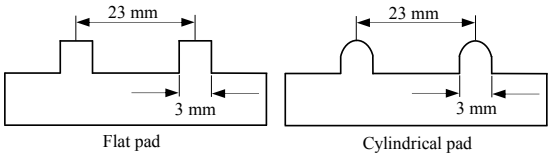

(b)

Figure 3.2: Bridge type flat and cylindrical fretting pads, (a) pictures and (b) geometry of flat and cylindrical fretting pads.

Test set-up

Figure 3.3 illustrates the schematic view of flat on flat contact of bridge type fretting fatigue test configuration. In this types of test configurations, the contact pressure required to produce fretting was transmitted to the contact area, through the loading pads shown in Figure 3.2 (a). Each pad has two bases (contacting surfaces) through which the load is exerted on the specimen. The pad span, which was defined as the distance between the centres of the fretting pad feet, was chosen to be 23 mm. In the experimental tests, 3 mm pad's base was selected for bridge type cylindrical pad and compared with the results obtained for the same geometry for flat pad configuration tests performed in

previous study [Majzoobi et al., 2011].

The fretting fatigue tests were carried out on a universal 200 kN Dynamic Servo fatigue machine. The pressure required to produce fretting was transmitted to the contact area between the specimen and two pads via a calibrated proving ring as shown in Figure 3.4. The pads were clamped to the specimen by the same normal loads as used in real conditions. The specimen was then pulled by axial load using dynamic servo testing machine. The experiments were conducted for the stress ratio of R_s= 0.1, frequency of 60 Hz at a contact force of F= 1200 N and maximum stress amplitudes (σ_{axial} of 130, 150, 180, 200 and 280 MPa.

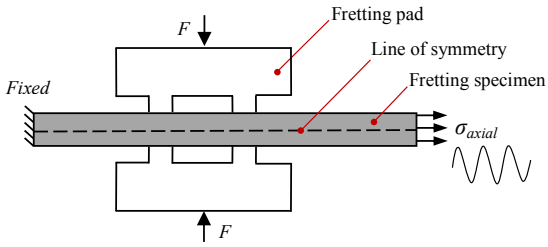

Figure 3.3: Schematic view of fretting fatigue flat on flat contact of bridge type test configuration.

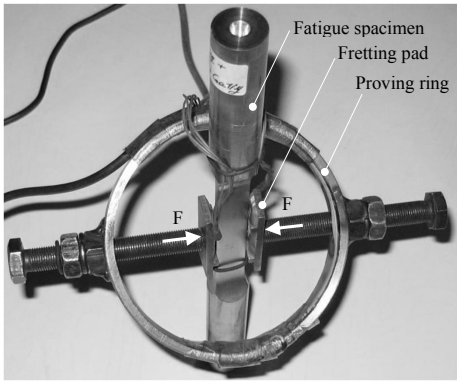

Figure 3.4: The proving ring assembly used for fretting fatigue tests [Hojjati Talemi, 2010].

The surface crack growth was measured using replica. For this purpose,

the test was stopped at every 5000 cycles, a replica was stuck to the crack zone, and crack growth was measured by optical microscopy. Surface replicas are made using small strips or pieces of transparent acetate tape. The area of interest is covered by the acetate tape, with a small amount of acetone applied between the component and tape. Acetone partially dissolves and softens the acetate tape allowing it to flow against the specimen and into surface features. After the acetone dries, the acetate tape is removed as a replica of the surface and the crack length was measured by microscopy. Fractography of fractured surfaces was also performed using optical microscopy.

Experiments observations and results

Figure 3.5 indicates a comparison between the S-N curves obtained for plain fatigue and fretting fatigue for flat bridge type pad. It can be clearly observed that fretting fatigue can reduce the fatigue life considerably. The reduction is more significant for lower stresses i.e. 130, 150 MPa.

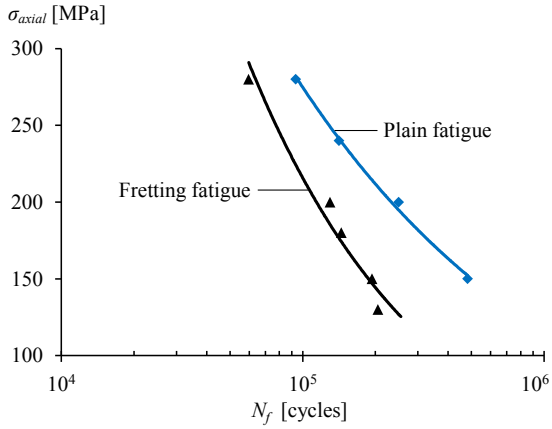

Figure 3.5: Comparison between the plain fatigue and fretting fatigue lives [Hojjati Talemi, 2010].

Figure 3.6 compares fretting fatigue crack propagation lifetime for bridge type flat and cylindrical contact configurations with contact width (pad feet= 3 mm). The surface crack propagation was measured experimentally using replica as described above from crack length of 200 μm till final rupture of fatigue specimen. From Figure 3.6, it can be seen that the crack propagates faster for cylindrical contact when compared with flat contact configuration.

The same trend has been observed by Farrahi et al. [Farrahi et al., 2005].

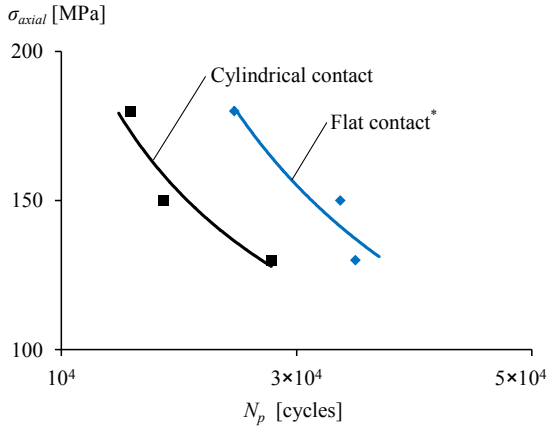

Figure 3.6: Comparison between fretting fatigue crack propagation lifetime for bridge type flat and cylindrical contact configuration with pad feet= 3 mm, (*) taken from [Hojjati Talemi, 2010].

Figure 3.7 shows deep pitting in the contact zone of fatigue specimen under fretting fatigue condition.

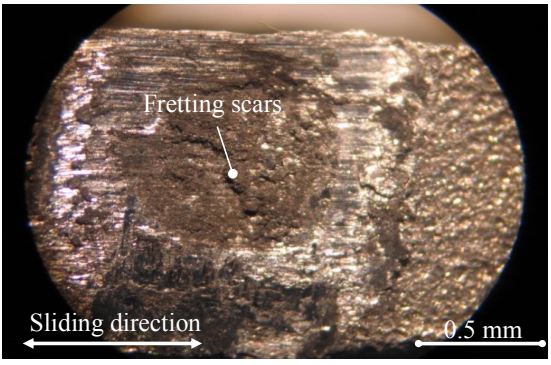

Figure 3.7: Deep pitting in the contact zone under fretting fatigue condition for flat bridge type contact experiment.

Figure 3.8 indicates a fracture surface of a fatigue specimen after failure under fretting loading condition. It clearly indicates that the fracture surface consists of three quite distinct regions; a fretting fatigue zone created by crack

initiation site, a crack growth zone and a tensile region, which gives rise to fracture of specimen when it is sufficiently weakened by the development of crack zone. It is generally thought that crack initiation is governed primarily by the local contact stresses and propagation is more related to the far-field or bulk stresses [Hills and Nowell, 1994].

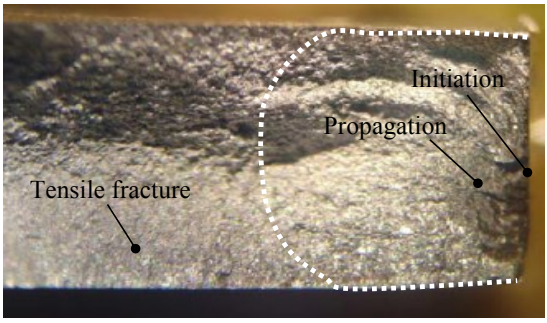

Figure 3.8: Fracture surface of a fatigue specimen after failure under fretting loading condition for flat bridge type contact experiment.

3.2.2 Single clamp type pad

Material and specimen

The tested material was aluminium 2024-T3, a tempered aerospace aluminium with good fatigue properties. All the test specimens (dog-bone for tensile test, fatigue test specimen and fretting pads for fretting fatigue test) were produced from a single sheet of aluminium 2024-T3. The material chemical compositions from the specification sheet is tabulated in Table 3.2. The measured yield strength σ_{yield} and ultimate tensile strength σ_{ult} are given in Table 3.3. Figure 3.9 shows the microstructure of AL 2024-T3 used in this study. The average grain size of 97 μm was calculated based on methodology described in ASTM E112-12 (Standard Test Methods for Determining Average Grain Size).

Table 3.2: Chemical composition of AL 2024-T3 (wt%)

AL 2024-T3	Al	Si	Fe	Cu	Mn	Mg	Cr	Zn	Ti	Other
Max	Base	0.5	0.5	4.9	0.9	1.8	0.1	0.25	0.15	0.05
Min				3.8	0.3	1.2				

The fretting specimen geometry conforms to currently-accepted standards

for uni-axial fatigue test specimens ASTM E466-96 as illustrated in Figure 3.10. These specimens were laser cut from as-received 2024-T3 rolled stock with cross-section 10 mm by 4 mm. The geometry of a typical fretting pad is also presented in Figure 3.10. The pads were manufactured by laser cutting a cylindrical profile of desired radius of 50 mm on both ends of sections cut from as-received 2024-T3 rolled stock with a 10 mm by 4 mm cross-section.

Table 3.3: Mechanical properties of AL 2024-T3

AL 2024-T3	$\sigma_{yield}[MPa]$	$\sigma_{ult}[MPa]$
Measured	383 ± 5	506 ± 9
Specification	≥ 325	≥ 450

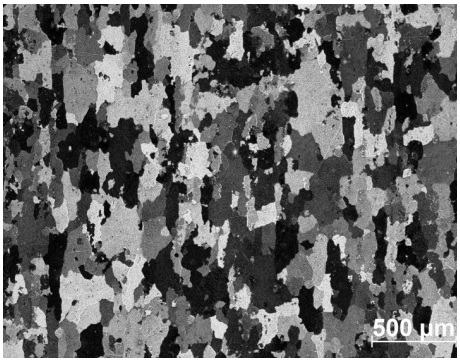

Figure 3.9: Microstructure of AL 2024-T3.

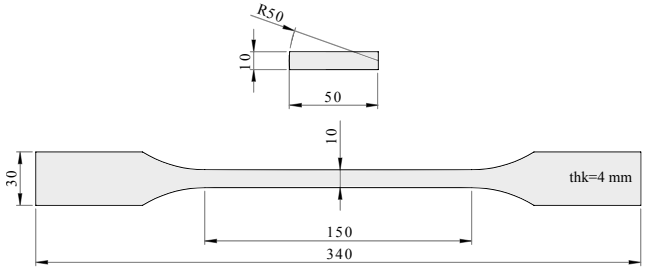

Figure 3.10: Geometry of the fretting pad and fatigue specimen.

Before establishing contact between the as-received laser cut surface of the

specimens, the regions of contact surface were polished lightly first with sandpaper 800 grit followed by 1200 grit and finally cleaned with a pass by a cloth with acetone to remove all residual traces of debris remaining from this preparation process. Each of these polishing actions was made along the direction of subsequent tangential loading (rolling direction). The average roughness (R_a) values transverse to the polishing direction were in the range of 0.2 to 0.3 μm . While there is no standard for surface preparation of fretting fatigue test currently, these values of surface roughness for the pads and specimen surfaces fall near the range mandated by the American Society for Testing and Materials (ASTM) standard for sliding wear test (ASTM G 115-93).

Test set-up

The schematic view of experimental set-up of fretting fatigue for cylindrical contact is illustrated in Figure 3.11. Two identical fretting pads are pushed against the fatigue specimen using constant load, F, which is called contact load and at the same time the specimen is subjected to oscillatory fatigue load. Therefore, at presence of these two loads, fretting fatigue failure occurs.

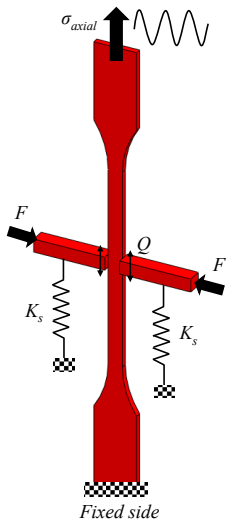

Figure 3.11: Schematic view of the fretting fatigue single clamp type pad experimental set-up.

The fretting fatigue test rig has been designed and constructed as an addi-

tional fixture to a 100 kN ESH servo-hydraulic load frame by De Pauw et al. [De Pauw et al., 2013a]. The additional fixture is rigidly fixed on the upright poles of the load frame. The 100 kN hydraulic cylinder of the load frame is used to apply the axial dynamic force in the dog-bone specimen. The normal force, F, is applied with a single servo-hydraulic actuator. A C-beam construction ensures that there are two equal and opposite normal forces. The tangential force, Q, between the dog-bone specimen and the pads is generated by means of leaf springs. The compliance of the leaf springs and the elastic deformation of the dog-bone specimen generate the tangential force, which is proportional to the fatigue load. A lateral load cell is attached to the C-beam, which measures the contact load directly. The induced tangential load is measured by attaching a strain gauge to the compliance springs. Data acquisition is done entirely on the control computer at a sample frequency of 1024 Hz. The schematic view and picture of fretting fatigue test rig are illustrated in Figs 3.12 and 3.13, respectively.

The fretting fatigue experiments were performed using parameters as: $N_f \approx 10^5...10^6$, axial stress ratio R_s= 0.1, tangential load ratio R_Q= -1, test frequency f= 10 Hz. The additional adjustable parameters for fretting fatigue experiments were kept constant for all the experiments: F= 543 N; pad radius R= 50 mm. All experimental loading conditions for fretting fatigue (FF) experiments are tabulated in Table 3.4.

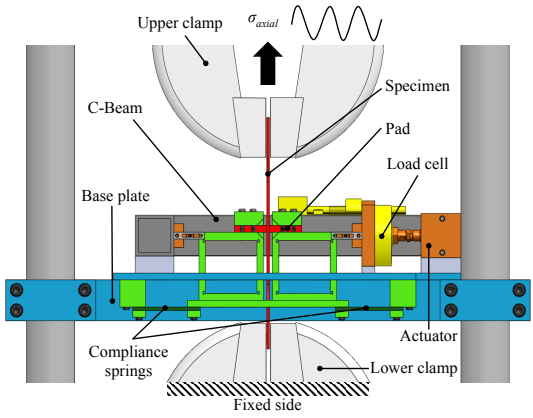

Figure 3.12: Schematic view of the fretting fatigue additional fixture with adjustable compliant springs mounted on universal servo-hydraulic machine [De Pauw et al., 2013b].

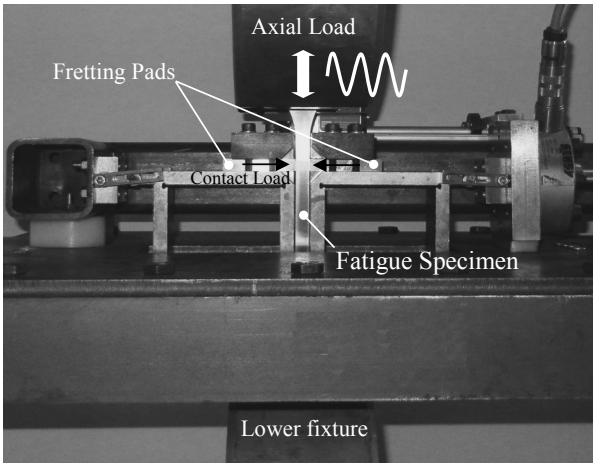

Figure 3.13: Picture of fretting fatigue test rigs with adjustable compliant springs.

Table 3.4: Test conditions of fretting fatigue experiments

Test No.	σ_{axial} [MPa]	F [N]	Q_{max}/F [-]
FF1	100	543	0.29
FF2	115	543	0.34
FF3	135	543	0.41
FF4	135	543	0.29
FF5	160	543	0.36
FF6	190	543	0.61
FF7	205	543	0.59
FF8	220	543	0.49
FF9	220	543	0.59

Experiments observations and results

S-N *curve*:

Figure. 3.14 shows fretting fatigue lifetime at different stress levels. Also, the obtained lifetimes were compared with the plain fatigue and published fretting fatigue lifetime from literature. The total lifetime of the experiments has been considered after complete fracture of the dog-bone specimens. In this study, in order to validate the developed numerical tool-kit for prediction of fretting fatigue crack initiation and propagation some limited number of experiments at stress level of 135, 160, 205 and 220 MPa, were carried out. However, some more experimental results performed by same test rig from

work of De Pauw et al. [De Pauw et al., 2013b] along with experimental results reported in literature from work of szolwinski et al. [Szolwinski and Farris, 1998] were used in order to be concrete about the validation of predicted numerical results.

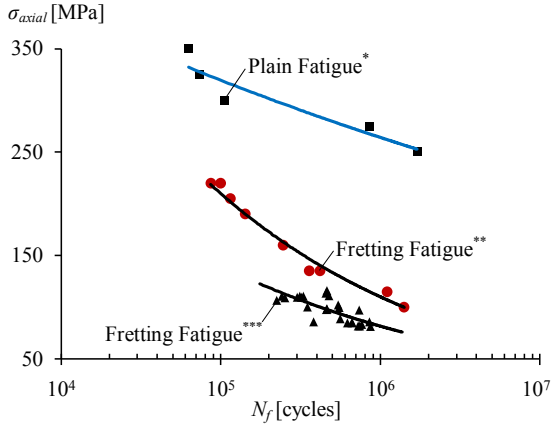

Figure 3.14: *S-N* curve of the plain fatigue and fretting fatigue experiments. (*) plain fatigue experiments taken form [De Pauw et al., 2013b]. (**) except four tests at stress levels of 135, 160, 205 and 220 MPa, the rest of points are taken from [De Pauw et al., 2013b]. (***) the fretting fatigue lifetimes data taken from literature [Szolwinski and Farris, 1998].

Fractography:

Fig 3.15 shows the damage and fretting scars of specimen FF9 after failure under fretting fatigue loading condition. As shown in Figure 3.15 the fretting wear scar has a width of approximately 1 mm. The crack that led to failure is initiated at the edge of the contact (side of applied axial load).

Figure 3.16 indicates the fracture surface of experiment FF9. A fully propagated fatigue crack was initiated from the left hand side of the specimen. At the right side of the specimen, one can observe a small crack coming from the second line contact. The figure clearly indicates that the fracture surface consists of three distinguished regions. A fretting fatigue crack nucleation site induced at contact interface followed by crack propagation zone and brittle fracture due to overloading. The propagated fatigue crack was initiated at the middle of the specimen and propagates symmetrical through the fatigue specimen. The crack shape was semi elliptical and was clearly growing more in depth than

through thickness. Three different zones can be distinguished, namely crack initiation site, crack propagation area and final tensile fracture surface.

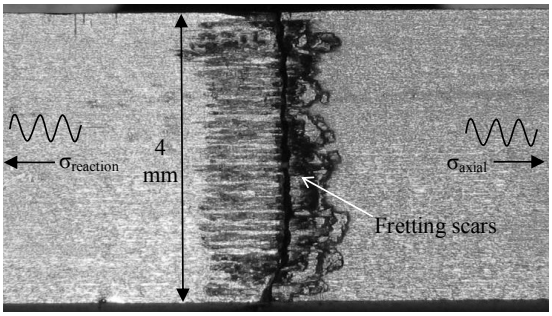

Figure 3.15: Fretting scar of the fretting fatigue experiment FF9.

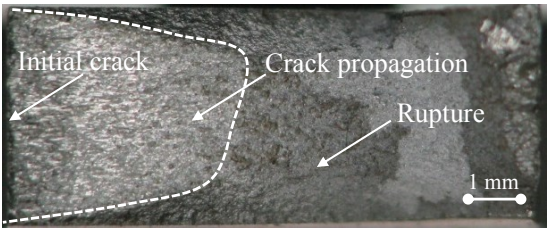

Figure 3.16: Fracture surface of the fretting fatigue specimen FF9.

Fretting fatigue contact alignment:

During mounting fretting fatigue specimen and pads, one of the main adjustments, which can lead to different fretting fatigue crack initiation and consequently propagation response, is related to contact alignment. The proper and uniform contact pressure distribution results in a line contact between fretting pad and fatigue specimen as can be seen in Figure 3.15. This alignment can be contorted visually or using some advanced techniques such as pressure films or digital image correlation technique as elaborated later on. A sheet of pressure sensitive film was placed in between the fretting pad and fatigue specimen in order to check the alignment of fretting contact. Figure 3.17 shows the pressure sensitive film at two different position of fretting pad. From the Figure 3.17 (a), it can be noted that the good alignment results in a line contact, which leads to formation of initial crack at centre of contact and consequently crack propagates through the middle plate of fatigue specimen up to final rupture.

However, Figure 3.17 (b) depicts a bad contact stress distribution, which leads to faster crack initiation due to edge effect phenomenon and eventually crack advances from edge of contact and through the side surface of fatigue specimen as illustrated schematically in Figure 3.17. Nonetheless, it is not clear that this misalignment results faster or shorter crack propagation lifetime.

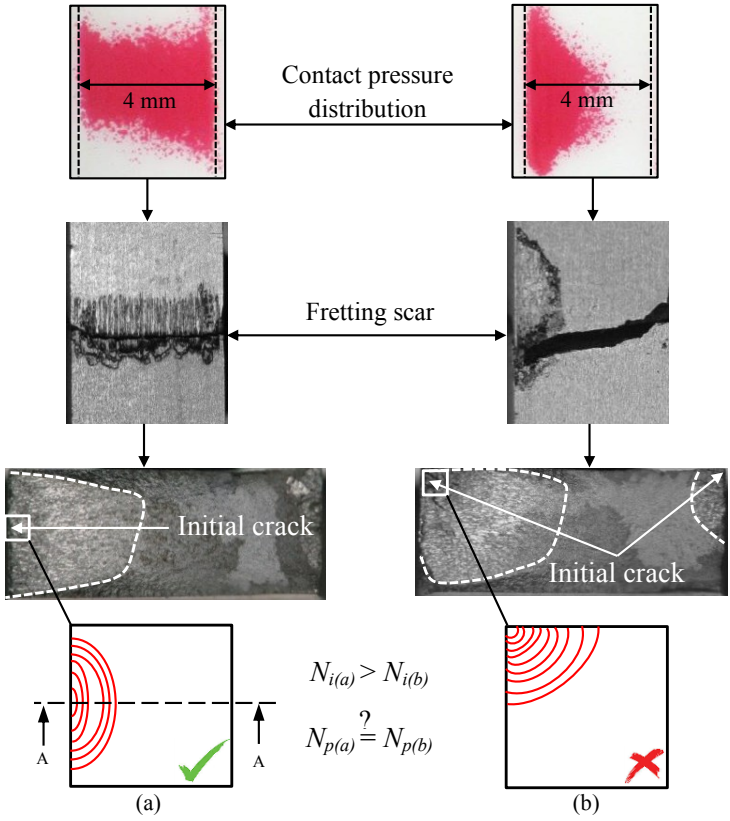

Figure 3.17: Fretting fatigue contact alignment analyse using pressure film. (a) the good aligned and (b) misaligned contact between fretting pad and fatigue specimen.

Crack propagation trajectory:

Figure 3.18 is the (A-A) cross section shown in 3.17 (a), which illustrates that the fretting fatigue crack nucleates at edge of contact. Following, the initial crack propagates under mixed mode condition up to two times of semi contact width ($2a$) and after that the crack propagation is governed by axial

stress perpendicular to contact interface. The same behaviour has been also observed by other researchers [Hills and Nowell, 1994, Szolwinski and Farris, 1998, Hoeppner et al., 1994]. The initial crack angle was measured for all experiments, which were between -35° and -45°.

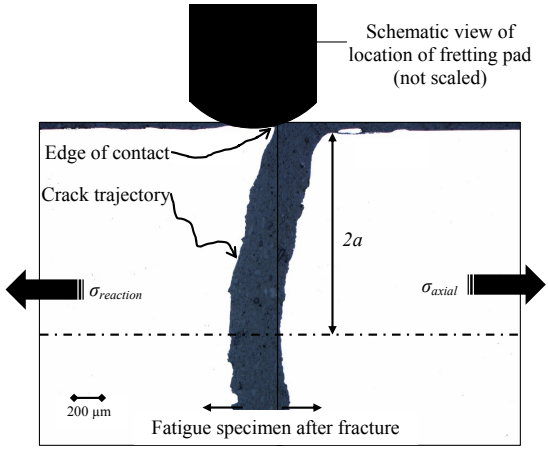

Figure 3.18: Fretting fatigue crack propagation trajectory for FF1 (A-A cross section view of Figure 3.17 (a)).

3.2.3 Single and Double Bolted Lap Joint

Mechanical fasteners such as bolted connections have been used in many structural joints, for instance air-planes and vehicles. Many studies have been focused on fatigue and fretting fatigue behaviour of these types of connections [Wagle and Kato, 2009, Benhamena et al., 2010, Wagle and Kato, 2011]. Fretting occurs due to oscillatory relative displacement between two components that are in contact together, which results in damage at contact interface. Once these components face cyclic fatigue load at the same time, fretting fatigue phenomenon occurs. In this section two coupon scale tests, namely Single Bolted Lap Joint (SBLJ) and Double Bolted Lap Joint (DBLJ) are used to study fretting fatigue contact characteristics such as COF and slip amplitude at contact interfaces.

SBLJ (static test)

A SBLJ experimental specimen was configured by fastening two identical halves together through a single bolt, as schematically illustrated in Figure 3.19. AL

2024-T3 alloy panels of t= 4 mm thick were machined and cut to dimensions as described in the ASTM D5961/D5961M-01 standard, giving an overall length of 115 mm and a width of 40 mm, as shown in Figure 3.20. Circular fastener holes of 8.25 mm in diameter were drilled at the centre of the specimen width with a free edge distance of 15 mm. Socket head steel bolt (M8-8.8) was used to clamp the specimen halves and the tightening torque was applied with a calibrated torque wrench. To avoid eccentricity in the applied load, which would lead to undesirable bending effects, end tabs of the same aluminium alloy 2024-T3 were bonded to each end of the test specimen as seen in Figure 3.19.

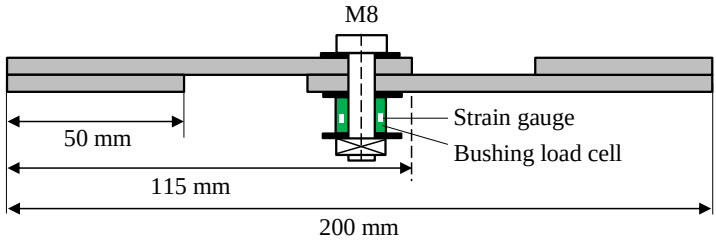

Figure 3.19: Assembly view of the SBLJ specimen.

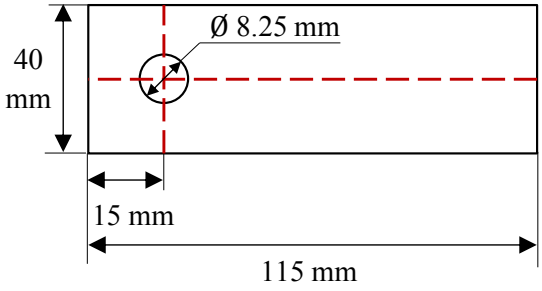

Figure 3.20: Geometry of the SBLJ specimen.

Specimens were prepared first by polishing lightly with sandpaper 800 grit followed by 1200 grit and finally cleaned with a pass by a cloth with acetone to remove all residual traces of debris remaining from this preparation process. Special care was taken for alignment of the specimens in the lower and upper grips as well as the relative alignment of the specimen halves to each other.

For this purpose, a special fixture was used to assemble the SBLJ aiming to centring the bolt, load cell and plates to avoid having contact between inner side of the bolt hole and the bolt shank. The contact load was applied using a torque wrench after centring the Al plates, the load cell and the bolt using the special fixture.

Bolted joint specimens were tested with a servo hydraulic testing machine, according to the above-mentioned ASTM standard as depicted in Figure 3.21. In order to obtain experimentally the bolt clamping force in a bolted joint, there are different kinds of methods such as torque wrench method, angle control method and load cell strain gage method. In this research, the load cell and strain gage method was used, as it has better accuracy compared to other methods. The load cell comprised of a steel bush and two strain gauges positioned between the nut and the plate (see Figure 3.19). This load cell was used to measure the compressive force due to the tightening torque. Two strain gauges were attached to the outer surface of the steel bush parallel to the bush axis as can be seen Figure 3.21.

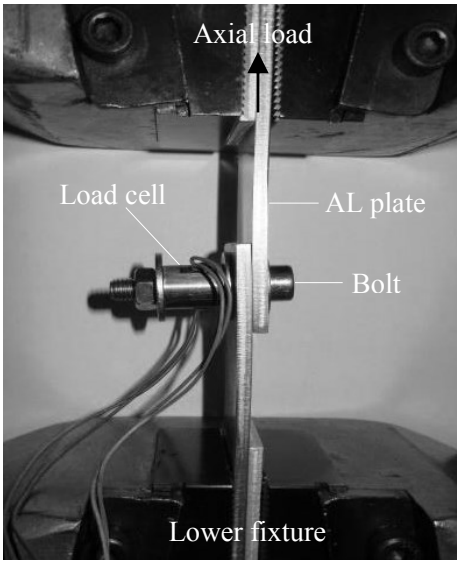

Figure 3.21: SBLJ specimen mounted on universal servo-hydraulic fatigue machine.

The bolt elongation due to the pre-load can be computed using the axial deformation formula. Therefore, the bolt was tightened until the bolt elongates

through the distance of deformation. In this way the desired pre-load was attained. But, it is impractical in many cases to measure bolt elongation. There is a good estimation of the torque required to produce a given clamping force using an analytical formula presented by:

$$F_{cl} = \frac{T_{cl}}{k_{cl} d_{bolt}} \tag{3.1}$$

In this equation, T_{cl} is the torque, F_{cl} is the initial clamping force , d_{bolt} is the bolt nominal diameter (mm) and k_{cl} is the torque factor defined as a term, which depends on friction coefficients, lead and thread angles, and mean diameter of the bolt. However, k_{cl} depends on different factors such as the surface smoothness, accuracy and degree of lubrication. The torque factor was determined based on Hookes law by measuring compressive axial strain of the steel bush placed between the nut and the Al plate [Chakherlou et al., 2012]. In order to do so, the bush load cell with a cross section area of 113 mm and elastic modulus of E_{bush}=210 GPa was calibrated using a 25 N.m torque wrench.

At the bush outer surface, two strain gauges were stuck on axial directions every 180° to measure the compressive axial strain induced by clamping force. Therefore, by having the bush cross section and the axial stress, the axial force in the bush and eventually the clamp force were determined. The torques were applied in 2.5 N.m increments from 2.5 to 25 N.m to the bolt using the torque wrench. The axial strain from each of the strain gauges were recorded for each applied torque. This procedure was repeated three times for each case to obtain the mean value of compressive strains (ϵ_c). Figure 3.22 (a) shows the average compressive strains of three tests and the applied torques for the specimen. The linear relation between the mean strain and the applied torque shows that the bush load cell is in elastic region even under maximum applied value of the torque. Subsequently, the corresponding clamping forces can be written as:

$$F_{cl} = E_{bush} A_{bush} \epsilon_c \tag{3.2}$$

Figure 3.22 (b) displays the relation between the measured clamping forces and the applied torques for the joint. According to the obtained linear equation for fitted curve on the graph and also Equation 3.1, a torque factor K_{cl} of 0.34 was experimentally obtained for the joint.

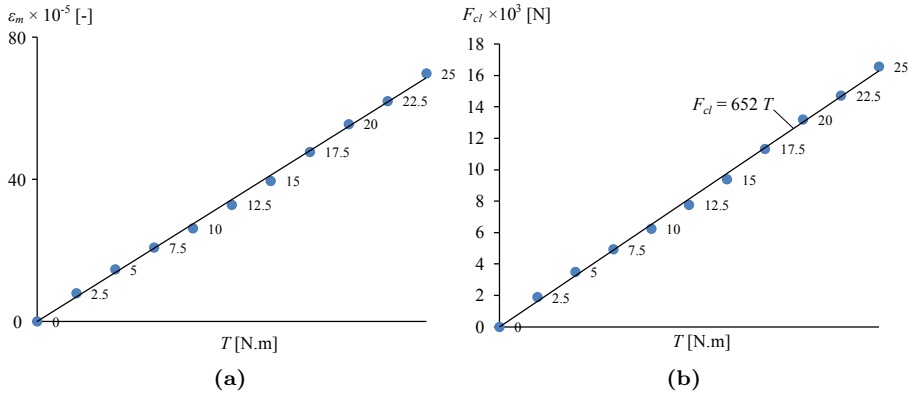

Figure 3.22: Relation between (a) the applied torque and the axial strain and (b) the clamping force and the applied torque of bush load cell at the joint.

Figure 3.23 illustrates the variation of applied axial load versus displacement for SBLJ connection at F_{cl}= 14 kN clamping force. As shown in the figure, the elastic elongation of joint was used for validating FE model, which is elaborated later on. By increasing the axial load, the joint slips and eventually the bolt faces a shearing failure mode.

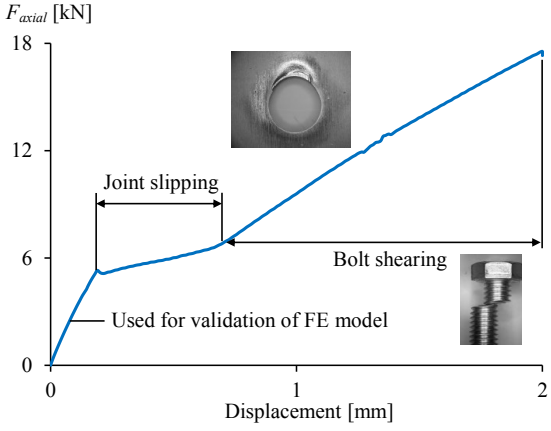

Figure 3.23: Applied axial force versus displacement diagram for SBLJ.

DBLJ (static and fatigue test)

The same AL plates with the same dimensions and finishing surface were used for DBLJ test configuration. Two series of static and fatigue tests were performed in order to characterize fretting fatigue properties. Figure 3.24 illustrates the schematic view of DBLJ, which was used in this study. Figure 3.25 shows the DBLJ specimen mounted on servo-hydraulic machine. For static and dynamic tests the clamping force was chosen 14 and 16 kN, respectively. The static test was performed at a velocity of 0.01 mm/s. Figure 3.26 shows the variation of applied axial load versus the displacement. The failure was observed in the middle plate and its mode was bearing failure as depicted in the Figure 3.26.

Three fatigue tests were performed in order to monitor the failure mode of DBLJ under fretting fatigue loading condition. performed fretting fatigue test for DBLJ under partial slip regime is a challenging task, since controlling the slip amplitude at contact interface between the connected plates is difficult in practice. It is almost impossible to measure the slip amplitude at contact interface between the middle plate and side plates experimentally. Therefore, in this study in order to select the right loading conditions the combination of FE modelling and experimental technique was used. The details of FE model is elaborated later on in Chapter 4. Eventually, based on results of FE model the loading condition was selected.

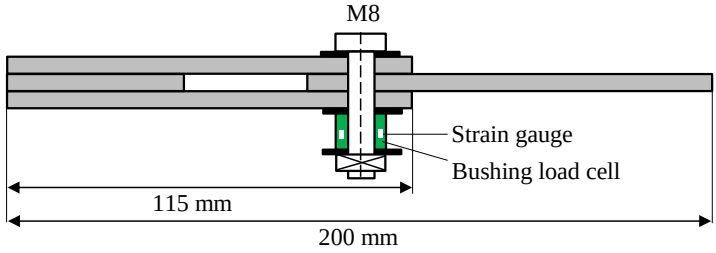

Figure 3.24: Geometry and assembly view of the DBLJ specimen.

Figure 3.27 depicts the schematic view of fretting fatigue failure mechanism in DBLJ. As shown in the figure, the contact stress distribution between middle plate and side plates comes from the tightening of the bolt after applying the clamping force F_{cl} and the tangential stress at contact interface induced by

applying remote axial load. Combination of these loads results in the generation of initial fretting crack at contact interface and advancing the crack till final rupture of the middle plate as shown in Figure 3.27.

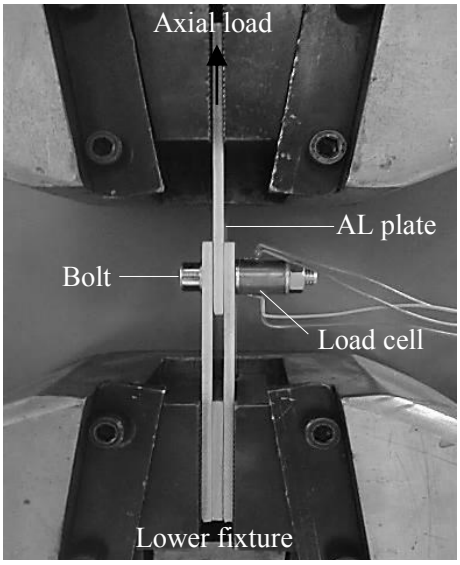

Figure 3.25: DBLJ specimen mounted on universal servo-hydraulic fatigue machine.

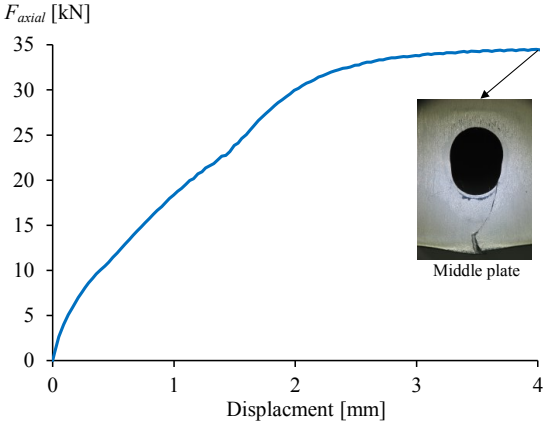

Figure 3.26: Applied axial force versus displacement diagram for DBLJ.

Figure 3.28 illustrates the S-N curve for three performed tests of DBLJ

specimen. At this time just three fretting fatigue tests were carried out. The main aim of this part of the study was characterizing behaviour of the DBLJ subjected to fretting fatigue loading condition such as failure mode, slip amplitude at contact interface and location of initial crack. Figures 3.29 (a) and (b) show the fretting scars and fracture surface of middle plate of DBLJ specimen after final rupture, respectively.

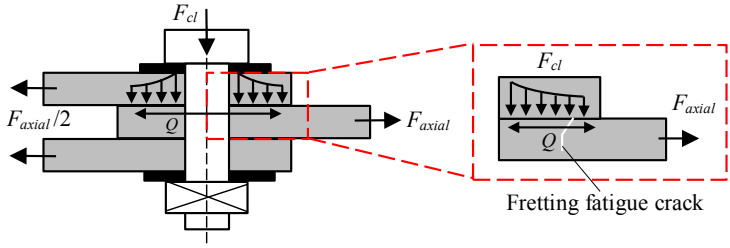

Figure 3.27: Schematic illustration of load distributions of DBLJ connection subjected to fretting fatigue loading condition.

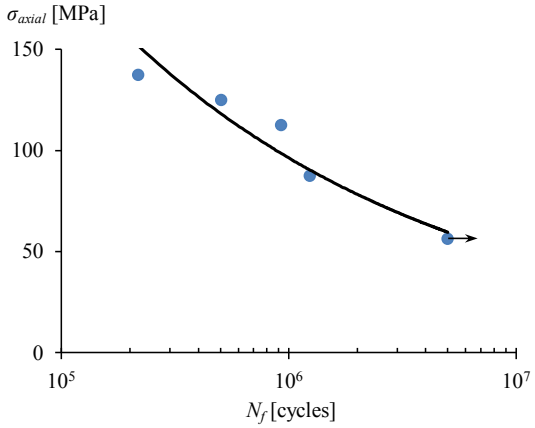

Figure 3.28: Stress versus the number of cycle for DBLJ experiments under partial slip regime condition (arrow indicates specimen was not fractured).

Figure 3.29 (a) depicts two distinguished regions of sticking and slipping at contact interface between middle plate and one of the side plates. Figure 3.29 (b) shows that the initial fretting crack nucleates at slipping region at a distance respect to bolt hole at side of applied axial load.

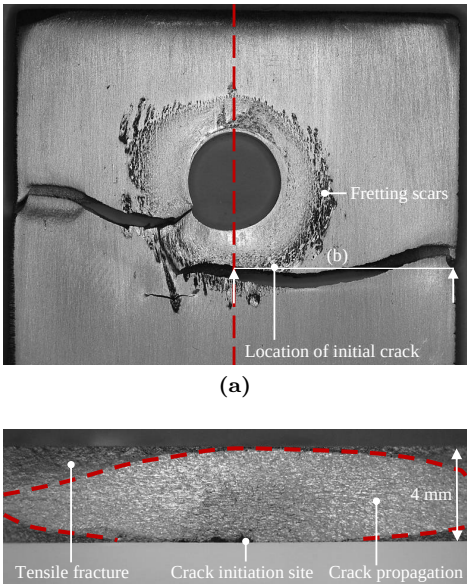

Figure 3.29: (a) Fretting scars in the middle plate of DBLJ and (b) fracture surface of the middle plate and the location of initial crack.

3.3 Measuring COF using DIC technique

Digital Image Correlation (DIC) is a full-field image analysis method, based on grey value digital images, that can determine the contour and the displacements in two and three dimensions of an object under load. Due to rapid new developments in high resolution digital cameras for static as well as dynamic applications, and computer technology, the applications for this measurement method has broadened. DIC techniques have proven to be a flexible and useful tool for deformation analysis.

DIC technique is used to monitor the displacement field, which is calculated based on the best correlation between the image of a deformed surface and a reference image of the un-deformed surface. This calculation was based on the Sum of Squared Differences (SSD) correlation criterion. Due to occurring micro slip at contact interface between fretting pad and fatigue specimen, the accuracy of analysis depends on the surface speckle pattern and lighting. In this study for measuring COF, a three dimensional (3-D) DIC technique was used in order to monitor relative displacement amplitude between connected

components, which are subjected to fretting fatigue loading condition. For this purpose, the three above mentioned experimental configurations were used to measure COF by means of DIC technique.

3.3.1 Fretting fatigue experimental set-up

In order to use the fretting fatigue test rig shown in Figure 3.13 for measuring COF some preparation needed to be done. The surface of specimen and pad were coated by spraying a uniform white layer of paint and, after drying, covered with black speckles. The area of interest monitored by the camera was approximately 20×20 mm. Two special lamps were used for lightening. The experimental DIC set-up and positioning of cameras and lights are depicted in Figure 3.30.

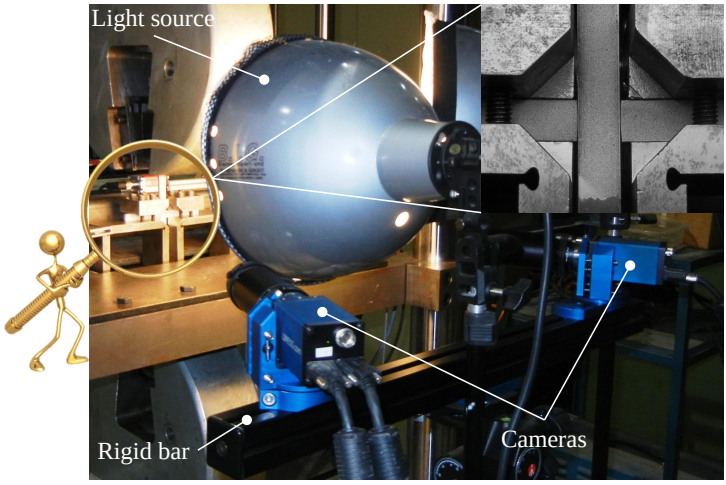

Figure 3.30: Experimental set-up used for calculating COF using the DIC technique for fretting fatigue test configuration.

Figure 3.31 illustrates the speckled fatigue specimen and fretting pads, which are mounted on fretting fatigue test rig. The subset size was selected to capture three speckles per subset which is used for calculating the SSD functions [Sutton et al., 2009]. The displacement of fretting pad and fatigue specimen was then calculated based on minimizing this SSD function. The digital images were obtained from a stand-alone system provided by Limess Messtechnik & Software [Limess Messtechnik & Software GmbH, 2013] con-

taining two synchronized monochromatic 14 bit cameras with a resolution of 2452 by 2054 pixels (5 megapixels). The use of two cameras allowed to obtain positions and displacements in three dimensions using the VIC3D software of Correlated Solutions [Vic3D, 2013] as shown in Figure 3.32.

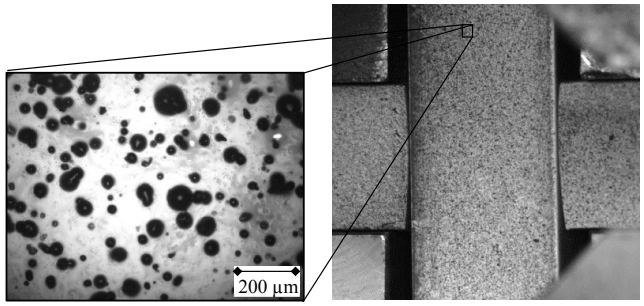

Figure 3.31: Speckled specimen and pads mounted on fretting fatigue test rig.

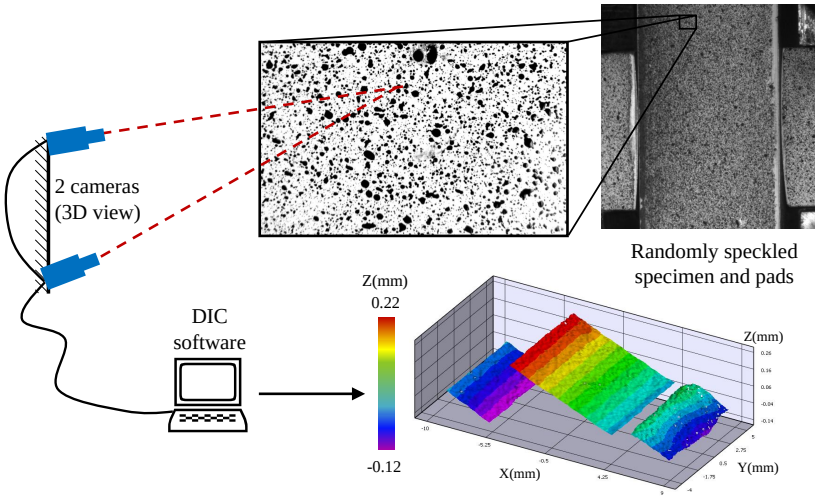

Figure 3.32: Two digital camera used for 3-D displacement measurements along with randomly speckle pattern applied to the fretting fatigue test set-up.

Using 3D measuring technique gives the opportunity to measure displacement of surfaces that are not in same depth of focus, which is the case in fretting fatigue test as two fretting pads are in contact with fatigue specimen.

Moreover, 3D displacement field measurement is a helpful reference to detect the alignment of the fretting fatigue contact configuration, which is one of the most important parameters to have line contact between the pads and specimen. In order to calculate COF using DIC technique, the fretting fatigue test was performed at σ_{axial}= 175 MPa (R_s= 0.1). The test was carried out under partial slip regime. It has been proven by different researchers [Hills and Nowell, 1994, Szolwinski et al., 1997] that after 10^3 cycles under partial slip condition the variation of COF stabilizes. Therefore, after 10^3 cycles, the cyclic load followed by quasi static loading up to σ_{axial}= 250 MPa, which yields to gross sliding condition. The slip was taken as the relative displacement between the averaged data inside Area Of Interest (AOI) inside the pads and specimen, in the direction of the applied load as shown in Figure 3.33.

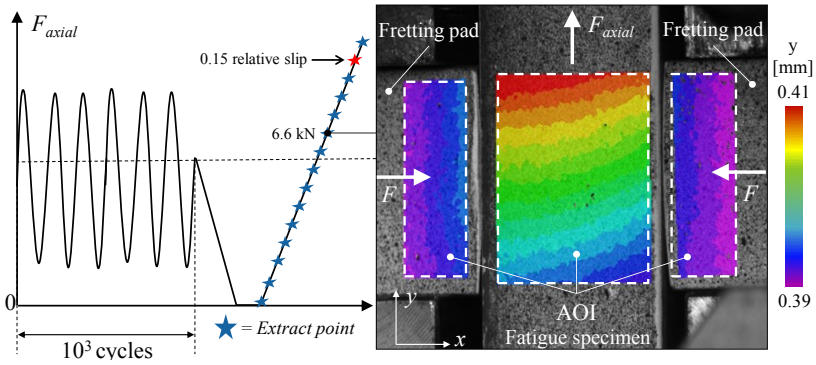

Figure 3.33: Loading sequence for calculating COF using DIC technique. The slip between pads and specimen was calculated inside the Area Of Interest (AOI).

Figure 3.34 (a) shows the variation of monotonic axial load versus relative slip amplitude at both sides of contacts between the pads and specimen. Afterwards, the gross sliding axial load, $F_{(gs)}$, was defined as the load at which a slip of 0.15 mm occurs based on BS EN 1090-3:2008 standard (Execution of steel structures and aluminium structures) [BS EN 1090-3, 2008]. Using the related gross sliding tangential load, $Q_{(gs)}$, $\mu_{(gs)}$= 0.48 was calculated under gross sliding condition as depicted in Figure 3.34 (b). Following Hills and Nowell [Hills and Nowell, 1994] methodology as discussed in Chapter 2 (section 2.2.4), by using Equation 2.31, the μ_{slip}= 0.65 was found for slip zone COF, which is in good agreement with COF that has been reported for the same material by

Szolwinski et al. [Szolwinski et al., 1997].

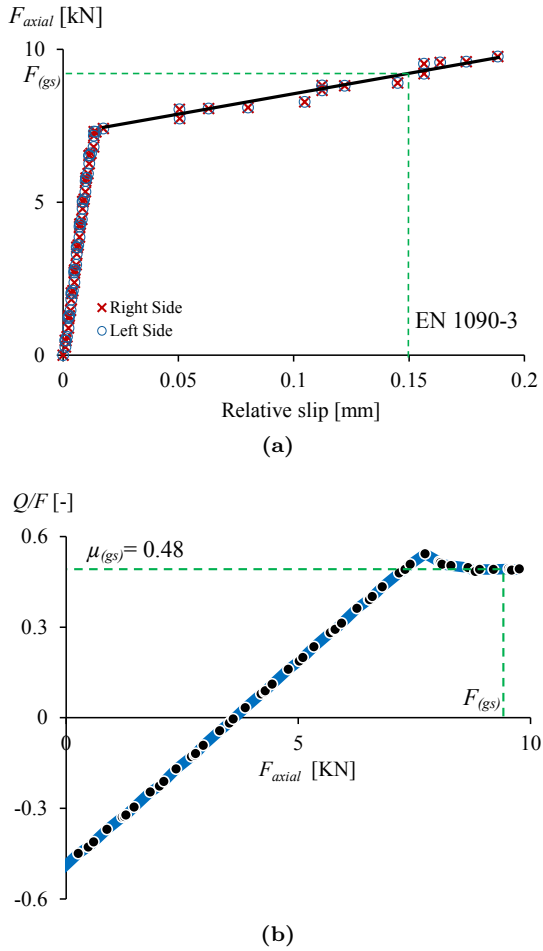

Figure 3.34: (a) Axial load versus relative slip amplitude at both sides of fretting contact and (b) normalized tangential load versus applied axial load.

Figure 3.35 illustrates the displacement contour plot in y-direction calculated using DIC method. From the figure, it can be noted that as expected by increasing the applied axial load the displacement of fretting pads in y-direction become uniform at $F_{axial} \approx 9$ KN.

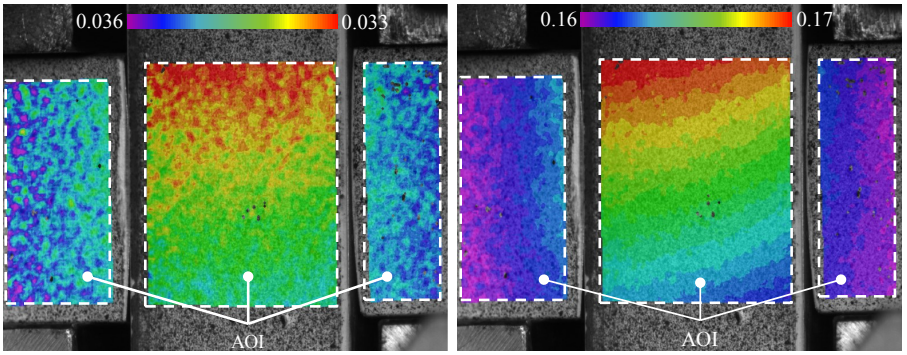

(a) F_{axial}= 0.3 kN **(b)** F_{axial}= 2.8 kN

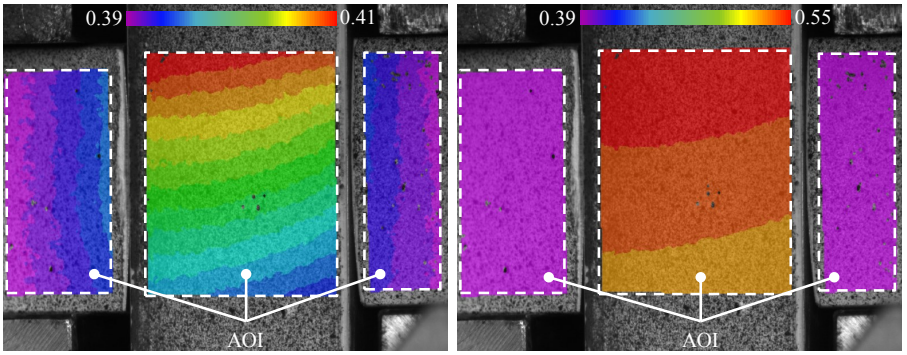

(c) F_{axial}= 6.6 kN **(d)** F_{axial}= 9 kN

Figure 3.35: Displacement contour plot in y-direction calculated using DIC method for fretting fatigue test configuration at four different loading steps

3.3.2 SBLJ experiment

In the next step, the DIC technique was implemented to SBLJ experiment for measuring the COF under partial slip loading condition. Figure 3.36 illustrates the SBLJ specimen mounted on a fatigue machine, digital cameras and light sources. The same technique as elaborated earlier was used to speckle the side edge of AL plates in order to measure relative slip amplitude during monotonically increasing axial load. The specimens were prepared with the same roughness as explained in section 3.2.3.

Figure 3.37 depicts the displacement variation contour plot along the y-direction at early stage of test. It can be noted that using DIC technique gives the chance of monitoring small relative moment at micro level between

connected parts as shown in Figure 3.37. By increasing the axial load, the connected plates slides over each-other, which leads to transformation from sticking to partial slip and eventually gross sliding regime. In order to calculate COF at onset of gross sliding, the same criterion applied to fretting fatigue test, was also used for SBLJ test.

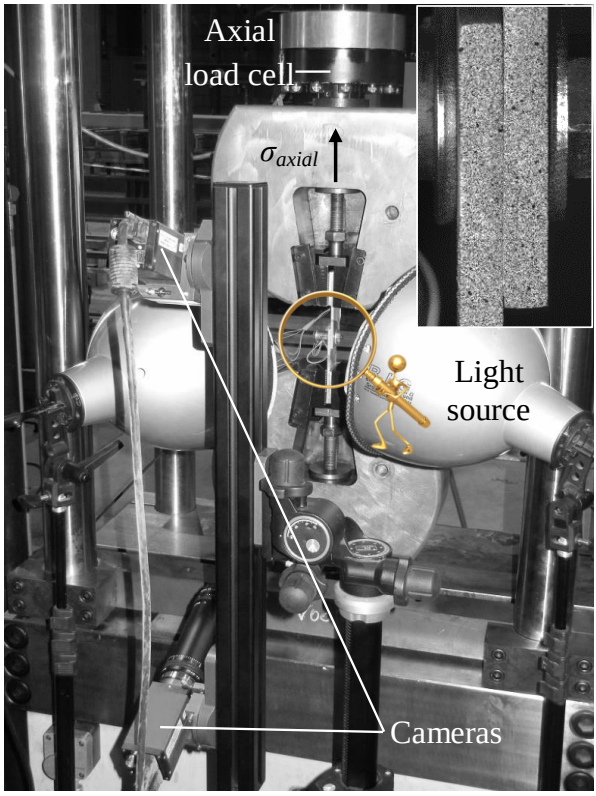

Figure 3.36: Experimental set-up used for calculating COF using DIC technique for SBLJ specimen.

Figure 3.38 illustrates the variation of applied axial load versus measured relative slip amplitude. Relative slip amplitude was measured by subtracting the displacement amplitude between the averaged data inside Area Of Interest (AOI) in each of the AL plates in y-direction (direction of the applied load). Using this technique, the COF was found to be $\mu_{(gs)} \approx 0.39$ at onset of gross sliding i.e. 0.15 relative slip amplitude according to [BS EN 1090-3, 2008].

As it can be noticed the measured COF for SBLJ is less then what is measured for fretting fatigue test. There are two possible reasons for this difference. The first one, which can be also the main reason, is the way how these two tests performed, i.e. fatigue test versus quasi-static test. In fretting fatigue test, the COF measured after applying 10^3 cyclic load, followed by a monotonic load. However, the SBLJ test was performed by increasing the axial load monotonically. As mentioned above, it is known that by increasing number of fretting fatigue cycles, COF rises exponentially [Szolwinski et al., 1997]. The second reason for this difference can be related to the surface preparation of the specimens. In fretting fatigue test, the surface of fretting pads was not polished using sandpapers to avoid loosing the curvature of pads. Pads were used as laser cut, which results slightly higher roughness value, which leads to higher COF compared to the SBLJ test configuration, for which all contact surfaces were polished using sandpaper as described earlier.

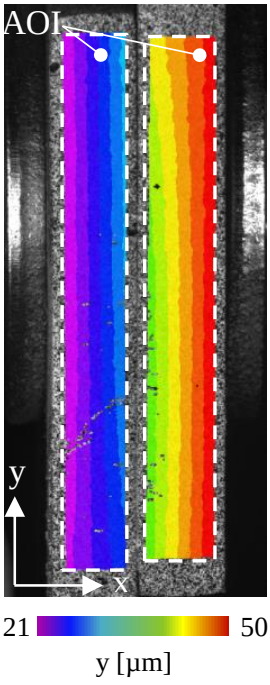

Figure 3.37: Displacement contour plot distribution in AOI for SBLJ at early stage of test.

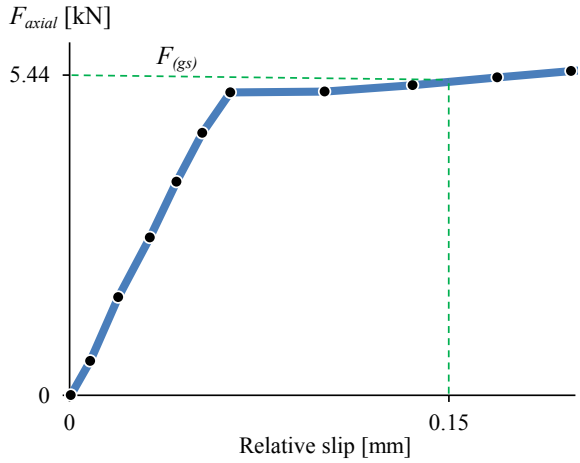

Figure 3.38: Applied axial load versus calculated relative slip amplitude using DIC technique for SBLJ test.

3.3.3 DBLJ experiment

According to BS EN 1090-3:2008 standard [BS EN 1090-3, 2008], the DBLJ test configuration should be used in order to find the slip factor (the onset of gross sliding). Therefore, to be sure about the effect of cyclic load on increasing the COF, the same DIC technique was implemented to DBLJ experimental configuration. Figure 3.39 shows the speckled specimens for DBLJ test configuration. In order to measure COF, after applying 10^3 fatigue cycle a monotonic load was applied from zero up to 35 kN till final rupture of the middle plate. Other test conditions were kept the same as static test (see Section 3.2.3), i.e. F_{cl}= 14 kN and the velocity was 0.01 mm/s for applied monotonic load. Figure 3.40 indicates the field variation of displacement in y-direction for DBLJ test configuration at three different loading steps, i.e. 0.82 kN, 11 kN and 17.5 KN axial load.

Figure 3.41 illustrates the variation of applied axial load versus calculated relative slip amplitude at each side of the contact i.e. Left Side (LS) and Right Side (RS). The same as fretting fatigue and SBLJ test, the relative slip amplitude was measured by subtracting the displacement amplitude between the averaged data inside Area Of Interest (AOI) of the middle plate from the side plates (i.e. LS and RS) in y-direction (direction of the applied load).

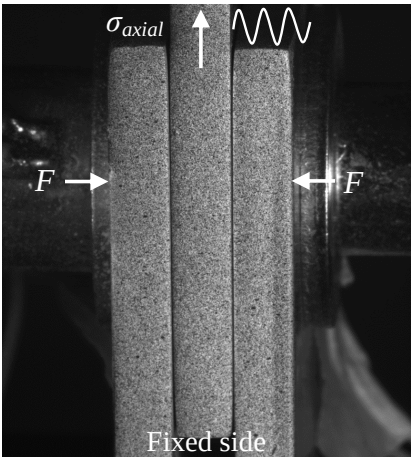

Figure 3.39: DBLJ speckled specimens that were used for measuring COF by means of DIC technique.

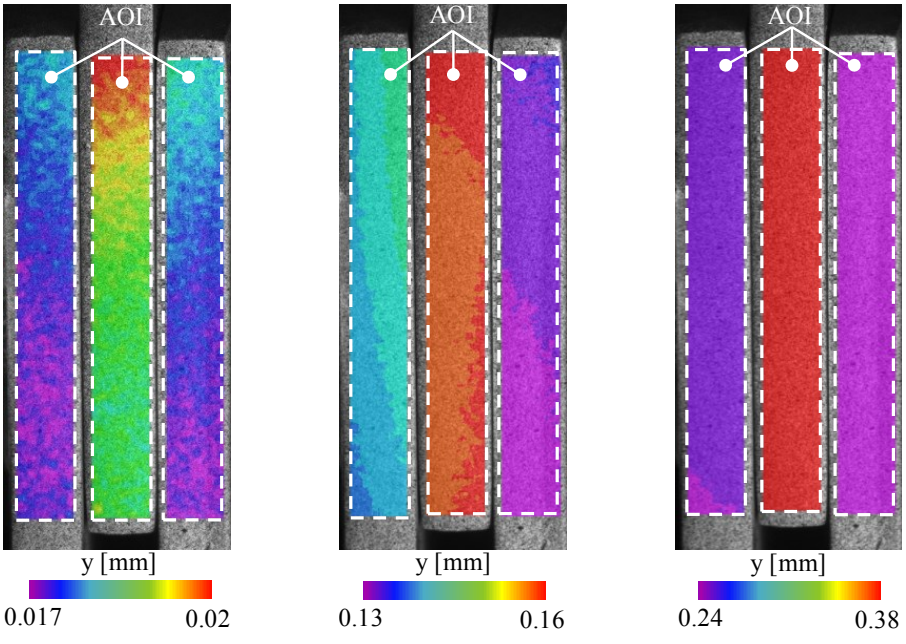

(a) F_{axial}= 0.82 kN **(b)** F_{axial}= 11 kN **(c)** F_{axial}= 17.5 kN

Figure 3.40: Displacement contour plot in y-direction calculated using DIC method for DBLJ test configuration at three different loading steps.

Figure 3.41 also depicts that up to 10 kN there is almost zero relative slip between the middle plate and the side plates, which can be considered as sticking region. By increasing the axial load up to the $F_{(gs)}$ the joint starts to slip, however, it is shown later on by means of FE approach that some parts of the contact area are still in sticking. Therefore, up to 18 kN axial load, the joint is under partial slip regime contact condition. For an axial force equal to $F_{(gs)}$, the whole contact surfaces are sliding over each other, which results in gross sliding condition as depicted in Figure 3.41.

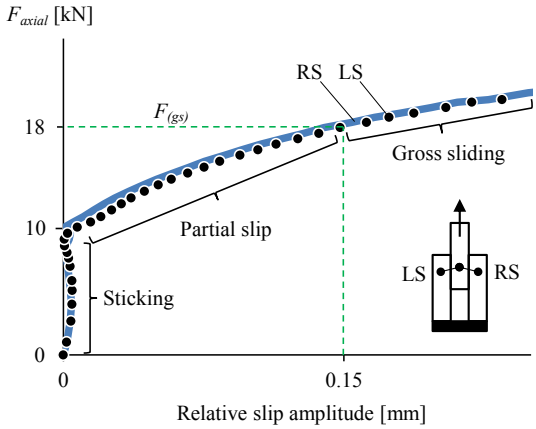

Figure 3.41: Applied axial load versus calculated relative slip amplitude using DIC technique for DBLJ test. Three different regions of sticking, partial slip and gross sliding can be distinguished based on applied axial load.

Figure 3.42 illustrates the variation of COF versus the calculated relative slip amplitude at both sides (i.e. LS and RS) of DBLJ specimen. The measured COF at both sides of contact were almost the same value ($\mu_{(LS)} = 0.65$ and $\mu_{(RS)} = 0.64$), which gives more confidence about the DIC measuring technique. As mentioned earlier for calculating COF at each side of the contact, the axial load at 0.15 mm relative slip amplitude is divided by the clamping force, which was measured at beginning of the test.

Figure 3.43 shows the variation of the clamping force versus the relative slip amplitude. As shown in the figure by increasing the relative slip amplitude at contact interface up to 0.15 mm, the clamping force declines from 14 kN to 12.7 kN, which is around 9% drop. However, The variation of clamping force is almost constant after around 1 μm relative slip. In order to find the

correct COF the variation of clamping force should be taken into account, which resulted to $\mu_{(LS)} = 0.71$ and $\mu_{(RS)} = 0.70$.

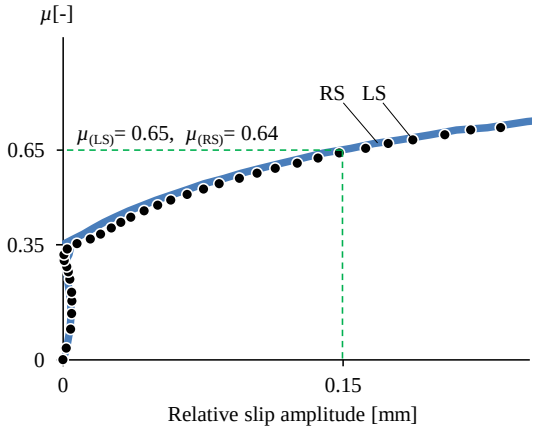

Figure 3.42: Variation of COF versus the calculated relative slip amplitude at both sides (i.e. LS and RS) of DBLJ specimen.

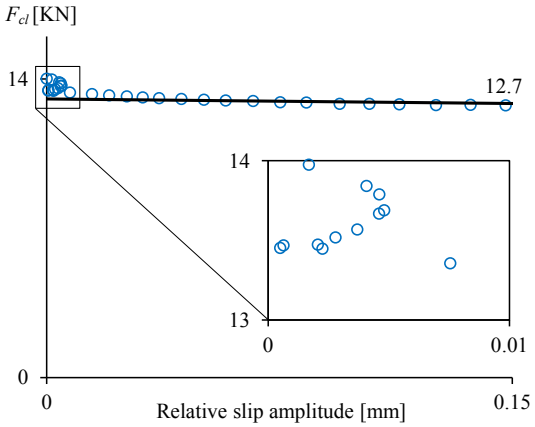

Figure 3.43: Applied axial load versus calculated relative slip amplitude using DIC technique for SBLJ test.

3.4 Automotive shock absorber durability test

In order to address fretting fatigue failure for shock absorber application as introduced in Chapter 1, some durability tests were performed. For this purpose the shock absorber was mounted on a servo-hydraulic machine as depicted in Figure 3.44. As shown, one side of the sample was fixed and the cyclic load was applied to the other side of shock absorber. One of the main issues during performing the shock absorber durability test is that the oil temperature rises due to high test frequency. This temperature rise can be up to 100°C, which leads to melting some parts inside of the shock absorber made of polyethylene. Therefore, during the test to monitor the oil temperature, a thermocouple temperature sensor was attached to outer side of compensating tube. Thus, two cooling fans were used for cooling down the oil temperature during the test as depicted in Figure 3.44.

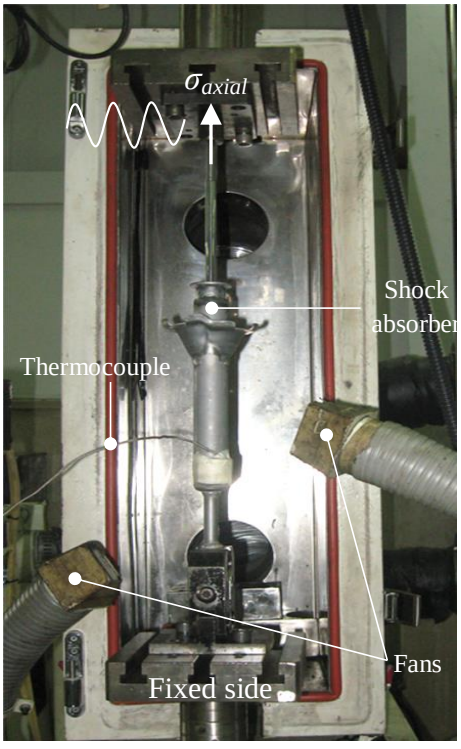

Figure 3.44: Shock absorber durability test set-up, which was mounted on servo-hydraulic machine.

The loading condition was selected in the way that can be matched with the real loading condition of shock absorber, as mounted on a vehicle. Thus, the tests were carried out under frequency of 14 Hz, an amplitude of ± 20 mm and the oil temperature was kept in range of 60°C-80°C. Figure 3.45 illustrates the schematic view of loading distribution of over washer and disc. According to the shown loading condition, it is possible to consider the washer as a fretting pad and the disc as fatigue specimen, which is subjected to bending fatigue load induced by oil pressure during compression and rebound cyclic loading. The oil pressure varies between the maximum and zero value (i.e. zero load ratio) during rebound and compression cycles, respectively, same as elaborated in Chapter 1 (Section 1.3). The clamping force F_{cl} comes from tightening of the piston nut by a torque equal to T_{cl}= 13.73 Ncm. Both washer and disc were made of CK101 *spring steel strip* with σ_{ult}= 520 MPa and σ_{yield}= 420 MPa. Spring steel is a low-alloy and medium-carbon steel with a very high yield strength. This allows disc and washer made of spring steel to return to their original shape despite significant bending induced by oil pressure during rebound and compression cycles. Figure 3.46 illustrates the geometry of disc and washer that were used in this study to characterise fretting fatigue behaviour.

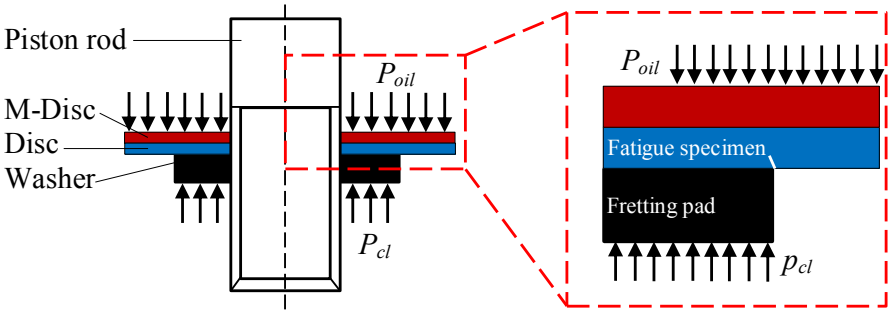

Figure 3.45: Schematic view of fretting fatigue loading distribution for shock absorber's piston valve

During lab scale durability test, one of the main challenges is finding the on set of failure. Normally, based on shock absorber test standards (depends on the design), the quasi-static test is performed to find the variation of damping force at different working speeds. The maximum and minimum damping force must be in the predefined range given by designer. For instance, Figure 3.47

indicates two different valve designs based on using different valve thickness. The damping force can be affected by variation of valve disc thickness and piston hole size. However, when it comes to fatigue test it is not easy to detect this variation due to high test frequency and oil temperature. Therefore, some tests was performed up to 10^4 and 2×10^4 cycles and the maximum and minimum damping forces were recorded after each 200 and 500 cycles, respectively. After disassembling the shock absorber no damage was found in the disc in the first test (test 1, 10^4), while in the second test (test 2, 2×10^4) the disc was fractured.

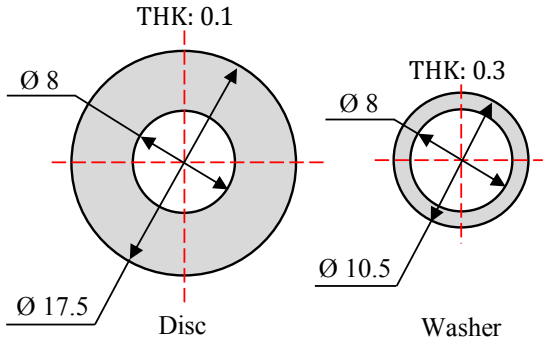

Figure 3.46: Shock absorber's disc and washer dimensions

Figure 3.48 illustrates the variation of measured damping force versus the number of cycles for both tests. For the test 1, the maximum and minimum value of damping forces were constant, however, for the test 2 after around 11×10^3 cycles, the minimum value of the damping force decreased gradually, while the maximum damping force was constant. The maximum and minimum damping force is related to rebound and compression stroke, respectively. This interesting results reveal that for the second test, during compression stroke more oil goes through the piston valve, which is due to rupture of disc in the piston valve.

Four more tests were performed at same loading condition and stopped at 2×10^4 cycle. After disassembling the samples, it was observed that the disc was fractured. The same behaviour was observed for all performed experiments. In order to be concrete about the failure mode under applied loading condition, some random shock absorber samples from in-service (i.e. tested on real vehicle) disassembled and compared with the observed lab scale test. Figures 3.49 (a)-

(c) illustrate the failed disc in the lab experiment (a) and in-service samples (b) and (c). From the figures, it can be noticed that for both in-service samples and lab experiments the fretting scars appear at contact interface between the washer (fretting pad) and the disc (fatigue specimen). By comparing these two results it can be concluded that, fretting fatigue failure is the main cause of disc failure of shock absorber's piston valve.

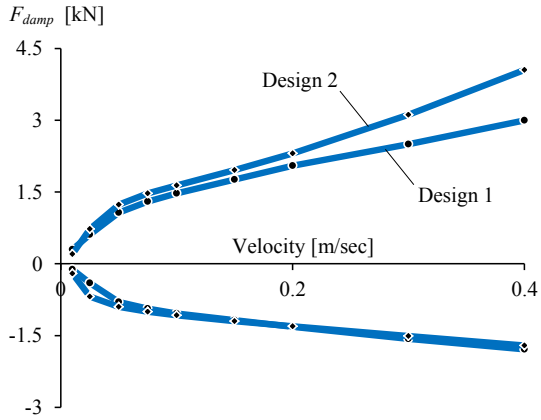

Figure 3.47: Damping force versus different applied velocities for two different valve design. The design variables are not given due to confidentiality policy of F&S® company.

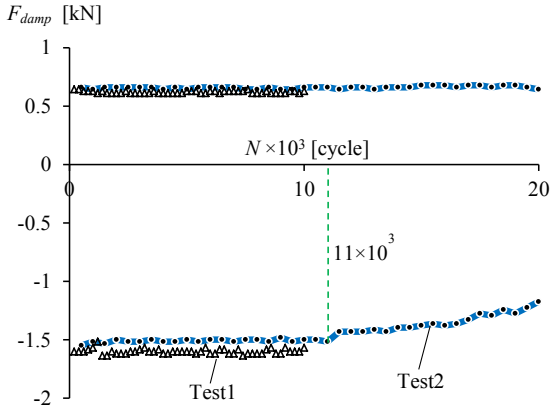

Figure 3.48: Variation of maximum and minimum damping force versus number of cycles

In order to see the fracture surface of the disc, it was cut as illustrated schematically in Figure 3.50. From the figure it can be noted that, multiple fretting cracks appears at contact interface between the washer and the disc. Figure 3.51 depicts two of these cracks with fifty times magnification, which nucleate at contact interface and after propagation intersect each other.

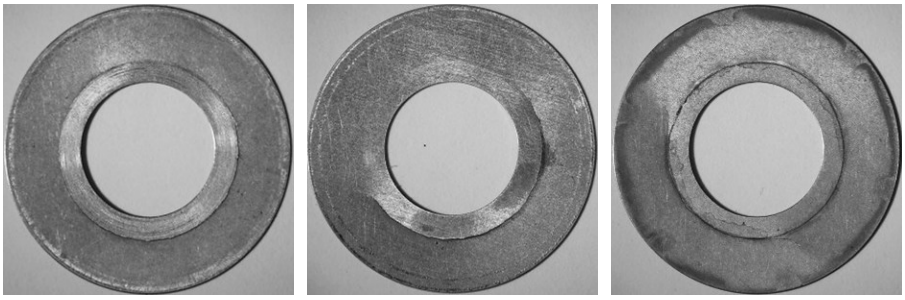

(a) Lab experiment **(b)** In-service sample 1 **(c)** In-service sample 2

Figure 3.49: Failed shock absorber valve disc for both lab experiments and in-service samples.

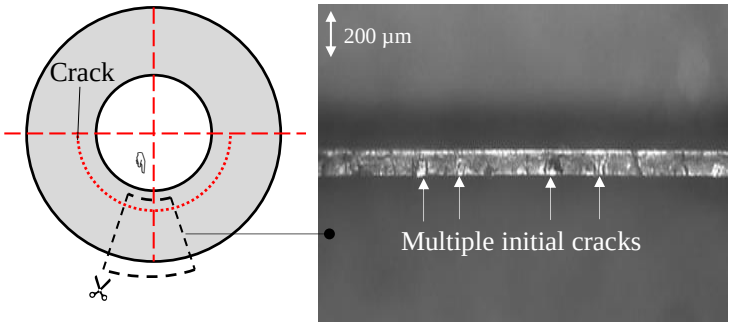

Figure 3.50: Multiple initial cracks after disc failure

Figure 3.52 illustrates the schematic view of fractured valve disc and how it was cross sectioned and embedded in epoxy resin to monitor the crack path trajectory. As it can be seen from the cross section (A-A) view, fretting crack initiates at washer-disc contact interface and propagates up to final rupture of disc. The crack propagation starts with around 40° under mode-mixity (stage I), becomes perpendicular to contact interface (Mode I) far from the contact (stage II) and the valve disc faces the sudden fracture eventually (stage III).

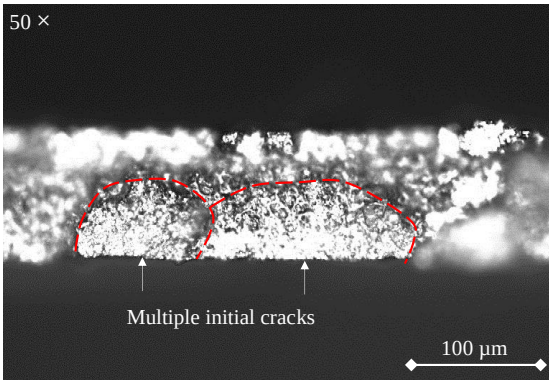

Figure 3.51: Close view of two intersected initial cracks

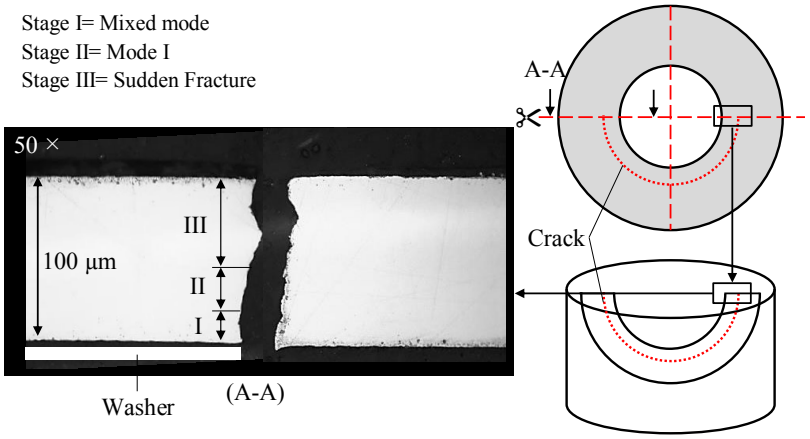

Figure 3.52: Fretting fatigue crack propagation trajectory in shock absorber's valve disc.

3.5 Summary and conclusions

In this chapter, different fretting fatigue experimental set-ups were used to monitor fretting fatigue failure mechanism. These experimental set-ups were fretting fatigue bridge type and single clamp tests. As expected the results show that fretting fatigue lifetime is less than the plain fatigue lifetime for both experimental configurations. The crack initiation and propagation mechanisms are the same for both experimental set-ups.

Digital Image Correlation (DIC) technique was used in order to monitor fretting fatigue frictional properties. For this purpose, three different test configurations were used, i.e. single clamp fretting fatigue set-up along with Single and Double Bolted Lap Joints (SBLJ and DBLJ). The results reveal that DIC technique is capable of determining the COF for contacts subjected to fretting fatigue loading condition by mean of just experimental approach. As expected the measured COF under static loading condition (i.e. SBLJ test) was less than the COF obtained from fretting fatigue tests (i.e. fretting fatigue and DBLJ tests). The discrepancy between two obtained COF for fretting fatigue and DBLJ tests is related to different test configuration that were used for measuring COF and also to the well known scatter nature of COF. However, in this study this scatter results was not investigated further and the obtained values for each test was implemented to their FE model as will be elaborated in Chapter 4.

Eventually, the fretting fatigue failure mechanism was observed in automotive shock absorber's piston valve component i.e. washer-disc connection. The interesting results show that fretting damage appears at contact interface between washer and disc, which causes the initial crack nucleation and advancing the crack up to the final rupture of valve disc.

Chapter 4

FEA of fretting and fretting fatigue contact

"This chapter presents the FEA modelling of fretting and fretting fatigue contact for different lab scale tests along with some practical applications"

4.1 Overview

In this chapter, three categories of fretting fatigue FE contact models are highlighted in different groups based on experimental test configurations as follows:

1. FEA of fretting contact.
2. FEA of fretting fatigue contact.
3. FEA of practical applications.

Next, using developed fretting fatigue contact models, effects of different loading conditions on fretting relative slip amplitude at contact interface are presented for single clamp flat and cylindrical contact configurations. Furthermore, different fretting fatigue contact behaviours for all three groups are monitored using FE modelling approach.

4.2 FEA of fretting contact

In order to model fretting contact, a parametric FE model was developed in ABAQUS using Python script. Figure 4.1 illustrates the FE mesh along with the applied loading and boundary conditions. Al 2024-T3 was selected for both fretting pad and fatigue specimen with Modulus of Elasticity of E= 72.1 GPa, a Poisson's ratio of ν= 0.33, yield and ultimate stress of σ_{yield} = 383 MPa, σ_{ult} = 506 MPa, respectively. To solve the cylindrical fretting contact model, only half the experimental set-up needs to be modelled as illustrated in Figure 4.1. The length of the specimen, width of the specimen and the radius of pad were selected as L= 40 mm, b= 10 mm and R= 20 mm, respectively. Both the fretting pad and the specimen had a depth of 4 mm.

As depicted in Figure 4.1 the specimen was restricted from vertical movement along its bottom surface and free to roll in the x-direction along its bottom edge. Both sides of fretting specimen were restricted from movement in x-direction. The Multi-Point Constraint (MPC) was applied at the top of fretting pad in order to avoid it from rotating due to the applied contact load. MPCs are advanced features where nodes and degrees of freedom are connected together in the FE analysis. They are often used to simulate a boundary condition effect, when regular boundary conditions do not provide the correct behaviour. For instance, in fretting contact model in order to avoid the effect

of concentrated contact load, the MPCs can be applied at top of fretting pad. One use of MPCs is a master and slave situation: the displacement at node i (the slave node) is needed to be the same as at node j (the master node). In FE model of fretting contact, the point at which the normal force was applied, was considered as a master node and all nodes at top of fretting pad considered as slave nodes.

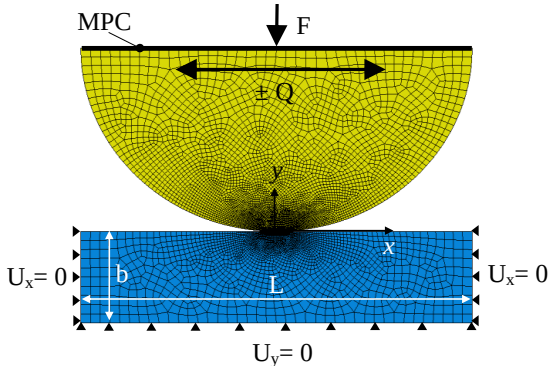

Figure 4.1: FE model of fretting contact.

The loading sequence was applied in five steps. In the first step, the contact load (F= 150 N) was applied and increased gradually up to the maximum value and kept constant for remaining time steps. Fretting load (tangential load, Q= 50 N) was then applied at top of fretting pad with loading ratio equal to -1. Therefore, in order to apply one full fretting cycle maximum tangential load Q_{max}, mean tangential load Q_{mean}, minimum tangential load Q_{min} and mean tangential load Q_{mean} were applied, respectively. A two-dimensional, 4-node (bilinear), plane strain quadrilateral, reduced integration element (CPE4R) was used. The mesh size of 5 μ m $\times$ 5 μm was considered at contact interface and decreased gradually far from the contact region for all models. This mesh size was gained by mesh convergence study, which is elaborated later on in this chapter. The contact between the fretting pad and the fatigue specimen was defined using the master-slave algorithm in ABAQUS®for contact between two surfaces. The circular surface of the pad was defined as a slave surface and top surface of the specimen was defined as a master surface. Lagrange multiplier formulation of friction was included in the contact pair to define the frictional behaviour of the connected parts. The friction coefficient of μ= 0.5 was considered in this case study model.

In order to verify the contact model, two assumptions were taken into account. The first one was the elastic behaviour of material, while the second was the half space assumption. Thus, the boundaries can be considered infinite if one half of the fretting specimen width, b, is equal to or greater than ten times the contact half width, a, or in other words $b/a \geq 10$. In this study, the analytical and FE contact half widths were $a_{Analytical}$= 160 μm and a_{FEA}= 164 μm, respectively. Figure 4.2 illustrates the variation of frictional shear stress at contact interface from step 2 till step 5. The figure also shows the good correlation between the FEA model and the analytical solution for shear stress distribution at contact interface as elaborated in Chapter 2. Figures 4.3 (a)-(c) show the von-Mises contour plot at maximum, mean and minimum applied tangential loads. As expected the stress distribution shows the high stress gradient near contact edges during maximum and minimum applied loading steps.

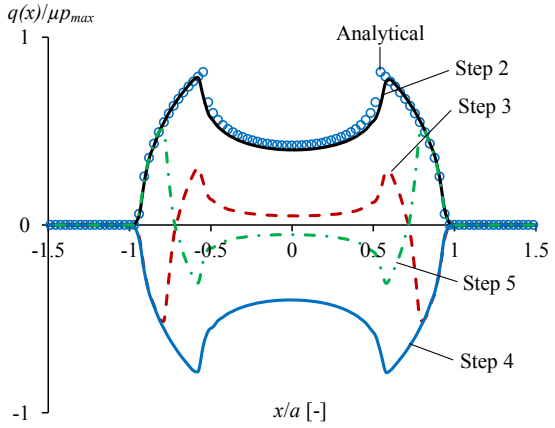

Figure 4.2: Variation of frictional shear stress during one full cyclic loading.

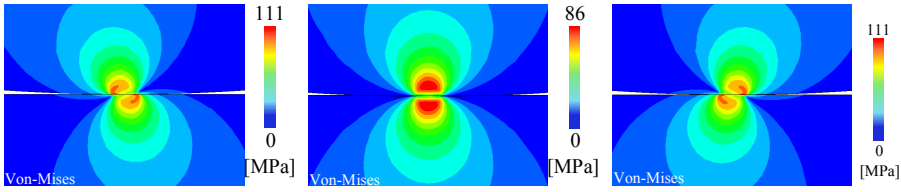

(a) Maximum (step 2) **(b)** Mean (step 3) **(c)** Minimum (step 4)

Figure 4.3: Fretting stress distribution inside fretting pad and specimen at maximum, mean and minimum loading steps.

Figures 4.4 (a) and (b) indicate the variation of normalized tangential stress and slip distribution at contact interface along the x-direction for one full fretting cyclic load, respectively. As can be seen from the figures, the maximum location of tangential stress and slip amplitude occurs near contact edges during cyclic loading.

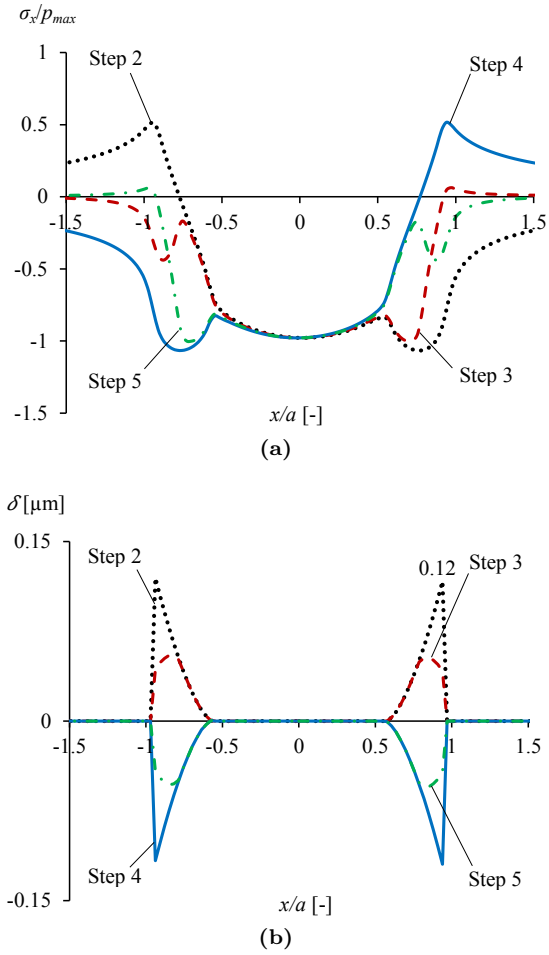

Figure 4.4: Variation of (a) normalized tangential stress and (b) relative slip amplitude at contact interface during one full cyclic loading.

4.3 FEA of fretting fatigue

4.3.1 Bridge-type pad contact

Based on ASTM standard for fretting fatigue testing, these type of fretting fatigue tests typically involve two bridge-shaped fretting pads pushing against the gage section of fatigue specimen [ASTM E2789-10, 2011]. In experimental tests, these types of pads are not restricted to the rig's frame and are therefore free of any additional external loading. Slip at contact interface is then generated when the specimen is subjected to fatigue load. Displacement in the pad produces the tangential load transmitted to the pad at contact interface. In this section, different types of contact geometries; namely, cylindrical pad and flat pad with different contact-span were modelled in order to study the stress distribution and potential location of fretting fatigue initial crack.

The FE model for flat bridge type pad configuration is shown in Figure 4.5. Note that only one-quarter of the test configuration is considered due to double symmetry with respect to the x and y axes. As shown in the figure both left sides of fretting pad and fatigue specimen were restricted to move in x-direction and bottom of the specimen was just free to roll in x-direction. Al 7075-T6 was selected for fretting specimen with Modulus of Elasticity of E= 72.1 GPa and a Poisson's ratio of ν= 0.33, yield and ultimate stress of σ_{yield} = 503 MPa, σ_{ult} = 590 MPa, respectively. Steel 410 for fretting pad with Modulus of Elasticity of E= 210 GPa and a Poisson's ratio of ν= 0.33, yield and ultimate stress of σ_{yield} = 420 MPa, σ_{ult} = 700 MPa, respectively.

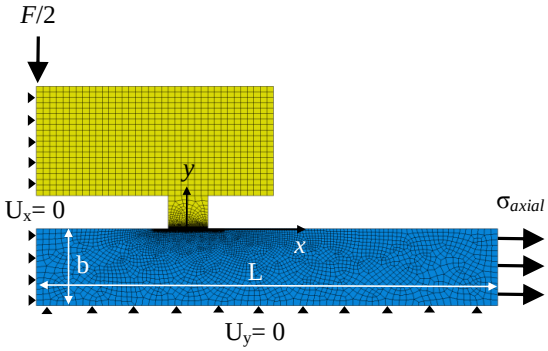

Figure 4.5: FE mesh of bridge type flat contact along with the applied loading and boundary conditions.

The length and width of the fatigue specimen were selected as L= 35 mm, b= 7.05 mm, respectively. Both the fretting pad and the specimen had a depth of 4.5 mm. Different fretting pad geometries with different contact width i.e. 3 mm, 6 mm and 9 mm were simulated for both cylindrical and flat type contact configurations as schematically illustrated in Figure 4.6. It is worth to mention that for bridge type fretting fatigue contact configuration, the contact width considered to be equal to the pad span as shown in Figure 4.6. Therefore, the semi contact width, a is equal to 1.5 mm, 3 mm and 4.5 mm for different contact configurations.

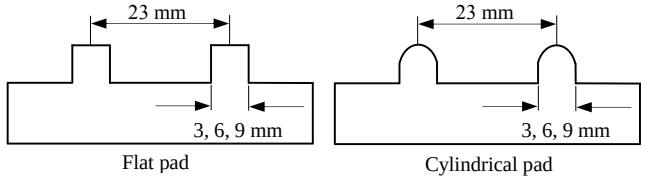

Figure 4.6: Fretting pads geometries that were used for FE modelling

The loads have been applied to the FE model in two steps. In the first step, the contact force $F/2$= 600 N has been applied to establish contact between pad and specimen. In the second step, the maximum bulk stress, σ_{axial}= 150 MPa has been applied to the right side of fatigue specimen. To have reliable FEA results, the loads must be applied in small increments due to non-linear behaviour of the contact problem.

The "master-slave" interfacial algorithm developed for contact modeling in the FE code, ABAQUS®, the Lagrange multiplier of friction, was used. The COF of μ= 0.5 was considered for all bridge type contact FE models. A two-dimensional, 4-node (bilinear), plane strain quadrilateral, reduced integration element (CPE4R) was used. In order to have more accurate stress distribution at contact interface, the FE mesh was refined in the contact region. The mesh refinement was conducted until an appropriate convergence of stress state was achieved, i.e. when the maximum stress between subsequent mesh refinements was less than a specific amount. In this investigation, a difference of 5% between the two consecutive steps was used as the convergence criterion. Figure 4.7 illustrates the mesh convergence study by plotting the normalized tangential stress (σ_x) for different mesh sizes at contact interface between cylindrical bridge type fretting pad and fatigue specimen. According to the mesh conver-

gence study, an acceptable element size was determined to be at least 5 μm $\times$ 5 μm in the refined contact zone.

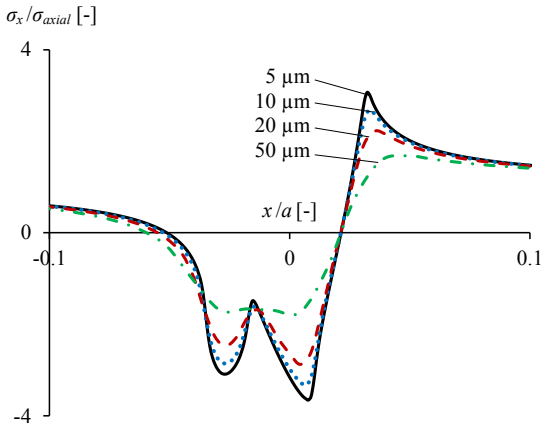

Figure 4.7: Normalized tangential stress distribution versus the normalized contact distance used for mesh convergence study of cylindrical bridge type contact configuration

Effect of contact geometry

In terms of effect of contact geometry on stress distribution, for all different geometries the maximum stress is created at contact region. Stress values are higher near the edge of contact, which is the region of interest at which failure is expected to occur. Also, observations from experiments and test results confirm this fact. With comparison of the amount of stress obtained from analysis of two types of contact geometry, it was observed that the amount of stress in contact region in cylindrical-flat contact is higher than that in flat-flat contact. This can be explained as whereas the compression force to the pad is the same in both cases, for the cylindrical case the contact area is less and therefore the contact stress is higher. Some typical stress contours i.e. tangential, normal and shear stresses (σ_x, σ_y and τ_{xy}) for cylindrical-flat and flat-flat configurations are depicted in Figures 4.8 (a) to (f). The stress contours show the distribution of stresses within the specimen under maximum axial stress of 150 MPa and normal load of 1200 N. It is interesting to mention that the maximum von-Mises stress for both types of contact geometries occurs at contact edge.

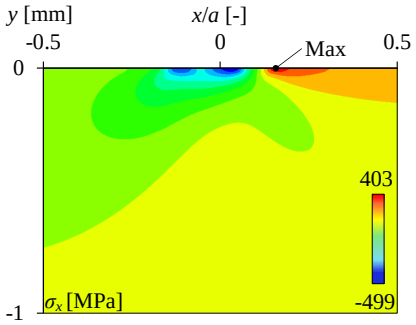

(a) σ_x= tangential stress (CP)

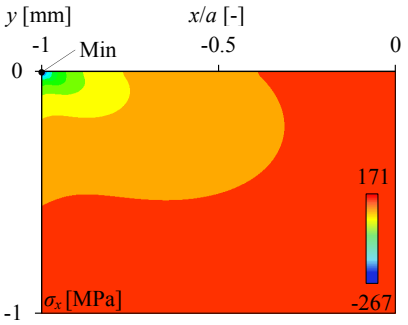

(b) σ_x= tangential stress (FP)

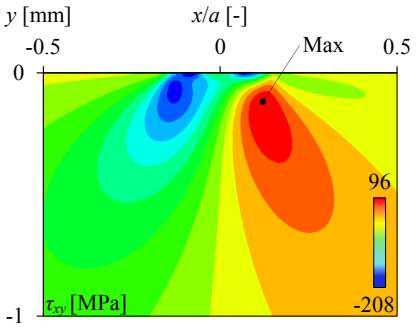

(c) τ_{xy}= shear stress (CP)

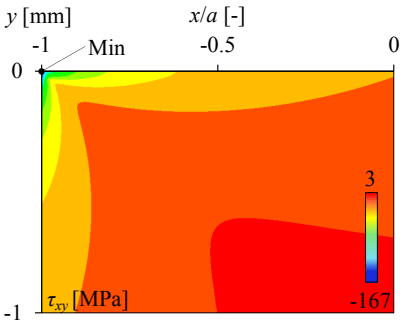

(d) τ_{xy}= shear stress (FP)

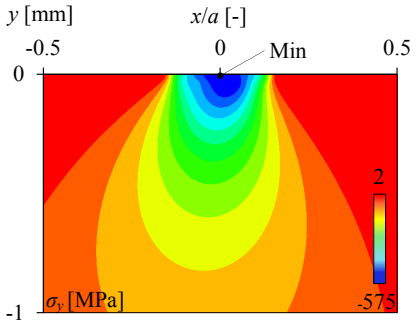

(e) σ_y= normal stress (CP)

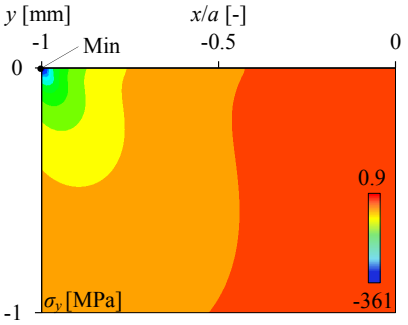

(f) σ_y= normal stress (FP)

Figure 4.8: Stress distribution inside fatigue specimen for cylindrical and flat bridge type contact configurations with contact width, a= 1.5 mm (at σ_{axial}=150 MPa and F= 1200 N), CP= Cylindrical Pad and FP= Flat Pad.

Figures 4.9 (a)-(b) show the comparison between normalized tangential stress distribution at contact interface for different contact widths. As the

figures suggest, with increase of contact width the maximum tensile tangential stress increases for both cylindrical and flat pads. However, for cylindrical on flat type contacts the stress is significantly higher than that for flat on flat contacts. As it can be seen from Figure 4.9 (a) for cylindrical-flat contact, the compressive stress is high at almost contact centre.

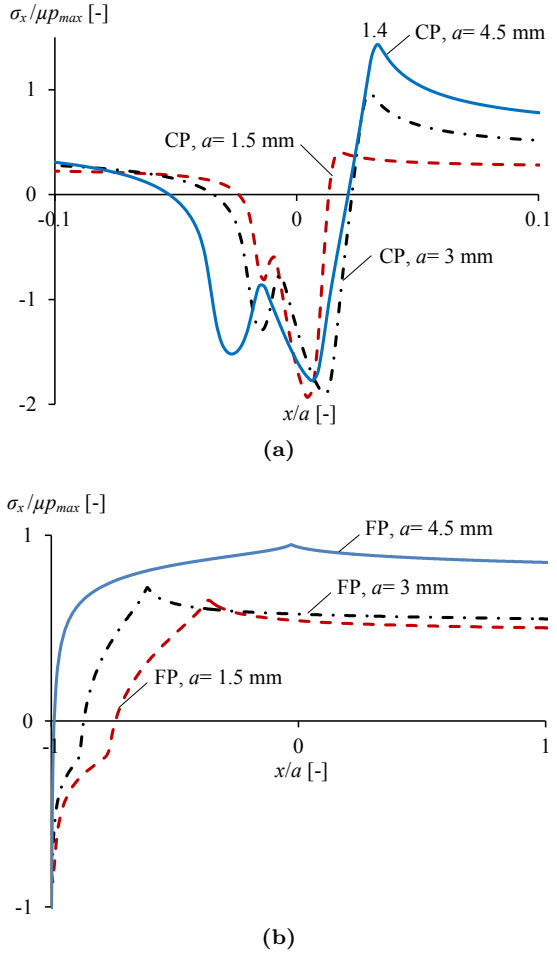

Figure 4.9: Normalized tangential stress distribution across the normalized contact distance for different contact widths of cylindrical and flat bridge type contact configuration. For cylindrical pad $p_{max} = 564$ MPa and for flat pad $p_{max} = 362$ MPa

Figures 4.10 (a)-(b) illustrates the comparison between normalized frictional

stress distribution at contact interface for different contact widths. As expected for bridge type cylindrical contact configuration there are generally three regions at contact interface corresponding to sticking, sliding and gapping of contact status. While, for bridge type flat contact configuration, the contact status depends on different parameters as elaborated later on.

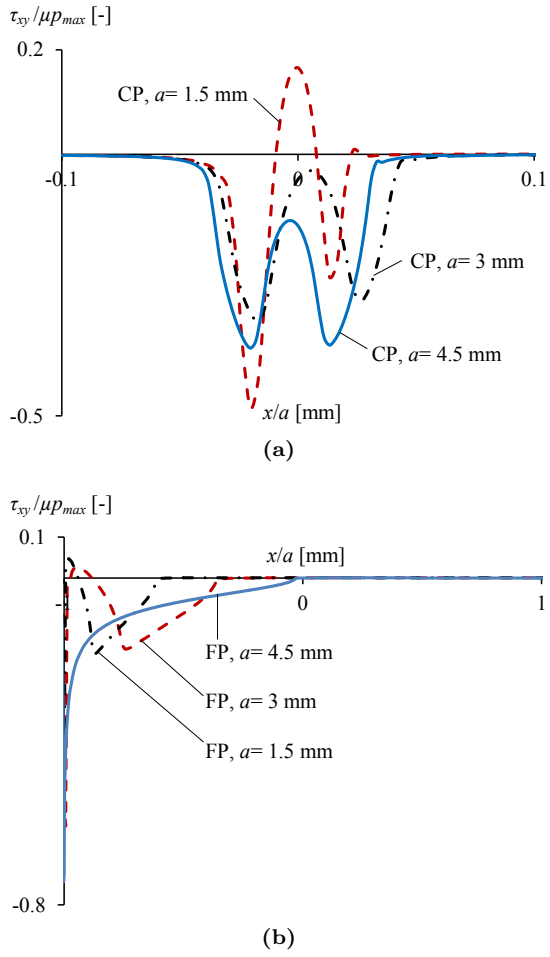

Figure 4.10: Normalized frictional shear stress distribution versus normalized contact distance for different contact width of cylindrical and flat bridge type contact configuration. For cylindrical pad $p_{max} = 564$ MPa and for flat pad $p_{max} = 362$ MPa.

In the basic coulomb friction model, two contact surfaces can carry shear

stresses up to a certain magnitude across their interface before they start sliding relative to each other. This state is known as sticking. The coulomb friction model defines an equivalent shear stress q(x), at which sliding on the surface begins as a fraction of contact pressure p(x) ($q(x) = \mu p(x)$). Once the shear stress is exceeded ($q(x) \geq \mu p(x)$), the two surfaces will slide relative to one another. This state is known as sliding. Sticking happens when $q(x) \leq \mu p(x)$. Figure 4.10 (a) illustrates that for all cylindrical pads sticking and slipping regions do exist as elaborated in Chapter 2.

For flat-flat contact configuration, stress singularity appears only at the internal contact edge and it is obvious that there is no singularity at the external contact edge. For instance Figure 4.11 illustrates the frictional shear stress distribution across the contact interface for flat-flat contact configuration with a= 1.5 mm. As schematically shown, the singularity appears at the internal corner of contact. As shown in Figure 4.11 for a= 1.5 mm three different contact status can be distinguished, namely sticking, slipping and gapping. The same behaviour can be seen for a= 3 mm, however, for a= 4.5 mm there is no sticking region and the fretting pad and the specimen is sliding over each other at contact edge as shown in Figure 4.10 (b).

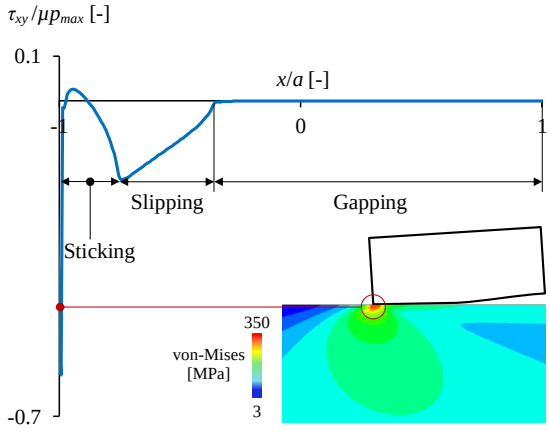

Figure 4.11: Normalized frictional shear stress distribution over contact interface. Three different contact regions i.e. sticking, slipping and gapping.

As it is reported by Hills and Nowell [Hills and Nowell, 1994] the fretting fatigue crack usually initiates in the region with the highest stress gradient distribution over the contact interface. This fact can be valid for flat-flat contact

configuration as the maximum location of von-Mises equivalent stress occurs at contact edge and this location completely corresponds with what occurs in most experimental observations. However, in case of cylindrical-flat configuration it does not represents the exact location of initial crack as will be elaborated more in details later on.

Effect of boundary and loading conditions

All above presented stress distribution results at contact interface for bridge type contact configuration are valid for the experimental set-up, which was used in this study as elaborated in Chapter 3 (section 3.2.1). However, there is a possibility that the bridge type contact be used in different set-up, which affects the boundary conditions in the FE model. Therefore, in this section one of the main factors, which can significantly affect the stress distribution at contact interface was studied. Figure 4.12 schematically depicts two possible stress distributions at contact interface between pad and specimen at absence of axial load for bridge type flat contact configuration.

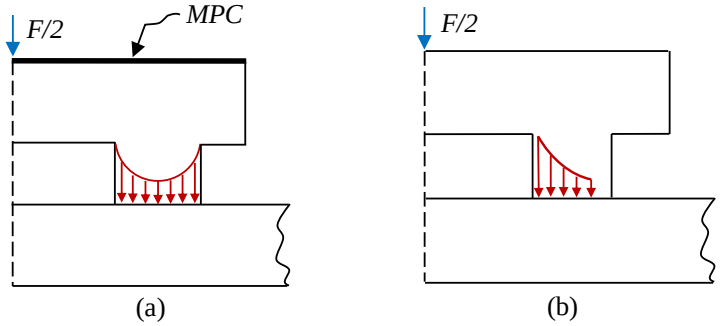

Figure 4.12: Schematic view of normal stress distribution at contact interface at absence of axial stress for (a) uniform and (b) concentrated contact load.

Figure 4.13 depicts the normal stress distribution at contact interface between fretting pad and specimen using uniform normal load and a concentrated load. From the figure it can be noted that at presence of uniform load the contact load distributed over all contact area. However, there is zero contact pressure near to the external edge of contact, when concentrated load was applied at top of fretting pad.

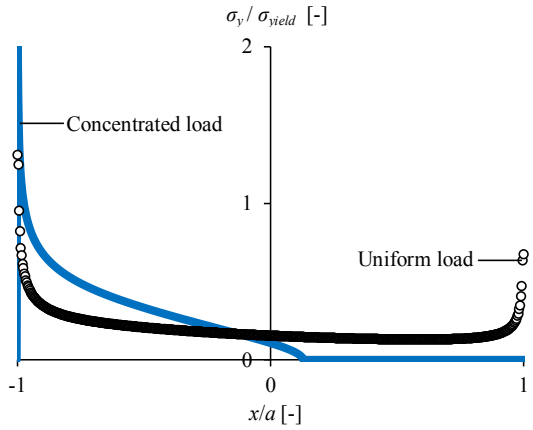

Figure 4.13: Normalized contact stress distribution versus normalized contact distance for a= 3 mm and F= 1200 N).

Figure 4.14 illustrates the frictional shear stress distribution at contact interface for both uniform and concentrated contact loads after applying the axial stress. As it can be seen from figure, the stress distribution is completely different in the two cases. After using MPCs or applying uniform normal stress at top of fretting pad the contact line is divided to two regions of gapping and slipping. However, at presence of concentrated load, the contact line is divided into three regions i.e. gapping, slipping and sticking regions. Nonetheless, both of these results can be acceptable, depending on type of test rig, which is used for applying normal load against specimen.

There are some studies that have used proving ring to apply normal load to the specimen [Mutoh and Xu, 2003, Jayaprakash et al., 2010]. In this type of test rigs, the normal load transmits to the fretting pad by a bolt, which is pushed against the top of fretting pad at centre that can be modelled by applying concentrated load at top of pad as schematically illustrated in Figure 4.12 (b). In contrast, there are some test-rigs, which use the same proving ring but with different mechanism for applying normal load [Pape and Neu, 1999, Swalla and Neu, 2001]. In this type of test apparatus, the load applied to the centre of the loading pad through a solid ball in contact with a loading screw, and subsequently transferred to the fretting pads by two cylinders located over the centre of the fretting pad feet, which leads to the parabolic stress distribution over entire contact interface between the fretting pad feet and the specimen as

shown in Figure 4.12 (a).

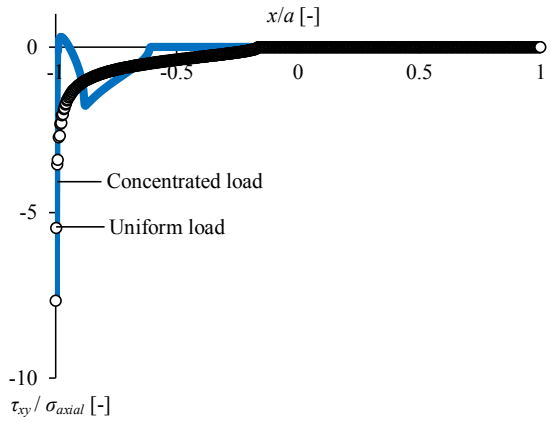

Figure 4.14: Normalized frictional shear stress distribution versus normalized contact distance for a= 3 mm, F= 1200 N and σ_{axial}= 150 MPa.

ANSYS®VS ABAQUS®

In this section, two commercial FEA packages, namely Ansys and Abaqus are compared to analyse the fretting fatigue bridge type flat contact configuration. The stress distribution along the contact interface between the two bodies obtained using both codes was compared and analysed. For both cases the geometry and material were the same as explained above for flat-flat bridge type contact with contact width of 3 mm.

ANSYS®. ANSYS (version 12) model consists of four-node plane strain elements (PLANE182) to model the fretting pad and the fatigue specimen. Furthermore, contact elements CONTACT172 and TARGET169 were used at contact interface between the pad and specimen to model contact behaviour. The function of contact elements in ANSYS is to allow load transfer between the connected parts without penetration. The Augmented Lagrange method of friction was used with a COF of 0.5. As elaborated earlier loads were applied in two steps, first the contact load, F= 1200 N was applied to establish the contact between fretting pad and specimen and followed by either the maximum bulk stress (σ_{axial}= 280 MPa) applied at right side of the fatigue specimen (see Figure 4.5). ANSYS Parametric Design Language (APDL) was used in order to model a parametric FEA model of fretting fatigue bridge type configuration.

ABAQUS®. The ABAQUS model was elaborated earlier, however, just for sake of completeness is briefly mentioned here. In ABAQUS (version 6.10), the four-noded plain strain, reduced integration elements (CPE4R) were used to model both pad and specimen. The contact between pad and specimen were modelled using the master-slave interfacial algorithm, which uses Lagrange multiplier of friction. Table 4.1 presents a comparison of some modelling parameters used in ANSYS and ABAQUS.

Table 4.1: Comparison of modelling parameters in ANSYS and ABAQUS

	Number of nods	Number of elements	Number of DOF	CPU time (second)	Element size (μm)
ABAQUS®	14264	14025	28434	16.8	25
ANSYS®	10126	10574	20147	70.8	25

It can be seen that although ABAQUS model has larger number of DOF than ANSYS model, its CPU time is much lower than ANSYS CPU time. It is clear that the solution solver of ABAQUS 6.10 is faster that that of ANSYS 12. The normalized von-Misses stress obtained using ANSYS and ABAQUS are shown in Figure 4.15. It can be seen from the figure that the stress distributions obtained using both codes are very similar. However, the ANSYS maximum von-Mises stress is higher than the ABAQUS one at contact interface. This may be due to the different contact algorithm using in each package.

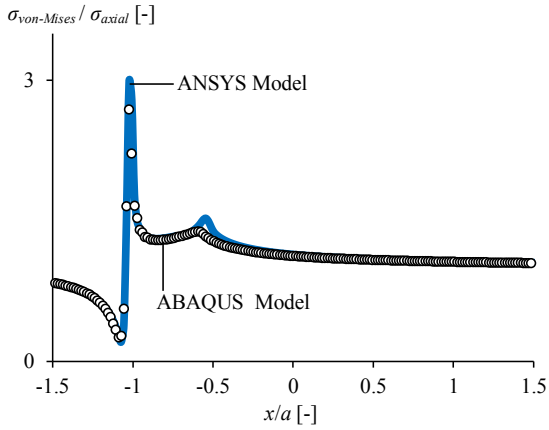

Figure 4.15: Comparison of normalized von-Mises stress distribution over contact interface between ANSYS and ABAQUS models.

The normalized tangential stress and shear stress distribution along the contact interface obtained using both software packages are compared in Figures 4.16 and 4.17, respectively, and show good agreement between ANSYS and ABAQUS. As expected ANSYS gives higher maximum tangential stress than ABAQUS. However, the maximum frictional shear stress distribution at contact interface calculated by ABAQUS is slightly higher that the one calculated by ANSYS.

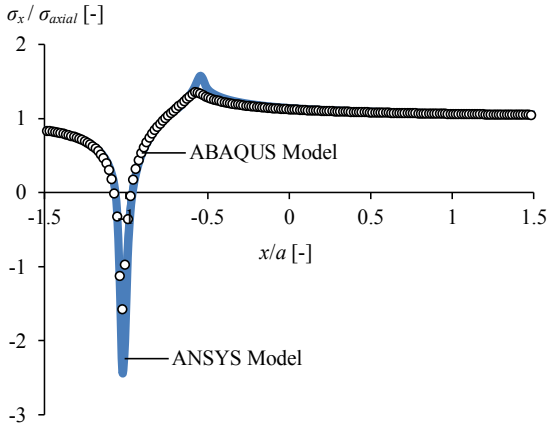

Figure 4.16: Comparison of normalized tangential stress distribution over contact interface between ANSYS and ABAQUS models.

In commercial FE codes, there are in general four different contact algorithms, namely Pure penalty, Augmented Lagrange, Pure Lagrange multiplier and a mixed Lagrange-penalty (Lagrange multiplier on contact normal and penalty on frictional direction). In Abaqus, Pure Lagrange (PL) contact algorithm was used. In such a method, Lagrange multipliers are used and contact forces are considered as separate DOF's. Therefore, contact stiffness does not need to be dealt with. In ANSYS, however, the PL algorithm did not shown convergence for this particular bridge type fretting fatigue contact configuration. Therefore, the Augmented Lagrange (AL) contact algorithm was used and convergence has been achieved. In this method, a penalty function together with Lagrange multipliers is used to solve the contact problem. The contact stiffness is automatically calculated once the penetration or sliding exceeds a certain limit. As the penetration should be minimized, high contact stiffness could be calculated resulting in higher contact stresses.

Therefore, it is expected that ANSYS would produce higher stresses than ABAQUS. From FEA and analytical solution of a simple cylindrical pad contact carried out (see Section 4.2), it was confirmed that the stresses produced using PL algorithm were closer to the analytical solution than those produced using AL algorithm.

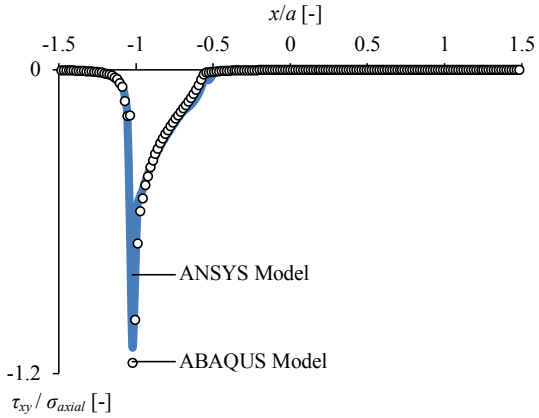

Figure 4.17: Comparison of normalized frictional shear stress distribution over contact interface between ANSYS and ABAQUS models.

4.3.2 Single clamp contact

Cylindrical contact

To solve the fretting fatigue cylindrical contact model only half the experimental set-up needs to be modelled as illustrated in Fig 4.18, because the experimental set-up is ideally symmetric about the axial centreline of the specimen. As depicted in Fig 4.18, the specimen was restricted from vertical movement along its bottom surface and free to roll in the x-direction and along its bottom edge. The length of the specimen, width of the specimen and the radius of pad were selected as L= 40 mm, b= 5 mm and R= 50 mm, respectively. Both the fretting pad and the fatigue specimen had a depth of 4 mm. Al 2024-T3 which was used for experimental tests, was selected for both the pad and the specimen with Modulus of Elasticity of E= 72.1 GPa and a Poisson's ratio of ν= 0.33. The contact between the fretting pad and the fatigue specimen was defined using the master-slave algorithm in ABAQUS®for contact between two surfaces. The circular surface of the pad was defined as a slave surface and top surface

of the specimen was defined as a master surface. The Lagrange multiplier of friction was used. The COF of μ= 0.65 was considered for single clamp cylindrical contact configuration FE models. A two-dimensional, 4-node (bilinear), plane strain quadrilateral, reduced integration element (CPE4R) was used.

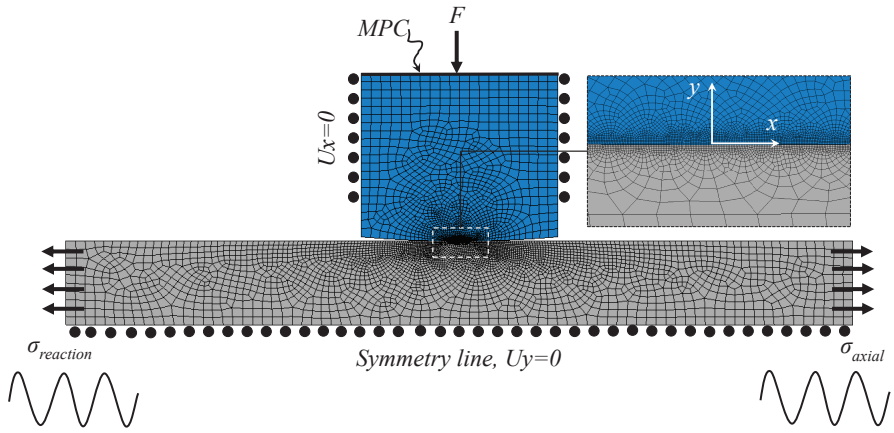

Figure 4.18: FEA mesh and loading and boundary conditions for fretting fatigue cylindrical contact configuration under single clamp contact category.

Both sides of cylindrical pad were restricted just to move in vertical direction. The MPC was also applied at the top of pad in order to avoid it from rotating due to the applied contact load. In order to model the effect of attached spring to the fretting pad for generating the tangential load Q, the reaction stress, $\sigma_r = F_r/A_s$ can be calculated based on $F_r = F_{axial} - Q/A_s$, where A_s is cross section area of the fatigue specimen. The loading sequence was applied in six steps. In the first step, the contact load was applied and increased gradually up to the maximum value and kept constant for remaining time steps. Since the experiments were carried out under stress ratio of R_s= 0.1, therefore, in the second step the mean axial and reaction stresses were applied at the same time at the right and left sides of specimen, respectively. In the third, fourth, fifth and sixth steps, maximum, mean, minimum and finally mean value of axial and reaction stresses were applied respectively to match the experimental cyclic loading condition as illustrated in Figure 4.19. The loading conditions for the FE model of cylindrical contact configuration were the same as the experimental that is tabulated in Table 3.4.

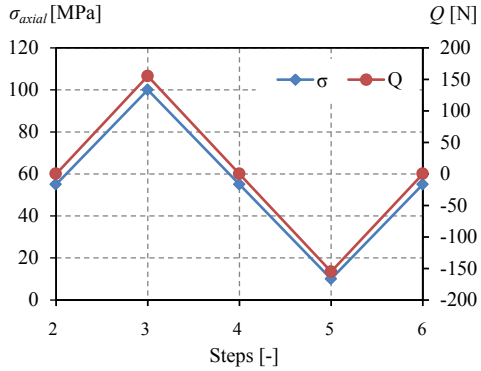

Figure 4.19: One full cyclic loading sequence applied to fretting fatigue cylindrical contact configuration for FF1.

Mesh convergence study:

The mesh size at contact interface should be fine to capture the relaxed stress state near the leading and trailing edges of contact. The leading edge is edge which is at clamped side of the specimen and trailing edge is near the side where axial stress was applied. In order to do mesh convergence study, the modelling with mesh refinement was continued until an appropriate convergence of the stress state was achieved. In this study the convergence criterion selected as when the maximum stress between subsequent mesh refinements was less than a specific amount. For this purpose, a difference of 1.5% between the two consecutive steps was used as the convergence criterion, which was defined as follows:

$$e_{cp} = \left| \frac{\sigma_{max}^{i+1} - \sigma_{max}^{i}}{\sigma_{max}^{i+1}} \right| \times 100 \tag{4.1}$$

where e_{cp} is the convergence parameter, σ_{max}^{i} is the maximum stress in i^{th} model and σ_{max}^{i+1} is the maximum stress in $(i+1)^{th}$ model. According to mesh convergence study results, an acceptable element size was determined to be at least 5 μm $\times$ 5 μm in the refined contact zone. Figure 4.20 shows the variation of tangential stress using different element sizes at the contact interface for cylindrical fretting pad. Figure 4.20 (b) indicates close-up view of the variation of normalized tangential stress at contact interface near the trailing edge of contact i.e. $x/a \approx 1$. Figure 4.21 illustrates the variation of maximum value of normalized tangential stress distribution at contact interface versus different mesh sizes.

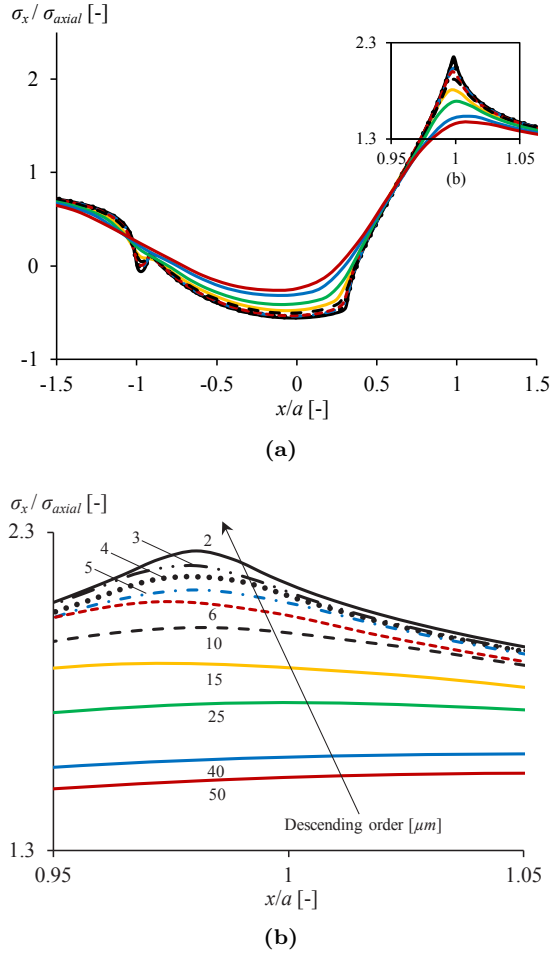

Figure 4.20: Variation of normalized σ_x at contact interface for different mesh sizes.

Jayaprakash et al. [Jayaprakash et al., 2010] have reported the relationship between tangential stress at the contact edge and mesh size for a bridge type contact configuration with sharp corners. They have found that there was a transition in slope at a mesh size of 5 μm and the stress became much sensitive to mesh size when the mesh size was smaller than 5 μm. However, they could not find a logical reason for this transition behaviour. According to literature the minimum mesh size that has been used for fretting fatigue contact problem was in the range of 5 μm to 50 μm [Tsai and Mall, 2000, Iyer and Mall, 2001, Giner et al., 2009, Madge et al., 2007], some of them are tabulated in

Table 4.2. It is worth to mention that for cylindrical contact configuration the behaviour was not the same as reported by Jayaprakash et al. [Jayaprakash et al., 2010].

Table 4.2: Different mesh sizes that have been used for fretting fatigue contact problem.

Reference	Minimum mesh size at contact interface (μm)
[Golden and Nicholas, 2005]	5
[Fadag et al., 2008]	6
[Lykins et al., 2001a]	6.2
[Nicholas et al., 2003]	6.5
[Nishida et al., 2003]	10
[Massingham and Irving, 2006]	25
[Tsai and Mall, 2000]	50

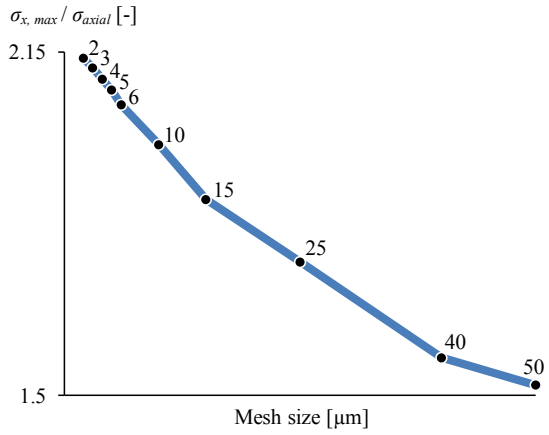

Figure 4.21: Variation of normalized maximum tangential stress at contact interface versus different mesh sizes.

FE model verification:

In order to verify the contact model, the FE results were compared with the analytical solution. For single clamp cylindrical contact configuration, the analytical and *FE* semi contact widths were $a_{Analytical}$= 462 μm and a_{FE}= 469 μm, respectively. Figure 4.22 (a) and (b) illustrate the variation of the normalized contact pressure and frictional shear stress distribution at contact interface at maximum applied stress loading step. The figures also show the excellent correlation between FEA results and analytical solution for shear stress distribution at contact interface.

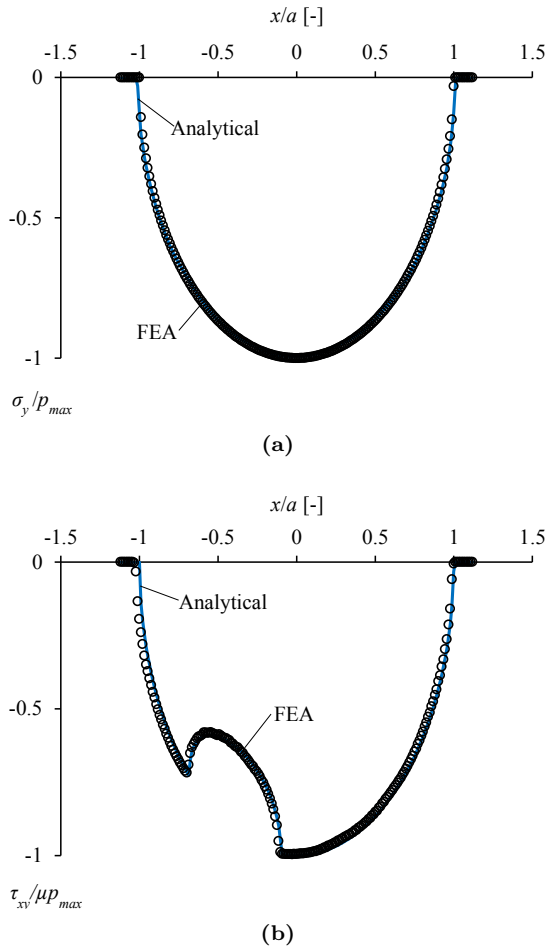

Figure 4.22: Comparison between FEA and analytical results of normalized (a) normal and (b) frictional shear stress distribution at contact interface for single clamp cylindrical contact configuration.

Non-proportional loading condition:

Figures 4.23 (a)-(c) show the typical von-Mises contour plot at maximum, mean and minimum loading steps, respectively. The figure shows that the stress gradient is high at contact edge at maximum loading step. Figures 4.24 and 4.25 present the variation of normalized tangential stress and slip distribution at contact interface for one full fretting cyclic load, respectively. From Figure 4.24 it can be noticed that the location of maximum stress varies during one cyclic loading steps. This variation is related to nature of non-proportional loading

condition of contact problem subjected to fretting fatigue loading condition.

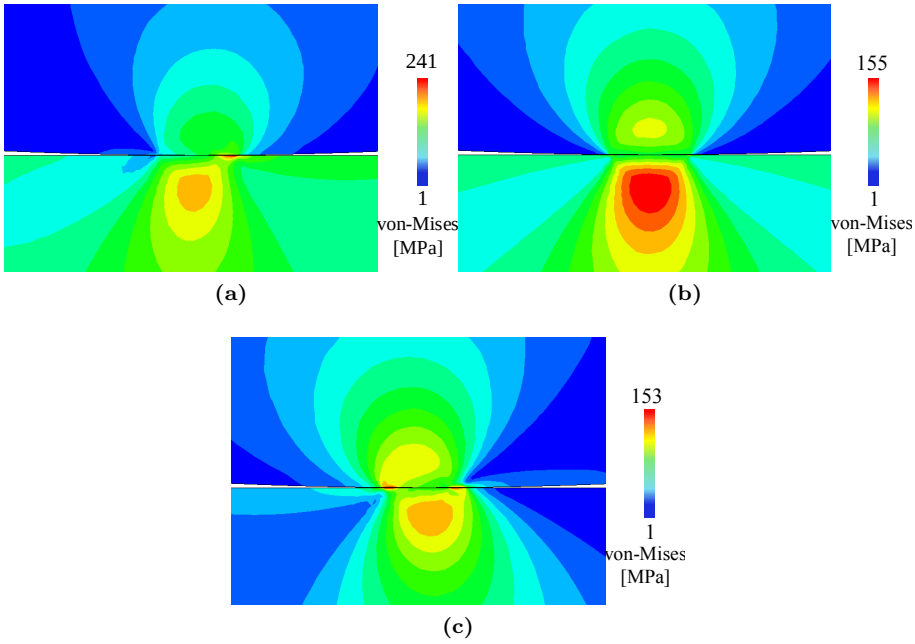

Figure 4.23: von-Mises contour plot of stress distribution in fretting pad and fatigue specimen at (a) maximum, (b) mean and (c) minimum loading steps for σ_{axial}= 100 MPa, Q_{max}= 155 N and F= 543 N (FF1).

One case study was carried out in order to show the non-proportional loading condition of fretting fatigue contact problem. For this purpose stresses were extracted from FE model at a node at trailing edge of contact interface as illustrated in Figure 4.26 and monitored during one full cyclic loading condition. The FE loading condition was selected for FF1 i.e. σ_{axial}= 100 MPa and Q_{max}= 155 N. Figure 4.27 indicates the variation of tangential stress (σ_x), normal stress (σ_y) and shear stress (τ_{xy}) extracted from FE model for one full cyclic loading steps. As expected the normal stress distribution is almost constant during the cycle as constant contact load was applied to the fretting pad. However, the ratio between tangential stress, σ_x and shear stress, τ_{xy} continuously varies during the cycle. It is well known that during constant amplitude cyclic loading, as the magnitude of the applied stresses vary with time, the size of Mohr's circle of stress also varies with time. In some cases, even though

the size of the Mohr's circle varies during cyclic loading, the orientation of the principal axes with respect to the loading axes remains fixed, which is called *proportional loading*. In many cases, however, the principal directions of the alternating stresses are not fixed, but the orientation of the principal axes with respect to the loading axes changes, which is called *non-proportional loading*.

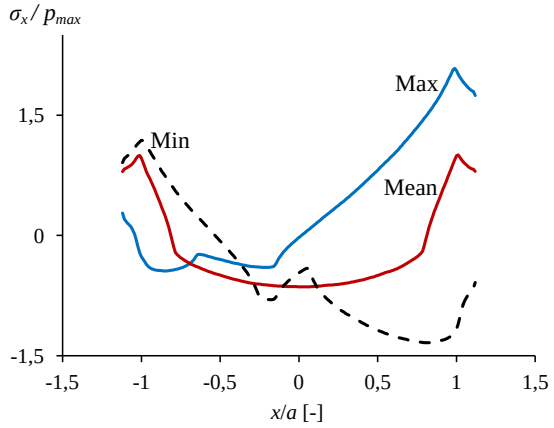

Figure 4.24: Variation of normalized tangential stress distribution over contact interface at σ_{axial}= 190 MPa and p_{max}= 187 MPa.

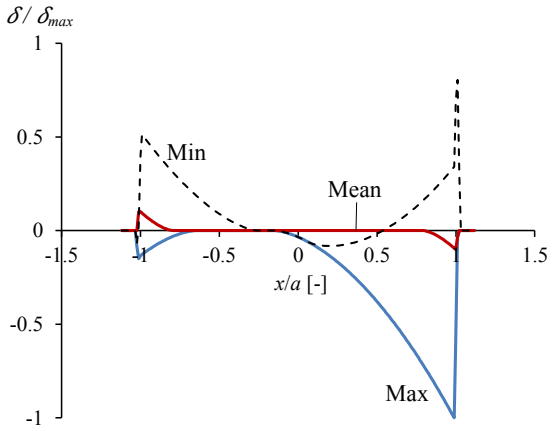

Figure 4.25: Variation of normalized relative slip amplitude over contact interface at σ_{axial}= 190 MPa and δ_{max}= 2.4 μm.

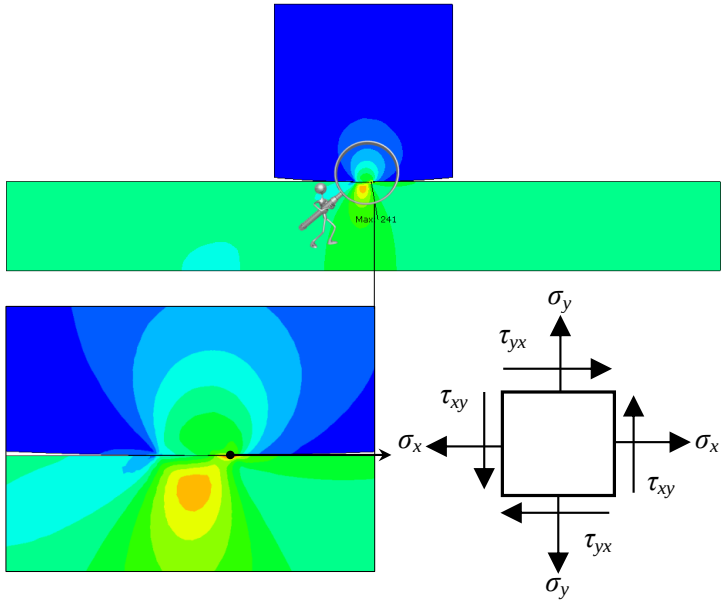

Figure 4.26: Extracting stress components at a node at contact interface from FE model for FF1 (σ_{axial}= 100 MPa, Q_{max}= 155 N and F= 543 N).

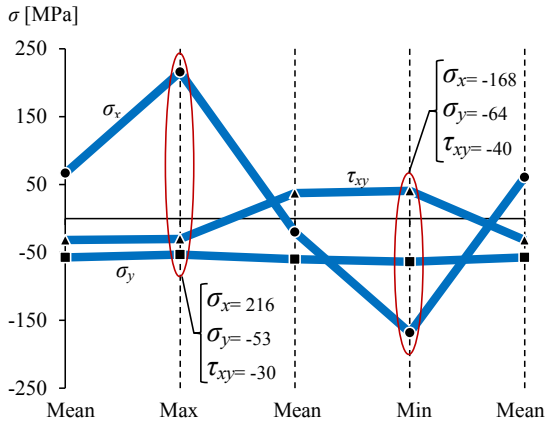

Figure 4.27: Variation of extracted stress components from FE model during one full cylic loading steps.

The values of stresses at maximum and minimum loading steps were selected to calculate the principal stresses and monitor variation of orientation

of principle axes with respect to the loading axes. The components of stress extracted from FE model at maximum and minimum loading steps are shown in Figure 4.27. By substituting the stress components into the stress transformation Equations 4.2 to 4.5, the principal stresses and the orientation of principal axes ($2\alpha_p$) respect to the loading axes can be found as schematically illustrated in Figure 4.28.

$$\sigma_{x'} = \frac{\sigma_x + \sigma_y}{2} + \frac{\sigma_x - \sigma_y}{2}\cos(2\alpha_p) + \tau_{xy}\sin(2\alpha_p) \tag{4.2}$$

$$\sigma_{y'} = \frac{\sigma_x + \sigma_y}{2} - \frac{\sigma_x - \sigma_y}{2}\cos(2\alpha_p) - \tau_{xy}\sin(2\alpha_p) \tag{4.3}$$

$$\tau_{x'y'} = -\frac{\sigma_x - \sigma_y}{2}\sin(2\alpha_p) + \tau_{xy}\cos(2\alpha_p) \tag{4.4}$$

$$2\alpha_p = \arctan\left(\frac{2\tau_{xy}}{\sigma_x - \sigma_y}\right) \tag{4.5}$$

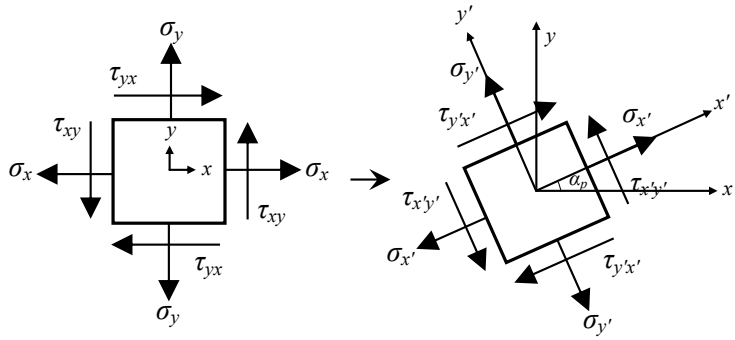

Figure 4.28: Schematic view of stress transformation in a representative element.

Figure 4.29 (a) and (b) show the Mohr's circles of stress at maximum and minimum loading steps during the loading cycle. As shown the orientations of the principal stress axes continuously rotate with respect to loading axes (i.e. x-y axes). These results prove that fretting fatigue is subjected to complex loading conditions consist of local non-proportional and multi-axial state of stress at contact interface between fretting pad and fatigue specimen. This complex stress state is result of three different independent loads namely, contact, tangential and axial loads which are acting simultaneously, but with dif-

ferent impact on stress state. As shown even by applying in phase loading condition between tangential and axial loads the stress state at contact interface is non-proportional which makes it more complex. This complex stress state have significant effects on fretting fatigue crack initiation and crack propagation behaviour as will be discussed later on in Chapters 5 and 6.

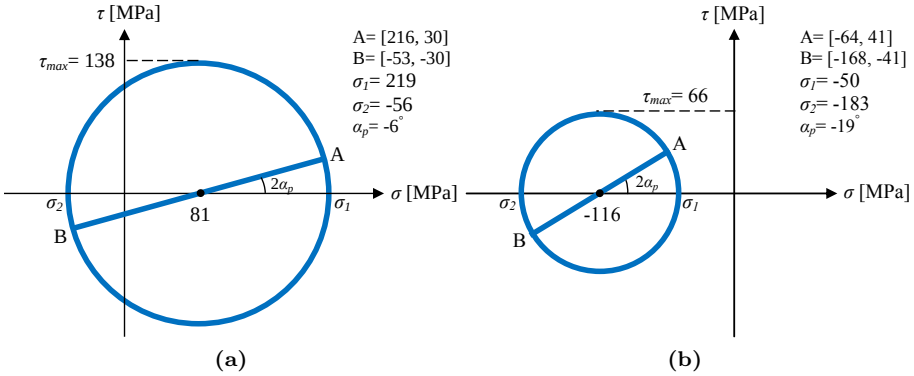

Figure 4.29: Mohr's circles of stress at (a) maximum and (b) minimum loading steps.

Effect of boundary and loading conditions:

Despite verifying the FE model with the analytical solution, it is necessary to consider the real experimental set-up configuration, when dealing with FE simulation. To this end, some of the available boundary conditions that have been used widely in literature were modelled and the results were compared to each other. Four different FE models namely, Model I, Model II, Model III and Model IV were simulated and compared to each other. The loading and boundary conditions of each of them are schematically shown in Figure 4.30.

Loading and boundary conditions of Model I was the same as elaborated earlier. Model II consists of three regions: the fatigue specimen, the fretting pad and fretting pad holder. In this model, a plate with low modulus of elasticity is attached to the side of the fretting pad, which is called pad holder as named in [Tsai and Mall, 2000, Lykins et al., 2001a, Iyer and Mall, 2001, Wang et al., 2007]. The primary purpose of the pad holder is to restrain the pad in the x and y directions prior to the application of load. Therefore, the stiffness of the pad holder should be low enough to have a minimal effect on the interaction between

the fretting pad and fatigue specimen. The loading and boundary conditions of Model II are illustrated in Figure 4.30 (b). The specimen was constrained at its far end in the negative x-direction, restricted from vertical movement and was free to roll in the x-direction and along its bottom edge. The cylindrical pad is rigidly fixed to the pad holder with the pad holder being free to roll in the y-direction along the side opposite to the fretting pad. MPCs were also applied at the top of fretting pad as well as the border between fretting pad and holder in order to prevent it from rotating due to the application of loads and effect of concentrated loads. The material properties of the pad holder differ from the other two regions. An Elastic Modulus and a Poisson's Ratio of 0.03 MPa and 0.3 were then signed to the pad holder, respectively. Finally, the loads were applied in two steps. First the normal load F was applied and then held constant. Next, the maximum tangential load and axial stress was applied simultaneously.

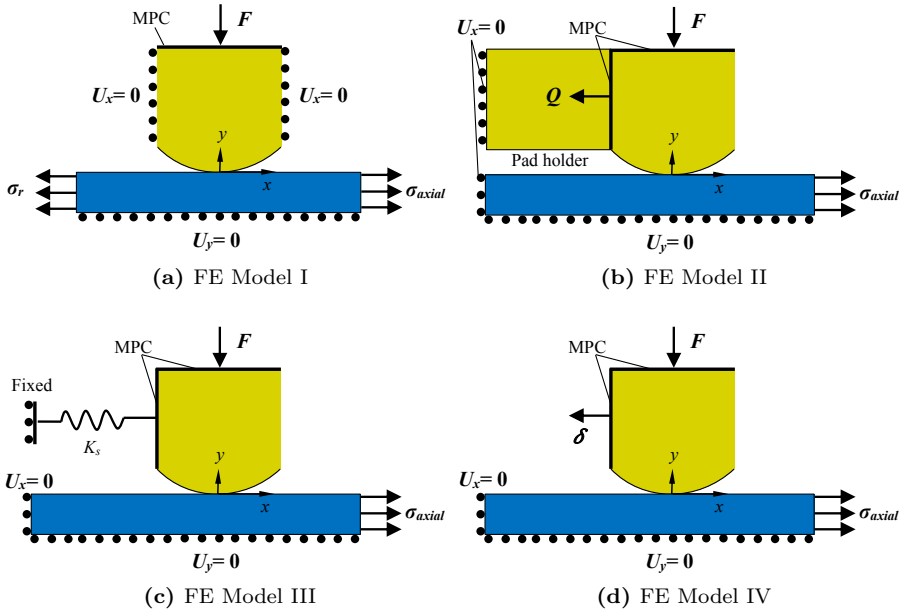

Figure 4.30: Different fretting fatigue single clamp cylindrical contact configurations are shown. (a) Model I, (b) Model II, (c) Model III and (d) Model IV.

In contrast to Model II that has directly applied tangential load to the fretting pad, some researchers have tried to generate tangential load at contact

interface between fretting pad and fatigue specimen [Madge et al., 2007, Giner et al., 2009, Ding et al., 2011]. In this study two ways that are mostly used in literature were selected to model fretting fatigue contact problem. In order to generate tangential load, one of the possibilities is adding a spring or beam element at the right side of the fretting pad as depicted in Model III in Figure 4.30 (c). The sequence of applying the normal and axial load is the same as in previous models, just because of the frictional contact and the way the pad is supported (stiffness of attached spring), a tangential load Q is generated on the fretting pad. The magnitude of the tangential load and the bulk stress on the left part of the specimen depend on the compliances of both the specimen and the fretting pad support (k_s). Giner et al. [Giner et al., 2009] and H-Gangaraj et al. [H-Gangaraj et al., 2011] have represented these compliances in their model by attaching spring and beam element of stiffness k_s, respectively. Moreover, the MPCs were used to guarantee an uniform distribution of concentrated forces over the top and right sides of fretting pad.

The tangential load at contact interface can be also modelled by imposing displacement to the fretting pad [Madge et al., 2007]. Figure 4.30 (d) indicates the boundary and loading conditions of this type of models i.e. Model IV. The sequence of applying normal and axial load is the same as mentioned above. Both sides of fretting pad as well as top of pad are restricted using MPCs to prevent it from rotating due to the application of displacement, and also to guarantee an uniform distribution of concentrated force over the top surface of fretting pad. The magnitude of displacement was calibrated for the desired tangential load, which was applied at right side of pad. In experimental set-up it is possible to measure the global displacement of fretting pad. In this study in order to find accurate displacement amplitude, Q was applied to right side of fretting pad to measure the related displacement that should be applied to generate the same tangential load. This step was just modelled to find the displacement amplitude instead of experimental measurements.

For all simulated FE models, the length and width of the specimen was L= 20 mm and b= 2 mm, respectively. The radius of fretting pad was considered as R= 50.8 mm. All of the regions had an unit depth. A two-dimensional, 4-noded (bilinear), plane strain quadrilateral, reduced integration element (CPE4R). The mesh size of 5 μm $\times$ 5 μm was considered for all models at contact interface. The contact between the fretting pad and the fatigue specimen was defined using the master-slave algorithm in ABAQUS®for contact between two surfaces

along with a COF of 0.75. Al 7075-T6 was selected for both fretting pad and fatigue specimen with Modulus of Elasticity of 71.7 GPa and a Poisson's of 0.32. For all models the normal load, maximum axial stress and tangential load ratio were considered as F= 40 N, σ_{axial}= 90 MPa and $Q_{max}/\mu F$= 0.6, respectively.

Figure 4.31 depicts the variation of tangential stress, σ_x over the contact interface for different models. As it can be seen, there is a good correlation between all models. A slight deviation can be seen at the leading edge of contact, which in particular can be related to the value of Elastic Modulus of pad holder, stiffness of attached spring and the displacement that was applied to pad. However, at trailing edge of contact, which is also the region of interest for crack initiation formation, all of models give the same results. Figure 4.32 illustrates the distribution of tangential stress, σ_x in depth of 2 mm of fatigue specimen at x/a =1. This graph reveals that despite a slight difference between tangential stress, σ_x that was distributed over the contact interface, the tangential stress distributions at x/a= 1 beneath the contact line was completely matched for different models that were simulated in this study.

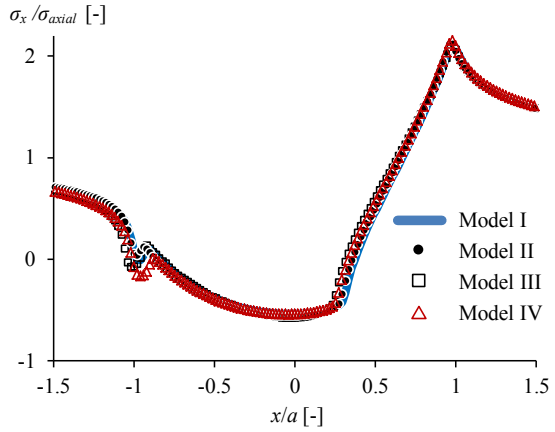

Figure 4.31: Compression between different FE models of fretting fatigue cylindrical contact configuration with different loading and boundary conditions.

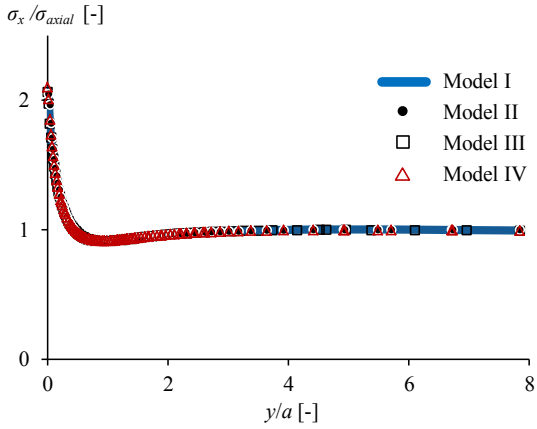

Figure 4.32: Comparison of tangential stress σ_x distribution in depth of 2 mm of fatigue specimen at x/a =1 (a= 0.18 mm) for different FE models.

Conformal contact

There is another type of fretting fatigue single clamp contact configuration, which consists of only one flat pad at each side of fatigue specimen without any compliance spring attached to the fretting pads. Despite the amount of relative slip is less than in the fretting-bridge configuration, it has proved to be sufficient to generate a fretting condition [Sabsabi et al., 2011]. Figure 4.33 illustrates a simple geometrical fretting fatigue configuration under conformal contact conditions. The symmetrical relative slip produced by this conformal contact configuration is at contact edges.

In conformal contact configurations, the nominal contact area is independent of the loading, F due to the abrupt change of the pad geometry, in contrast to non-conformal contacts, such as Hertzian contacts (cylindrical contact). The abrupt change in geometry typical of conformal contacts also exhibits four edges that behave as singular lines at the end of the contact area. Due to double symmetry conditions, a quarter 2-D FE model was simulated to represent the fretting fatigue test configuration, as schematically illustrated in Figure 4.33. The rectangle $L \times b$ corresponds to the analysed specimen and had a length of L= 4b= 20 mm, the half-width of the fretting pad a was 5 mm, and the distance between the contact interface and the point of the fretting pad at which normal loads were applied was 10 mm.

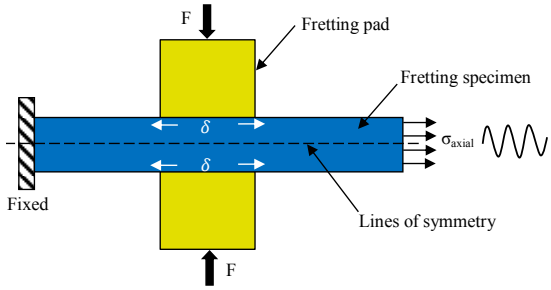

Figure 4.33: Schematic view of the fretting fatigue single clamp flat on flat (conformal) contact configuration.

A two-dimensional, 4-node (bilinear), plane strain quadrilateral, reduced integration element (CPE4R) was used. The mesh size of 5 μm $\times$ 5 μm was considered at the right end of the contact and decreased gradually far from the contact region. The contact between the fretting pad and the fatigue specimen was defined using a masterslave algorithm in ABAQUS®for contact between two surfaces. The bottom surface of the pad was defined as a slave surface and top surface of the specimen was defined as a master surface. Al 7075-T6 which was used for experimental tests from literature [Sabsabi et al., 2011], was selected for both the pad and the specimen with Modulus of Elasticity of E= 72.1 GPa and a Poisson's ratio of ν= 0.33. The Lagrange multiplier approach was included in the contact pair to enforce the contact constraints at the contact region. A Coulomb friction model with a coefficient of friction (COF) of 0.8 was used in this study [Sabsabi et al., 2011].

The loading sequence was applied in six steps. During the first load step, the normal load was increased up to a maximum value and kept constant for the remaining time steps. An axial stress σ_{axial} was applied from the second time step onwards, under reverse cyclic load (R_s= -1). Due to the non-linearity of the contact problem, loads were applied in sufficiently small time increments.

Due to the very small edge radius of the fretting pad and the relative high yield stress of the aluminium alloy, localized plastic deformation occurs at microscopic scale and fretting damage at contact interface is related to localized plasticity. Thus, enhanced fretting fatigue analyses are necessary. Therefore, in order to understand fretting fatigue crack nucleation process, a detailed study of the contact stress state and the localized plastic deformation at the contact

interface is important. Several plasticity models can be considered: elastic/perfectly plastic, isotropic strain and kinematic strain hardening. The FE results indicate that the quantity of plastic deformation was not much affected by the selection of material plasticity models. Moreover, Kindervater et al. [Kindervater et al., 2000] reported that material tests with Al 7075 and Al 2024 have not shown any sensitivity of the properties to the strain rate. Therefore, they have used elasto-plastic with isotropic hardening for their simulations. Based on the above reasons, a bilinear elasto-plastic constitutive equation, which defines an isotropic hardening with the von-Mises yield surface, was implemented to characterize the elasto-plastic response of the Al 7075-T6 subjected to fretting fatigue loading condition.

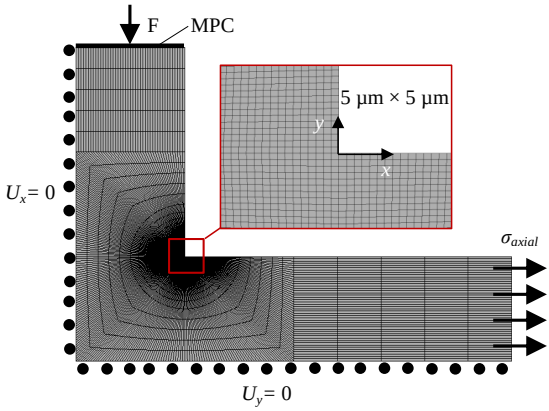

Figure 4.34: FE model of fretting fatigue single clamp flat contact configuration.

In order to monitor the stress distribution at the edge of the conformal contact configuration, the von-Mises stress distribution inside the specimen at maximum and minimum applied axial stress is depicted in Figure 4.35. From the figure, it can be seen that at maximum applied axial load (tension) the amount of existing plasticity is localized and a small scale yielding assumption can be applied. In contrast, at minimum applied axial load (compression) the amount of plastic deformation is relatively high (around 100 μm). This observation reveals that the effect of micro plastic deformation should be taken into account, when dealing with crack initiation lifetime prediction in case of conformal contact configuration.

Figure 4.36 illustrates the equivalent plastic strain (PEEQ) contour plots

at minimum and maximum applied axial load respectively at F= 8 kN and σ_{axial}= 190 MPa.

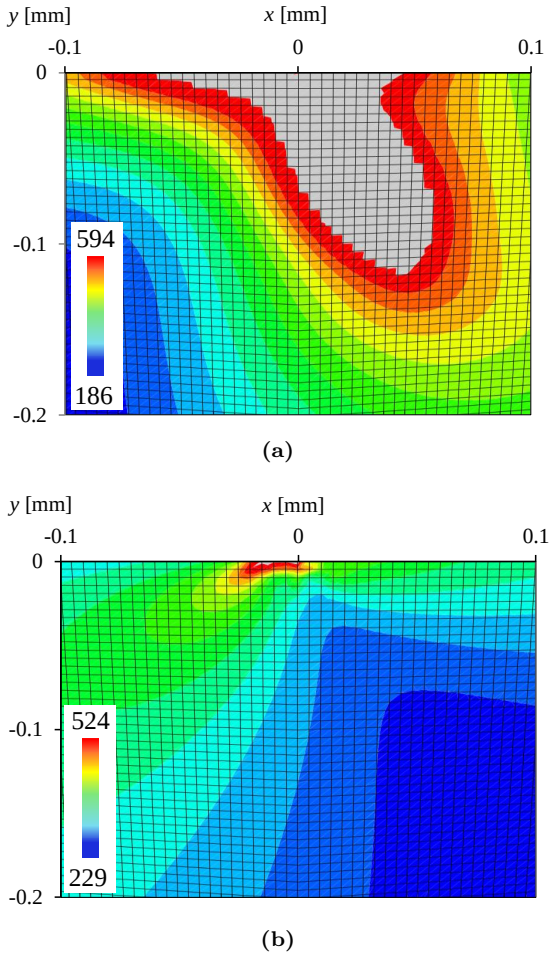

Figure 4.35: von-Mises stress distribution (in MPa) near the edge of contact for (a) compression and (b) tension axial loads for F= 8 kN and σ_{axial}= 190 MPa.

4.4 On fretting fatigue FE slip map

As mentioned above for the present complete contact configuration, the amplitude of slip is less than in other type of fretting fatigue contact configurations.

In this section the slip amplitude is monitored at contact interface in order to have clear idea about the effect of different fretting fatigue variables such as axial stress and contact load on fretting fatigue relative slip amplitude. For this purpose, five different axial stresses from 110 MPa to 190 MPa at three different contact loads i.e. 2, 4 and 8 kN were selected based on the experiments from literature that have performed by Sabsabi et al. [Sabsabi et al., 2011] for the same contact configuration.

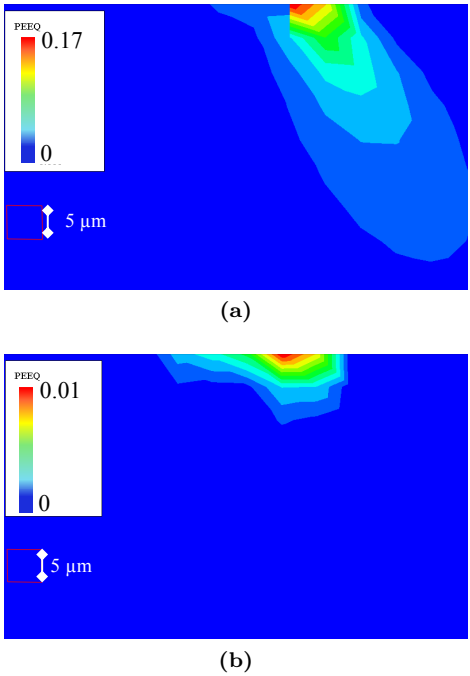

Figure 4.36: Contour plots of equivalent plastic strain (PEEQ)at (a) compression and (b) tension axial loads at F= 8 kN and σ_{axial}= 190 MPa.

Figure 4.37 (a) shows that slip amplitude at low axial stresses (i.e. 110 and 150 MPa) is almost zero regardless of contact load magnitude and the contact state is almost a sticking condition. By rising axial stress from 110 MPa to 190 MPa, as expected slip amplitude increases to about 0.08 μm which confirms that in this particular complete contact configuration the slip amplitude is less than other type of experimental configurations.

Moreover, these interesting results show that the effect of axial stress and

contact load on fretting fatigue slip amplitude is not linear. As expected slip amplitude rises almost in all cases by increasing axial stress. Figure 4.37 (b) illustrates the iso-contour plot of fretting fatigue FE slip map for conformal contact configuration.

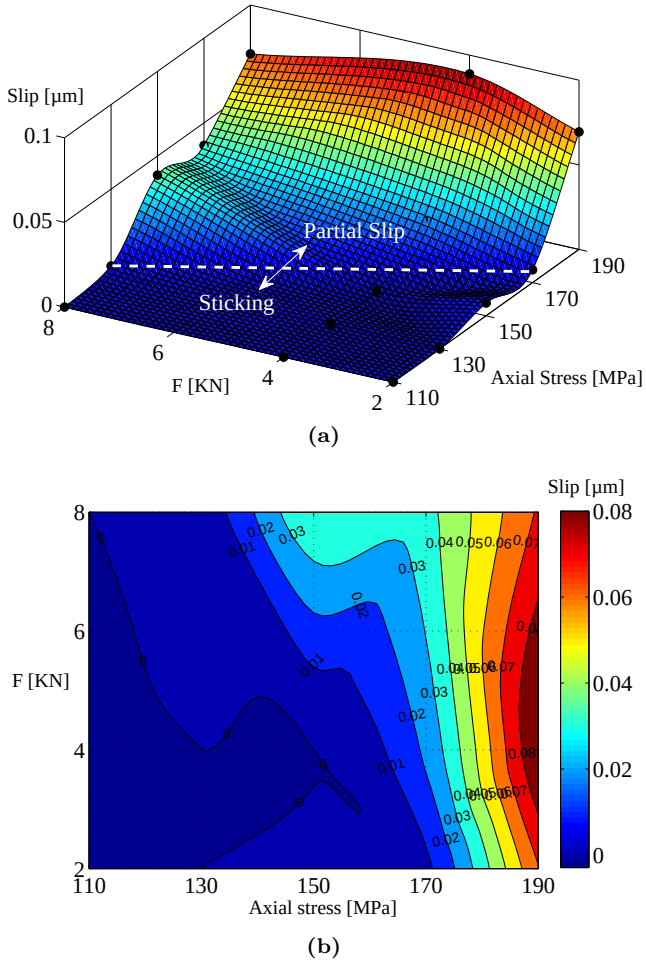

Figure 4.37: Variation of maximum slip amplitude versus axial stress and contact load for conformal contact configuration (a) 3-D contour plot (b) 2-D iso surface plot.

The local slip map, which can be obtained by numerical tool such as FE modelling approach can be used to select the proper combination of different axial stress and contact load to achieve the desired slip amplitude at contact

interface. As can be seen in Figure 4.37 (a) for the axial stresses and contact loads above line, the slip amplitude is high enough to be considered as partial slip regime. Otherwise, the contact condition is close to sticking. It is worth to mention that the concluded results are only valid for the given friction coefficient of 0.8 as mentioned above. A detailed study of the influence of friction coefficient for a conformal contact is given in [Giner et al., 2005].

As the role of local slip amplitude in fretting fatigue phenomenon is crucial, the same approach was implemented to single fretting fatigue single clamp cylindrical contact configuration, in order to study the effects of different fretting fatigue primary variables on local relative slip amplitude. For this purpose, a FE model of cylindrical contact, as illustrated in Figure 4.18, was developed using python programming language in ABAQUS®, for parametric study of effect of different primary variables on local slip amplitude. The radius of contact surface of pad was 25 mm. The specimen length, width and thickness were equal to 20 mm, 2 mm and 6.35 mm, respectively. Al 7075-T6 was used for both pad and specimen. The Lagrange multiplier of friction is included in the contact pair to define the friction behaviour of the contact region (μ= 0.5). The rest of model parameters were the same as elaborated earlier.

One approach to studying the interaction effects between two or more factors in an experimental program is known as factorial design. This efficient experimental strategy, which often falls under the more generic term 'design of experiments', calls for the variation of factors together with a final aim of relating the change in experimental response to the change in the factors. Often used in industrial research and development or process improvement, factorial design and subsequent statistical analysis of the experimental results can provide a method for quantitative identification of not only main effect of factors, but also any potential interaction between factors. In this study, after getting the output data from parametric study the effects of two of primary variables namely, axial stress and contact pressure on slip amplitude were investigated. This understanding will help us to choose appropriate boundary conditions for modelling the actual fretting fatigue problem in laboratory scale and numerical codes.

As mentioned, Python programming language was used for parametric study in order to investigate the effect of different primary variables and their interaction effects on local slip amplitude. To this end, four axial stresses (i.e. 30, 60, 90 and 150 MPa), seven contact loads (i.e. 5, 50, 300, 600, 900, 1200 and

1500 N) and constant 18 N tangential load were selected for FE simulations. In total with these variables 28 (4×7= 28) numerical simulations were performed. Eventually, MATLAB [MATLAB 7.12] code was used to post process the FE outputs for monitoring the interaction effect of primary variables on fretting fatigue local slip amplitude. For this purpose, for each FE model maximum local slip amplitude at contact interface was extracted for each combination of axial stress and contact load. Then, a surface was interpolated through these points at each axial stress and contact load.

Figure 4.38 shows the variation of maximum slip amplitude at contact interface versus contact load for different applied axial stresses. For all stress levels the local slip amplitude increase sharply from almost zero to certain value by rising the contact load from 5 to 50 N. After 50 N contact load, by increasing the contact load the slip amplitude increases high applied axial stress continuously, and for lower tested axial stresses (i.e. 30, 60, 90 MPa) the slip amplitude reaches a plateau up to 600 N contact load and increases gently till 1200 N. However, as can be seen from the Figure 4.38 by rising the contact load from 1200 to 1500 N the maximum local slip amplitude at contact interface drops for all applied axial stresses. Eventually, As expected by increasing the axial stress, the local slip amplitude rises.

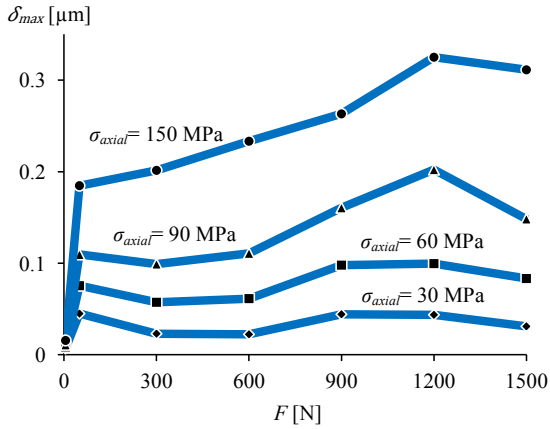

Figure 4.38: Variation of maximum slip amplitude versus contact load for different axial stresses in case of single clamp cylindrical contact configuration.

In order to find a fretting fatigue slip map a surface was fitted through each obtained data from FE models. Figure 4.39 (a) shows the 3-D contour

plot of variation of slip amplitude versus different axial stresses and contact loads. The same behaviour of conformal contact configuration can be seen for cylindrical contact. Figure 4.39 (b) illustrates the iso-contour plot of fretting fatigue slip map for single clamp cylindrical contact configuration. As also mentioned above this slip map helps to find the loading condition for fretting fatigue problem, which can lead to better understanding of its behaviour under different circumstances.

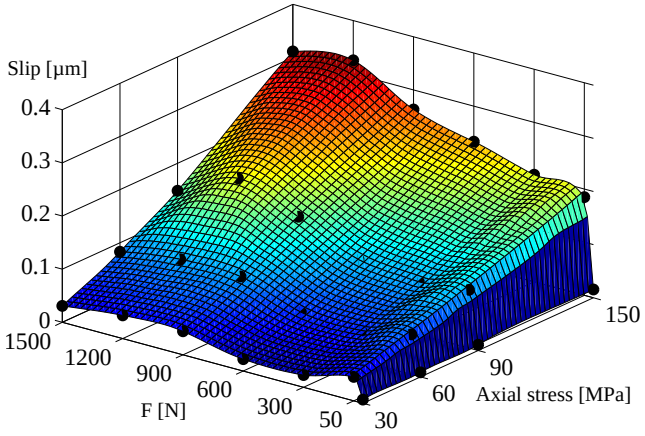

(a)

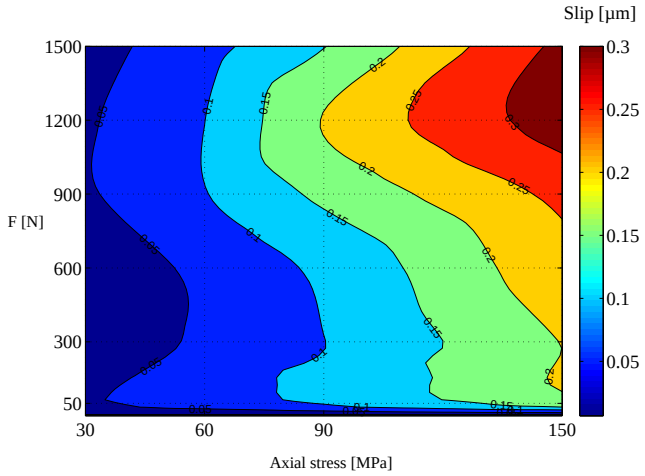

(b)

Figure 4.39: a) 3-D contour plot (b) 2-D iso-surface plot view of interpolated surface through different variation of local slip amplitude versus different applied axial stresses and contact loads

4.5 FEA of Bolted Lap Joints (BLJ)

As mentioned earlier and shown above FE modelling approach is convenient methodology to investigate behaviour of fretting fatigue contact under different contact conditions. Therefore, using FE approach enhances the possibility to easily study more details compared to performed tests in a laboratory such as the distribution of slip at contact interface under different loading conditions. To this end, the preceding section focuses on characterising fretting fatigue behaviour of SBLJ and DBLJ by means of 3-D FE modelling approach. In order to model SBLJ and DBLJ, a few simplifications were made which may not cause any significant effect on the results. These simplifications can be listed as:

- A circular shape was used for the nut and bolt head. The socket shape of the bolt head was ignored.
- The washers were tied to the bolt head and nut because of having the same material elastic properties.
- Modelling of the bolt threads was ignored as there is no contact between threads and inner surface of hole.

4.5.1 Single Bolted Lap Joint (SBLJ)

A SBLJ model was generated using ABAQUS®software. One half of experimental configuration needs to be model due to symmetry condition with respect to x-y plane in terms of both the geometry and loading. The model included two identical plates of Al alloy 2024-T3, with a thickness of 4 mm and a 8.25 mm diameter hole as well as a M-8 steel bolt to clamp the plates. The dimensions of the modelled Al plates were the same as performed SBLJ static test in Chapter 3. Isotropic material properties with elastic behaviour were defined to all components. Steel bolt, nut, load cell bush and washers with an elastic modulus of E= 210 GPa and a Poisson's ratio of ν = 0.33 and material properties with an elastic modulus of E= 72.4 GPa and a Poissons ratio of ν = 0.33 was set for properties of the Al plates.

Figure 4.40 illustrates 3-D FE model of SBLJ along with the applied loading and boundary conditions, the same as static experimental set-up of SBLJ described in Chapter 3. The model consists of five different parts: two Al plates, three washers, bolt, nut and bushing load cell. Symmetric displacement

boundary conditions were applied to the nodes on the symmetry planes. The loads were applied in two steps. Clamping contact load (F_{cl}) was applied in the first step to establish contact between contact pairs. In the second step axial stress was applied to the right side of Al plate. During the first step all three translational degrees of freedom (DOFs) at both left and right sides of the Al plates were restrained during applying clamping load. After applying clamping load the constraints at the right side of Al plate were removed and the axial load was applied instead as shown in Figure 4.40. 3-D structural 8-node linear brick, reduced integration, hourglass control (C3D8R) elements were used with the master-slave contact algorithm on the contact surface between Al plates interface, Al plates and the washers. The rest of contact pairs defined as a tie constant to reduce the computation time. As the vicinity of the bolt hole was the critical zone to be analysed, density of the mesh was appropriately refined in this region as shown in Figure 4.40. The minimum mesh size at contact interface was 0.1 mm and increased gradually far from contact.

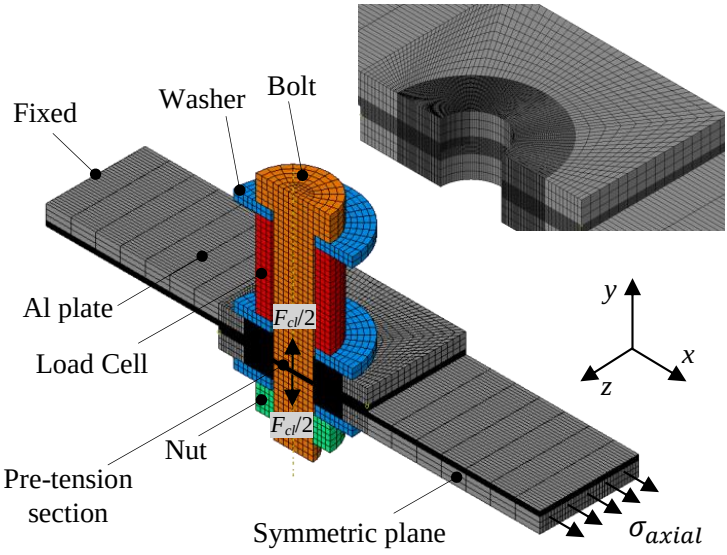

Figure 4.40: FE model of SBLJ along with the applied loading and boundary conditions.

A small sliding contact condition was used between the contact pair to transfer loads between the two bodies. The connecting contact surfaces were defined as a contact pair that enabled ABAQUS®to determine if the contact

pair was touching or separated. The contact region consisted of stick and slip regions under fretting fatigue loading condition. The stick region did not have a relative movement between contact surfaces. The slip region showed a small relative movement between contact surfaces on interface between two Al plates which is commonly observed in a fretting fatigue experiments. The penalty of friction was included in the contact pair to define the friction behaviour of the contact region as the Lagrange multiplier of friction did not converge in this particular SBLJ model. The coefficients of friction μ= 0.71 and μ= 0.2 were considered in this study for Al plates pairs and washer to Al plates, respectively.

In order to apply clamping load (F_{cl}) a pre-tension section in the bolt was defined as shown in Figure 4.40. When modelling the bolt with solid elements, the pre-tension section is defined as a surface in the bolt shank that effectively partitions the bolt into two regions. In continuum elements the pre-tension section is defined as a surface inside the fastener that "cuts" it into two parts. The pre-tension section can also be a group of surfaces for cases where a fastener is composed of several segments. Therefore, in the FE model the clamping load applied by applying a concentrated load, which is a self-equilibrating force carried across the pre-tension section in the bolt shank, to the pretension nodes.

Fretting fatigue behaviour of SBLJ

Before investigation fretting fatigue behaviour of SBLJ it is essential to validate the FE model versus experimental results. Figure 4.41 illustrates the variation of axial load versus displacement for both FE model and static experimental test. As mentioned in Chapter 3 (section 3.3.2), the COF$\approx$ 0.4 was measured for SBLJ under static condition. For this purpose the FE model was simulated for both COFs i.e. 0.4 and 0.71 and compared to the experimental results. As can be seen from Figure 4.41, there is good correlation between both FE models and experimental results. The slight discrepancy between two FE models with different COFs reveals that the joint with COF= 0.4 slips sooner, when compared with COF= 0.71.

Figure 4.42 depicts the von-Mises stress contour plot for assembly view SBLJ including blot, nut, washers, bushing load cell and Al plates. The figure shows the critical areas, at which the stress gradient is high. Since the whole joint is subjected to bending, the maximum stress appears in bolt and by increasing the axial load the bolt faces the shearing failure mode as discussed in Chapter 3.

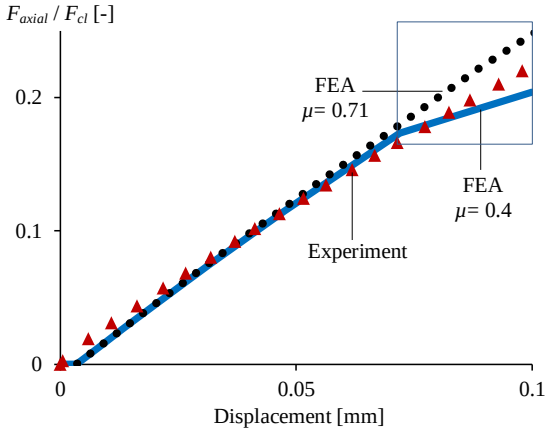

Figure 4.41: Comparison between FE models with two COF (i.e. 0.4 and 0.71) and experimental results for F_{cl}= 14 KN.

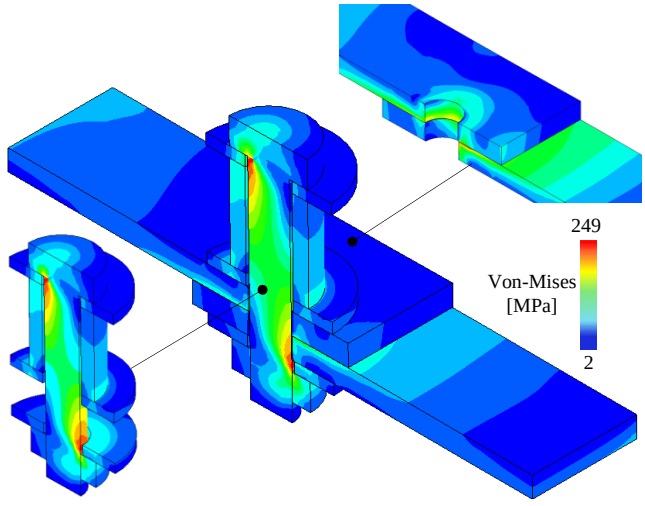

Figure 4.42: von-Mises stress contour plots for assembly view SBLJ.

Figures 4.43 (a) and (b) show the distribution of tangential and maximum principle stresses at contact interface between two Al plates. The high stress gradient is located at some distance from the hole near the contact edge (i.e. the side that the axial stress applied), which is also the potential location of initial crack in experimental results as reported in [Wagle and Kato, 2009]. Figure 4.43 (c) indicates that the maximum frictional shear stress happens at

almost the same distance as the maximum principle stress. Figure 4.43 (d) illustrates that the contact interface between two connected Al plates can be divided in three distinguished region namely, sticking, slipping and gapping.

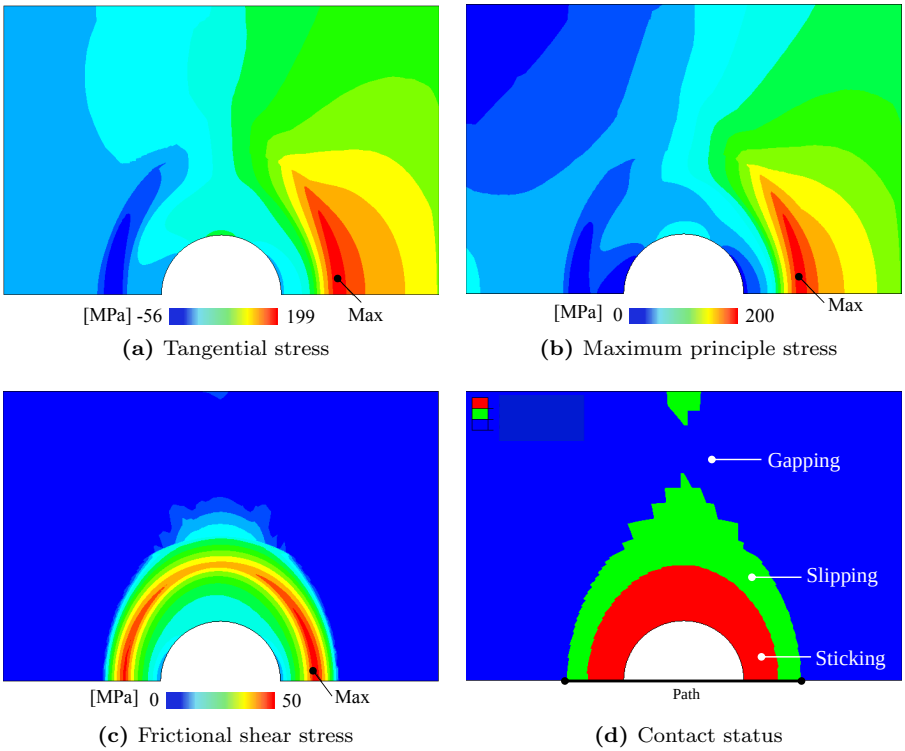

(a) Tangential stress **(b)** Maximum principle stress

(c) Frictional shear stress **(d)** Contact status

Figure 4.43: Stress distribution at contact interface for SBLJ subjected to fretting fatigue loading condition at σ_{axial}= 20 MPa, F_{cl}= 14 kN and μ= 0.71.

Figure 4.44 (a) illustrates the variation of normalized frictional shear stress distribution versus the normalized contact distance with respect to hole radius over symmetric line at contact interface between Al plates (see Figure 4.43 (d)). The variation of shear stress confirms that the contact status is sticking near both hole edges and slipping at both contact edges. Figure 4.44 (b) indicates that as expected by increasing the axial stress from 20 MPa to 35 MPa, the contact situation is shifting from partial slip regime (PSR) to gross sliding condition (GSR). Figure 4.45 shows the variation of contact status for FE model of SBLJ by showing the slip distribution over entire contact between Al plates. As figure shows by increasing the axial load (applied axial stress)

the contact condition transfers from partial slip to gross sliding regime.

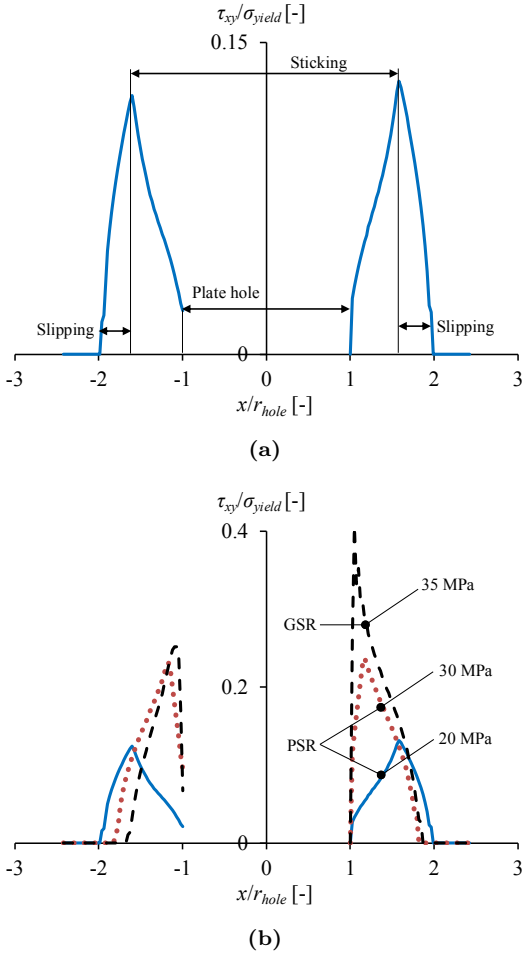

Figure 4.44: Variation of frictional shear stress at contact interface between Al plates at different axial stresses for F_{cl}= 14 kN and μ= 0.71.

Figure 4.46 depicts the variation of tangential stress at contact interface between two Al plates. The shape of stress distribution is comparable to tangential stress distribution for fretting fatigue single clamp cylindrical contact configuration. The maximum stress appears near contact edge and as expected increases by rising the applied axial stress.

As mentioned earlier the stress state is multiaxial for contact problems sub-

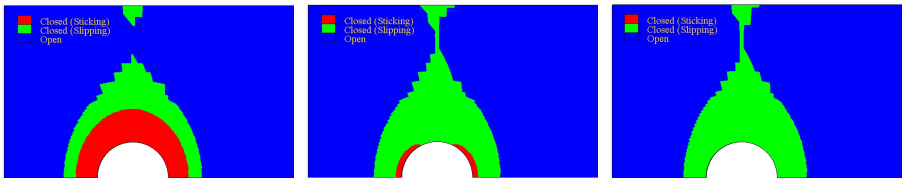

(a) σ_{axial}= 20 MPa **(b)** σ_{axial}= 30 MPa **(c)** σ_{axial}= 35 MPa

Figure 4.45: Variation of contact status over entire contact interface between Al plates for different applied stress at F_{cl}= 14 KN and μ= 0.71.

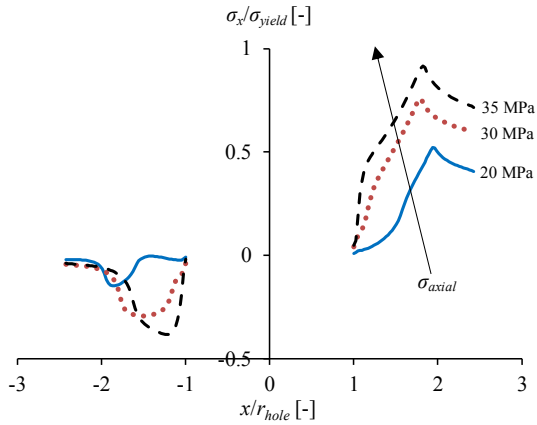

Figure 4.46: Variation of tangential stress distribution versus displacement for different applied axial stress at F_{cl}= 14 kN and μ= 0.71.

jected to fretting fatigue loading condition. Therefore, by assuming that the damage causing stress is the equivalent multiaxial damage stress, the location of initial crack can be related to the location of maximum value of equivalent multiaxial damage stress (σ^*) at contact interface between two Al plates. More detailed information and validation of this criterion will be elaborated in Chapter 5. Figures 4.47 (a) and (b) show the normalized equivalent multiaxial damage stress contour plot at contact interface between two Al plates and location of fretting fatigue crack initiation in SBLJ specimen for the same material taken from [Wagle and Kato, 2009], respectively.

As can be seen from Figures 4.47 (a), the maximum location of σ^* predicts the location of crack near the edge of contact, which is in good agreement with the experimental observation from literature [Wagle and Kato, 2009]. Nonethe-

less, to find the exact location of initial crack the same loading and boundary conditions as the experimental test should be applied to the developed FE model for SBLJ.

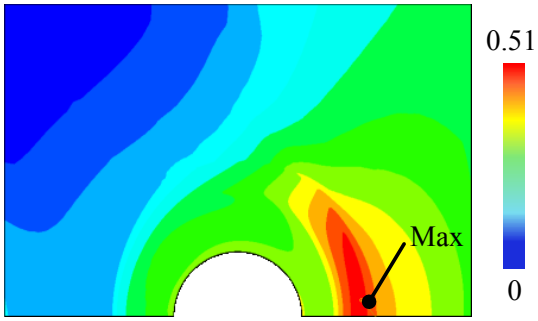

(a) σ^*/σ_{yeild}

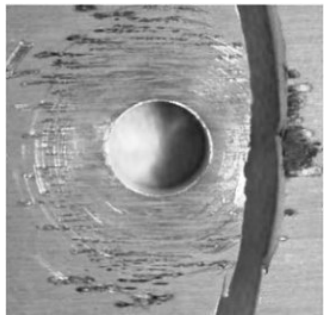

(b) Fretting fatigue initial crack location of SBLJ after [Wagle and Kato, 2009]

Figure 4.47: (a) Predicted location of initial crack in SBLJ connection subjected to fretting fatigue loading condition using FE approach at σ_{axial}= 20 MPa, F_{cl}= 14 kN and μ= 0.71, compared with the (b) experimental result.

4.5.2 Double Bolted Lap Joint (DBLJ)

Figure 4.48 depicts 3-D FE model of DBLJ along with the applied loading and boundary conditions. As shown in the figure, the model consists of three different parts: Al plates, bolt and washers. Only one-quarter of the experimental set-up explained in Chapter 3 was modelled due to double symmetry with respect to the x-y and x-z planes. The same material properties as used for SBLJ were implemented to DBLJ.

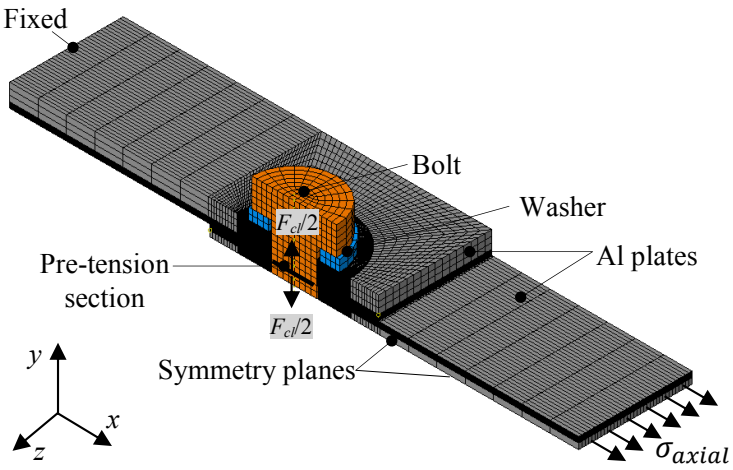

Figure 4.48: FE model of DBLJ along with the applied loading and boundary conditions.

The loads were applied in two steps, clamping contact load (F_{cl}) was applied in the first step to establish contact between contact pairs. In the second step axial stress was applied to the right side of Al plate. During the first step all three translational degrees of freedom (DOFs) at both left and right sides of the Al plates are restrained during applying clamping load. After applying contact load the constraints at the right side of Al plate were removed and the axial load was applied instead as shown in Figure 4.48.

3-D structural 8-node linear brick, reduced integration, hourglass control (C3D8R) elements were used with the master-slave contact algorithm on the contact surface between Al plates interface and Al plates and the washers. The rest of contact pairs defined as a tie constants to reduce the computation time. The minimum mesh size at contact interface was 0.1 mm and increased gradually far from contact. The penalty of friction was included in the contact pair to define the friction behaviour of the contact region. The coefficients of friction μ= 0.71 and μ= 0.2 were considered in this study for Al plates pairs and washer to Al plates, respectively.

Fretting fatigue behaviour of DBLJ

Figure 4.49 illustrates the comparison between FE model of DBLJ and experimental results. From the figure it can be seen that the the variation of axial

load versus the displacement from the FE model shows good correlation with the experimental one.

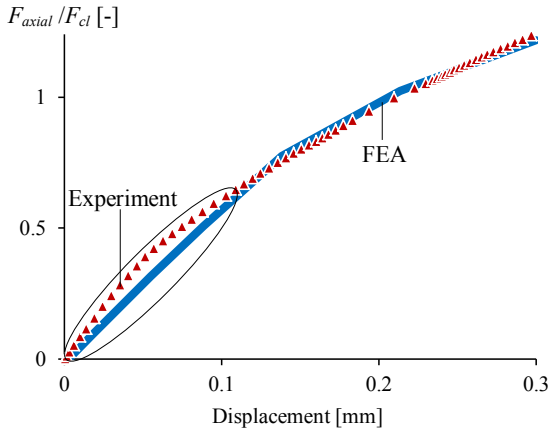

Figure 4.49: Comparison between FE model of DBLJ and experimental results for F_{cl}= 14 kN and μ= 0.71.

It is worth to mention that, the COF used in the model was based on the experimental measurement as elaborated in Chapter 3. It does not reflect any non-linearity of the COF during the test, which may be present depending on the state of the contact surfaces, in particular size of asperities and level of changes of the roughness due to contact pressure. Thus, it is very likely in an experiment that the COF is not constant. This micro mechanism was not considered in the FE model and not further investigated. The friction between two surfaces was modelled at macro level, which may explains the slight discrepancy in stiffness between FEA and experiments at the early stage of loading as highlighted in Figure 4.49.

Figures 4.50 (a) and (b) show the distribution of tangential and maximum principle stresses at contact interface between two Al plates. As it can be noted the same as SBLJ connection, the the high stress gradient is located at some distance from the hole near the contact edge (i.e. the side where the axial stress applied), which is also the potential location of initial crack in experimental results as shown in Chapter 3. Figure 4.50 (c) indicates that the maximum frictional shear stress happens at almost the same distance as the maximum principle stress. Figure 4.50 (d) reveals that the same as other fretting fatigue contact configuration under partial slip regime, three different contact status

can be distinguished at contact interface namely, sticking, slipping and gapping.

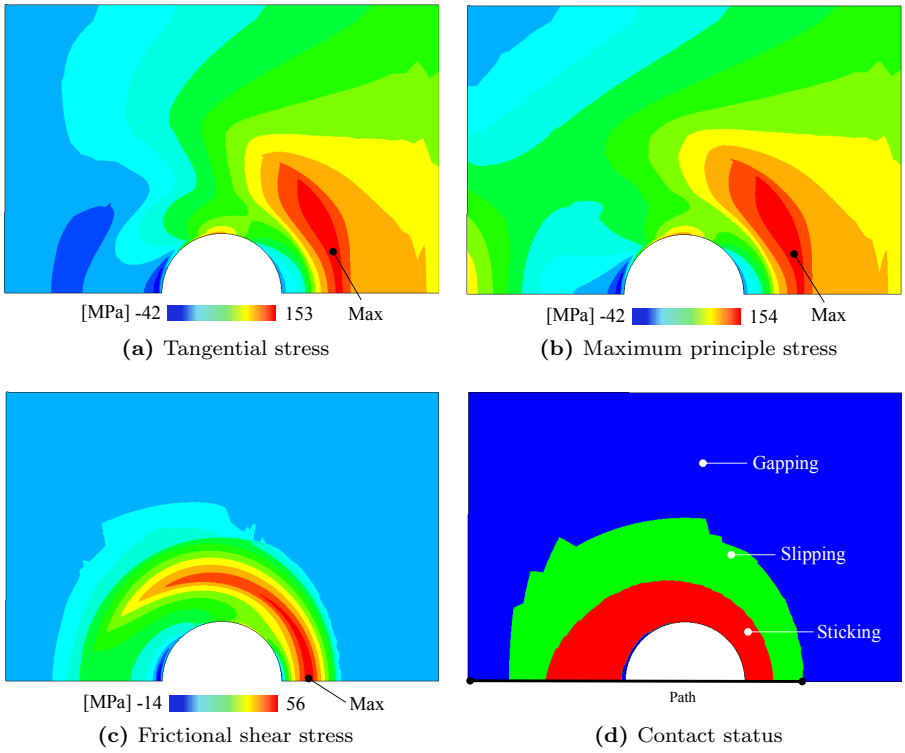

(a) Tangential stress **(b)** Maximum principle stress

(c) Frictional shear stress **(d)** Contact status

Figure 4.50: Stress distribution at contact interface for DBLJ subjected to fretting fatigue loading condition at σ_{axial}= 78.5 MPa (F_{axial}= 14 kN), F_{cl}= 16 kN and μ= 0.71.

Figure 4.51 illustrates the variation of normalized frictional shear stress distribution versus the normalized contact distance with respect to hole radius over symmetric line at contact interface between Al plates (see Figure 4.50 (d)). The variation of shear stress confirms that the contact situation is sticking near both edges of hole and slipping near both edges of the contact line. As expected by increasing the applied axial stress from 45 MPa to 78.5 MPa the maximum shear stress at contact interface rises. However, the contact condition stays under partial slip regime as also depicted in Figure 4.50 (d).

Figure 4.52 shows the variation of tangential stress at contact interface between two Al plates for DBLJ connection. The maximum stress appears near the contact edge. From the figure it can be seen that the maximum

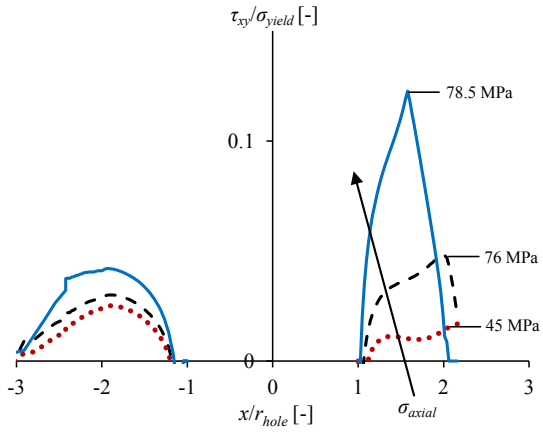

Figure 4.51: Variation of frictional shear stress at contact interface between Al plates at different axial stresses for F_{cl}= 14 kN and μ= 0.71.

tangential stress rises as the applied axial stress increases.

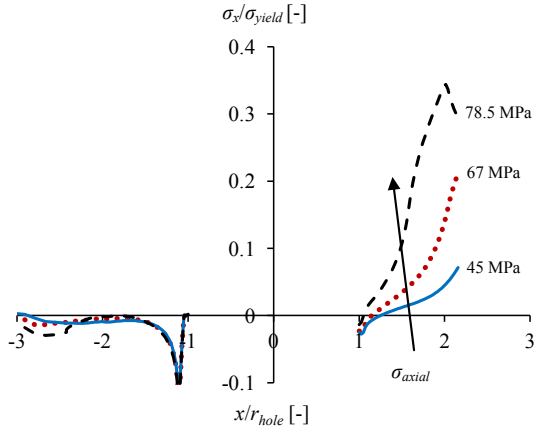

Figure 4.52: Variation of tangential stress distribution at contact interface between Al plates at different axial stresses for F_{cl}= 14 kN and μ= 0.71.

Figure 4.53 compares the location of initial crack between predicted FE result and the experimental observation for DBLJ connection subjected to fretting fatigue loading condition. As mentioned for SBLJ model, by assuming the equivalent multiaxial damage stress as the damage causing stress, the location of initial crack can be related to the location of maximum value of equivalent

multiaxial damage stress (σ^*) at contact interface between two Al plates. Figure 4.53 shows the normalized σ^* contour plot at contact interface between two Al plates. By comparing the FE results with the experimental observation, it can be found the predicted location of crack is almost in good agreement with the experimental results as depicted in Figure 4.53.

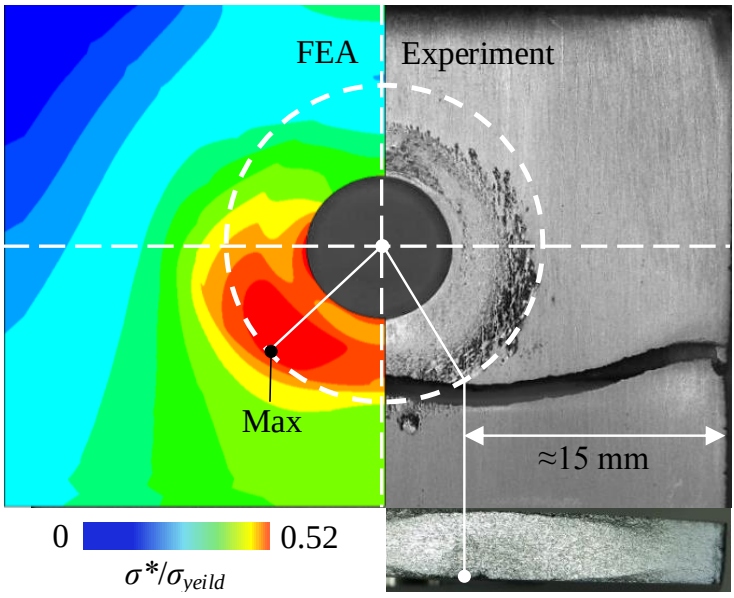

Figure 4.53: Comparison between fretting fatigue initial crack location predicted by FE approach and observed in experimental test for DBLJ connection at F_{cl}= 16 kN, σ_{axial} = 78.5 MPa and μ= 0.71.

These interesting results confirm that the FE modelling approach can be used to characterise contact behaviour of SBLJ and DBLJ subjected to fretting fatigue loading condition. Therefore, FE models can be developed further in order to investigate fretting fatigue crack initiation and propagation for more complex geometries such as SBLJ and DBLJ connections.

4.6 FEA of washer-disc contact

As shown and discussed in Chapter 3, from experimental observation it can be seen that fretting fatigue failure can be main cause of failure of disc in washer-disc contact configuration of shock absorber's piston valve. However,

the same as other fretting fatigue contact problems damages and micro cracks are hidden between two connected surfaces. Therefore, FE modelling approach can be used to monitor the stress and slip distribution at contact interface between washer-disc contact configuration, which results in understanding of fretting fatigue behaviour of this type of contact configuration.

Figure 4.54 illustrates the simplified FE model of washer-disc contact configuration of the shock absorber piston valve configuration as elaborated earlier in Chapters 1 and 3. The FE model consists of four parts, namely disc, M-disc, piston block and washer, as shown in Figure 4.54. The geometries of disc and washer were the same as shown in Chapter 3 with 0.1 and 0.3 mm thickness, respectively. The piston block was selected as part of piston valve, which M-Disc, disc and washer are pushed against it by tightening the piston nut. Figure 4.55 shows the geometry of metering disc (M-disc) that is used inside the piston valve of shock absorber.

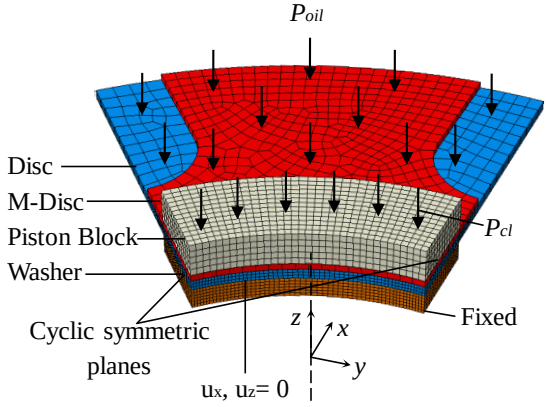

Figure 4.54: FE model of washer-disc contact of shock absorber piston valve along with the loading and boundary condition.

Due to cyclic symmetry boundary condition it was not necessary to model the entire washer-disc contact configuration but rather only one-eight of full configuration was modelled. Cyclic symmetry occurs when the geometry, loads, constraints and results of a partial model can be copied around an axis in order to give the complete model. Thus, the result is a smaller analysis which takes less time to analyse. Using the cyclic symmetry capability in ABAQUS®, the nodes on the two cyclically symmetrical faces were coupled or tied as shown

in Figure 4.54. This allows out of plane motion (unlike planar symmetry constraints) and was therefore valid for representing a cyclically repeating segment of the M-disc. The bottom side of washer was fixed and restricted from movement in all directions. The inner surfaces of all components were in contact with piston rod, which was not modelled, therefore, these surfaces just were allowed to move in z-driction.

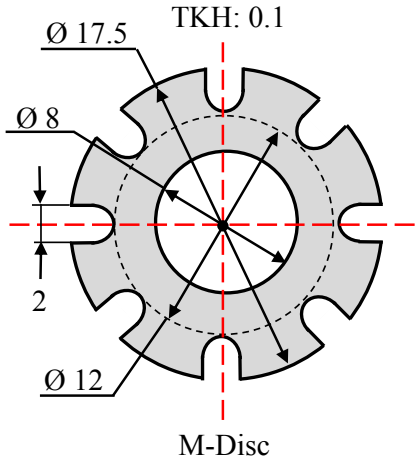

Figure 4.55: Geometry of metering disc (M-disc).

3-D structural 8-node linear brick, reduced integration, hourglass control (C3D8R) elements were used along with the master-slave contact algorithm on the contact surface between the washer and disc. The rest of contact pairs defined as a tie constants to reduce the computation time. Mesh density was appropriately refined at contact interface between washer and disc. The minimum mesh size at contact interface was 50 μm and increased gradually far from contact. A small sliding contact condition was used between the contact pair to transfer loads to the washer-disc contact surface. The connecting surfaces were defined as a contact pair that enabled ABAQUS®to determine if the contact pair was touching or separated. The penalty of friction was included in the contact pair to define the friction behaviour of the contact region. In practice, in the production line the components of piston valve are assembled without any lubrication and after applying the clamping pressure the washer and disc sticks to each other. Nonetheless, after assembling the final shock absorber the whole piston valve is floated inside the shock absorber oil. Therefore, the

contact between washer and disc was considered to be lubricated. Thus, the COF of μ= 0.15 was considered in this study as suggested for lubricated steel to steel contact in [Van Beek, 2013].

The loads were applied in two steps. First the clamping pressure applied on top of piston block in order to stablish the contact between the washer and the disc. Second, the oil pressure was applied on top of M-disc and disc in order to simulate the rebound cycle. The magnitude of clamping and oil pressure were selected as 10 and 0.2 MPa, respectively, as used in [Liang et al., 2012].

4.6.1 Fretting fatigue behaviour of washer-disc contact

In order to characterise fretting fatigue behaviour of washer-disc contact configuration, different stress distribution at contact interface were monitored. Figure 4.56 depicts the von-Mises stress distribution of assemble view of washer-disc contact with deformation scale of 50. The maximum stress appears at contact surface between washer and disc.

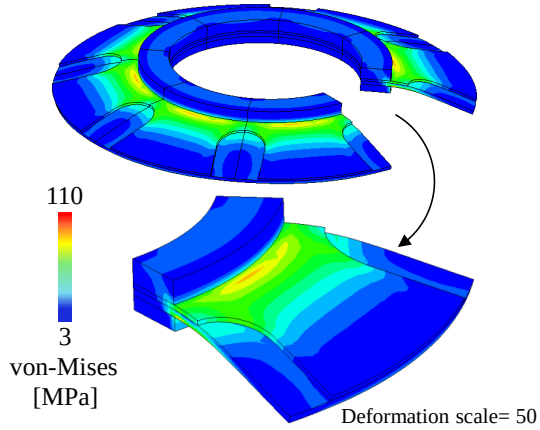

Figure 4.56: von-Mises stress distribution of washer-contact configuration.

Figure 4.57 (a) illustrates the contact status at contact interface between washer and disc. As shown the narrow slipping band occurs at contact edge and the rest of contact area was sticking. Figure 4.57 (b) shows the variation of shear stress distribution at contact interface. As expected the maximum shear stress appears near contact edge inside slipping band. However, the

maximum value of shear stress is low due to low COF, defined between two contact surfaces for the applied loading conditions.

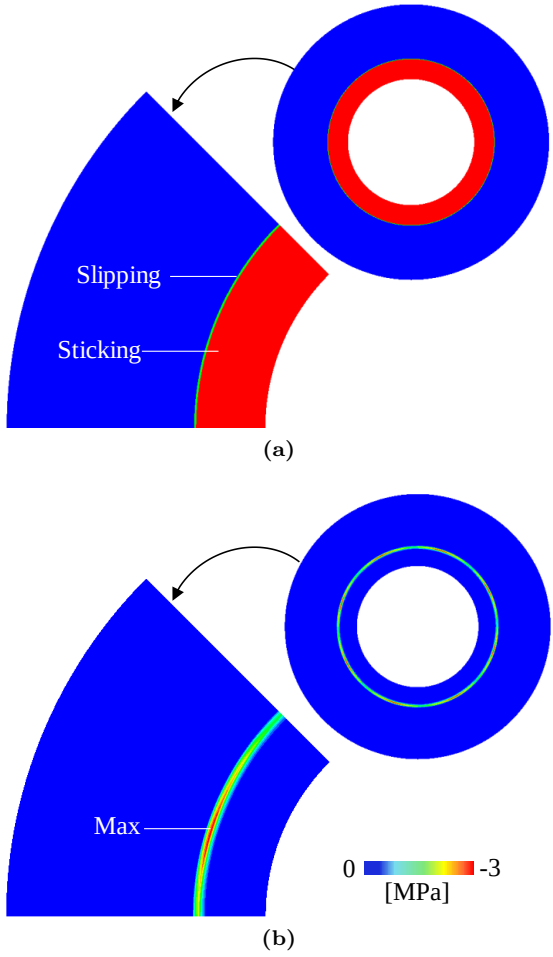

Figure 4.57: (a) Contact status and (b) frictional shear stress distribution at contact interface between washer and disc.

Figures 4.58 (a) and (b) indicates the variation of normalized contact pressure and frictional shear stress distribution with respect to clamping pressure (P_{cl}) versus the normalized contact distance with respect to radius of washer (r_w) at centre of modelled segment of full contact configuration. Figure 4.58 (a) shows that by increasing the applied oil pressure from 0.2 to 1 MPa, the maximum contact pressure rises. It is also worth to mention that in experi-

mental test different oil pressures can be achieved by testing at different speeds (different test frequencies). The maximum location of peak pressure occurs at contact edge and stays the same as the oil pressure increases. Figure 4.58 (b) depicts that by rising the applied oil pressure the maximum frictional shear stress increases and for all applied pressures the stick-slip regime stays the same.

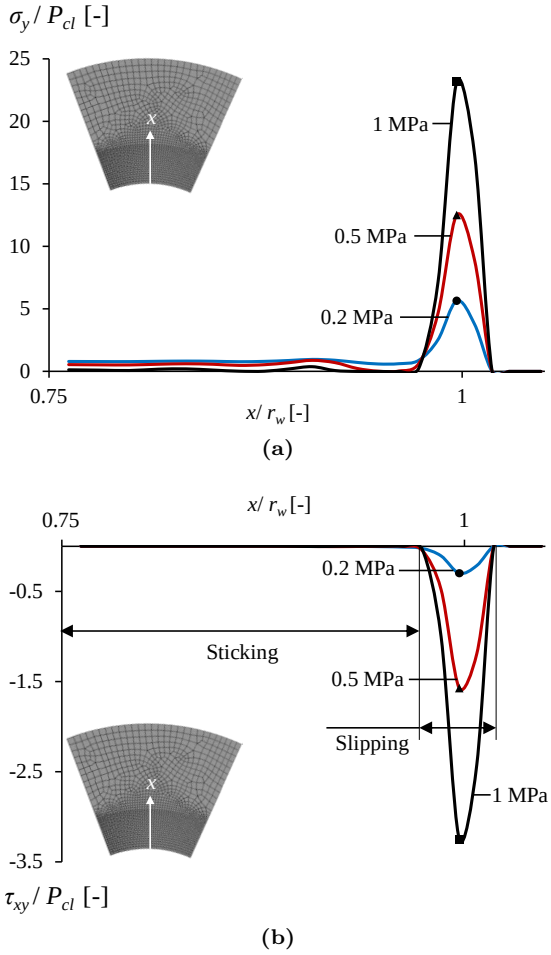

Figure 4.58: Normalized (a) contact pressures and (b) frictional shear stress distribution at contact interface between washer and disc.

To estimate the location of initial crack, the same criterion was used as elaborated above. In order to do so, it was assumed that the equivalent multiaxial

damage stress is the damage causing stress. The location of initial crack can be related to the location of maximum value of equivalent multiaxial damage stress (σ^*) at washer-disc contact interface. Figure 4.59 compares the location of initial crack between predicted FE result and the experimental observation for washer-disc contact configuration. By comparing the FE results with the experimental observation, it can be found the predicted location of crack is in good agreement with the experimental result.

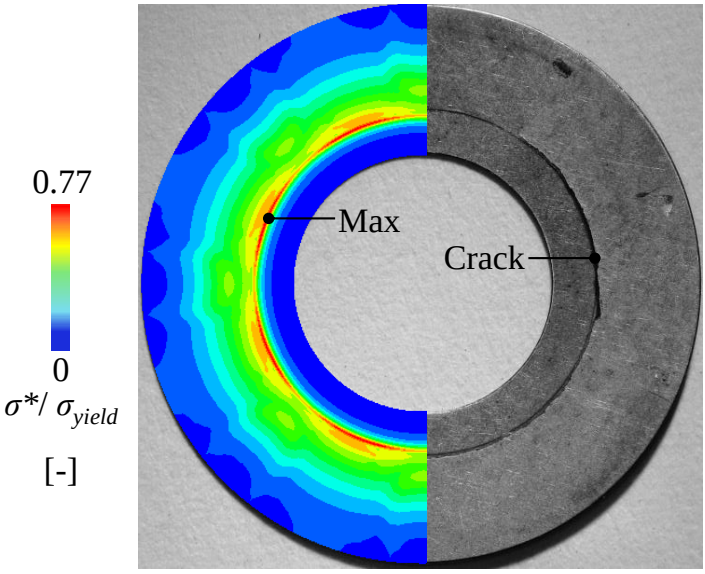

Figure 4.59: Comparison of location of initial crack between observed experimental result and predicted FE approach at P_{cl}= 10 MPa, P_{oil} = 1 MPa and μ= 0.15.

Figure 4.60 illustrates the variation of normalized equivalent multiaxial damage stress respect to applied clamping pressure for different applied oil pressures. By increasing the applied oil pressure the maximum value of equivalent multiaxial damage stress rises. Moreover, the location of maximum value of σ^* is located at contact edge for all applied oil pressures. These results reveal that all fretting fatigue characteristics can be found in washer-disc contact configuration and more important the FE modelling approach is capable of monitoring these features.

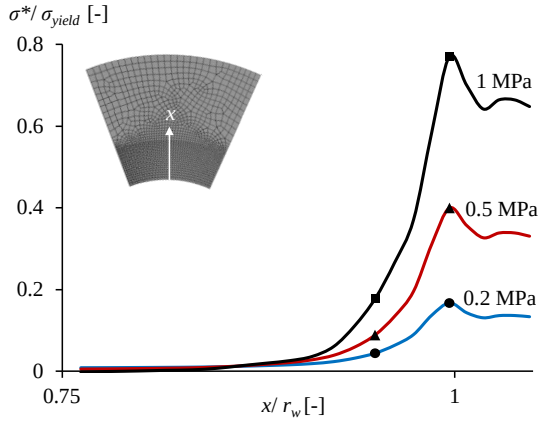

Figure 4.60: Variation of normalized equivalent multiaxial damage stress versus normalized contact distance.

4.7 Summary and conclusions

In this chapter, different categories of fretting fatigue FE contact models were simulated in different groups based on experimental test configurations. These groups were namely, FEA of fretting contact, FEA of fretting fatigue contact and FEA of practical applications including bolted lap joints (SBLJ and DBLJ) and washer-disc contact configuration of shock absorber. It was shown that the use of finite element analysis is a convenient method to study the behaviour of structures or details of structures subjected to fretting fatigue loading condition. It was revealed that using FE modelling approach gives extra information such as local relative slip and stress distributions at contact interface, which is not possible to be monitored using experimental approaches.

Using developed fretting fatigue contact models, effects of different loading conditions on fretting relative slip amplitude at contact interface were investigated for single clamp flat and cylindrical contact configurations. Based on the FE models a parametric study was done in order to find the interaction effects of two primary variables namely, axial stress and contact force, on fretting fatigue FE slip amplitude. To this end, a fretting fatigue slip map was proposed based on the FE model that can be used for monitoring the local slip amplitude and consequently, choosing right fretting fatigue parameters for performing experimental tests. Furthermore, it is possible to extend this method to investigate more about interaction effects of different primary and secondary

variables of fretting fatigue on local slip amplitude, which play a significant role in fretting fatigue contact problem.

Eventually, fretting fatigue behaviour of SBLJ, DBLJ and washer-disc contact configuration was monitored. It was found that FE modelling approach enhances the possibility to easily investigate more details compared to performed experimental tests in a laboratory and practical applications such as the distribution of relative slip amplitude, contact pressure or stresses at contact interfaces. It was shown that once the FE model is calibrated with help of experimental test or other calculation methods such as analytical one, it even offers the great capability of performing large parametric studies to check the influence of different parameters on behaviour of different structures subjected to fretting fatigue loading condition.

Chapter 5

FEA of fretting fatigue crack initiation

"In this chapter Continuum Damage Mechanics (CDM) approach is introduced to find a predictor tool to estimate fretting fatigue crack initiation lifetime under elastic and elasto-plastic conditions."

5.1 Overview

As mentioned earlier in general, fretting fatigue failure process can be divided into two main portions, namely crack initiation and crack propagation. Fretting fatigue crack initiation characteristics are very difficult to detect because damage such as micro-cracks is always hidden between two contact surfaces.

In this chapter Continuum Damage Mechanics (CDM) approach is used to find a predictor tool for fretting fatigue crack initiation lifetime. For this purpose, uncoupled damage evolution law is developed to model fretting fatigue crack initiation lifetime under elastic and elasto-plastic condition. In order to find the location of initial crack two different approaches, namely, stress and energy based methodologies are discussed. The suggested criteria are implemented to experimental tests for single clamp cylindrical contact configuration from Chapter 3.

In addition, the FE modelling approach was used to monitor the effect of different fretting fatigue primary variables on localized plasticity in an Aluminium alloy (Al 2024-T3) test specimen. A bilinear elasto-plastic isotropic hardening model with a von-Mises yield surface was implemented to simulate the material behaviour of the Aluminium alloy. Moreover, the effect of different fretting fatigue primary variables, such as axial stress, contact geometry, and COF, on localized plasticity was investigated. Eventually, the relationship between the location of maximum localized plasticity and Ruiz fretting damage parameter with the crack initiation site is discussed.

5.2 Developing uncoupled damage model

The background of Continuum Damage Mechanics (CDM) approach was elaborated in Chapter 2 (section 2.3.2). According to Lwemaitre [Lemaitre, 1985], the usual way to predict the conditions of failure in structural condition can be performed in three steps as below:

1. The stress and strain fields are first calculated with elastic or plastic constitutive equations. For instance, by means of FE modelling approach.

2. In a second step, the obtained results are used to calculate the condition of macro-crack initiation with help of damage constitutive equation. For instance, the number of cycles to fretting fatigue crack initiation.

3. Eventually, the growth of crack through the structure by means of fracture mechanics approach, using concepts of stress intensity or strain energy release rate.

Based on these steps, it is assumed implicitly that the state of damage of the structure does not influence the sate of stress or strain. Therefore, there is no coupling between damage initiation and propagation of damage, as the propagation part is performed using fracture mechanics approach. Thus, in this section the uncoupled damage modelling approach is introduced to predict fretting fatigue crack initiation lifetime for both elastic and elasto-plastic material behaviour.

5.2.1 Under elastic condition

A high cycle fatigue damage evolution law can be derived from a dissipation potential function Equation 2.77 (section 2.3.2). By hypothesizing the elastic behaviour of material, the dissipation potential function φ can be written based on *thermodynamics force*, $\dot{Y}$ as introduced by Lemaitre [Lemaitre, 1987] as:

$$\varphi = \frac{C}{\frac{\beta}{2}+1}\left(\frac{-Y}{C}\right)^{\frac{\beta}{2}+1}\left(\dot{Y}\right) \tag{5.1}$$

Where C and β are material constants and Y is a thermodynamic variable associated with the damage parameter D. Y is also known as the damage strain energy release rate and is derived from the thermodynamic potential (ψ) as shown in Equation 2.70 (Chapter 2, section 2.3.2) and can be written as:

$$Y = -\rho\frac{\partial\psi}{\partial D} = \frac{\sigma*^2}{2E(1-D)^2} \tag{5.2}$$

Where ρ is the density, E is Young's modulus and σ^* the equivalent multiaxial damage stress. Substituting Equation 2.67 into 5.2 leads to:

$$Y = \frac{\sigma_{eq}^2}{2E(1-D)^2}R_v \tag{5.3}$$

Differentiating Equation 5.3 with respect to time yields:

$$\dot{Y} = \frac{dY}{dt} = \frac{2\sigma_{eq}\dot{\sigma}_{eq}}{2E(1-D)^2}R_v \tag{5.4}$$

The damage evolution law may be derived from Equation 5.1 by differentiating φ with respect to Y and assuming linear accumulation of damage strain energy release rate with respect to time ($\dot{Y}$= constant), i.e.,

$$\dot{D} = -\frac{\partial \varphi}{\partial Y} = \left(\frac{-Y}{C}\right)^{\beta/2} \left(-\dot{Y}\right) \tag{5.5}$$

Substituting Equations 5.2 and 5.3 into Equation 5.5, gives:

$$\dot{D} = \frac{2}{C^{\beta/2}\left(2E\right)^{(\beta/2)+1}} \times \frac{\sigma_{eq}^{\beta+1} R_v^{(\beta/2)+1}}{\left(1-D\right)^{\beta+2}} \dot{\sigma}_{eq} = \alpha \frac{\sigma_{eq}^{\beta+1} R_v^{(\beta/2)+1}}{\left(1-D\right)^{\beta+2}} \dot{\sigma}_{eq} \tag{5.6}$$

Where $\alpha = \frac{2}{C^{\beta/2}(2E)^{(\beta/2)+1}}$,

Integrating Equation 5.6 over one cycle to obtain $\partial D/\partial N$, assuming the variation of triaxiality ratio $T_x = \sigma_H/\sigma_{eq}$ and (1-D) within a cycle is negligible, results to:

$$\frac{\partial D}{\partial N} = \int_{t_1}^{t_2} \dot{D} dt = \int_{t_1}^{t_2} \alpha \frac{\sigma_{eq}^{\beta+1} R_v^{\beta/2+1}}{\left(1-D\right)^{\beta+2}} \dot{\sigma}_{eq} dt = \int_{\sigma_{eq,min}}^{\sigma_{eq,max}} \alpha \frac{\sigma_{eq}^{\beta+1} R_v^{\beta/2+1}}{\left(1-D\right)^{\beta+2}} d\sigma_{eq} \tag{5.7}$$

The integration of Equation 5.7 yields:

$$\frac{\partial D}{\partial N} = A \frac{\sigma_{eq,max}^{\beta+2} - \sigma_{eq,min}^{\beta+2}}{\left(1-D\right)^{\beta+2}} R_v^{\beta/2+1} \tag{5.8}$$

The constant A is equal to $\alpha/(\beta+2)$. $\sigma_{eq,max}$ and $\sigma_{eq,min}$ are the maximum and minimum von Mises stress, respectively. The damage variable D can be obtained as a function of number of cycles by integrating Equation 5.8 for the following conditions:

N= 0 $\rightharpoonup$ D= 0, the result is:

$$D = \left\{1 - \left[1 - A\left(\beta+3\right)\left(\sigma_{eq,max}^{\beta+2} - \sigma_{eq,min}^{\beta+2}\right) R_v^{\frac{\beta}{2}+1} N\right]^{\frac{1}{\beta+3}}\right\} \tag{5.9}$$

At $N = N_i \rightharpoonup D = 1$, N_i the number of cycles to initiation of macro cracks.

$$N_i = \frac{1}{A(\beta+3)} \left(\sigma_{eq,max}^{\beta+2} - \sigma_{eq,min}^{\beta+2} \right)^{-1} R_v^{-\frac{\beta}{2}-1} \tag{5.10}$$

The damage parameters A and β are material constants that can be determined by fitting Equation 5.10 into the experimental data, which will be elaborated later on. The stress components were calculated using the FE model described in the previous chapter (Chapter 4). The obtained damage parameters were then used to validate numerical results by experimentally proven fretting fatigue crack initiation lifetime measurements.

5.2.2 Under elasto-plastic condition

As proven in Chapter 4, for some types of fretting fatigue contact configurations, such as conformal contact configuration, the micro-plastic deformation plays important role in formation of initial crack. The developed damage model based on damage strain energy release rate (Equation 5.10) is not representative for such a case. Therefore, in this section a damage model is derived based on micro-plastic deformation.

According to Lemaitre [Lemaitre, 1987], it is proven that a dissipation potential function φ can be written as function of three variables, Y, $\dot{P}$ and $\dot{\pi}$, that are damage elastic energy release rate, rate of plastic strain and accumulated micro-plastic strain, respectively. Thus, it is sufficient to consider the following simple analytical formula, which is function of two material and temperature-dependent coefficients C and β. Moreover, many experimental results show that the dissipation potential function must be a non-linear function of Y [Lemaitre and Desmorat, 2005].

$$\varphi = \frac{C}{\frac{\beta}{2}+1} \left(\frac{-Y}{C} \right)^{\frac{\beta}{2}+1} \left(\dot{P} + \dot{\pi} \right) \tag{5.11}$$

Since the variables Y, $\dot{P}$ and $\dot{\pi}$ are positive, the damage rate is always positive. The non-linearity of damage with regard to stress is given by its dependence on $\dot{P}$ and $\dot{\pi}$, which are non-linear functions of stress. In case of fretting fatigue conformal contact macro-plasticity does not exist ($P = 0$) and the irreversible strain is micro-plastic. By assuming the linear accumulation of micro plasticity, the damage evolution law may be derived by differentiating the

dissipation potential function with respect to Y, Therefore, it can be rewritten as:

$$\dot{D} = -\frac{\partial \varphi}{\partial Y} = \left(\frac{-Y}{C}\right)^{\beta/2} (\dot{\pi}) \tag{5.12}$$

where, as mentioned earlier $\dot{\pi}$ is the accumulation of micro-plastic strain. Since very little information exists about this phenomenon, its constitutive equations can be formulated with some similarity with macro-plasticity. From the dissipation term σ:$e^{\mu p}$, the stress σ is the associated variable to micro plastic strain ($e^{\mu p}$), and then $\dot{\pi}$ can be written as:

$$\dot{\pi} = \sqrt{2/3\,(\dot{e}^{\mu p} : \dot{e}^{\mu p})} \tag{5.13}$$

To obtain the model written in terms of stress, $\dot{\pi}$ must be expressed as a function of stress. A possible three-dimensional expression for accumulated micro-plastic strain introduced by Lemaitre [Lemaitre, 1987] is

$$\dot{\pi} = \left[\frac{\sigma_{eq}}{K(1-D)}\right]^{m} \frac{|\dot{\sigma}_{eq}|}{1-D} \tag{5.14}$$

where, K and m are material constants. Substituting Y (Equation 5.3) and $\dot{\pi}$ (Equation 5.14) into Equation 5.12:

$$\dot{D} = \left(\frac{-\sigma_{eq}^2 R_v}{2CE(1-D)^2}\right)^{\beta/2} \left[\frac{\sigma_{eq}}{K(1-D)}\right]^{m} \frac{|\dot{\sigma}_{eq}|}{1-D} = \alpha \frac{\sigma_{eq}^{\beta+m} R_v^{\beta/2} |\dot{\sigma}_{eq}|}{(1-D)^{\beta+m+1}} \tag{5.15}$$

where, $\alpha = -1/\left(K^m (2CE)^{\beta/2}\right)$

Integrating Equation 5.15 over one cycle to obtain $\partial D/\partial N$, gives:

$$\frac{\partial D}{\partial N} = \int_{t_1}^{t_2} \dot{D} dt = \int_{\sigma_{eq,min}}^{\sigma_{eq,max}} \alpha \frac{\sigma_{eq}^{\beta+m} R_v^{\beta/2}}{(1-D)^{\beta+m+1}} d\sigma_{eq} \tag{5.16}$$

In order to perform integral in Equation 5.16, it was assumed that variation of triaxiality ratio and (1-D) are negligible within one cycle. Then quation 5.16

becomes:

$$\frac{\partial D}{\partial N} = A\frac{\sigma_{eq,max}^{m+\beta} - \sigma_{eq,min}^{m+\beta}}{(1-D)^{m+\beta+1}} R_v^{\beta/2} \tag{5.17}$$

where, $A = \alpha/(\beta + m + 1)$, then the damage variable D can be obtained as a function of number of cycles by integrating Equation 5.17 for the following conditions: $N{=}\ 0 \rightharpoonup D{=}\ 0$, the result is:

$$D = \left\{1 - \left[1 - A\left(\beta + m + 2\right)\left(\sigma_{eq,max}^{\beta+m+1} - \sigma_{eq,min}^{\beta+m+1}\right) R_v^{\beta/2} N\right]^{\frac{1}{\beta+m+2}}\right\} \tag{5.18}$$

At $N = N_i \rightharpoonup D{=}\ 1$, N_i the number of cycles to initiation of macro cracks.

$$N_i = \frac{1}{A(\beta + m + 2)}\left(\sigma_{eq,max}^{\beta+m+1} - \sigma_{eq,min}^{\beta+m+1}\right)^{-1} R_v^{-\beta/2} \tag{5.19}$$

where N_i is number of cycles to macro-crack initiation, $\sigma_{eq,max}$ and $\sigma_{eq,min}$ are the maximum and minimum von-Mises stress in a cycle, respectively, R_v is the mean value of triaxiality function, m is the power constant in Ramberg-Osgood equation, A and β are the damage parameters, i.e. material constants that can be determined by fitting Equation 5.19 into the calculated N_i from the experimental data which will be elaborated later on.

5.3 Location of fretting fatigue initial crack

In order to predict the number of cycles to initiation using developed uncoupled damage model, the location of fretting fatigue crack initiation should be predicted. To estimate the location of initial crack at the contact interface, there are many methods, which are based on critical plane approaches [Lykins et al., 2000], or monitoring some parameters such as Ruiz parameters at contact interface [Iyer and Mall, 2001]. In this study two different approaches were used to find the fretting fatigue crack initiation site. These approaches can be categorized in two different groups, namely stress and energy based approaches.

5.3.1 Stress based approach

The first approach was based on damage mechanics approach. As mentioned earlier damage is equally sensitive to shear energy but also to the volumetric

deformation energy since the growth of cavities and cracks are very sensitive to hydrostatic stress. Therefore, the location of initial crack can be estimated by considering that the equivalent multiaxial damage stress is the damage causing stress. Therefore, as also depicted in Chapter 4, the fretting fatigue crack initiation site can be related to the maximum value of σ^* (Equation 2.68) at contact interface between fretting pad and fatigue specimen.

In order to validate this approach the results were compared with the maximum value of maximum principal strain range ($\Delta\epsilon_{p,max}$) at contact interface. The formula of the maximum principal strain can be written as:

$$\epsilon_{p,max} = \frac{\epsilon_x - \epsilon_y}{2} \pm \sqrt{(\epsilon_x - \epsilon_y)^2 + \epsilon_{xy}^2} \tag{5.20}$$

where ϵ_x, ϵ_y and ϵ_{xy} are the strain components.

Figure 5.1 (a) illustrates the variation of $\Delta\epsilon_{p,max}$ inside fatigue specimen subjected to fretting condition for R= 127 mm, F= 5201 N, σ_{axial}= 115.8 MPa, μ= 0.65 and $Q/\mu F$= 0.8 loading conditions. Figure 5.1 (b) show the equivalent multiaxial damage stress distribution inside the specimen for the same loading conditions.

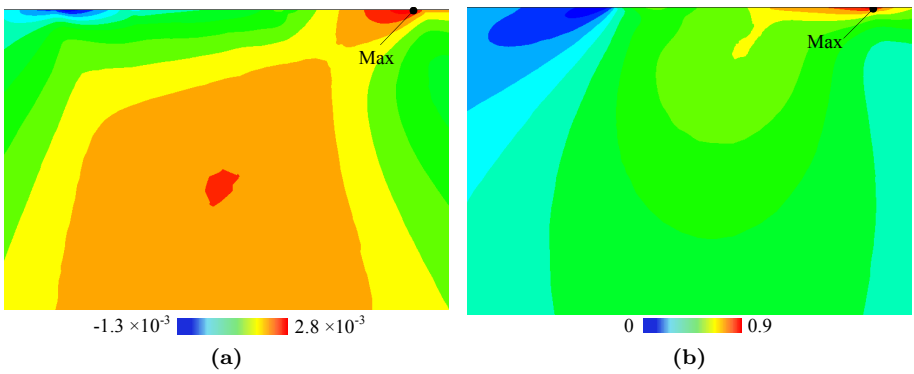

Figure 5.1: (a) Maximum principal strain range contour plot and (b) normalized equivalent multiaxial damage stress (σ^*/σ_{yield}) at a= 1.28 mm, R= 127 mm, F= 5201 N, σ_{axial}= 115.8 MPa, μ= 0.65 and $Q/\mu F$= 0.8.

It can be seen that the maximum location of σ^* predicts the location of initial crack near the trailing edge of contact, which is in good agreement with

the location of initial crack predicted by maximum location of maximum principal strain range and experimental observations. For instance at mentioned loading condition, the predicted crack initiation location using this approach was at x/a= 0.978, which is in good agreement with predicted location with maximum principal strain range criterion which was x/a= 0.980. This criterion was implemented to fretting fatigue experimental loading condition taken from literature [Szolwinski and Farris, 1998] in order to calculate the crack initiation lifetime, which is elaborated in this Chapter.

5.3.2 Energy based approach

The proposed stress based criterion was based on pure stress distribution, which includes the triaxiality nature of stress at contact interface. However, it was found that this stress distribution is not highly sensitive to small variation of applied axial stress. To be concrete about this fact, the above criterion was applied to two performed experimental tests, namely FF1 and FF2 from Table 3.4 in Chapter 3. Figure 5.2 illustrates the variation of maximum equivalent multiaxial damage stress (σ^*) at contact interface for FF1 and FF2. From figure it can be noted that, by changing the axial stress from 100 MPa to 115 MPa the the predicted location of initial crack by σ^* does not change ($x/$a= 0.99).

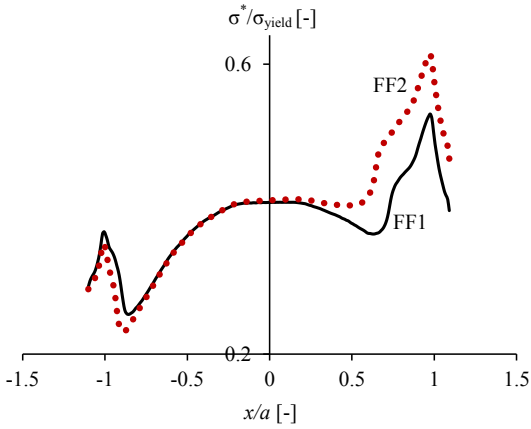

Figure 5.2: Variation of normalized σ^* at contact interface for FF1 and FF2.

Therefore, some other parameters such as slip amplitude, which is sensitive to small variation of applied stress, should be taken into account. The relation-

ship between fretting damage and stress distribution at contact interface was first provided by Ruiz et al. [Ruiz et al., 1984]. They proposed two different damage parameters for fretting fatigue, namely fretting wear (K_1) and fretting fatigue (K_2). The fretting wear parameter is a measure of frictional work at contact interface and can be written as; $K_1 = \tau \times \delta$, where τ is a local value of frictional shear stress and δ is a local slip amplitude within the contact region. Fretting wear parameter should be able to predict the location of damage initiation at contact interface, but neglects the effects of axial bulk stress, which is considered as an important parameter of fretting fatigue damage process. The fretting fatigue parameter is based on the additional effect of axial stress by taking into account the effect of tangential stress at contact interface, and can be written as; $K_2 = \sigma_x \times \tau \times \delta$. Ruiz fretting wear and fretting fatigue parameters can be used to assess components subjected to fretting fatigue and predict initial crack location. However, Hills and Nowell [Hills and Nowell, 1994] discussed severe limitations to their application, for instance no account is taken of factor such as surface roughness and indirectly through the influence of the COF on stress state and displacement at contact interface.

According to both Ruiz parameters outside the contact interface there is no damage, as shear stress is zero. Besides, at sticking region within the contact interface where there is no slip, thus Ruiz parameters predict zero damage. In this investigation the location of initial crack was calculated based on maximum location of dissipated energy at contact interface during one full cyclic loading condition. The concept of cumulative dissipated energy, E_d, for fretting test is introduced by Mohrbacher et al. [Mohrbacher et al., 1995]. Dissipated energy can be calculated from the tangential force versus displacement loops as illustrated in Figure 5.3. The dissipated energy during one full fretting fatigue cyclic loading under partial slip condition is summation of dissipated energy in each step of applied stress and tangential load. The total dissipated energy after one cycle can be written as:

$$E_d = \sum_{i=1}^{4} \tau_i \times \delta_i \tag{5.21}$$

where, τ_i is frictional shear stress distribution and δ_i is local slip amplitude. Figure 5.4 depicts the variation of dissipated energy after one full cyclic fretting cycle for each of the modelled fretting fatigue problems as tabulated in Table 3.4.

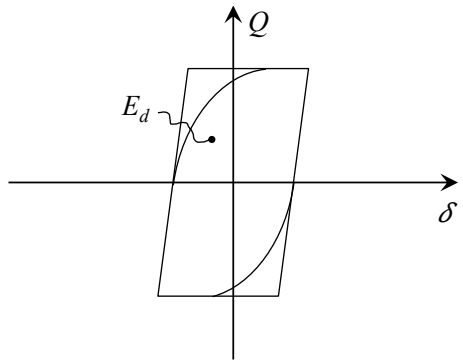

Figure 5.3: Schematic view of dissipated energy after one full fretting cycle.

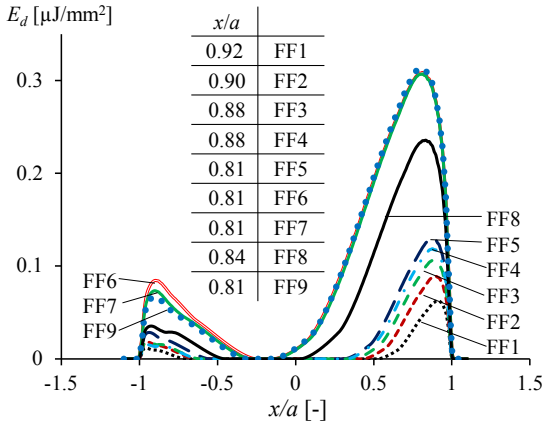

Figure 5.4: Dissipated energy distribution and its maximum value after one full fretting cycle versus normalized contact distance.

The maximum location of dissipated energy is located near edge of contact as shown in Figure 5.4, where the fretting fatigue cracking occurs based on experimental observation. By comparing the predicted location of initial crack with frictional shear stress distribution at contact interface, it was noticeable that the location of crack is at slipping band near the edge of contact. However, in some cases the crack initiation location is near the location of maximum stick zone, which is the location of maximum shear stress as will be elaborated later on in this chapter.

Despite the small discrepancy between two criteria, both of them predicted

the location of crack near the trailing contact edge. For predicting crack initiation lifetime by means of FE modelling approach, it is common that the stress and strain states are averaged in area or volume, also called process zone, at crack initiation site. The size of process zone is determined as the distance at which the stress is normally independent of mesh refinement. Therefore, small difference in predicted location of initial crack can not result in a big difference in predicted crack initiation lifetime.

5.4 Effects of localized plasticity

Many studies have investigated fretting fatigue behaviour; however, the majority have assumed elastic deformation and very few have considered the effect of plasticity [Shin, 2009]. The main goal of this section is to monitor the effect of different fretting fatigue primary variables on localized plasticity in an Aluminium alloy (Al 2024-T3) test specimen. In order to do so, the stress distributions at the contact interface were extracted using FE modelling approach at the contact interface under elasto-plastic conditions. The effect of different fretting fatigue primary variables, such as axial stress, contact geometry, and coefficient of friction, on localized plasticity was investigated. Finally, the relationship between the location of maximum localized plasticity and Ruiz fretting damage parameter with the crack initiation site is discussed.

According to Endo and Goto [Endo and Goto, 1976], at presence of plastic deformation the crack initiation process is related to localized-plastic deformation at the contact interface. The propagation of the initial crack is then governed by contact stress and bulk stress fields, respectively. In both crack initiation and early stage of crack propagation the effect of contact stress is important. There are many numerical investigations concerned with monitoring stress state at the contact interface. The majority of them considered linear elastic material for their model [Iyer and Mall, 2001, Massingham and Irving, 2006, Wang et al., 2007]. Few have considered the effect of plasticity, some of them can be found here [Tsai and Mall, 2000, Goh et al., 2001, Goh et al., 2006, Shin, 2009].

5.4.1 Materials and FE model

In order to study the effect of localized plasticity on fretting fatigue behaviour, the single clamp cylindrical contact FE model was used with the boundary

condition as elaborated in Chapter 4. The length and width of the specimen were L= 20 mm and b= 6.35 mm, respectively. Both fretting pad and fatigue specimen had a depth of 12.7 mm. Aluminium alloy, Al 2024-T3 was used in this investigation for both fretting pad and specimen. Yield stress, modulus of elasticity and Poisson's ratio of the material were obtained as $\sigma_{yield} = 350$ MPa, E= 71 GPa and μ= 0.33, respectively. Therefore, in order to fundamentally understand crack nucleation and propagation in fretting fatigue, a detailed understanding of the contact stress state and the localized plastic deformation at the contact interface is important. A bilinear elasto-plastic constitutive equation, which defines an isotropic hardening with the von Mises yield surface, was implemented to characterize the elasto-plastic response of the Aluminum alloy Al 2024-T3 as depicted in Figure 5.5. von-Mises yield criterion is based on the observation that a hydrostatic pressure cannot cause plastic yielding of the material.

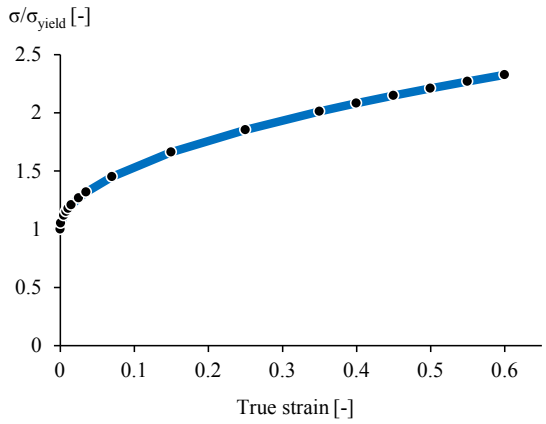

Figure 5.5: True plastic stress versus true plastic strain curve of 2024-T3.

5.4.2 Effect of primary variables

There are more than 50 factors that can affect behaviour of material subjected to fretting fatigue loading condition such as, COF, normal contact load, slip amplitude, applied axial stress, interface stress distribution, etc. These variables can be divided in two sets of primary and secondary variables [Dobromirski, 1992]. Some variables such as cyclic axial stress, relative slip amplitude, COF, contact geometry and normal contact load that have more influence on fretting

fatigue lifetime can be considered as primary variables. The rest of variables considered as secondary variables, which have less effect on fretting fatigue lifetime. In this study several parametric studies were carried out by means of FE modelling technique to study the effects of the fretting fatigue primary variables on the localized plasticity at the contact interface.

Effect of contact geometry

To study the effect of contact geometry i.e. pad radius (R), a contact load of 7 kN was applied on the top surface of the fretting pad. Since the coefficient of friction is an input parameter and can be changed by some surface treatments such as surface roughness, lubrication, coating and mechanical treatments, in this study the coefficient of 0.5 was used to compare different primary variables to check the localized plasticity at lower coefficient of friction to compare with what was measured experimentally and reported by Szolwinski and Farris [Szolwinski and Farris, 1998].

The reaction stress applied at left side of specimen was based on a tangential force (Q) of 2240 N. Three different contact radii (R= 25 mm, 50.8 mm and 75 mm) along with different axial stresses (σ_{axial}= 90 MPa, 120 MPa and 160 MPa) were used to study the effects of different contact geometries on the plastic deformation. The tangential stress, σ_x, governs the stress component along the contact interface and its variation over contact interface is shown in Figure 5.6 for different contact radii. As can be noted, in all cases the peak tangential stress, σ_x, is located near the contact edge interface. Form Figure 5.6, for all applied axial stresses the peak tangential stress gradually increases with decreasing of contact radius. Also, the maximum tangential stress exceeds the yield stress for all contact radii for axial stress 120 MPa and 160 MPa. While, in case of axial stress 90 MPa yielding just appears at two cases with smaller contact radius i.e. 25 mm and 50.8 mm.

Figures 5.7 (a) and (b) depict variation of von-Mises equivalent stress contour plot inside specimen for R= 50.8 and 75 mm, respectively. As can be seen from the figure, the plastic zone is initiated near to the contact edge for both contact radii. For R= 75 mm, there is no plastic deformation inside the specimen below the contact interface. However, for R= 50.8 mm in addition to the contact edge, the plastic deformation appears inside the specimen.

Figure 5.8 illustrates that the plastic zone is initialized at the contact edge

and propagates at -45° into the specimen as the contact radius drops from 75 mm to 25 mm at the same loading conditions. Despite, the growing of plastic deformation beneath the contact interface, as it is shown in Figure 5.8, the maximum plastic deformation still appears near the contact edge, where the nucleation of fretting fatigue initial crack is expected.

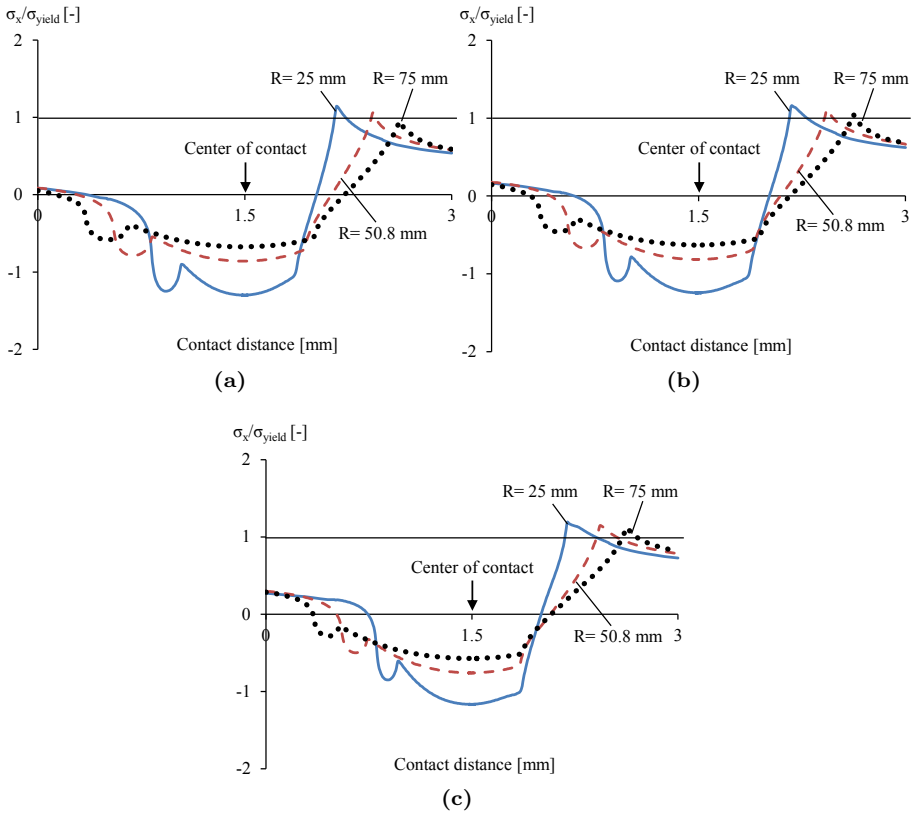

Figure 5.6: Comparison of normalized tangential stress distribution over the contact interface for different contact radii for (a) σ_{axial}= 90 MPa, (b) σ_x=120 MPa and (c) σ_{axial}= 160 MPa at (F= 7 kN, Q= 2240 N and μ= 0.5).

From these results it can be concluded that, after fretting fatigue crack nucleation, the initial micro-crack propagates at -45° into the specimen, which is in good agreement with experimental observations and published data from literature for the same material [Szolwinski and Farris, 1998].

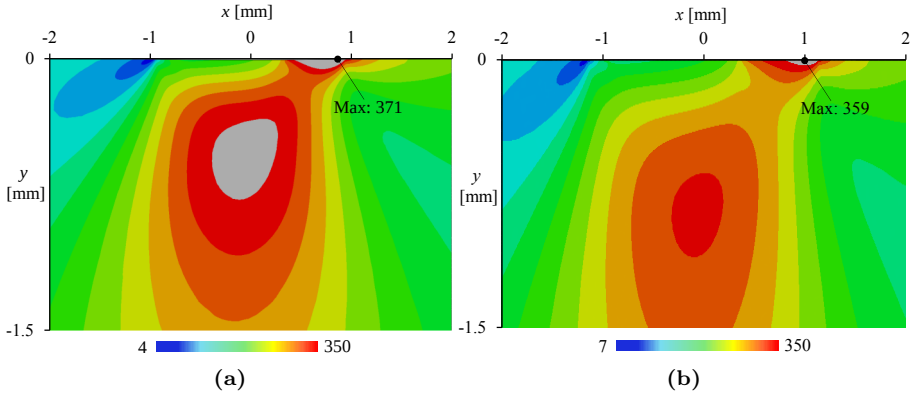

Figure 5.7: von-Mises stress contour plot inside the specimen for (a) R= 50.8 mm and (b) R= 75 mm at (F= 7 kN, σ_{axial}= 160 MPa, Q= 2240 N and μ= 0.5).

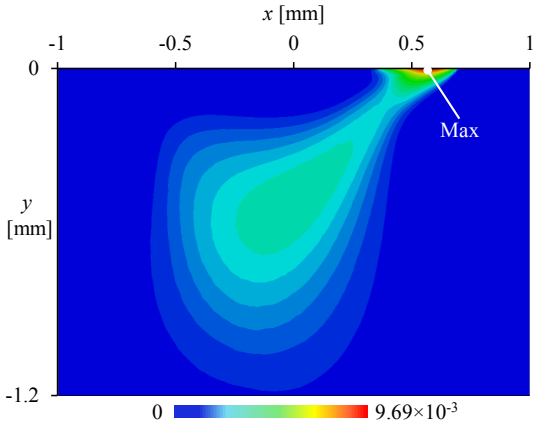

Figure 5.8: Equivalent plastic strain (PEEQ) contour plot at (F= 7 kN, σ_{axial}= 160 MPa, Q= 2240 N, R= 25 mm and μ= 0.5).

Effect of axial stress

For studying the effect of axial bulk stress, a contact load of 7 kN was applied on the top surface of the fretting pad. The contact radius and COF used were 50.8 mm and 0.5, respectively. The reaction stress was applied at the left hand side of the specimen based on a tangential force of 2240 N. Nine levels of axial stress amplitude between 90 MPa and 160 MPa were then used to investigate

the effect of axial stress variation on the plastic zone at the contact interface.

Figure 5.9 demonstrates the variation for maximum principal strain (MPS) along the contact interface. From the figure, it can be seen that the peak value of maximum principal strain at contact interface increases with increasing the axial bulk stress and for all cases this peak value is near the contact edge. For all stress levels except 90 MPa maximum plasticity appears near contact edge along the contact interface.

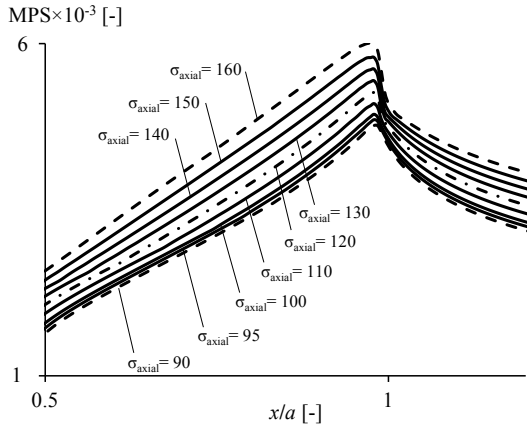

Figure 5.9: Maximum principal strain distribution at contact interface for different stress levels [MPa] at (F= 7 KN, Q= 2240 N, μ= 0.5, R= 50.8 mm).

Figure 5.10 depicts the equivalent plastic strain contour plot for axial stress 90 MPa. It can be seen that micro-crack nucleation may occur inside the specimen below the contact zone. This indicates that the stresses beneath the contact zone at a distance about a few μm are larger than the fretting stresses on the contact surface. It can be concluded that micro-crack nucleation may occur both inside the specimen below the contact interface and at the contact surface.

Effect of COF

The COF is one of the main factors that can affect the stress and strain distribution in the contact region and consequently the crack nucleation site. In this study, a contact load of 7 kN, was applied on the top surface of the fretting pad with contact radius 50.8 mm. The maximum range of stress i.e. 160 MPa was

applied on the right side of the specimen. The reaction stress applied at left side of specimen was based on tangential force of 2240 N. Nine different COF between 0.4 and 1.2 were used to study their effects on the localized plastic deformation at the contact interface.

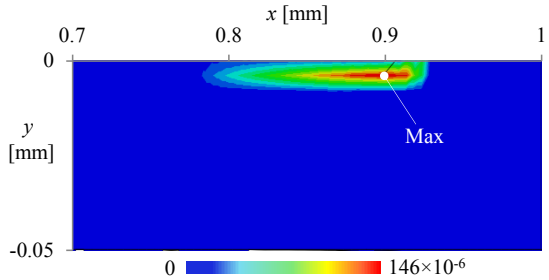

Figure 5.10: Equivalent plastic strain (PEEQ) contour plot at (F= 7 KN, σ_{axial}= 160 MPa, Q= 2240 N, R= 50.8 mm and μ= 0.5).

Figure 5.11 shows the normalized frictional shear stress distribution along the contact interface for different COFs. The figure indicates that with increasing the COF from 0.4 to 1.2 the maximum value of shear stress sharply increases. Other than increasing the maximum shear stress values, the increasing COF also leads to the change of the stick and slip zone. As shown in Figure 5.11, the stick zone increases as the value of COF increases and subsequently the slip zone decreases. This is because the increased COF caused enhanced adherence between fretting pad and specimen at the contact interface.

5.4.3 Fretting damage and localized plasticity

In this section the location of maximum localized plasticity at the contact interface is monitored at different COFs and compared with the peak value of Ruiz parameter (k_2), then the location of the initial crack is discussed. The boundary and loading conditions were the same that used in previous section. Ruiz fretting fatigue parameter (k_2) shows a peak close to the edge of the contact, where cracks usually start in practice. Wear damage and fretting fatigue parameters can be used to assess components subjected to fretting fatigue and predict initial crack location. However, it has been reported by Endo et al. [Endo and Goto, 1976] and Lamacq et al. [Lamacq et al., 1997] that fretting fatigue cracks are assumed to initiate by localization of plastic deformation at contact interface.

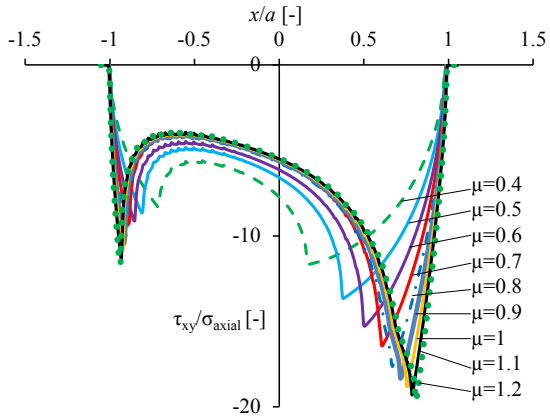

Figure 5.11: Frictional shear stress distribution at contact surface for different COF at (σ_{axial}= 160 MPa, F= 7 kN, Q= 2240 N, R= 50.8 mm).

In order to study the effect of different COFs on location of fretting fatigue initial crack, three different criteria were used, namely, the peak value of Ruiz fretting fatigue, maximum equivalent plastic and maximum principal strain at the contact interface. Figure 5.12 illustrates the peak value of these criteria over the contact interface for different COFs at presence of plasticity. From Figure 5.12 and as mentioned above, with increasing the COF the slipping region decreases. It can be clearly seen that the peak value of k_2 is near to the contact edge and by increasing the COFs the location of initial crack remaines constant. These numerical results confirm the restriction that has been mentioned by Hills and Nowell [Hills and Nowell, 1994]. The location of maximum value of equivalent plastic strain for COFs 0.4 and 0.5 is constant. This value declines when COF increases from 0.5 to 0.9 and tends to be closer to the location of maximum stick zone than the contact edge. The maximum stick zone is the location of maximum shear stress at the contact interface, which is also the border between sticking and slipping region. From COFs 0.9 till 1.2 the location of peak value of equivalent plastic strain is the same as maximum stick zone. Moreover, for lower COFs i.e. 0.4 to 0.6 there is a good correlation between the predicted location of initial crack by Ruiz k_2 parameter and using location of maximum equivalent plastic strain. The third criterion i.e. the location of peak value of maximum principle strain at the contact interface remain constant from COF 0.4 to 0.8 and is in a good agreement with location of maximum k_2. Finally, location of this peak value sharply plummets at COF 0.9

then follows the location of maximum stick zone the same as second criterion. These results indicate that at lower COFs the parameter k_2 can predict the right location of initial crack. Nonetheless, at higher COFs, especially larger than 0.9, this criterion is not valid.

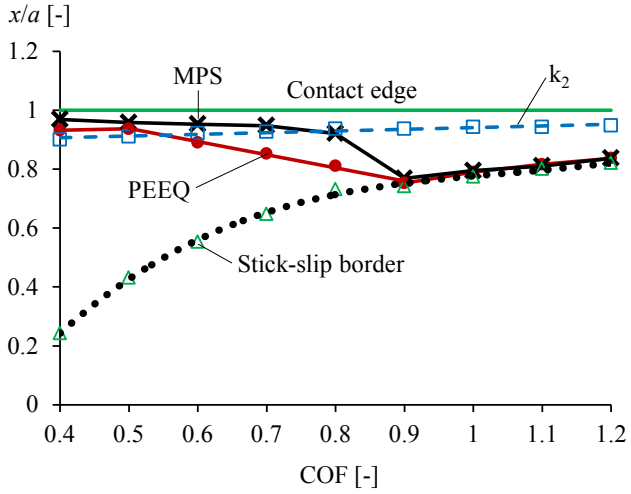

Figure 5.12: Comparison between fretting fatigue crack initiation location base on different criteria at (σ_{axial}= 160 MPa, F= 7 kN, Q= 2240 N and R= 50.8 mm).

Figure 5.13 indicates the relationship between the location of the maximum equivalent plastic strain and the location of the maximum stick zone ($+c$) at the contact interface. These results demonstrate that the location of maximum plastic strain changes with increasing COF and also suggest that the location of the initial micro-crack can be related to the maximum plastic deformation. As mentioned above, the restriction of parameter k_2 has been revealed by [Hills and Nowell, 1994]. In addition, Lamacq, et al. [Lamacq et al., 1997] have shown that the fretting fatigue cracks initiate at the location of maximum plastic deformation. Therefore, by using modelling technique and monitoring the location of the localized plastic deformation would be a good solution to find the initial crack site in fretting fatigue case, which is subjected to localized plastic deformation.

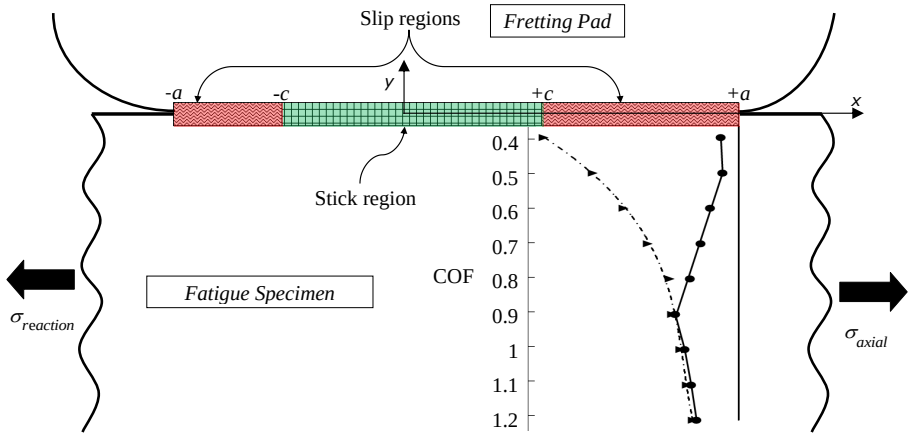

Figure 5.13: Schematic view of variation of maximum equivalent plastic strain with increasing COF along the contact interface.

5.5 Validation of crack initiation model

In this section, in order to validate the developed damage evolution law, it was conjuncted with FE model. For this purpose the uncoupled damage evolution law was implemented to fretting fatigue problem at various fretting condition such as contact geometry, axial stress, normal load and tangential load. The predicted results were validated with published experimental data from literature.

5.5.1 Material and FE model

To validate the prediction model, the experimental data from Szolwinski and Farris [Szolwinski and Farris, 1998] were used to simulate the fretting fatigue crack initiation lifetime. The mechanism of fretting fatigue was based on single clamp cylindrical contact configuration. In the experimental testes that have been carried out by Szolwinski and Farris [Szolwinski and Farris, 1998], they have tried to change some of the primary variables such as contact radius R= 127, 178, 229 mm, normal contact force 5201 N $\leq F \leq$ 7226 N , Axial stress 81 MPa $\leq \sigma_{axial} \leq$ 115.8 MPa and tangential stress ratio $0.21 \leq Q/F \leq 0.52$. Aluminium alloy, Al 2024-T351 was used in their investigation for both pad and specimen. Yield stress, modulus of elasticity and Poisson's ratio of the material were obtained as σ_{yield} = 310 MPa, E= 74.1 GPa and ν= 0.33, respectively. The single clamp cylindrical contact fretting fatigue configuration was modelled

as elaborated in Chapter 4. The length and width of the specimen were L=40 mm and b=6.35 mm, respectively. Both fretting pad and fatigue specimen had a thickness of 12.7 mm. The coefficient of friction μ= 0.65 was considered in this study as measured in reference [Szolwinski et al., 1997].

Table 5.1 shows the experimental data from literature which were used for FE simulations. Stress ratio for all test was considered as R_s= -1. The experimental data are tabulated in three major categories based on different contact radii, as it can be seen in Table 5.1. According to [Szolwinski and Farris, 1998] the experimental crack initiation lifetime was defined as the difference between the observed failure life and the estimated propagation life. A propagation life was estimated for each of the fretting fatigue tests as the time for a 1 mm semi-elliptical crack to grow under the influence of the bulk applied stress amplitude to a depth of 6.35 mm (the mid-plane of the specimen). The selection 1 mm initial crack length for this case study was not arbitrary, it was based on both an understanding of the nature of the near-surface contact stress field and fractographic evidence from failed specimens as observed and reported by Szolwinski and Farris in [Szolwinski and Farris, 1998].

The first step to estimate the fretting fatigue crack initiation lifetime is to choose the proper developed damage evolution model. Therefore, all loading conditions were applied to the FE model in order to monitor the stress distribution at trailing contact edge, which is critical region. It was found that the maximum stress for all loading conditions did not exceed the yield limit and the assumption of elastic material behaviour was valid for this case study. Thus, the developed damage model for elastic behaviour of material (i.e. Equation 5.10) was selected to estimate the fretting fatigue crack initiation lifetime.

5.5.2 Procedure to determine damage parameters

To compute the crack initiation life the process area approach was used. The process area averaging was applied considering a semi-circular shape at origin of crack initiation as shown in Figure 5.14. The average triaxiality function R_v and the maximum and minimum equivalent stress i.e. $\sigma_{eq,max}$ and $\sigma_{eq,min}$ were then calculated inside the process zone at centre of predicted crack initiation site. The size of process zone (radius of semi-circle) was determined as the distance at which the stress is independent of mesh refinement. The effect of different process zone radii on fretting fatigue crack initiation lifetime was also studied which is explained later on.

Table 5.1: Experimental data including loading conditions and number of cycles to failure and initiation [Szolwinski and Farris, 1998]

Test no.	R [mm]	F [N]	Q/F	σ_{axial} [MPa]	N_f [cycle]	N_i [cycle]
1	127	7560	0.22	110.3	314000	287136
2	127	5427	0.31	110.3	241475	214611
3	127	6228	0.23	84.8	668277	602810
4	127	5370	0.35	88.4	563946	507097
5	127	7226	0.31	101.9	545489	510349
6	127	5201	0.52	115.8	465000	442226
7	127	6215	0.35	109.2	302804	275025
8	127	7070	0.27	108.8	253883	225702
9	127	6275	0.36	98.2	464166	424295
10	127	7118	0.27	85.4	381535	317654
11	178	6268	0.27	100	349520	312035
12	178	6994	0.34	113.1	455759	431062
13	178	7085	0.21	85.2	665073	600638
14	178	7251	0.31	99.4	552250	513985
15	178	6176	0.27	84.7	621442	555830
16	178	5319	0.36	97.4	459882	418911
17	178	6460	0.34	106.4	225535	195200
18	178	5351	0.38	110.6	330659	303994
19	299	6223	0.32	97	739250	697722
20	299	6268	0.32	85.4	856524	792621
21	299	7072	0.24	81.8	747135	673075
22	299	7073	0.25	81.8	729715	655655
23	299	5293	0.31	81	867330	790864
24	299	5325	0.26	82.9	768364	697565
25	299	7002	0.34	109.5	320864	293281
26	299	6187	0.33	110.8	479540	453080
27	299	7153	0.24	97.9	463324	423051

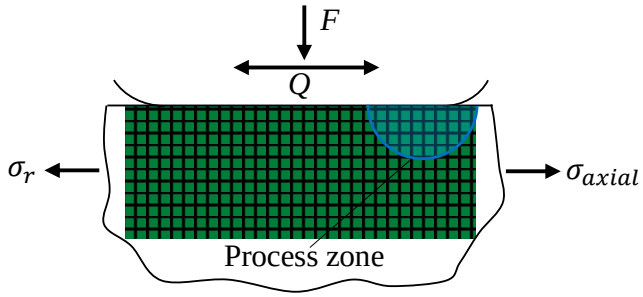

Figure 5.14: The process zone at location of fretting fatigue initial crack.

Three experimental tests were chosen to determine damage parameters, since the damage parameters A and β of damage model are unknown mate-

rial constants. The calibration tests were selected based on covering the broad range of axial stress and contact force that were used for experimental tests. For each of these tests, the average triaxiality function R_v and the maximum and minimum equivalent stress i.e. $\sigma_{eq,max}$ and $\sigma_{eq,min}$ were calculated inside the process zone at centre of predicted location for crack initiation with semi-circle radius of 50 μm at the contact interface and substituted into the damage evolution law Equation 5.10. The values of the damage parameters were found using regression analysis to calculate the best least square fit between the predicted cycles to initiation and the experimental data for crack initiation, which has been calculated by Szolwinski and Farris [Szolwinski and Farris, 1998]. The regression method can be used to predict numerical number of cycle to initiation from experimental results. But actual values differ from predictions, these are the regression errors (Error = experimental value of N_i - predicted value of N_i). The overall size of the error is measured using the Root-Mean Square Error (RMSE) as follow:

$$RMSE = \frac{\sum_{1}^{n} \left(N_{i,Experimental} - N_{i,Predicted}\right)^2}{n} \tag{5.22}$$

Where, n is the number of scatter data. Non-linear regression then was used to minimise the RMSE between the values in the data being fitted (Experimental data), and the values generated by the regression equation (Predicted numerical data). Numerical values for each test are summarised in Table 5.2. Figure 15 illustrates the best numerical predicted fitted curve in order to determine damage parameters. This methodology leads to following values: A= 5.5×10^{-11} and β= -0.019 and the damage evolution law for crack initiation life becomes:

$$N_i = 6.09 \times 10^9 \left[\sigma_{eq,max}^{1.981} - \sigma_{eq,min}^{1.981}\right]^{-1} R_v^{-1} \tag{5.23}$$

Figure 5.15 depicts the predicted crack initiation life versus the calculated experimental results from [Szolwinski and Farris, 1998]. The scatter band of $\pm$75 % is widely used in literature to predict fatigue and fretting fatigue lifetime [Szolwinski and Farris, 1998, Lykins et al., 2001a]. As shown in the Figure 5.15, all of the predicted crack initiation lifetime by means of developed damage model fall within the scatter bands of $\pm$50 %, which can be the evidence to establish confidence in robust predictive capability of proposed damage mechanics approach to estimate fretting fatigue crack initiation lifetime. This

interesting results show the importance of multiaxial nature of stress state at the contact interface which can be modelled by considering the triaxiality stress at the contact region, which introduced in developed damage evolution model.

Table 5.2: Numerical non-linear regression data to find the damage parameters

Test no.	R [mm]	σ_{axiaxl} [MPa]	R_v [-]	$\sigma_{eq,min}$ [MPa]	$\sigma_{eq,max}$ [MPa]	$N_{i,predicted}$ [cycles]	Error [%]
1	127	110.3	1.24	215	262	2.87×10^5	14.42
4	127	88.4	1.235	199	227	5.07×10^5	9.91
9	127	98.2	1.245	224	256	4.24×10^5	13.92

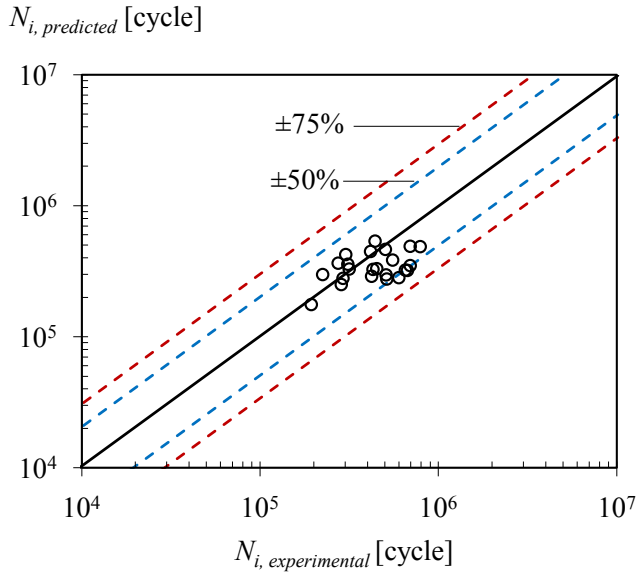

Figure 5.15: Predicted versus experimental fretting fatigue crack initiation lifetime.

Effect of process zone size

As mentioned above the average triaxiality function and the maximum and minimum equivalent stress were extracted inside the process zone with 50 μm. In order to find the effect of the process zone radius on crack initiation life this radius increased to 1 mm, which was the initial crack length in this case study. Figure 5.16 shows the results of predicted initiation life versus the experimental life for process zone radius of 1 mm. As it can be seen, the results are almost

the same and fall within the ±50 % error band with maximum 15% difference between 1 mm and 50 μm process zone size. Thus, it can be concluded that different process zone radius does not affect much the fretting fatigue crack initiation lifetime. However, this size should be selected not too far from the selected initial crack length.

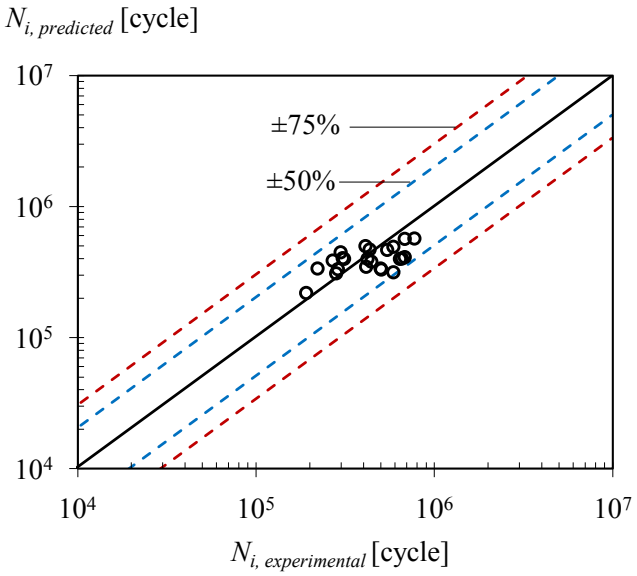

Figure 5.16: Predicted versus experimental fretting fatigue crack initiation lifetime for process zone radius of 1 mm.

Figure 5.17 illustrates typical variation of triaxiality ratio and function inside the process zone (1 mm) at location of initial crack. However, form Figure 5.18 it can be noticed that the variation of the average triaxilaty function R_v inside the process zone stays almost constant. The relation between the averaged triaxiality function and the averaged von-Mises stress range is almost linear for both process zone radii i.e. 50 μm and 1 mm.

5.6 Summary and conclusions

In this chapter Continuum Damage Mechanics (CDM) approach was used to find a predictor tool for fretting fatigue crack initiation lifetime. For this purpose, uncoupled damage evolution law was derived for HCF using the principle

of thermodynamics to predict fretting fatigue crack initiation lifetime for both elastic and elasto-plastic behaviour of material. In order to find the location of initial crack two different approaches, namely, stress and energy based methodology were discussed. The suggested criteria were implemented to experimental tests for single clamp cylindrical contact configuration. The results between both criteria predicted the crack location near the trailing contact edge, which was in agreement with the experimental observation.

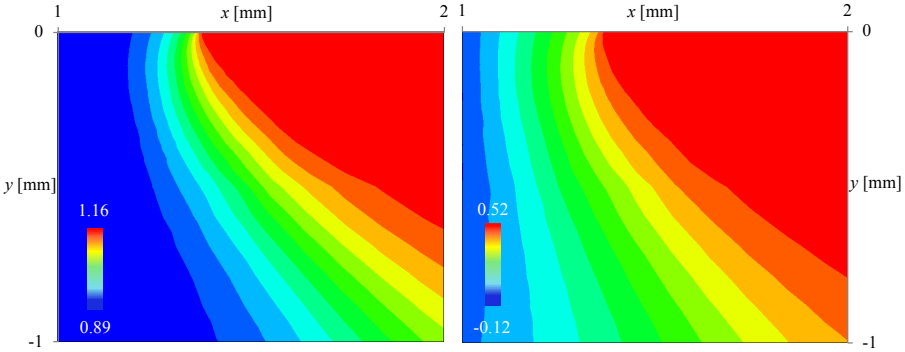

(a) R_v **(b)** T_x

Figure 5.17: Distribution of (a) triaxiality function (b) ratio inside the process zone at (R= 127 mm, F= 6215 N, σ_{axial}= 98.2 MPa, Q/F= 0.36, μ= 0.65).

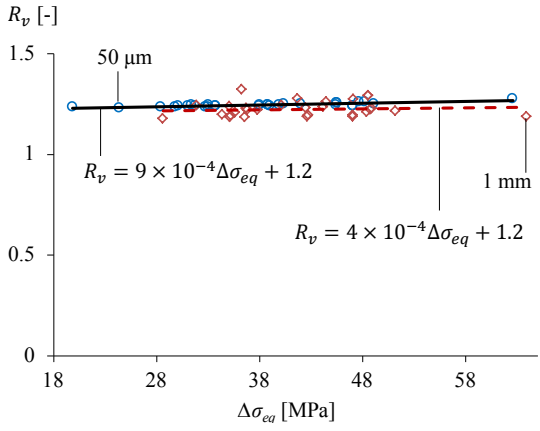

Figure 5.18: Variation of average triaxiality function against range of equivalent stress over process zone area

The developed damage model has been implemented to fretting fatigue problems form literature. Damage parameters were computed based on regression analysis to calculate the best least square fit between the estimated cycles to crack initiation and the experimental data. Eventually, using the developed damage model and the multiaxial stress state, which were extracted using the concept of process zone, cycles to crack initiation were calculated and compared with experimental data from literature. Results of predictor tool showed a good correlation compared to the experimental data. From the results it can be noticed that the multiaxial nature of stress state at contact interface between fretting pad and fatigue specimen in fretting fatigue phenomena plays crucial role to predict the number of cycles to fretting fatigue crack initiation. Moreover, these results prove that fretting fatigue's multiaxial behaviour can be modelled using damage mechanics approach which takes into account the effect of multiaxial state by means of considering the effect of stress triaxiality at the contact interface.

A parametric study was carried out to investigate the effect of different primary variables, e.g. contacts geometry, axial stress and COF on localized plasticity. Eventually, the relation between location of maximum localized plasticity and Ruiz fretting damage parameters with crack initiation site was discussed. The following conclusions can be drawn based on this study:

- The peak value of von-Mises stress and the maximum plastic deformation located near the contact edge for all cases. Also these results demonstrate that in general the fretting stresses were sharply decreased away from the fretting contact interface. There was one case where the peak von-Mises stress and the maximum plastic deformation were located inside the fretting fatigue specimen below the contact edge. When the plastic zone was initiated at the contact edge, it propagated at -45° into the fretting fatigue specimen in most cases where the plasticity appeared both at contact surface and subsurface inside the specimen.

- The maximum equivalent plastic strain increased with decreasing the contact radius. For all contact radii, the maximum plastic deformation occurred near the contact edge, for smaller radius, i.e. 25 mm, the plastic deformations were located both at contact interface and inside the fretting fatigue specimen beneath the centre of the contact zone.

- By increasing the axial stress, the maximum tangential stress increased. At the minimum stress levels the location of maximum equivalent stress or

location of maximum plastic deformation was closer to the contact edge, when compared with other levels of stress. The location of maximum equivalent stress was almost at the same location for axial stresses from 100 MPa up to 160 MPa.

- By increasing the COF from 0.4 to 1.2, the maximum value of shear stress increased. Also the stick zone increased as the COF values increased and consequently the slip zone decreased.

- By changing the COF, the location of maximum plastic deformation was changed. And the comparison between Ruiz fretting fatigue parameter and monitoring the plastic deformation revealed that considering the effect of plasticity may give good insight for finding the location of crack nucleation.

The results from this parametric investigation are helpful in explaining the effect of localized plasticity on fretting fatigue behaviour and experimental observations of micro-crack nucleation. Numerical results clearly indicate that in order to provide more accurate information for predicting micro-crack nucleation in the fretting fatigue tests, plastic analysis using FE techniques is crucial. Also the plastic deformation, stress state and size of stick and slip zones in the contact interface are very important since these parameters are believed to be the primary factors for prediction of crack initiation lifetime in fretting fatigue.

Chapter 6

FEA of fretting fatigue crack propagation

"In this chapter fretting fatigue crack propagation modelling approaches are presented "

6.1 Overview

The main aim of this chapter is to introduce fretting fatigue crack propagation model, which takes into account the effect of crack-contact interaction. For this purpose, in the first step the general developed crack propagation model is introduced using conventional FEM and XFEM approaches. In order to verify the developed codes, two different benchmark studies, namely, Double Edge Notch Tension (DENT) specimen and Double Cantilever Beam (DCB) specimen, are modelled. Eventually, to estimate the crack propagation lifetime, the developed codes i.e. both conventional FEM and XFEM approaches are implemented to fretting fatigue crack propagation problem.

6.2 Crack propagation model

In this study, two different approaches, namely, conventional FEM and XFEM were used to model two dimensional crack propagation problems. Before, application to fretting fatigue case the general model was implemented to some case study applications such as DENT and DCB specimens. In following section, the basic concept of crack propagation model using conventional FEM and XFEM are presented.

6.2.1 Conventional FEM model

For modelling crack propagation by means of conventional FEM, which is also called re-meshing technique approach, the crack should be modelled using embedded line, which is called "seam" in ABAQUS®, at estimated location of initial crack. In order to model sharp crack propagation based on conventional FEM technique two steps are important. The first step is capturing singularity at crack tip. For a sharp crack the stress field becomes singular at the crack tip. Including the singularity at the crack tip for a small-strain analysis improves the accuracy of the J-integral, Stress Intensity Factors (SIFs) and in general the stress and strain fields calculations. The second step is refining the mesh at each crack propagation increment. The re-meshing technique requires re-mesh the new model and crack tip after advancing the crack in each increment of crack propagation.

To this end, the partitioning of the geometry was defined by the circular lines centred at the crack tip. This partitioning strategy facilitates the gener-

ation of a focused mesh. The crack tip was meshed using a ring of collapsed quadratic quadrilateral elements, which are generally used to obtain a mesh singularity at the crack tip. Specification of the mid-side node parameter and the crack-tip element degeneracy allows different singularity types to be defined. In the present study a value of 0.25 was used for the mid-side node parameter as illustrated in Figure 6.1. This definition moved the mid-side nodes on the element sides adjoining the collapsed edge to the 1/4 points of the elements. At the crack tip, the element sides were collapsed with single-node-type degenerate element control. These settings combine to create a $1/\sqrt{r}$ singularity in strain. The circular partitioned areas were meshed using the "swept meshing" technique, which allows the mesh to be regular and focused. The inclusion of the seam and singularity definition causes to create automatically collapsed elements with correct connectivity definitions.

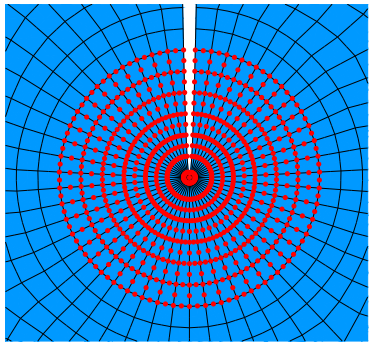

Figure 6.1: Focused mesh around crack tip along with the contour integral circular rings.

The "single node" degeneracy method was used for the elements at the crack tip. In this approach the collapsed element edges are defined by repeating nodes in the element connectivity. After each increment of crack propagation the mode I (K_I) and mode II (K_{II}) SIFs were extracted using domain form of interaction integral method, which available in ABAQUS®. This approach is based on path independent J-integral and also mesh independent. All the elements within the crack front and one layer of elements outside the crack front were used to determine the first contour integral. In computing the additional contour integrals, ABAQUS®automatically adds a single layer of elements to the group of elements that were used to calculate the previous contour integral. These steps are available in ABAQUS®for modelling stationary cracks. In

order to propagate the crack a script was written using Python programming language in conjunction with ABAQUS®solver. It means that the pre and post processing were carried out using Python code and the ABAQUS®solver was using to solve the model in each individual crack propagation step.

6.2.2 XFEM model

Modelling stationary cracks using conventional FEM needs the geometry of cracked body to be matched with the mesh. Therefore, modelling crack propagation using mesh refinement techniques are really cumbersome, especially in 3-D and complex models. As elaborated in Chapter 2, XFEM decreases inadequacy associated with re-meshing of the crack tip. The XFEM technique is the extended version of FEM approach. It allows local enrichment functions to be easily incorporated into a FE approximation. For the purpose of fracture mechanics analysis, the enrichment functions typically consist of the near-tip asymptotic functions that capture the singularity around the crack tip and a discontinuous function that represents the jump in displacement across the crack line (in case of 2-D) as explained in Chapter 2.

There are a lot of studies, which are aimed to implement XFEM feature in conjunction with conventional FE software. For instance, Giner et al. [Giner et al., 2008] have carried out a two-dimensional implementation of XFEM within the ABAQUS®software by means of user elements subroutine. Since after ABAQUS®6.9 the XFEM feature has been added by developers, in this study this capability was used to model the 2-D crack propagation by means of XFEM approach. However, there are some limitations that should be overcome by using Python programming techniques. One the major restrictions is extracting the SIFs at the crack tip for a 2-D stationary crack. The implemented XFEM features in ABAQUS®does not provide the function of extracting J-integral or SIF. Therefore, after modelling cracked specimen based on the stress and displacement fields at the crack tip, a Python script was written to extract the original form of the J-integral for a line contour surrounding the crack tip and SIFs consequently. However, after releasing ABAQUS®6.11 there is an alternative way to extract J-integral and SIFs by means of contour integral crack function.

Some limitations of modelling discontinuities, such as cracks, as an enriched feature (XFEM) in ABAQUS®, which are reported by their developers, can be written as:

- An enriched element cannot be intersected by more than one crack.
- A crack is not allowed to turn more than 90° in one increment during an analysis.
- Only asymptotic crack-tip fields in an isotropic elastic material are considered for a stationary crack.
- Adaptive re-meshing is not supported.

Nevertheless, these are not the only limitations. In general XFEM approach is developed to be a mesh refinement independent method, while this not the reality with the implementation in ABAQUS®. It was found that the mesh should be refined at crack tip to capture real stress and strain field around it. The same fact has also been realized by Vethe [Vethe, 2012]. He found that to achieve an accurate results the mesh size at crack tip has to be at least below 3% of the crack size [Vethe, 2012]. However, by refining the mesh at area of interest the results are accurate.

6.2.3 Crack propagation direction

The direction of the crack propagation can be determined as function of the stress and strain fields at the crack tip. There are several criteria can be chosen to calculate crack propagation direction. Some of the most widely used mixed mode criteria are: the Maximum Tangential Stress Criterion (MTS), the Maximum Energy Release Rate criterion (MERR), the zero K_{II} criterion (K_{II}= 0) criterion.

Maximum Tangential Stress (MTS)

Based on this criterion, the next crack propagation angle is defined to be perpendicular to the maximum tangential stress at the crack tip [Erdogan and Sih, 1963]. The near crack tip stress field for a homogeneous, isotropic linear elastic material is given by:

$$\sigma_{\theta\theta} = \frac{1}{\sqrt{2\pi r}} \cos\frac{\theta}{2}\left[K_I \cos^2\frac{\theta}{2} - \frac{3}{2}K_{II}\sin\theta\right] \tag{6.1}$$

$$\tau_{r\theta} = \frac{1}{2\sqrt{2\pi r}} \cos\frac{\theta}{2}\left[K_{II}\sin\theta - K_{II}(3\cos\theta - 1)\right] \tag{6.2}$$

where r and θ are polar coordinates centred at the crack tip in a plane orthogonal to the crack face. The direction of crack propagation then can be obtained using either the condition $\partial\sigma_{\theta\theta}/\partial\theta = 0$ or $\tau_{r\theta} = 0$, i.e.,

$$K_I \sin\theta_p + K_{II}(3\cos\theta_p - 1) = 0 \tag{6.3}$$

$$\theta_p = \arccos\left[\frac{3K_{II}^2 + \sqrt{K_I^4 + 8K_I^2K_{II}^2}}{K_I^2 + 9K_{II}^2}\right] \tag{6.4}$$

where the crack propagation angle θ_p is measured with respect to the crack plane, i.e., $\theta_p = 0$ represents the crack propagation in "straight ahead" direction and $\theta_p \leq 0$ if $K_{II} \geq 0$, while $\theta_p \geq 0$ if $K_{II} \leq 0$.

Maximum Energy Release Rate (MERR)

By considering a crack segment of length l kinking out the plane of the crack at an angle θ_p. When l is infinitesimally small compared with all other lengths (including the length of the original crack), the SIFs, K_I^k and K_{II}^k at the tip of the putative crack can be expressed as linear combination of K_I and K_{II} [Hayashi and Nemat-Nasser, 1981]. The existing SIFs prior to kinking for the original crack are:

$$K_I^k = \left(\frac{4}{3+\cos^2\theta}\right)\left(\frac{1-\theta/\pi}{1-\theta/\pi}\right)^{\frac{\theta}{2\pi}}\left(K_I\cos\theta + \frac{3}{2}K_{II}\sin\theta\right) \tag{6.5}$$

$$K_{II}^k = \left(\frac{4}{3+\cos^2\theta}\right)\left(\frac{1-\theta/\pi}{1-\theta/\pi}\right)^{\frac{\theta}{2\pi}}\left(K_{II}\cos\theta - \frac{1}{2}K_{II}\sin\theta\right) \tag{6.6}$$

For the crack segment the relation between energy release rate (G^k) and SIFs at small crack tip can be written as:

$$G^k = \frac{1}{E}\left[(K_I^k)^2 + (K_{II}^k)^2\right] \tag{6.7}$$

The MERR criterion postulates that the original crack initially propagates in the direction that maximizes G^k. Finding G^k will establish for the general mixed mode case the duality which is the basis of fracture mechanics: the equivalence in viewing fracture initiation from either a global energy balance or a local stress intensity point of view.

Criterion of local symmetry (Zero K_{II})

This criterion simply postulates that a crack initially propagates in the direction that makes K_{II}= 0, which proposed by Cotterell and Rice [Cotterell and Rice, 1980]. Implementation within a FE model involves the extension of a infinitesimally small crack from the crack-tip, whose direction is varied to attain a minimum for k_{II}. Hayashi and Nemat-Nasser [Hayashi and Nemat-Nasser, 1981] have provided a series of direction-dependent coefficients C_{ij}. At the crack tip, the stress intensity factors for different direction can be expressed as:

$$K_I^k = C_{11}K_I + C_{12}K_{II} \tag{6.8}$$

$$K_{II}^k = C_{21}K_I + C_{22}K_{II} \tag{6.9}$$

As mentioned, the KII=0 criterion postulates that a crack will propagate in the direction that makes $K_{II}^k = 0$. However, it was observed that the variation in Mode II SIF, K_{II}, with infinitesimally small crack direction is approximately linear over a wide range of angles. This linearity has been utilised in an improved algorithm in ABAQUS®for finding the optimum deflection angle. Therefore, some equation such as Equation 6.6 can be used to find the next crack propagation angle, in which leads to minimum value of K_{II}. In some loading conditions, which are not possible to reach K_{II}= 0, therefore ABAQUS®searches for minimum value of K_{II}.

6.3 Benchmark crack propagation problems

Before implementing the developed crack propagation code to fretting fatigue problem, the code was applied to a DENT and DCB specimen for both cases of conventional FEM using re-meshing and XFEM techniques. Then, the results were compared with analytical solution to validate the accuracy of the models.

6.3.1 DENT specimen

A DENT specimen was considered as cracked rectangular linear elastic plate with length and width equal to 20 and 10 mm, respectively as shown in Figure 6.2. The initial crack length and crack propagation increment was considered as 0.2 mm and 0.1 mm, respectively. A uniform tension stress (σ_{axial}= 80 MPa) was applied at both sides of the specimen at the same time. Due to sym-

metry boundary condition just half of the full DENT specimen configuration was modelled. To avoid rigid body motion error, the centre of specimen was restricted from movement in all directions.

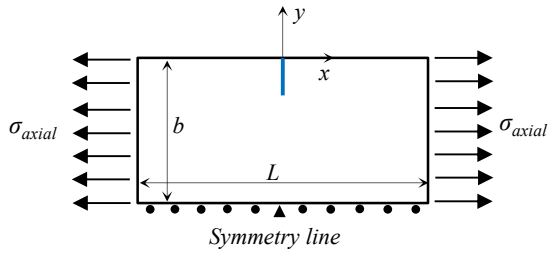

Figure 6.2: Double Edge Notch Tension (DENT) cracked specimen.

For modelling the crack propagation using conventional FEM, a two dimensional, 8-node, plane strain quadrilateral, reduced integration element (CPE8R) was used. The crack-tip singularity was modelled using the same element type. The mesh was collapsed at crack tip. Therefore, all the nodes at the crack tip had the same geometry location. The SIFs were evaluated based on domain integral over an area contained within a contour surrounding the crack tip. The contour integral output was requested for 14 contours.

To model the cracked DENT specimen using XFEM approach, a crack was defined inside a single mesh. To have accurate result the mesh at crack tip was refined sufficiently as depicted in Figure 6.3. The SIFs were extracted step by step during crack propagation. Eventually, the results of two different developed models were compared with the analytical solution given in [Anderson, 2005] and can be written as:

$$K_I = \sigma\sqrt{\pi l}\left[1.99 - 0.41(l/b) + 15.7(l/b)^2 - 38.48(l/b)^3 + 53.85(l/b)^4\right] \quad (6.10)$$

Figure 6.4 illustrates the comparison between the calculated SIFs at the crack tip using conventional FEM, XFEM and analytical solution for of DENT specimen. From the figure it can be seen that, the extracted results from FE model for both conventional FEM and XFEM show good correlation with analytical solution for all crack lengths.

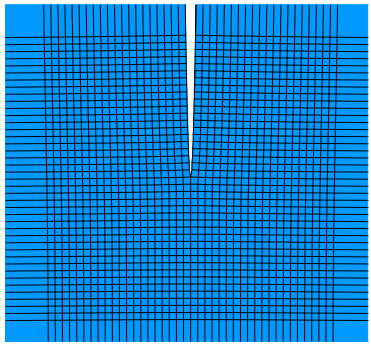

Figure 6.3: XFEM mesh refinement around crack tip (the minimum element size is 50 μm).

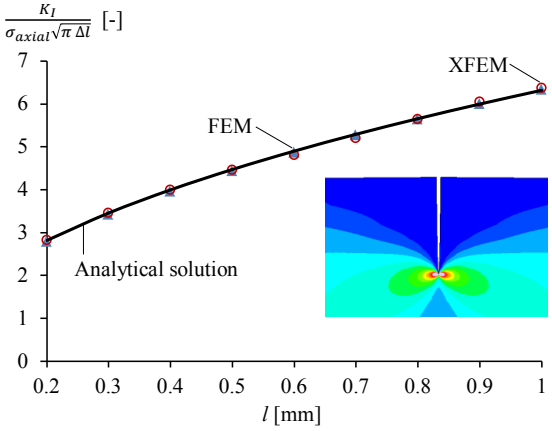

Figure 6.4: Comparison between conventional FEM, XFEM and analytical solution.

6.3.2 DCB specimen

The following DCB example shows the capability of developed XFEM model in order to propagate the crack under mixed-mode and quasi-static conditions. As shown earlier, the crack orientation angle is governed by the values of K_I and K_{II} and for this case study was computed through Equation 6.4. This problem is considered in References [Belytschko and Black, 1999] and is illustrated in Figure 6.5. It is known that the crack propagation of an initial crack l_0 located slightly off the mid-plane follows a path that departs away from the initial plane. The dimensions of the problem were l_0= 2, b= l_0 and L= $3l_0$. Plane strain condition was assumed with material properties as in previous section

and the concentrated load is F= 10 N. The crack propagation analysis was performed for two initial crack locations, whose offset from the mid-plane was ±0.035×b. Fifteen crack growth increments were considered, with a fixed value of $\Delta l = 0.05 \times l_0$.

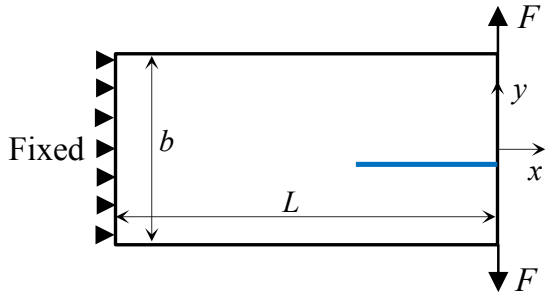

Figure 6.5: Schematic view of slightly eccentric crack in a cantilever beam.

Figure 6.6 shows the crack propagation path under mixed mode condition for the last increment of the propagation. The figure shows the expected crack propagation trajectory pattern for the two initial cracks considered, which was in qualitative agreement with previously reported results by Belytschko [Belytschko and Black, 1999].

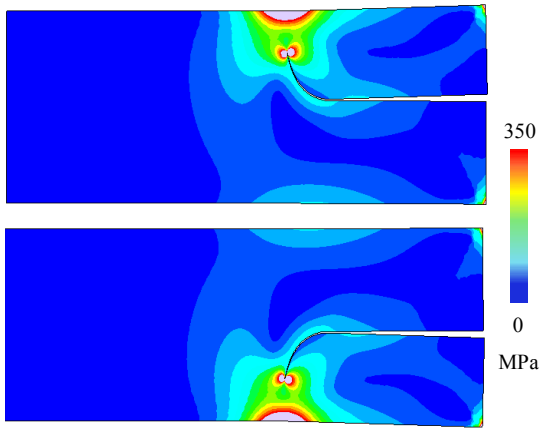

Figure 6.6: von-Mises stress contour plot of eccentric crack propagation at the last crack growth increment.

6.4 Fretting fatigue crack propagation

After validating the developed crack propagation models for both conventional FEM and XFEM approaches, the codes were extended to fretting fatigue crack propagation problem. To this end, the crack propagation model was implemented to single clamp flat (conformal) and cylindrical contact configurations. Moreover, in this study to consider fretting fatigue contact traction on crack propagation, the initial crack was inserted at the predicted location of initial crack in the developed fretting fatigue contact models. In this way the effect of crack propagation on variation of contact stresses in particular frictional shear stress and contact pressure were taken into account.

6.4.1 Crack propagation law

Paris law was used for calculating number of cycles to final rupture. The crack growth rate is related to ΔK and written as:

$$\frac{\Delta l}{\Delta N} \approx \frac{dl}{dN} = C_p(\Delta K)^{n_p} \tag{6.11}$$

where C_p= 1.41 $\times 10^{-12}$ $[(\text{mm/cycle})/(MPa\sqrt{mm})^{n_p}]$ and n_p= 3.353 are material constants for AL 2024-T3 [Szolwinski and Farris, 1998]. In this investigation for mixed-mode loading, ΔK was replaced by an equivalent SIF given by:

$$K_{eq} = \sqrt{K_{I,max}^2 + K_{II,max}^2} \tag{6.12}$$

Therefore, the number of cycles to crack propagation was calculated using.

$$\Delta N = \frac{\Delta l}{C_p(K_{eq})^{n_p}} \tag{6.13}$$

6.4.2 Single clamp flat (conformal) contact

To implement the crack propagation model to single clamp flat contact configuration, the experimental results were taken from literature [Sabsabi et al., 2011] for the same geometry and material properties as elaborated in Chapter 4. Sabsabi et al. [Sabsabi et al., 2011] have performed fretting fatigue tests with a square-ended fretting pad in stick and partial slip regimes as illustrated in Figure 4.33 (see Chapter 4). The cyclic bulk loading has been performed at constant amplitude, stress ratio R = -1 at a frequency of 15 Hz. Fifteen loading

combinations are reported here, varying the contact load and axial stress. They have used Al 7075-T6 for both pad and specimen. The material properties of Al alloy used in their study are listed in Table 6.1.

Table 6.1: Mechanical and fatigue properties of AL 7075-T6 [Sabsabi et al., 2011]

Young's modulus	E	72 [GPa]
Yield stress	σ_{yield}	503 [MPa]
Ultimate stress	σ_{ult}	572 [MPa]
Fatigue limit in torsion	τ_f	95.8 [MPa] (at 10^7 cycles)
Poisson's ratio	ν	0.33
Paris law coefficient	C_p	7.18×10^{-11} $[\frac{(mm/cycle)}{(MPa\sqrt{mm})^n}]$
Paris law exponent	n_p	2.613
Strain hardening exponent	m	10

Sabsabi et al. [Sabsabi et al., 2011] have divided the experiments into three categories based on different contact loads i.e. F= 2 kN, 6 kN and 8 kN. The applied loads for each test are listed in Table 6.2.

Table 6.2: Fretting fatigue experimental loading conditions for single clamp conformal contact configuration [Sabsabi et al., 2011]

Test no.	F [kN]	σ_{axial} [MPa]	N_f [cycle]
1	2	110	105958
2	2	130	64764
3	2	150	35181
4	2	170	24306
5	2	190	12509
6	4	110	92259
7	4	130	47714
8	4	150	32905
9	4	170	27391
10	4	190	9590
1	8	110	82549
2	8	130	43567
3	8	150	25872
4	8	170	23046
5	8	190	8760

As mentioned above, the initial crack was inserted at predicted location of initial crack, which was at contact edge for conformal contact configuration. In order to do so, the FE model of conformal contact was used as elaborated in Chapter 4. Due to sharp corners of conformal contact configuration, the small initial crack (50 μm length) occurs at early stage of the fretting fatigue lifetime. Since there is no clear explanation for crack initiation size in fretting fatigue case, in this study the initial crack length was selected based on below assumptions. First of all, in the CDM approach the initiation lifetime was calculated based on macro-crack initiation. Navarro et al. [Navarro et al., 2011] have shown that the chosen initial length has a relative effect on the initially predicted crack evolution rather than final lifetime. In some practical applications, for instance in the aerospace industry, the Eddy current technique is used for detecting these types of cracks as reported by Lykins et al. [Lykins et al., 2001b]. The smallest detectable crack size using Eddy current technique is around 760×380 μm semi-circular crack [Lykins et al., 2001b]. Moreover, there is no special criterion to define the fretting fatigue initial crack length, which depends on its practical application. Relying on the above mentioned reasons, an initial crack length of l_0= 200 μm was considered in this study for conformal contact configuration. The crack propagation increment, Δl, was considered to be 50 μm till crack propagates to 1 mm and then gradually increased up to final rupture.

The crack propagation steps was modelled using XFEM modelling approach as explained above. In the propagation process, it was assumed that the crack propagation takes place normal to the specimen surface, and the stress intensity factor (SIF) range is $\Delta K = K_{max}$, having assumed that K_{min}= 0 due to crack closure [Giner et al., 2009]. To compute the propagation life, it is necessary to calculate the SIF K_I. The SIFs calculation was performed by means of the path independent interaction integral function available in ABAQUS®.

Figures 6.7 (a)-(c) shows the effect of different variables such as axial stress and contact load on crack growth from 200 μm initial crack till 3.5 mm length. The figure also suggests that, for the analysed configuration by increasing contact load from 2 to 8 kN, the crack propagates slower in most cases. However, this variation is obvious at lower axial stresses (i.e. 110, 130 and 150 MPa) and almost negligible at high stress levels (i.e. 170 and 190 MPa). Furthermore, as expected crack propagation life drops drastically by rising axial stress regardless the contact load.

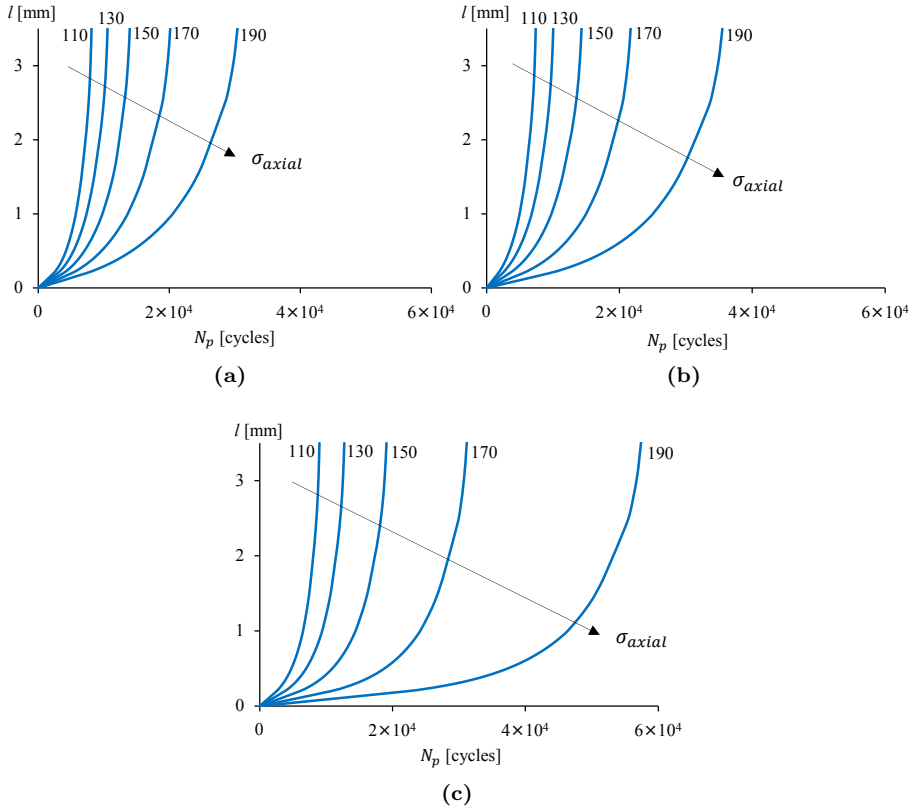

Figure 6.7: Variation of crack propagation lifetime versus crack length for different applied axial stresses and contact loads (a) 2 kN, (b) 4 kN and (c) 8 kN.

6.4.3 Single clamp cylindrical contact

Both conventional FEM and XFEM methods were applied to investigate fretting fatigue crack propagation of single clamp cylindrical contact configuration. There are several ways by which a crack can be defined to be short. Cracks, whose length is of the order of the grain size of the material, are called microstructurally small flaws. When the crack size is comparable to the near tip plasticity size, they are called mechanically short cracks. Cracks, whose physical length is very small (2 mm or less), are termed as physically small cracks. If the chemical inclusions in the material (or the environmental effects) cause the crack to exhibit anomalies in propagation rate, the cracks are said to be

chemically small. The present work deals with cracks of size 50 μm, which was selected based on considering the macro-crack initiation as crack initiation onset. Hence, fretting fatigue initial crack comes under the category of physically and micro-structurally small cracks. Therefore, the initial crack was inserted at predicted location of crack as elaborated in Chapter 5. Then the crack was propagated using the developed crack propagation codes under mixed mode condition.

Mixed mode behaviour

In order to study the effect of different crack propagation direction criteria on fretting fatigue crack propagation problem, the above mentioned criteria were implemented to FE model. For comparing the numerical models with experimental results, the crack propagation directions were also defined based on experimental observation. As discussed in Chapter 3, from experimental observation it can be noted that, after crack initiation, the initial crack propagates under mixed mode condition up to two times of semi contact width ($2a$) and after that the crack propagation is governed by axial stress and perpendicular to contact interface. The same behaviour has been also observed by other researchers [Hills and Nowell, 1994, Szolwinski and Farris, 1998, Hoeppner et al., 1994].

The initial crack angle was measured for all experiments, which were between -35° and -45°. Nevertheless, Giner et al. [Giner et al., 2008] has reported that different crack initiation angles do not strongly affect the orientation after a few crack increments. Based on these facts, the initial crack was inserted at angle of -40° and was forced to decrease gradually to reach zero angel at two times of semi contact width, i.e. 1 mm. This crack propagation path was more or less the same as what was observed in experimental tests. Hence, this crack propagation trajectory was considered as real crack path based on experimental observations.

Fig 6.8 illustrates the crack propagation directions using three different criteria i.e. MTS, MERR and KII= 0, which are usually used for proportional loading condition, did not match with the predefined crack path based on experimental observation.

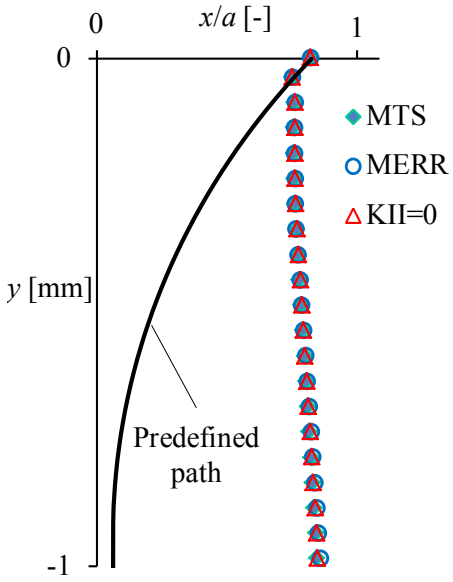

Figure 6.8: Comparison between crack propagation trajectories of three different criteria used for proportional loading condition and predefined crack path based on experimental observation for FF6.

Figure 6.9 depicts that the difference between normalised number of cycles to crack propagation (N_p/N_f) was around 21% (for FF6 experiment) between predefined crack path and other three criteria for different calculated crack growth trajectories. Based on the above reasons, the fretting fatigue crack propagation was modelled using predefined crack path based on experimental observation with an initial angle of -40°, which inserted into FE contact models for including the effect of crack contact interaction. In order to study the mixed mode crack propagation behaviour of contact subjected to fretting fatigue loading condition, the experimental tests for single clamp cylindrical contact configuration were used with the loading conditions elaborated in Chapter 3 and 4.

Figure 6.10 illustrates the variation of normalised equivalent SIFs (K_{eq}/K_{Ic}) versus crack length for different crack propagation direction criteria from the initial crack length of 50 μm up to 1 mm. From the figure, it can be noted that by increasing crack length all three criteria overestimate the value of K_{eq}, which results in lower number of crack propagation cycles and as crack length reaches two times of semi contact width ($2a$) the value of K_{eq} is almost equal

to that of predefined crack path criterion.

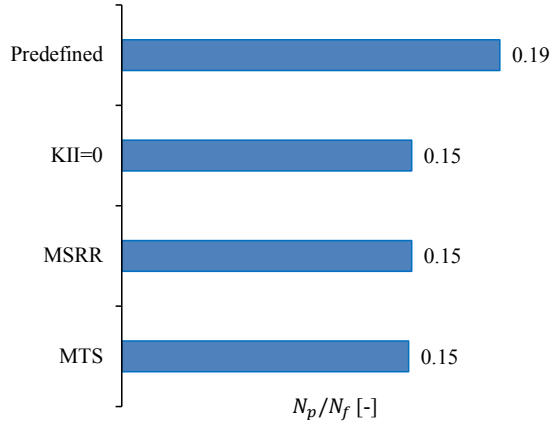

Figure 6.9: Comparison between normalized numbers of cycles to propagation and different crack propagation criteria for FF6.

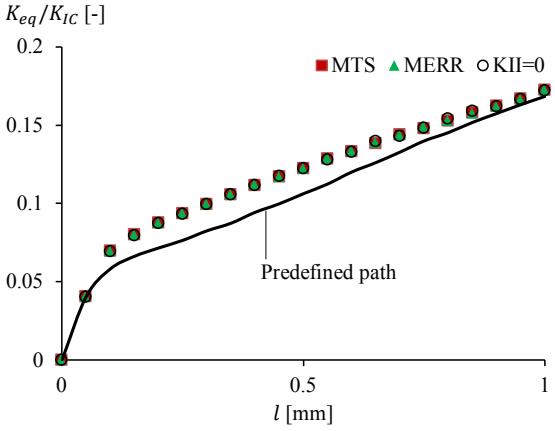

Figure 6.10: Comparing normalized equivalent SIFs (K_{eq}/K_{Ic}) for different crack propagation criteria for FF6 (K_{Ic}= 2083 MPa$\sqrt{mm}$).

Figure 6.11 shows a comparison of normalised fretting fatigue crack propagation lifetime between predefined crack path based on experimental observation and MTS criterion for all simulated models. The average error of 34% was found between predefined crack path and predicted by MTS criterion for all simulated models.

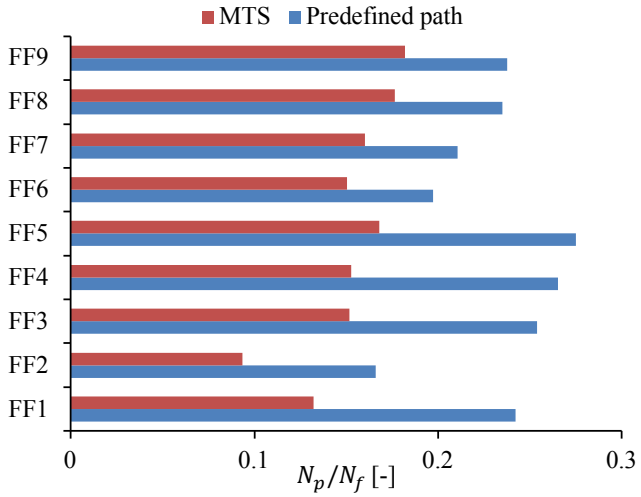

Figure 6.11: Comparison between normalized numbers of cycles to propagation of predefined crack path and MTS criterion for all models.

Figure 6.12 illustrates the variation of normalized equivalent SIFs versus the crack length for different models. Figure 6.13 indicates the variation of crack propagation lifetime for different crack length. As expected by increasing the axial stress the value of equivalent SIF increases, which results in higher crack propagation lifetime.

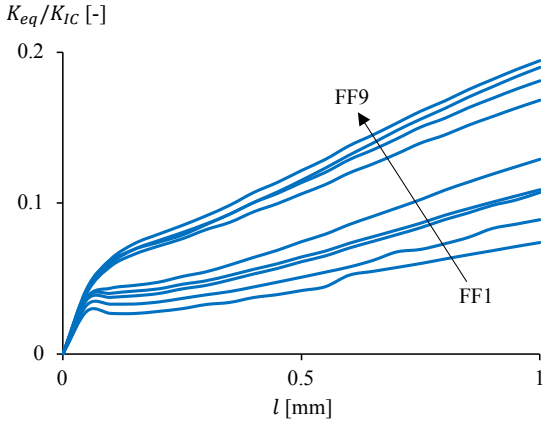

Figure 6.12: Variation of normalized equivalent SIFs versus the crack length for FF1 till FF9.

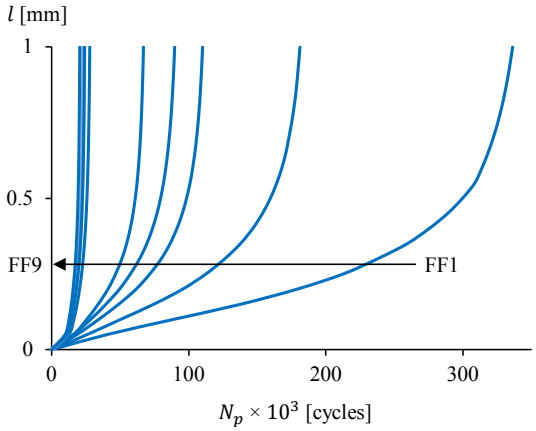

Figure 6.13: Variation of the crack length versus crack propagation lifetime for FF1 till FF9.

Figure 6.14 indicates the von-Mises stress distribution contour plot for different crack propagation crack propagation time steps. As mentioned above, the fretting fatigue initial crack was inserted with an angle of -40° at predicted location of crack for FF1 i.e. $x/a = 0.92$. Afterwards, it was forced to decrease gradually up to two times of semi contact width i.e. $2a = 1$ mm. Then, the crack was propagated perpendicular to the contact interface.

6.4.4 Conventional FEM VS XFEM

In order to validate the extracted SIFs, both conventional FEM using remeshing technique and XFEM crack propagation models were compared to each other. Furthermore, the results were compared with analytical solution in literature by using the theoretical contact stress fields to estimate K_I using weight function approach. For this purpose, fretting fatigue crack propagation was modelled by inserting the initial crack at trailing contact edge $x/a = 1$. For sake of comparison with analytical solution, the crack was forced to propagate perpendicular inside the specimen. An initial crack of length, $l_0 = 50$ μm, was introduced in the model. The crack length increment of $\Delta l = 50$ μm was considered for crack propagation. The length and width of the specimen along with the radius of pad were selected as $L = 20$ mm, $b = 10$ mm and $R = 101.6$ mm, respectively. Al 7075-T6 was selected for both pad and specimen with Modulus of Elasticity of 71 GPa and a Poisson's of 0.33. A COF of 0.8 was

used in this study. The normal load, tangential load and maximum axial stress were considered as F= 60 N, Q= 60 N, σ_{axial}= 80 MPa, respectively. The zero stress ratio was selected for both cases.

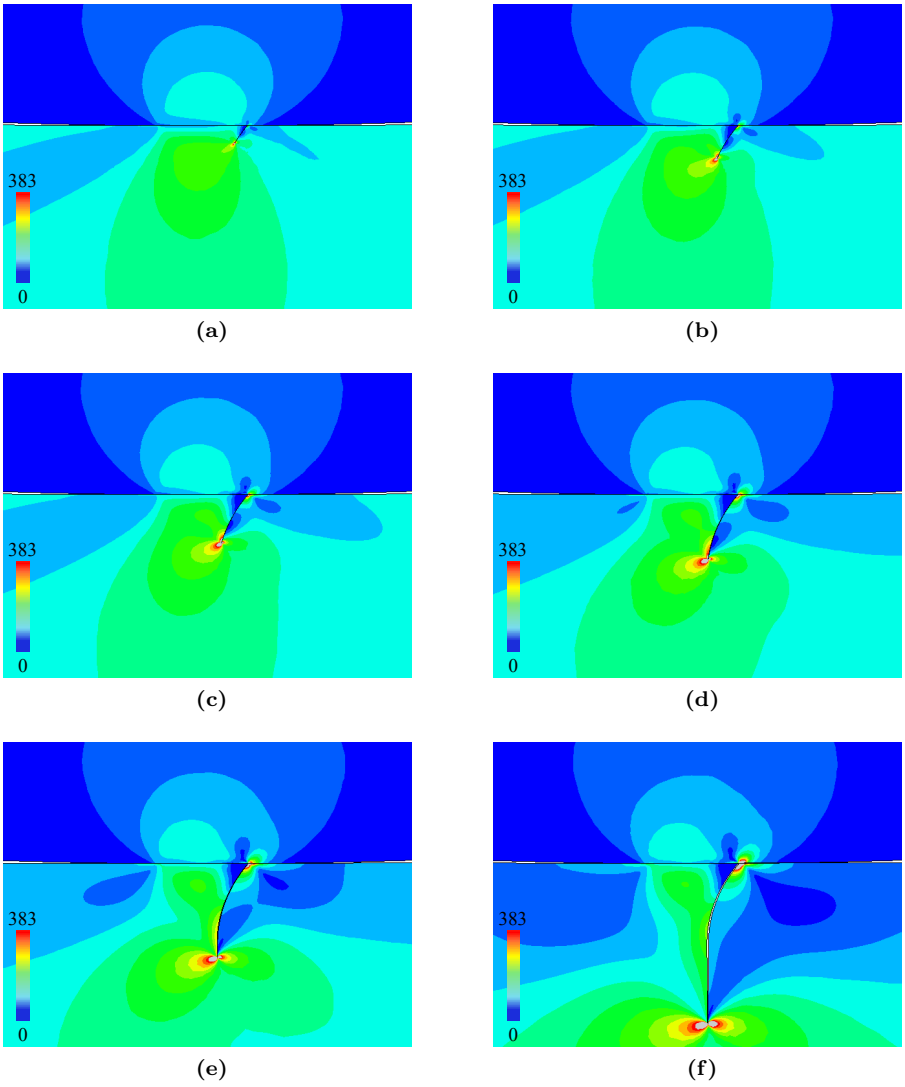

Figure 6.14: von Mises stress distribution contour plot of fretting fatigue crack propagation for FF1.

Eventually, the calculated SIFs were compared with analytical solution,

which was based on weight function method [Tada et al., 2000]. In the weight function (WF) approach, the stress distribution along the hypothetical crack location was calculated from FE contact model (solved for a configuration with no-crack) and combined with a weight function, W(y), specifically derived for a given geometry to yield K_I as:

$$K_I^{WF} = \sqrt{\frac{2}{\pi}} \int_0^l \sigma_x(x,y) w(y) dy \tag{6.14}$$

For a crack normal to the surface of specimen, the tangential stress σ_x was extracted from the FE contact model at location of hypothetical crack (x/a= 1). In this study, the weight functions W for both SENT and DENT specimens in a strip of finite width were used [Tada et al., 2000].

For SENT specimen the weight function gives the following expression:

$$K_I^{WF} = \sigma\sqrt{\pi l}\left[\frac{\sqrt{\frac{2b}{\pi l}\tan\left(\frac{\pi l}{2b}\right)}}{\cos\left(\frac{\pi l}{2b}\right)}\left[0.75 + 2.02(l/b) + 0.37\left(1 - (\sin(\pi l/2b))\right)^3\right]\right] \tag{6.15}$$

For DENT specimen the weight function gives the following expression:

$$K_I^{WF} = \sigma\sqrt{\pi l}\left[\frac{1.12 - 0.5(l/b) - 0.2(l/b)^2 + 0.47(l/b)^3 - 0.19(l/b)^4}{\sqrt{1-(l/b)}}\right] \tag{6.16}$$

Figure 6.15 depicts the variation of mode I SIFs versus different crack lengths for fretting fatigue problem using conventional FEM, XFEM and different analytical solutions, namely DENT specimen and weight function approach for both SENT and DENT specimens. As it can be seen from the figure, the results from FEM and XFEM for calculated SIFs nicely correlate to each other. However, the analytical values of SIFs estimate lower value at earlier stage of crack propagation to compare with FEM and XFEM crack propagation results. This is because of the effect of crack contact interaction on crack propagation, which is not taken into account in analytical solutions. Nevertheless, far from the contact zone analytical solutions, FEM and XFEM results converge approximately to same values. The reason for this convergence is related to dominate

behaviour of axial stress far from the contact zone. It can be concluded that the analytical approaches cannot account for interaction effects, so their application always introduces a certain degree of error in the SIF calculation when compared to the conventional FEM or XFEM solutions.

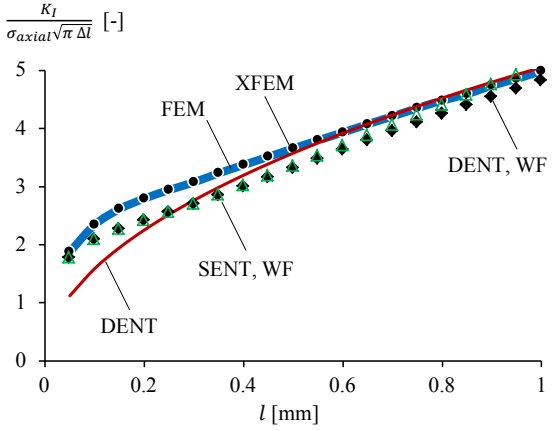

Figure 6.15: Comparison between extracted SIFs at crack tip for conventional FEM, XFEM and analytical solutions.

6.5 Summary and conclusions

In this chapter a general 2-D crack propagation model was developed using both conventional FEM and XFEM approaches by means of Python programming languages in conjunction with ABAQUS®. In order to verify the developed codes, two different benchmark studies, namely, Double Edge Notch Tension (DENT) specimen and Double Cantilever Beam (DCB) specimen, were modelled. Eventually, the developed codes i.e. both conventional FEM and XFEM approaches were implemented to 2-D fretting fatigue crack propagation problem. To sum up, in this study a python script was written to model the developed fretting fatigue crack propagation. In order to set up the crack propagation algorithm for the prediction of the crack path, a step by step process was used as depicted in Figure 6.16.

The results showed good correlation between FEM models using re-meshing technique and XFEM technique using single mesh approach. Moreover, by comparing the numerical results with analytical solutions, it was concluded

that the analytical values of SIFs are less than numerical values at earlier stage of crack propagation and converge far from the contact region. The reason was found that the analytical approaches cannot account for interaction effects, so their application always introduces a certain degree of error in the SIF calculation when compared to the conventional FEM or XFEM solutions.

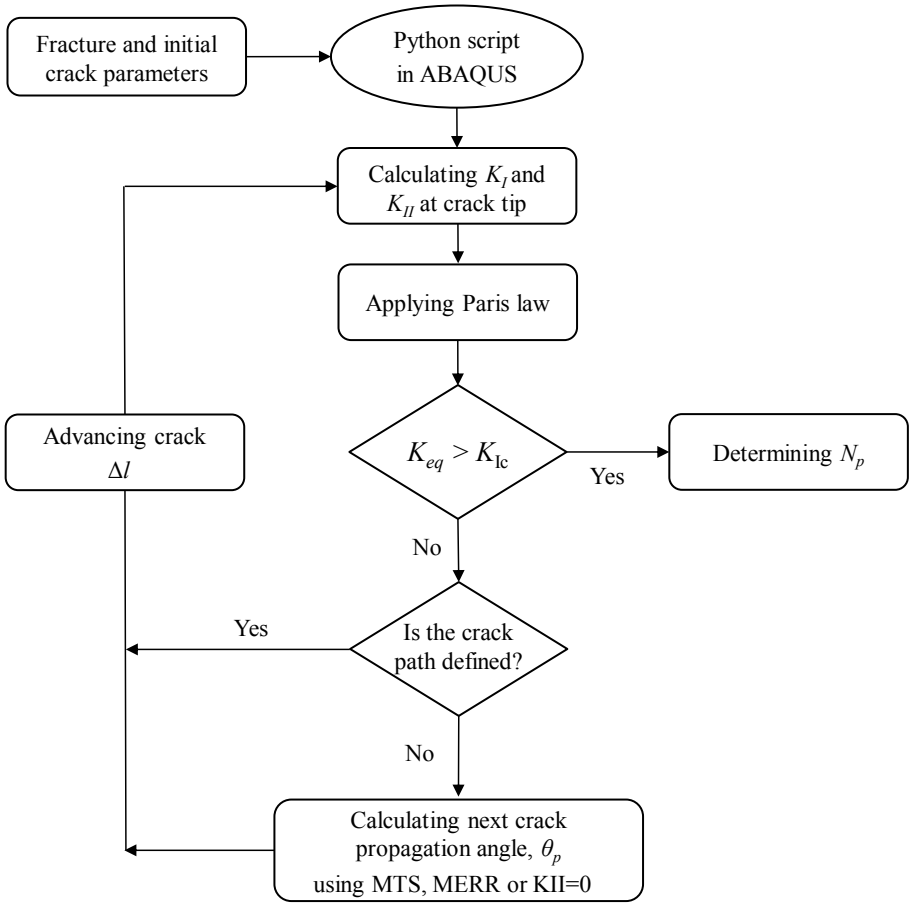

Figure 6.16: Fretting fatigue crack propagation process flowchart.

Crack propagation trajectory was modelled based on experimental observations and compared with three different criteria, which are usually used for proportional loading condition, available in literature i.e. MTS, MERR and KII=0. It was found that, the average error of number of cycles to crack propagation was around 34% between predefined crack path based on experi-

mental observation and predicted by MTS criterion for all simulated models. The main reason of observed discrepancy in estimation of crack growth trajectory is that, the fretting fatigue problem is subjected to non-proportional loading, which invalidates the application of conventional mentioned model and orientation criteria that are only useful for proportional loading. This local no-proportional loading condition comes from three different acting loads, namely axial, tangential and contact loads. However, this phenomenon should be investigated further as theoretical and practical support is not available for evaluating the growth of fatigue cracks under non-proportional cyclic loading conditions. There are a lot of factors that can affect crack propagation under non-proportional loading condition, most of which are not yet thoroughly understood. Some of these factor can listed as: the material model, the degree of cyclic plastic deformation and its direction ahead of the crack tip, the crack closure phenomenon [Giner et al., 2013], the related mean stress effect, the components geometry in general and especially the variable mode-mixity along a crack front [Vormwald and Zerres, 2012]. These factors were not investigated further in this study.

Chapter 7

Fretting fatigue FE based lifetime estimation tool

"In this chapter the developed fretting fatigue crack initiation and propagation models are combined in order to find a prediction tool to estimate fretting fatigue total lifetime"

7.1 Overview

In this chapter the developed FE models for fretting fatigue crack initiation and propagation are combined to predict total lifetime. To this end, the developed models are implemented to two different experimental set-ups, namely, single clamp cylindrical and flat contact configurations.

In terms of fretting fatigue crack initiation, both developed un-coupled damages models i.e. based on elastic and elasto-plastic behaviour of material are used to estimate the number of cycles to crack nucleation for single clamp cylindrical and flat contact configuration, respectively. The damage models are calibrated using experimental results and FE models by means of non-local approach to capture the stress gradient effect at contact interface. In order to propagate the fretting fatigue initial crack, the same results are used as elaborated in Chapter 6. Eventually, the fretting fatigue total lifetime is predicted by means of continuum damage mechanics and fracture mechanics approaches.

7.2 Fretting fatigue total lifetime estimation

In this section the developed damage models are implemented to two different single clamp contact configurations, namely, cylindrical and flat contact.

7.2.1 Cylindrical contact

The total lifetime of cylindrical contact configuration is predicted, while subjected to fretting fatigue loading conditions. For this purpose, the uncoupled damage evolution law combined with crack propagation model was implemented to performed fretting fatigue experimental tests. As elaborated in Chapters 3 and 4, Al 2024-T3 was selected for both the pad and the specimen with Modulus of Elasticity of E= 72.1 GPa and a Poisson's ratio of ν= 0.33. The FE model of fretting fatigue contact was the same as explained earlier in Chapter 4.

In order to select the proper damage model, the stress distribution at trailing contact edge was monitored for all simulated models. It was observed that the maximum stress for all loading conditions did not exceed the yield limit and the assumption of elastic behaviour of material was valid for this case. Therefore, the developed damage model for elastic behaviour of material was selected to estimate the fretting fatigue crack initiation lifetime. Figures 7.1

(a)-(f) illustrate the contour plot of hydrostatic stress, triaxiality ratio and function inside the specimen for one full cyclic loading the for FF1.

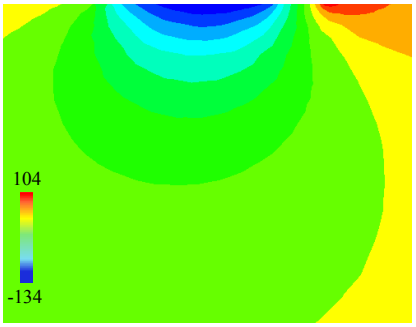

(a) Maximum σ_H (MPa)

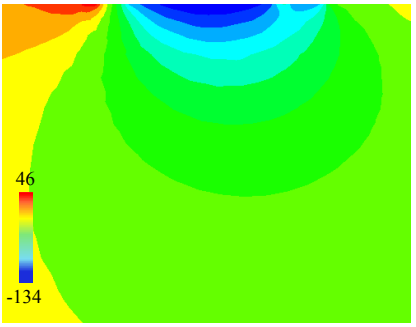

(b) Minimum σ_H (MPa)

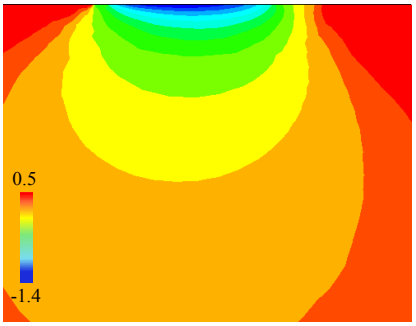

(c) Maximum T_x (-)

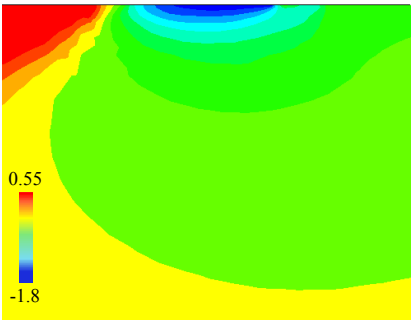

(d) Minimum T_x (-)

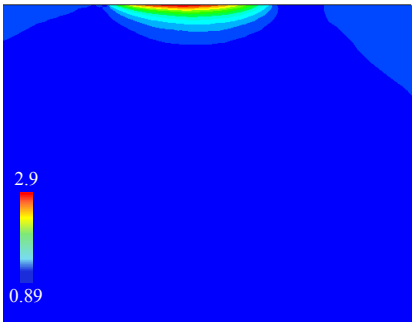

(e) Maximum R_v (-)

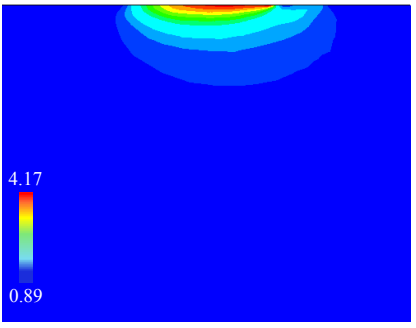

(f) Minimum R_v (-)

Figure 7.1: Variation of hydrostatic pressure (σ_H), triaxiality ratio (T_x) and function (R_v) inside the specimen for one full cyclic loading the for FF1.

Note that the variation of triaxiality ratio and function is high during one

applied cyclic load at contact interface. These variations prove the complexity of non-proportionality of multiaxial state of stress contact interface in fretting fatigue problem. However, it can be seen from Figures 7.1 (e) and (f) that this high variation is at centre of contact between pad and specimen. The variation of triaxiality function at and near contact edge is almost constant during on cycle. While, to overcome this small variation and using one value in the damage model, the non local averaging approach was used.

Non local approach

Due to fretting fatigue contact condition, the stress gradient is really high at edge of contact, and therefore all extracted data will be mesh dependent. To overcome this mesh dependency problem a methodology based on process zone method and the theory of critical distance was used to extract the required data for damage model. In this approach the stresses were averaged over a semi-circular area centred at the predicted location of crack initiation, having a radius equal to the critical distance L_c [El Haddad et al., 1980] defined by:

$$L_c = \frac{1}{\pi}\left[\frac{\Delta K_{th}}{\sigma_{0[10^6]}}\right]^2 \tag{7.1}$$

The average value of triaxiality function R_v and the maximum and minimum equivalent stress i.e. $\sigma_{eq,max}$ and $\sigma_{eq,min}$ were then calculated inside the process zone. Typical values for Al2024-T3 were considered for long crack threshold stress intensity factor range, ΔK_{th}= 100 MPa $\sqrt{mm}$ [Forman et al., 2005] and plain fatigue strength, $\sigma_{0[10^6]}$= 263 MPa, which results in $L_c \approx 50\ \mu m$. Moreover, the effect of different process zone radii on fretting fatigue crack initiation lifetime has been studied in previous Chapter 6, which revealed that changing this radius has minor effect on estimated fretting fatigue crack initiation life.

Calculation of damage parameters

Since the damage parameters A and β of the damage model are unknown material constants, experimental tests were chosen to determine and calibrate the damage parameters. Three calibration tests were selected covering the broad range of applied axial stress. Therefore, for each of selected experimental test, the average triaxiality function and the maximum and minimum equivalent stress were calculated inside the process zone. Extracted data were then sub-

stituted into the damage evolution law Equation 5.10. The values of the damage parameters were then found using regression analysis to calculate the best least square fit between the predicted cycles for crack initiation and the experimental data for crack initiation, as elaborated earlier. The experimental crack initiation lifetime was calculated by subtracting numerical crack propagation lifetime from the observed experimental total lifetime. Therefore, using the same procedure, damage parameters were calculated for experimental tests FF1, FF5 and FF8 for calibration, as listed in Table 7.1. As mentioned above for calculating crack initiation lifetime a Python script was written to facilitate the whole procedure.

Table 7.1: Summary of damage parameters from nonlinear regression analysis

Test no.	σ_{axial} [MPa]	x/a [-]	R_v [-]	σ^* [MPa]	-ln(A) [-]	β [-]
Calibrated results						
FF1	100	0.92	1.271	93	65.64602	7.1
FF5	160	0.81	1.279	155	65.64641	6.94
FF8	220	0.84	1.290	217	65.64707	6.72
Estimated results						
FF2	115	0.9	1.275	109	65.64571*	7.09*
FF3	135	0.88	1.279	129	65.64585*	7.03*
FF4	135	0.88	1.277	129	65.64585*	7.03*
FF6	190	0.81	1.281	184	65.64621*	6.88*
FF7	205	0.81	1.284	200	65.64632*	6.84*
FF9	220	0.81	1.287	216	65.64642*	6.79*
$*$ Calculated from Figure 7.2						

In this study the variation of damage parameters against the equivalent multiaxial damage stress was monitored at contact interface. Therefore, instead of considering one value for each damage parameter, A and β were plotted as a function of equivalent multiaxial damage stress (σ^*) during one full cycle as depicted in Figures 7.2 (a) and (b), respectively. From Figure 7.2 (b) and Table 7.1, it was realized that the variation of damage parameter A was almost constant for cylindrical contact configuration under applied loading conditions. Thus, the value of A was calculated as the average value of three calibrated values.

Total lifetime prediction

After predicting crack initiation in previous section and propagation lifetime in previous Chapter (Chapter 6), now it is time to combine them together to predict fretting fatigue total lifetime.

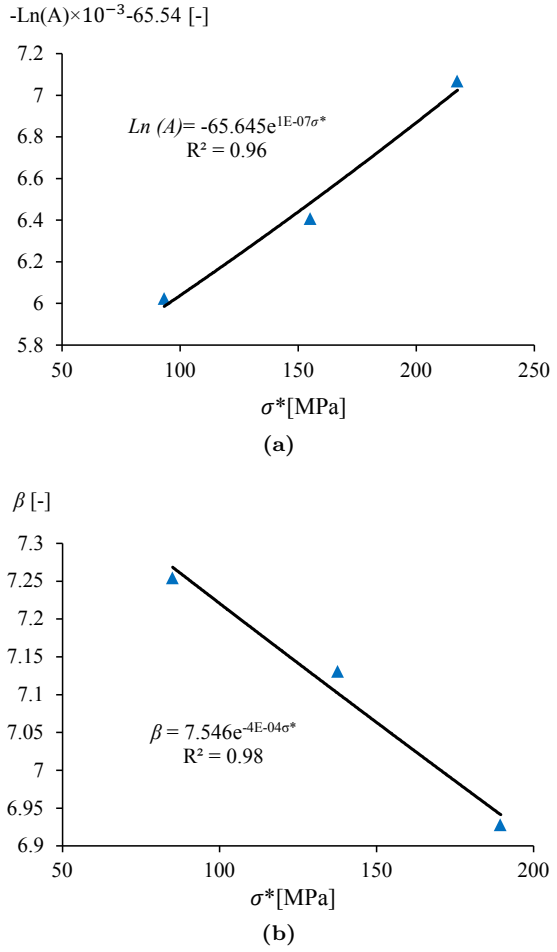

Figure 7.2: Variation of damage parameters (a) A and (b) β versus equivalent multiaxial damage stress (σ^*) during one full cycle for cylindrical contact configuration.

Figure 7.3 depicts the predicted fretting fatigue total lifetime versus the experimental one. From these results, it can be realised that the estimated results by using combination of uncoupled damage model and crack propagation model fall within the scatter bands of $\pm$ 50%, which can be evidence to establish confidence in robust predictive capability of proposed methodology to estimate fretting fatigue lifetime. From these results, it can be concluded that by restricting fretting fatigue variables to the multiaxial stress field in particular stress triaxiality at contact region, it is possible to predict its behaviour.

The effect of multiaxial state of stress at contact region was considered by including the triaxiality function distribution in the damage evolution model.

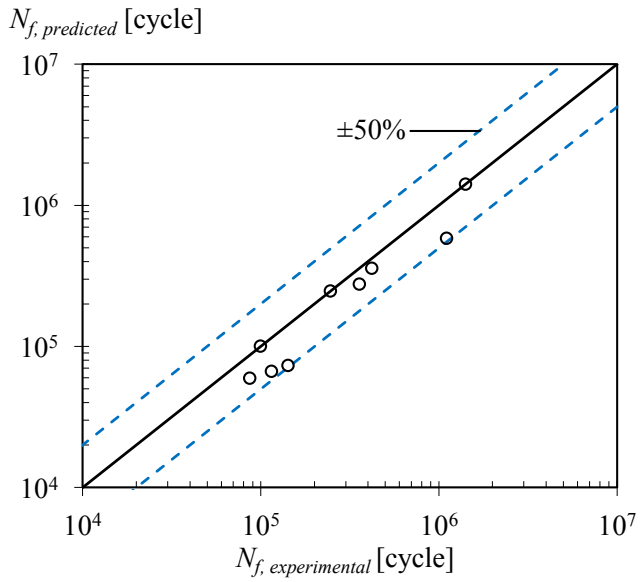

Figure 7.3: Predicted fretting fatigue total lifetime versus experimental observation for cylindrical contact configuration.

Figure 7.4 depicts the percentage of predicted lives for all nine experiments carried out for cylindrical contact configuration. The initiation life is taken as the number of cycles at which the crack 50 μm nucleates and the propagation life is taken as the number of cycles take for advancing crack from 50 μm to final rupture. As it can be seen in the figure for all modelled cases the fretting fatigue lifetime is dominated by the crack initiation portion. The average predicted initiation life was found to account for 69% of the total estimated life. Figure 7.5 represents variation of the predicted initiation and propagation life versus equivalent multiaxial damage stress, σ^*. As shown by increasing equivalent multiaxial damage stress both estimated initiation and propagation lifetimes decline.

In order to be concrete about the proposed methodology, results from the literature were used to estimate fretting fatigue total lifetime. For this purpose FE models were developed for fretting fatigue contact problem based on experimental results from Szolwinski and Farris [Szolwinski and Farris, 1998],

as elaborated in Chapter 5.

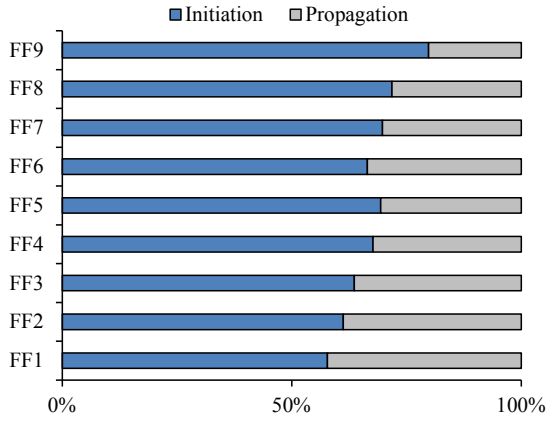

Figure 7.4: Estimated percentage of fretting fatigue crack initiation and propagation lifetime.

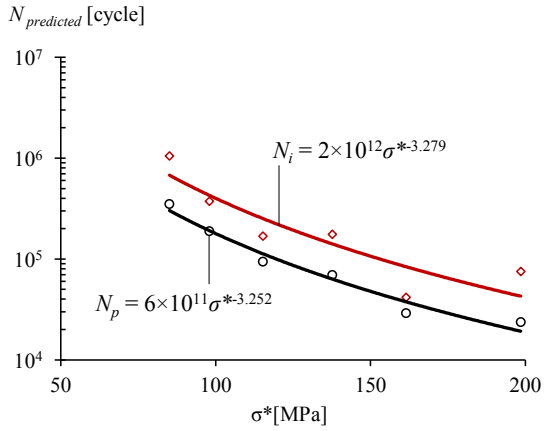

Figure 7.5: Variation of predicted initiation and propagation lifetimes versus equivalent multiaxial damage stress.

The fretting fatigue crack initiation lifetime has been already estimated in Chapter 5. Therefore, crack propagation was modelled by inserting a 1 mm crack length at predicted location of initial crack based on equivalent multiaxial damage stress approach in the contact model and propagated till final rupture of bulk material. The crack forced to propagate perpendicular to con-

tact interface based on experimental observation, which has been reported in [Szolwinski and Farris, 1998]. Eventually, by combining the estimated fretting fatigue initiation and propagation lifetime, the total lifetime was calculated. As depicted in Figure 7.6 predicted results are in good agreement with observed experimental data and most of them are conservative, which confirms the reliability of proposed approach.

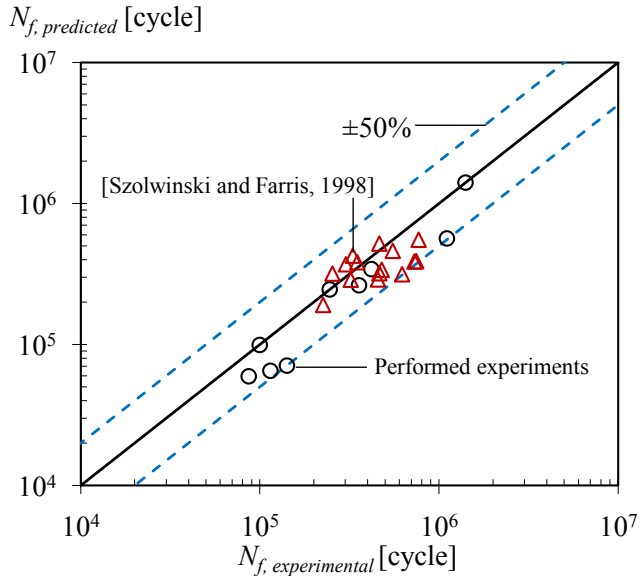

Figure 7.6: Estimated fretting fatigue total lifetime versus experimental results taken from literature [Szolwinski and Farris, 1998].

7.2.2 Flat contact

In order to predict fretting fatigue lifetime under elasto-plastic condition, single clamp flat contact configuration was chosen. The stress and strain fields has been calculated in Chapter 3 by means of FE modelling approach. Thus, to predict the initiation lifetime, the developed un-coupled damage model for elasto-plastic behaviour of material i.e. Equation 5.19 was used in conjunction with the FE model. Afterwards, the crack propagation lifetime was calculated using XFEM approach to advance the initial crack to the final rupture of specimen, as elaborated in Chapter 6.

Moreover, the predicted results were then compared with another life esti-

mation model, which was utilized in [Sabsabi et al., 2011] based on the variable initiation length model which have been proposed by Navarro et al. [Navarro et al., 2003], whereas in this work the initiation crack length is fixed as 200 μm. Eventually, all of predicted results were compared with observed experimental results.

Triaxiality distribution

Figures 7.7 (a) and (b) indicates the variation of T_x during one cycle. As can be seen the value of T_x varies from tension to compression and is not constant during one fretting fatigue cycle due to non-proportional loading condition. The average value of triaxiality ratio was used in order to determine the number of cycles to initiation by means of the derived damage evolution model. Figure 7.8 shows typical variation of average value of triaxiality function (R_v) versus equivalent multiaxial damage stress for all single clamp flat contact experiments. From the figure it can be noticed that, R_v increases non-linearly as σ^* rises.

Calculation of damage parameters

Same as cylindrical contact configuration, some experiments were chosen to determine damage parameters. These calibration tests were selected covering the broad range of axial stress for one contact load e.g. 2 kN. Since contact load variation from 2 to 8 kN does not have significant influence on fretting fatigue lifetime [Sabsabi et al., 2011], selecting other contact loads was assumed to give same accuracy. Therefore, for each of selected experimental tests, the average triaxiality function and the maximum and minimum equivalent stresses were calculated inside the process zone at the contact edge with semi-circle radius of L_c= 50 μm. Extracted data were then substituted into the damage evolution law, Equation 5.19. The values of the damage parameters were then found using regression analysis to calculate the best least square fit between the predicted cycles for crack initiation and the experimental data for crack initiation, which was calculated by subtracting crack propagation lifetime from the total lifetime, as described earlier.

Using the described procedure, damage parameters were calculated for experimental test 1 to test 5 (see Chapter 6, Table 6.2), and listed in Table 7.2. Moreover, both damage parameters A and β are plotted as a function of averaged equivalent multiaxial damage stress (σ^*) as shown in Figure 7.9 (a) and

(b), respectively.

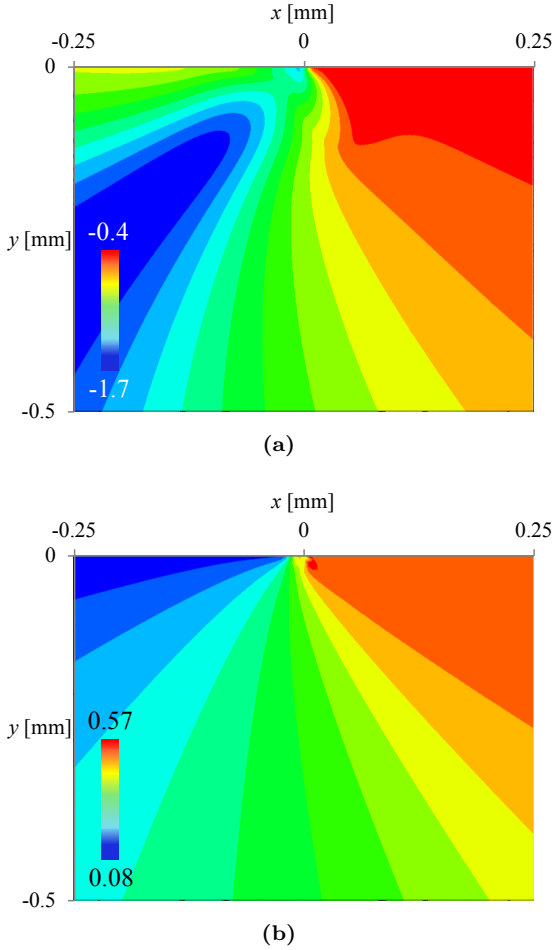

Figure 7.7: Variation of triaxiality ratio under (a) tension and (b) compression loading condition at F= 2 kN and σ_{axial}= 110 MPa.

It is also worth to mention that the damage parameters calculated for flat contact configuration show different trends respect to those calculated for cylindrical contact configuration, in spite of using almost the same Aluminium alloy. The main reason for this difference is related to localized plastic deformation at contact edge for flat contact and defining elasti-plastic material response. This difference in material definition leads to different von-Mises and triaxiality stress distributions, which causes different equivalent multiaxial damage stress

distribution. Eventually, this difference results in different trends for damage parameters.

Table 7.2: Summary of damage parameters from nonlinear regression analysis

Test no.	R_v [-]	σ^* [MPa]	-ln(A) [-]	β [-]
Calibrated results				
1	1.14	221	68.66	0.0161
2	1.08	217	68.87	0.0155
3	1.04	204	69.08	0.0196
4	1.02	183	69.70	0.0248
5	1.00	156	70.09	0.0678
Estimated results				
6	1.14	217	68.73*	0.0116*
7	1.10	204	68.82*	0.0129*
8	1.05	183	69.11*	0.0184*
9	1.02	155	69.56*	0.0319*
10	1.00	224	70.17*	0.0661*
11	1.13	219	68.67*	0.0108*
12	1.08	204	68.79*	0.0124*
13	1.04	181	69.12*	0.0186*
14	1.02	153	69.60*	0.0333*
15	1.00	217	70.21*	0.0697*
∗ Calculated from Figure 7.9				

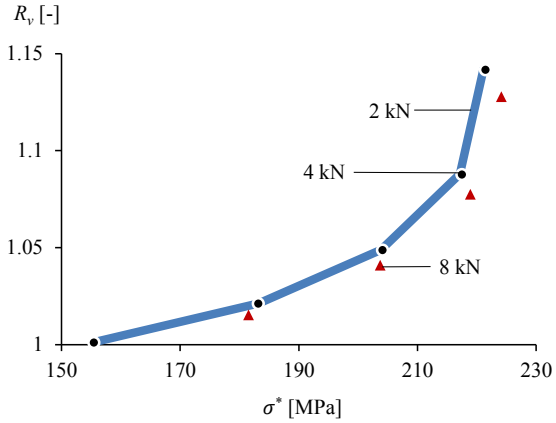

Figure 7.8: Variation of R_v against σ^* for all experimental tests at different contact loads.

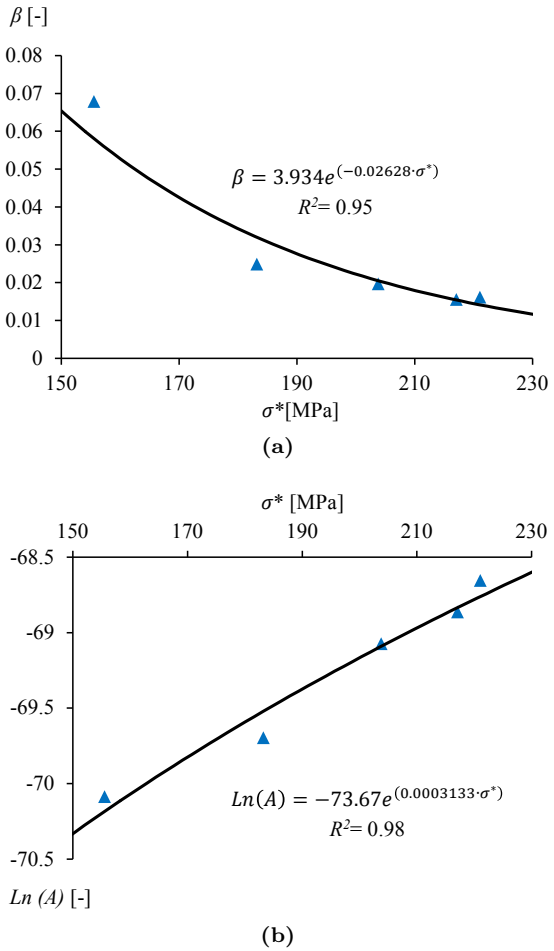

Figure 7.9: Variation of damage parameters (a) A and (b) β versus equivalent multiaxial damage stress (σ^*) during one full cycle for flat contact configuration.

Comparing with McDiarmid criterion

Furthermore, as mentioned above, the estimated results using CDM+XFEM approach were compared with the variable initiation length life estimation model proposed by Navarro et al.[Navarro et al., 2003]. Their model assumes that the initiation length is not an a priori fixed length, but it can be changed depending on the loading conditions. A combination of critical plane criteria and XFEM approaches was used for modelling crack initiation and crack prop-

agation portions, respectively. The McDiarmid criterion was chosen as critical plane approach as discussed in Chapter 2 (see Equations 2.95 and 2.96). The critical plane in the McDiarmid criterion is the plane where the shear stress range is maximum. Hereafter, the combination of McDiarmid criterion plus XFEM approaches is called McDiarmid+XFEM.

Figure 7.10 indicates the predicted total lifetime for each of the analysed tests compared with McDiarmid+XFEM approach and validated against experimental data tabulated in Table 6.2. As shown in Figure 7.10, all of the estimated CDM+XFEM model results lie within the scatter bands of ± 50%, which evidences the robust predictive capability of the proposed combination of damage and fracture mechanics approaches to estimate fretting fatigue lifetime.

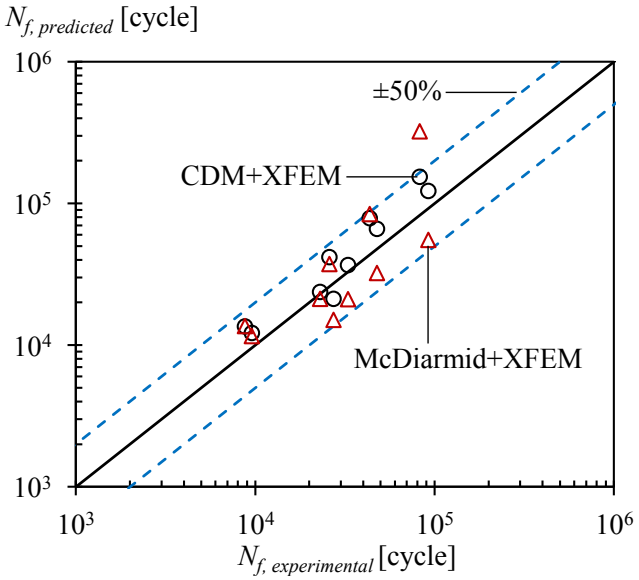

Figure 7.10: Fretting fatigue predicted versus experimental total lifetime from literature [Sabsabi et al., 2011], for single clamp flat contact configuration.

statistical analysis

A statistical parameter, Root Relative Squared Error (RRSE) method, was used in order to compare the accuracy and reproducibility of the two methods. This parameter allows determining whether the results are reliable or not. The RRSE normalizes the total squared error by dividing it by the total

squared error of the observed experimental results. Mathematically, the RRSE is evaluated by the equation:

$$RRSE = \sqrt{\frac{\sum_{i=1}^{n} \left(N_{e(i)} - N_{o(i)}\right)^2}{\sum_{i=1}^{n} \left(N_{o(i)} - \overline{N}_o\right)^2}} \tag{7.2}$$

where $N_{e(i)}$, is the value estimated for each test i and $N_{o(i)}$ is the observed experimental data for sample case i, and $\overline{N}_o$ is given by the formula:

$$\overline{N}_o = \frac{\sum_{j=1}^{n} N_{o(j)}}{n} \tag{7.3}$$

For a perfect estimation, the numerator is equal to zero in Equation 7.2 and RRSE= 0. Therefore, the RRSE index ranges from zero to infinity, with zero corresponding to the ideal fretting fatigue lifetime estimation. The values of RRSE for CDM+XFEM approach was 0.76, while RRSE value for McDiarmid+XFEM technique was 2.9. It can be concluded that the combination of the CDM and XFEM method provides an estimated life close to the experimental life as depicted in Figure 7.10. For the conformal contact problem analysed, the CDM approach produces better average results than the McDiarmid criterion. Figure 7.11 depicts the predicted lives for the fifteen experiments considered in this investigation. In the figure, the initiation life is taken as the number of cycles at which the long crack 200 μm initiates and the propagation life is taken as the number of cycles required for advancing crack from 200 μm to final rupture. As can be seen in the figure for all contact loads at lower axial stress amplitudes, the life is dominated by the crack initiation portion, and as expected, by increasing axial stress, the initiation lifetime declines. The average initiation life was found to account for 55 % of the total estimated life.

Figure 7.12 illustrates two fretting contact conditions, where the predicted fretting fatigue crack initiation life is plotted versus the computed local relative slip. As can be seen, crack initiation life increases with decreasing relative slip amplitude for different contact loads.

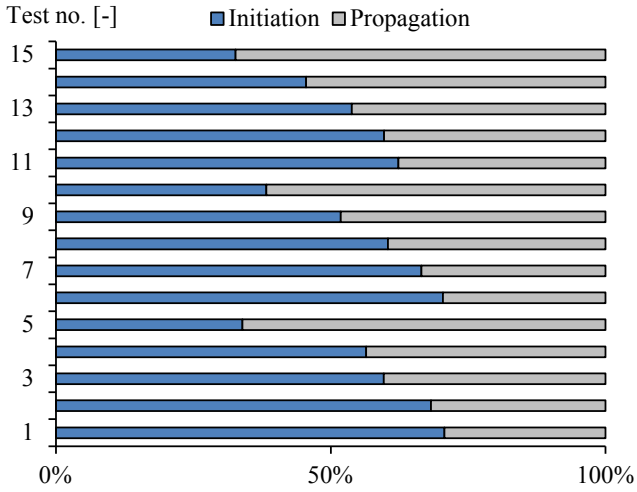

Figure 7.11: Predicted fretting fatigue total lifetime of the fifteen experiments tabulated in Table 6.2 by means of CDM+XFEM approach.

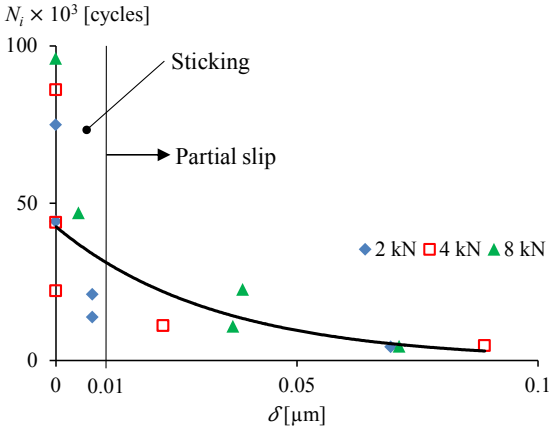

Figure 7.12: Relation between predicted crack initiation lifetime and slip amplitude.

Effect of process zone size

As shown in Chapter 4, for conformal contact configuration, the stress gradient is high at vicinity of contact edge due to the singularity. Therefore, the size of different process zones must have influence on estimated results. In order to check the sensitivity of the damage model to the process zone approach based on critical distance method, the size of the process zone varied between 20 and

80 μm. The damage parameters A and β were recalculated for each of the process zone radii.

From Figure 7.13, it can be noticed that by decreasing L_c to 20 μm, the estimated life increases. When L_c rises to 80 μm, the stress gradient around the edge of contact will drop rapidly. Therefore, the estimated lifetime for 80 μm diminishes when compared with other two radii. From these results, it can be concluded that even under the presence of singularity at the contact edge, the CDM approach is an effective tool to estimate fretting fatigue crack initiation lifetime. The same level of sensitivity has been found for cylindrical contact configuration as elaborated earlier.

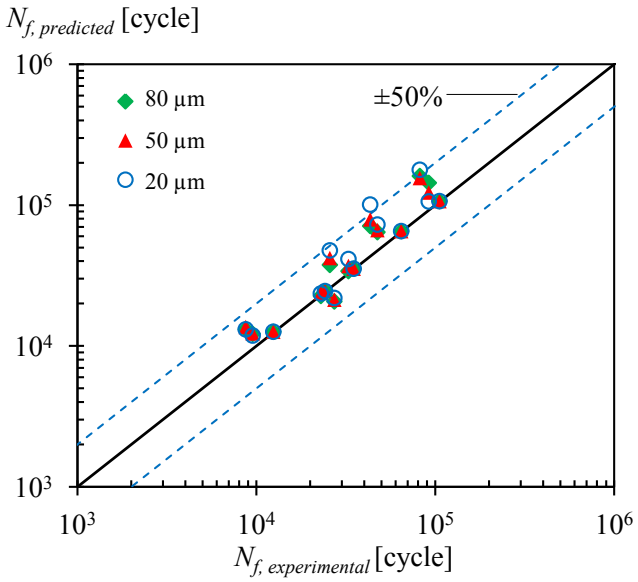

Figure 7.13: Predicted fretting fatigue total lifetime versus experimental results for different process zone radii.

7.3 Summary and conclusions

In this chapter in order to predict fretting fatigue total lifetime, the developed FE models for fretting fatigue crack initiation and propagation were combined. The developed models have been implemented to two different experimental set-ups, namely, single clamp cylindrical and flat contact configurations.

CDM approach was chosen, which is based on the principle of thermodynamics, for modelling crack initiation lifetime and the fracture mechanics approach was used to study the propagation of the initial crack till final rupture of the fatigue specimen. Fretting fatigue damage parameters were computed based on regression analysis to calculate the best least square fit between the estimated cycles to crack initiation and the observed experimental ones. Numbers of cycles to crack initiation were then calculated using the developed damage model. For crack propagation, the SIF calculation has been carried out using numerical models under XFEM framework. In terms of cylindrical contact configuration, the estimated results show a good correlation with the observed experimental ones. After separating crack initiation and propagation lifetimes, the average estimated initiation life was found to account for 69% of the total estimated life. The proposed model was also successfully implemented to experimental data from literature. The main aim of this investigation was to propose a reliable and robust approach to estimate fretting fatigue lifetime. In order to achieve this goal the same approach has been extended to flat contact configuration. The predicted fretting fatigue life using CDM+XFEM approach has been compared with the variable crack initiation method (McDiarmid+XFEM) and validated against observed experimental results. Predicted results using CDM+XFEM approach were in a good correlation with the observed experimental data. From the results, it can be concluded that combination of CDM and XFEM approach gives better results when compared with McDiarmid+XFEM approach.

Eventually, from the results, it can be concluded that combination of damage and fracture mechanics approach can be a good estimation tool for predicting fretting fatigue behaviour. Moreover the proposed approach can be applied to real application of fretting fatigue problems with more complicated geometries. Furthermore, this approach i.e CDM+XFEM, can be combined with FE modelling approach to investigate the effect of different fretting fatigue variables such as different phase differences between tangential, normal, axial loads and material impurities on fretting fatigue behaviour, as will be elaborated in Chapter 8.

Chapter 8

Effects of phase difference and material impurities on fretting fatigue initiation lifetime

"In this chapter, the developed crack initiation model is used in order to study the effect of phase difference between tangential, normal, axial loads and material impurities on fretting fatigue initiation lifetime"

8.1 Overview

In this chapter, the effect of phase difference between axial and tangential load on fretting fatigue behaviour is investigated. Moreover, by applying cyclic contact load instead of constant contact load, its effect on fretting fatigue response and crack initiation lifetime is investigated.

Furthermore, the sensitivity of fretting fatigue parameters and crack initiation lifetime is investigated by adding different types of surface and sub-surface geometrical inhomogeneities using the CDM combined with FE modelling approaches. Subsequently, effect of geometrical impurities on fretting fatigue parameters and crack initiation life are discussed.

8.2 Effect of phase difference

As proved earlier, fretting fatigue contact problem is highly non-linear and subjected to non proportional loading condition. The multiaxial nature of stress at contact interface can be highly influenced by phase difference between axial, tangential and contact load. In this section, the effect of phase difference between axial and tangential load along with effect of applying cyclic contact load instead of constant contact load on fretting fatigue behaviour is investigated.

8.2.1 Introduction

In contact problems subjected to fretting fatigue loading conditions, the stress state at and near contact interface is highly influenced by combination of contact, tangential and axial bulk load. Therefore, any combination of these loads varies the stress state distribution at and near contact interface. As shown earlier, the fretting fatigue crack initiation formation is highly localized process and depends on localized stress distribution at or near the contact edge. The phase difference between applied loads is one of the important factors that can influence the stress sate at and near contact interface and fretting fatigue damage threshold consequently. Although several studies on fretting fatigue has been reported in literature, most of the works were of in phase loading between axial and tangential loads. Moreover, most of the previous works were accomplished under a constant applied contact load and a little effort was done under a variable contact load.

Lee and Mall [Lee and Mall, 2006] have investigated the effect of phase

difference between axial cyclic load and tangential force on fretting fatigue parameters for Ti-6Al-4V. They have revealed that the relative slip and tangential force ranges were related to each other and their relationship was not influenced by phase difference under partial slip regime. They have reported that relative slip as well as tangential force changed by changing phase difference. However, they found that the effect of phase difference on total lifetime (crack initiation+crack propagation) was negligible at given tangential force and/or relative slip. Almajali [Almajali, 2006] has studied the effect of phase difference between axial and contact loads. Iyer and Mall [Iyer and Mall, 2000] have varied the applied contact load along with the applied axial load frequency on Ti-6Al-4V. They found that by increasing the contact pressure the fretting fatigue life has been reduced at 1 Hz and it has not been affected at 200 Hz. Iyer and Mall [Iyer and Mall, 2000] reported that the decrease of fretting fatigue total lifetime by increasing the contact load can be related to the increase in the local stress range amplification along the contact surface, without any regard to the increase in the local shear stress or slip amplitude. Jutte [Jutte, 2004] found that fretting fatigue total lifetime with variable contact loads was less than fatigue life for tests with equivalent constant contact loads.

In this section, there are two main aims; the first one is to investigate effect of phase difference (PD) between axial and tangential load on fretting fatigue parameters and initiation lifetime. The second goal is to determine the fretting fatigue behaviour under the cyclic contact load. For this purpose, a parametric FE model for fretting fatigue contact problem was modelled using Python language along with ABAQUS®. Crack initiation number of cycles was then predicted based upon the developed uncoupled damage model, which consists of the multiaxial stress state at location of initial crack and the damage parameters, which have been calibrated using experimental data.

8.2.2 Material and FE model

Al 2024-T3 was selected for both the pad and the specimen with modulus of elasticity of E= 72.1 GPa and a Poisson's ratio of ν= 0.33. To solve the fretting fatigue cylindrical contact model, a parametric FE model was developed using Python language along within the ABAQUS®software. In this study six different loading conditions were selected from the performed experimental tests as listed in Table 8.1.

In order to control the PD between tangential and axial loads, the same FE

Table 8.1: Selected performed fretting fatigue experimental tests.

Test no.	σ_{axial} [MPa]	R [mm]	F [N]	Q_{max} [N]	$N_{failure}$ [-]
FFPD1	100	50	543	155.165	1407257
FFPD2	115	50	543	186.25	1105245
FFPD3	135	50	543	223.7	358082
FFPD4	160	50	543	193.7	245690
FFPD5	190	50	543	330.15	141890
FFPD6	220	50	543	267.15	99607

model was used as elaborated in Chapter 4. However, just for sake of completes the FE model is briefly described in this section. As depicted in Figure 8.1, the specimen was restricted from vertical and horizontal movements along its bottom and right sides, respectively and free to roll in the x-direction along its bottom edge.

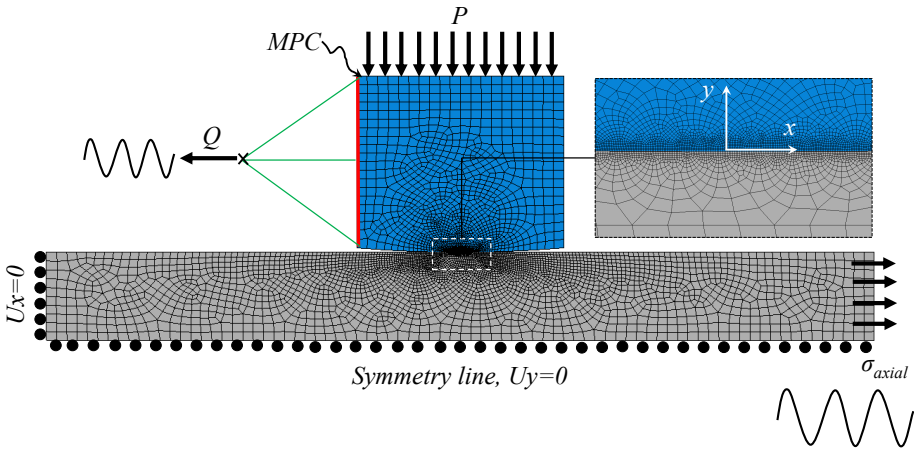

Figure 8.1: FE of fretting fatigue cylindrical contact model.

The MPC constrain was also applied at the right side of pad in order to avoid it from rotating due to the applied tangential load. The length of the specimen, width of the specimen and the radius of pad were selected as L= 40 mm, b= 5 mm and R= 50 mm, respectively. Both the fretting pad and the fatigue specimen had a 4 mm depth. A two-dimensional, 4-node (bilinear), plane strain quadrilateral, reduced integration element (CPE4R) was used. The mesh size of 5 $\mu m \times 5$ μm was considered at contact interface and decreased gradually far from the contact region. The contact between the fretting pad and the fatigue specimen was defined using the master-slave algorithm in ABAQUS®with COF

of μ= 0.65.

loading sequence

The loading sequence was applied in six loading steps. In step one, the contact pressure was applied and increased gradually up to the maximum value and kept constant for remaining time steps. Both sides of cylindrical pad were restricted to move just in vertical direction during applying contact pressure and released afterwards as illustrated in Figure 8.1. Figure 8.2 depicts schematically the applied cyclic load on the specimen and tangential load on the fretting pad with three PD = 0°, 90°, 180° between them.

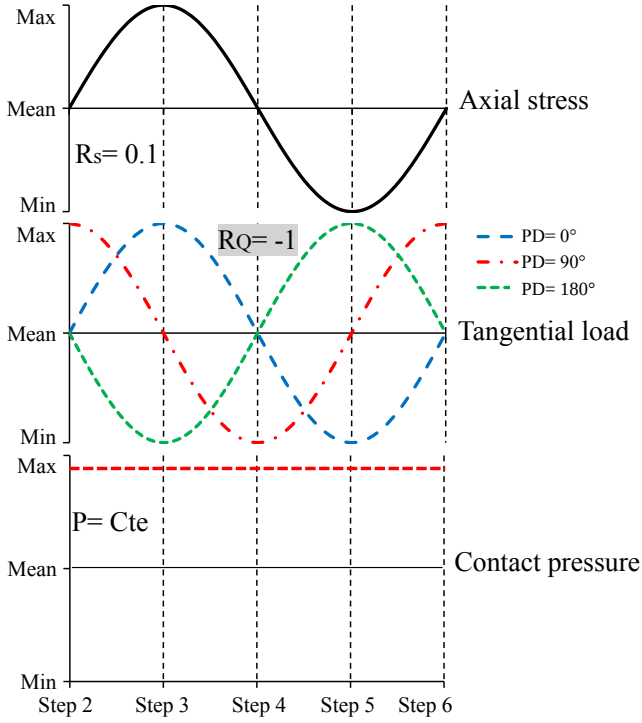

Figure 8.2: Loading sequence, phase difference between axial stress and tangential load.

For PD= 0°, which was the experimental test condition, the applied tangential load reached its maximum value when the maximum axial stress was applied. In case of PD= 90°, the mean value of tangential load was applied

along with the maximum axial stress as shown in Figure 8.2. Finally, for PD= 180°, the minimum tangential load was applied at maximum applied axial stress. Moreover, the axial stress and tangential load ratios were 0.1 and -1, respectively. In these PD cases, the contact pressure kept constant as shown in Figure 8.2. Furthermore, fretting fatigue behaviour was investigated under cyclic contact load, which is also called radial fretting load. In this case the stress ratios for applied stresses and loads were equal to 0.1 with PD= 0° as illustrated in Figure 8.3.

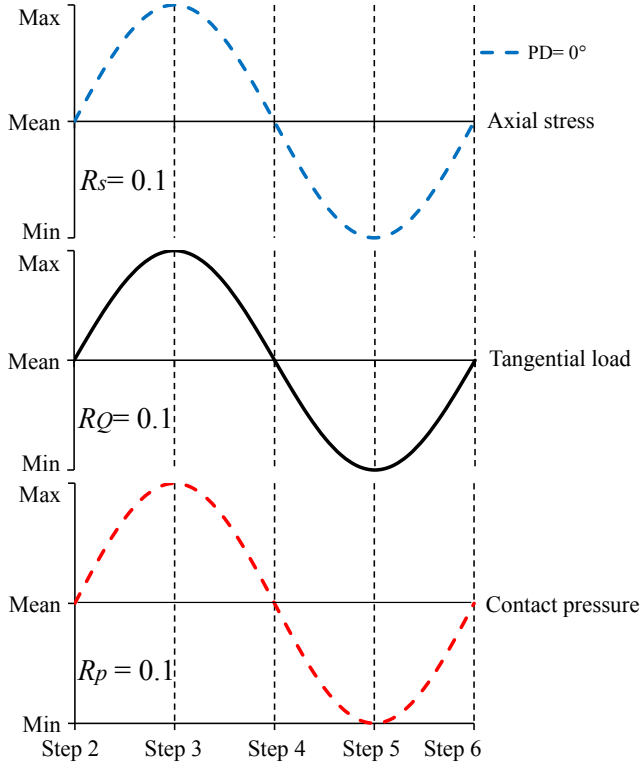

Figure 8.3: Loading sequence, applying cyclic contact load (contact pressure).

8.2.3 Effects of different PDs

In order to monitor the variation of stress state at contact surface, tangential stress distribution (σ_x) was extracted and compared for different PDs. Figures 8.4 (a)-(c) illustrate the normalized tangential stress distribution at contact

interface versus the contact distance which is normalized by semi-contact width. For all tests, the location of maximum stress is shifted to the left side (i.e. x/a= -1) of the contact interface for PD= 90° and 180°.

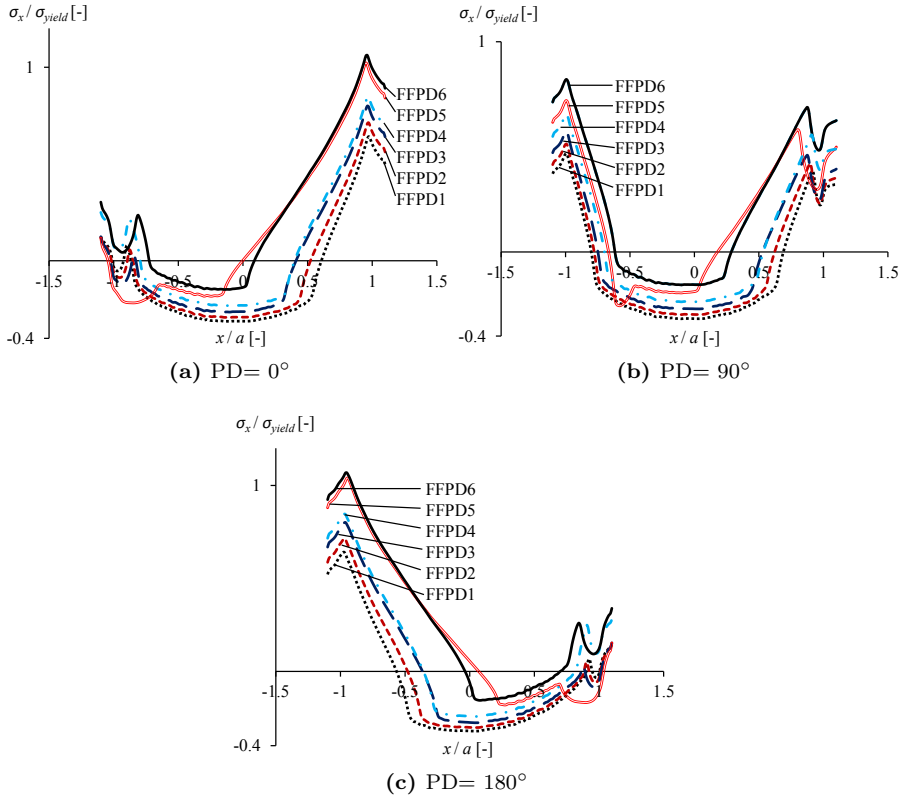

(a) PD= 0° **(b)** PD= 90°

(c) PD= 180°

Figure 8.4: Variation of tangential stress distribution at contact interface for different PDs.

These interesting results indicate the possibility of shifting the area of interest from the right side of contact (x/a= 1) in case of PD= 0° to other side of contact (x/a= -1) in cases of PD= 90° and 180°. This shifting phenomenon may lead to change in the location of initial crack, however, the location of initial crack is not governed only by the stress state at contact interface. In order to find a proper way to estimate the location of initial crack, slip distribution at contact interface can be taken into account as discussed earlier. For this purpose the location of initial crack was estimated based on the maximum location of dissipated energy at contact interface after one full cyclic loading.

Figures 8.5 illustrate the variation of dissipated energy after one full cyclic loading for each of the fretting fatigue models with different PDs. From the figure it can be seen that the location of maximum dissipated energy is shifted to the left side of contact interface (x/a= -1) for PD= 90° and 180°.

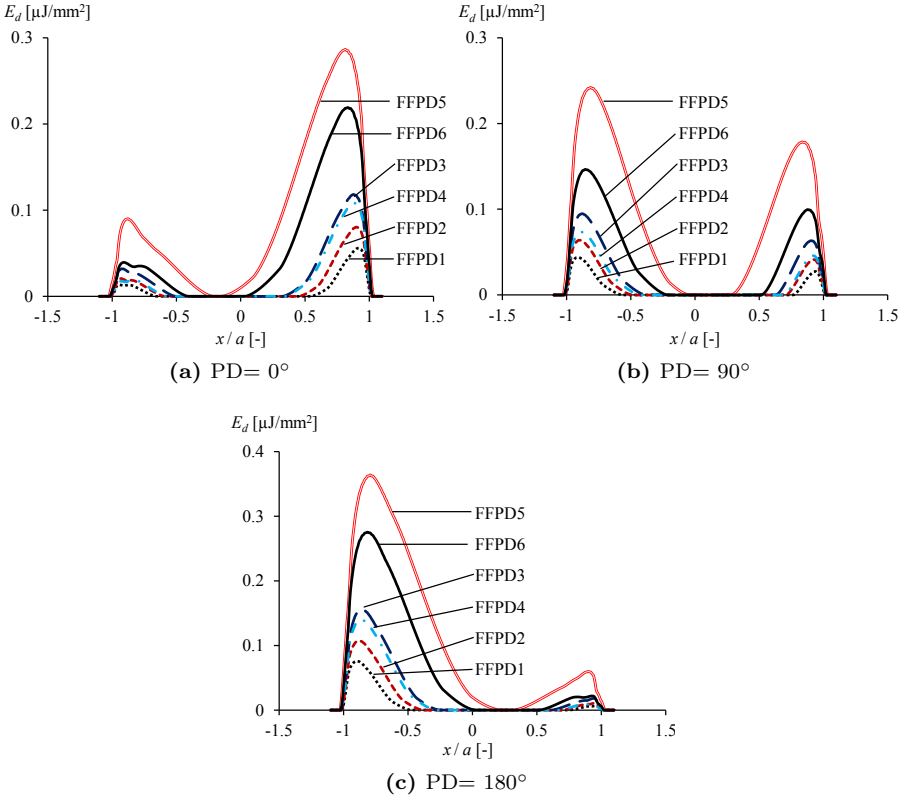

(a) PD= 0° **(b)** PD= 90°

(c) PD= 180°

Figure 8.5: Variation of dissipated energy distribution at contact interface for different PDs.

Figurers 8.6 (a) and (b) depict the comparison between different PDs for tangential stress distribution and dissipated energy at contact interface. These interesting results reveal that by changing the PD from 0° to 180° the stress distribution is mirrored, nonetheless, the dissipated energy for PD= 180° is not mirrored and is higher than PD= 0° case at the left side of contact interface.

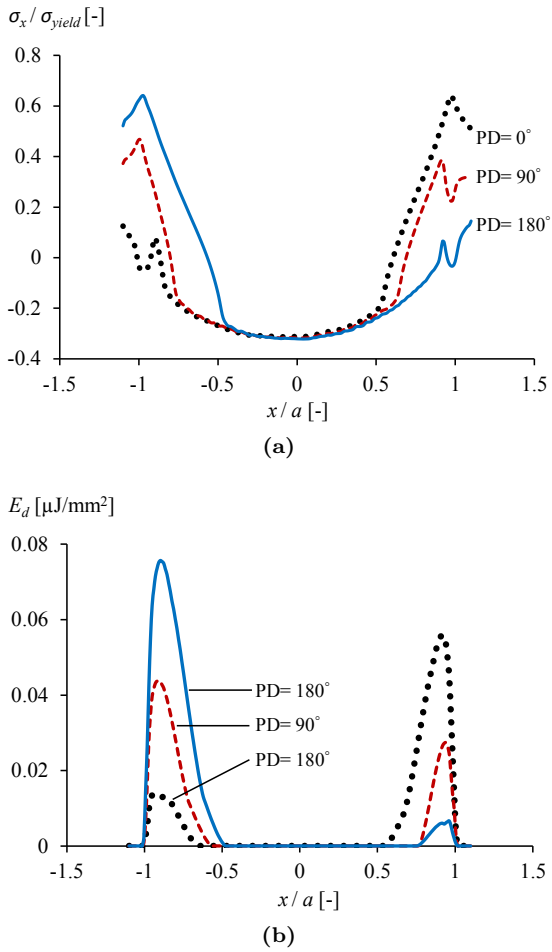

Figure 8.6: Comparison of (a) tangential stress distribution and (b) dissipated energy between different PDs for FFPD1.

8.2.4 Effects of cyclic contact load

Figure 8.7 indicates that, by applying the cyclic contact load, the location of initial crack is at the same edge as constant contact load. Figures 8.8 (a-b) show the variation of contact status under cyclic contact loading condition. From the figures it can be seen that the semi contact width (a) and the sticking region (c) are decreasing due to drop of contact load as expected. This change in stick-slip area results in change in dissipated energy distribution over the contact interface as shown in Figure 8.7.

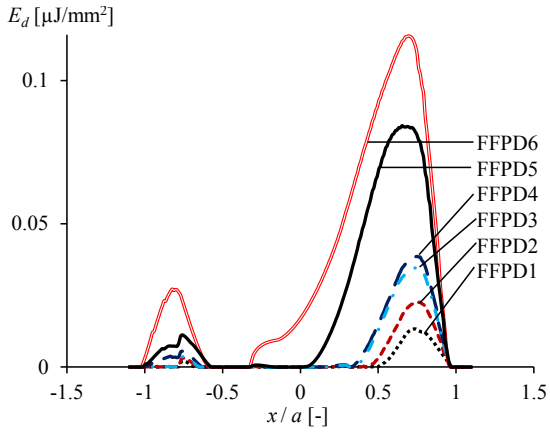

Figure 8.7: Distribution of dissipated energy under cyclic contact loading condition.

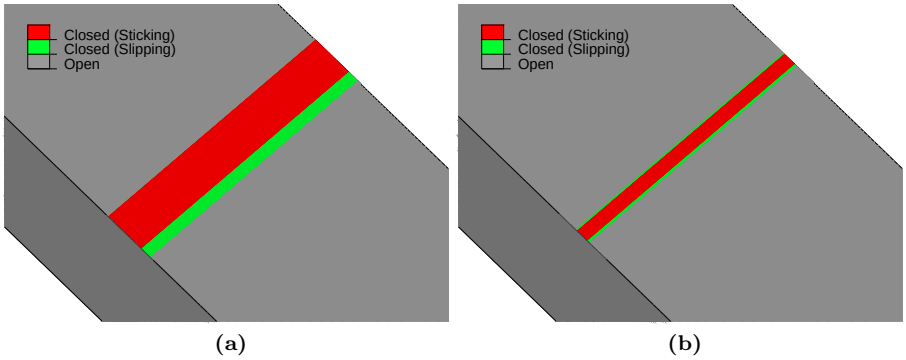

Figure 8.8: Top view of contact status at (a) maximum (step 3) and (b) minimum (step 5) under cyclic contact loading condition for FF1.

8.2.5 Crack initiation lifetime

The same procedure as elaborated in Chapter 7 for cylindrical contact configuration was used to predict fretting fatigue crack initiation lifetime under different PDs and cyclic contact loading conditions. For this purpose, the average value of triaxiality function, the maximum and minimum equivalent stress were calculated inside the process zone, then substituted in the damage model along with the damage parameters, which has been calibrated for the same material in Chapter 7.

Figure 8.9 illustrates comparison between estimated fretting fatigue crack

initiation lifetime for different PDs, cyclic contact loading condition and calculated experimental results. The experimental crack initiation lifetime was calculated by subtracting numerical crack propagation lifetime from the observed experimental total lifetime. From the figure it can be seen that by shifting the PD from 0° to 90° the crack initiation lifetime increases, nevertheless, this variation stays in the scatter of ±75% upper and lower bound. In contrary to PD= 90°, in case of PD= 180° the initiation lifetime estimated to be less than the 0° phase difference case. Furthermore, at presence of cyclic contact loading condition, it was found that the initiation lifetime decreases almost at the same order as PD= 180° as depicted in Figure 8.9.

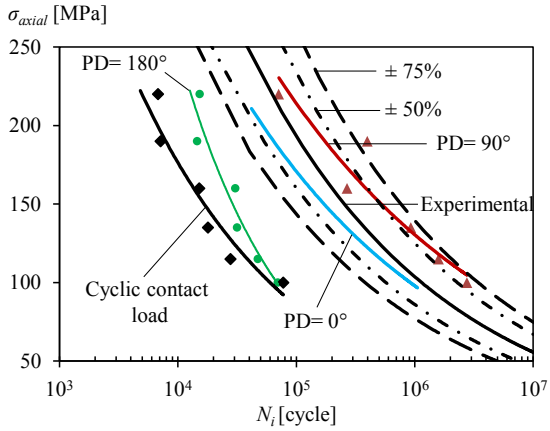

Figure 8.9: Fretting fatigue predicted crack initiation lifetime versus applied axial stress for different PDs and cyclic contact loading condition.

In order to interpret predicted crack initiation results, variation of some fretting fatigue parameters such as dissipated energy and stress state should be monitored. To this end, the variation of two parameters were monitored, namely energy lost after one cycle E_d^* and equivalent multiaxial damage stress σ^*. The total value of energy lost after one cycle was integrated over the distribution of dissipated energy over the contact distance and written as:

$$E_d^* = \int_{-a}^{a} E_d(x)dx \tag{8.1}$$

Figure 8.10 represents the variation of estimated fretting fatigue initiation lifetime versus the energy lost after one cycle for different PDs. From the figure

it can be seen that by increasing the energy lost value the number of cycles to initiation declines.

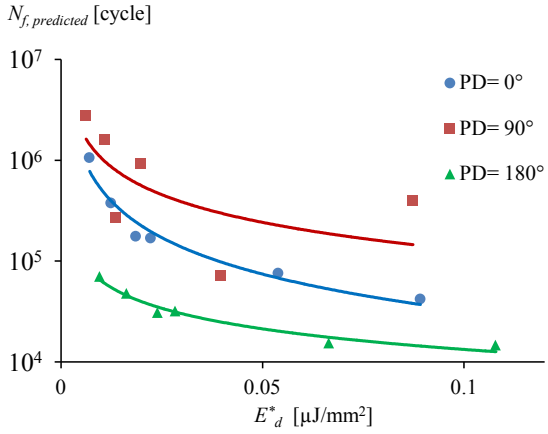

Figure 8.10: Estimated crack initiation lifetime versus dissipated energy after one cycle.

From Equation 5.10 it can be noted that, the predicted number of cycles to initiation can be written as function of equivalent multiaxial damage stress. As depicted in Figure 8.11 by increasing the axial stress in case of constant contact load the σ^* increases for all models as expected. As expected by declining the applied axial stress the number of cycles to initiation rises. Therefore, the variation of σ^* is in reverse relation to the predicted number of cycles to crack initiation. It means that for instance in case of FFPD1 (σ_{axial}= 100 MPa) the σ^* is higher for PD= 180° and lower for PD= 90° when compared to PD= 0° case, which leads to lower and higher crack initiation lifetime, respectively. In case of cyclic contact loading condition the σ^* increased when compared to the constant loading condition, which results in lower crack initiation lifetime. These results can be the reason for variation of the predicted fretting fatigue crack initiation lifetime at presence of phase difference and cyclic contact loading cases. The predicted results for fretting fatigue crack initiation lifetime is in line with observed experimental results for fretting fatigue total lifetime from literature as elaborated in introduction section and reported in [Iyer and Mall, 2000, Jutte, 2004]. However, the effect of phase difference and cyclic contact loading condition on crack propagation lifetime still need to be investigated.

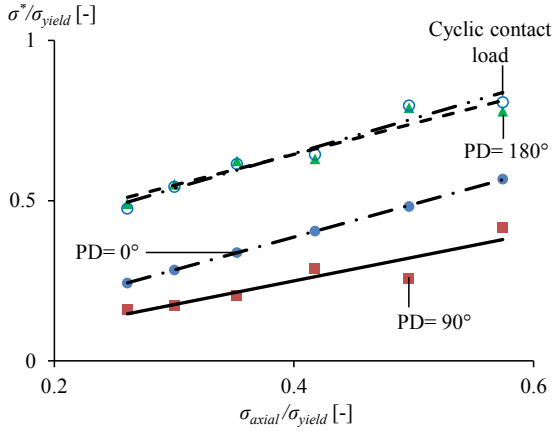

Figure 8.11: Equivalent multiaxial damage stress versus applied axial stress.

8.3 Effect of geometrical impurities

In this section the sensitivity of fretting fatigue parameters and crack initiation lifetime are investigated by adding different types of surface and sub-surface geometrical inhomogeneities by means of CDM approach and FE modelling technique.

8.3.1 Introduction

It has been shown that during high cycle fretting fatigue, a large fraction of lifetime is spend in initiation portion. It is also known that formation of fatigue cracks may occur at various geometrical inhomogeneities within the bulk materials [Gall et al., 2001]. In many rough alloys, fatigue crack initiates from grain boundaries, surface or sub-surface voids and inclusions. Voids and inclusions can be created during manufacturing process. There are different types of inclusions such as oxide film, aluminium carbide, magnesium oxides, etc. Murakami and Endo [Murakami and Endo, 1994] have reported the importance of fatigue crack formation at inclusions and voids in engineering alloys.

Figure 8.12 shows the SEM images of an area with an AlCuMg inclusion (region A) and a AlCuFeMn inclusion (region B) taken from [Suter and Alkire, 2001]. However, the formation of fatigue cracks from micro-voids has dragged more attentions compare to inclusions in literature [Murakami and Endo, 1994]. Both of these types of impurities act as stress riser and the local stress distri-

bution can be affected highly due to shifting the initial crack location to their site. Consequently, it is essential to quantify the sensitivity of fretting fatigue parameters and its initiation lifetime to these geometrical impurities. In this study localised stress distribution, slip amplitude and the location of initial crack are considered as the fretting fatigue parameters that can be affected by these type of inhomogeneities.

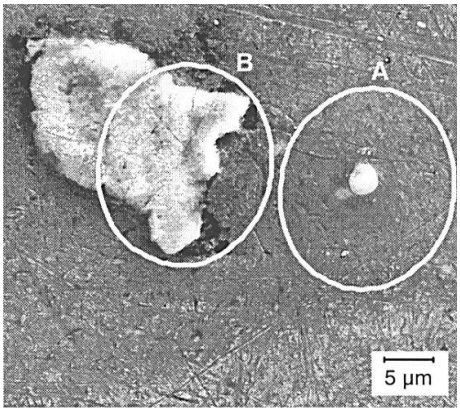

Figure 8.12: SEM pictures show the area of AL 2024-T3 [Suter and Alkire, 2001].

Investigating the effect of geometrical impurities on fretting fatigue behaviour experimentally is a challenging task, since the cracks and damages are always hidden between two contact surfaces. To overcome this issue, numerical techniques such as FE method is a suitable approach. Generally fretting fatigue test leads to quite scatter results in terms of lifetime. Therefore, fretting fatigue initiation lifetime can be influenced by different material impurities such as micro-voids, stiff and soft inclusions severely. Regarding modelling formation of voids and inclusions subjected to fatigue loading condition, numerous models have been developed in literature. Murakami and Endo [Murakami and Endo, 1994] summarized some them used for fatigue crack formation from inhomogeneities. Gall et al. [Gall et al., 2001] have modelled inclusions as bonded, debonded and cracked one. However, Tanaka [Tanaka and Mura, 1982] has revealed that the fatigue crack formation from the debonded inclusion is the same as initiation from a void. Therefore, in this work geometrical impurities are defined as micro-voids, stiff and soft inclusions. Two forms of surface and sub-surface impurities are investigated along with two sizes of small (5 μm) and large (20 μm) impurities for each group.

8.3.2 Modelling geometrical inhomogeneities

In order to model different geometrical impurities, the fretting fatigue cylindrical contact model was modified under same loading and boundary conditions by deleting one or some elements in case of micro-voids and changing the stiffness of the same elements in case of inclusions at $x/a = 1$. Two sets of surface and sub-surface, at two size of small (5 μm) and large (20 μm) impurities were modelled for each group. Figure 8.13 illustrates the schematic view of different material impurities at fretting fatigue contact edge, which were modelled in this investigation.

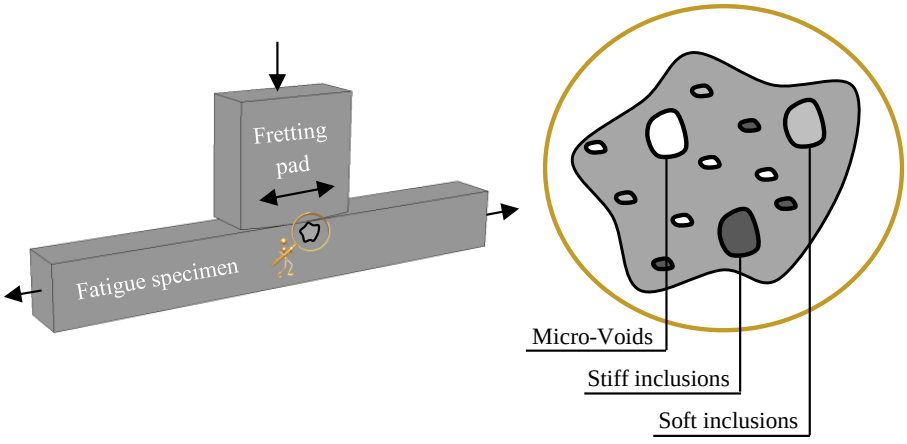

Figure 8.13: Schematic view of different types of geometrical inhomogeneities used for FE modelling approach

A Python script was written to model the inhomogeneities and post-processing the results of FE models. In this study six different loading conditions were selected from the performed experimental tests as listed in Table 8.1. It is worth to mention that, in order to perform parametric study, the size of micro voids and stiffness of inclusions were chosen arbitrary based on some suggestions in [Gall et al., 2001]. The main aim was to demonstrate the capability of proposed FE modelling approach to monitor their effects of fretting fatigue behaviour.

Figure 8.14 depicts the FE mesh of micro-voids for different inhomogeneities i.e. Surface Micro-Void (SMV) and Sub-Surface Micro-Void (SSMV). The awkward shape of large SSMV represents the worst case scenario for respective inhomogeneities. The sharp internal corners of impurities act as a stress riser,

which is near to the shape of empirical impurities as can be seen in Figure 8.12.

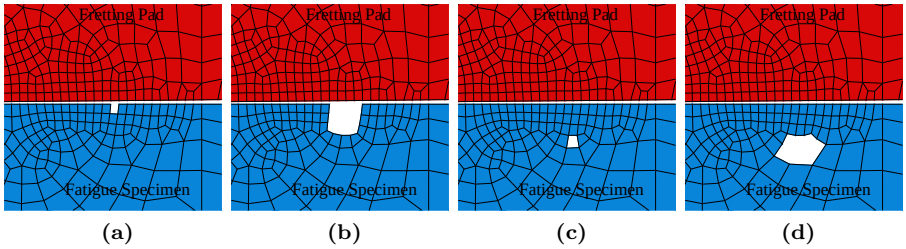

Figure 8.14: FE mesh for different micro-voids for (a) Small (5 μm) SMV, (b) Large (20 μm) SMV, (c) Small (5 μm) SSMV and (d) Large (20 μm) SSMV.

Figure 8.15 indicates the FE mesh of inclusions for different inhomogeneities i.e. Surface Inclusions (SI) and Sub-Surface Inclusions (SSI). As mentioned above, in this study two different types of inclusions, namely stiff and soft inclusions were modelled. For modelling stiff inclusions the stiffness of selected elements were changed to two times of the stiffness of the homogeneous ones. In order to model the soft inclusions the stiffness of selected elements were degraded to 20% of the virgin material.

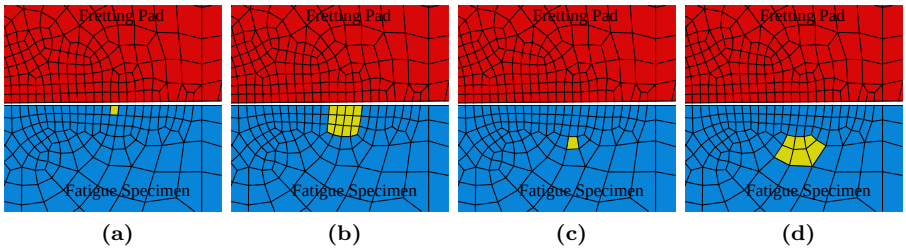

Figure 8.15: FE mesh for different stiff and soft inclusions for (a) Small (5 μm) SI, (b) Large (20 μm) SI, (c) Small (5 μm) SSI and (d) Large (20 μm) SSI.

8.3.3 Effects of geometrical impurities on fretting fatigue response

Fretting fatigue crack initiation lifetime can be affected by different parameters. However, it is proven that some of them, which are called primary variables have significant influence on fretting fatigue behaviour [Hills and Nowell, 1994].

These primary variables can be affected by inserting geometrical impurities into the contact model. In this section, the variation of some of these variables such as different stress distributions, slip amplitude and location of initial crack are monitored.

Stress distribution

The stress state is highly multiaxial in case of fretting fatigue. The developed damage model for predicting crack initiation lifetime depends on stress distribution near to the contact interface. Therefore, any types of geometrical impurities can easily change the stress contours near the area of interest for crack initiation. In this section some of these stress contours variation are monitored at presence of different types of geometrical impurities.

To check the effect of different geometrical impurities, FFPD1 is selected as a sample case and its behaviour is compared with the homogeneous model at maximum applied stress step. The same trends were observed for other models. Figures 8.16 (a)-(d) demonstrate the variation of stress contour plots for SMV and SSMV for different sizes (i.e. small and large). As expected the stress level is higher in all four cases, however, the maximum location of stress is at contact interface for small SSMV case (Figure 8.16-d). Stress concentration is higher to compare with homogeneous model and more localized at location of micro-voids.

Figurs 8.17 (a)-(d) represent the stress distribution at presence of stiff inclusions for SI and SSI for different sizes (i.e. small and large). From the figure it can be noted that the maximum stress level is less than the homogeneous model for both cases of small and large SSI, however, for all cases the averaged stress at location of impurities were higher than averaged stress in homogeneous model. The stress concentration was shifted from contact surface to the location of impurity. Figures 8.18 (a)-(d) illustrate the stress distribution around the soft inclusions for SI and SSI for different sizes (i.e. small and large). The figures reveal that the stress distribution shape is like the homogeneous model. The maximum value of von-Mises stress is just less than the homogeneous model for both small and large SI. The same as stiff inclusions cases, due to higher stress concentration at location of inclusion, it was found that the average stress at location of inclusions is higher to compare with the homogeneous model.

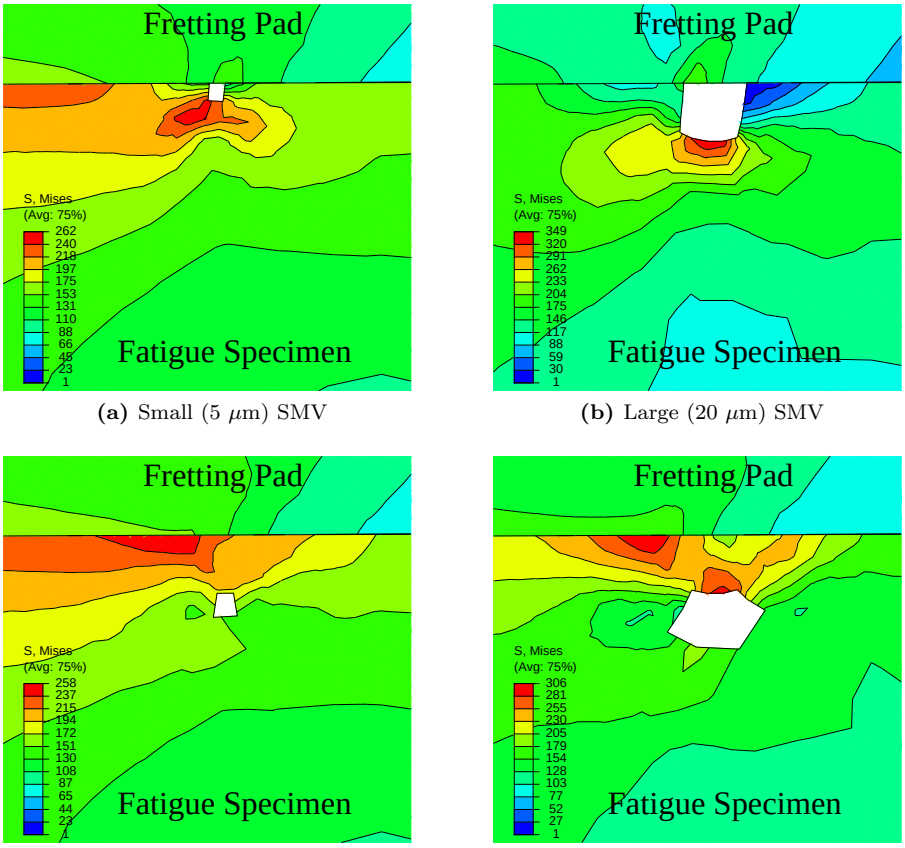

(a) Small (5 μm) SMV

(b) Large (20 μm) SMV

(c) Small (5 μm) SSMV

(d) Large (20 μm) SSMV

Figure 8.16: von-Mises stress distribution at and near contact edge for different micro-voids.

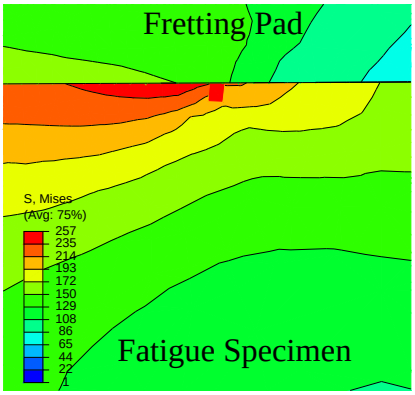

(a) Small (5 μm) SI

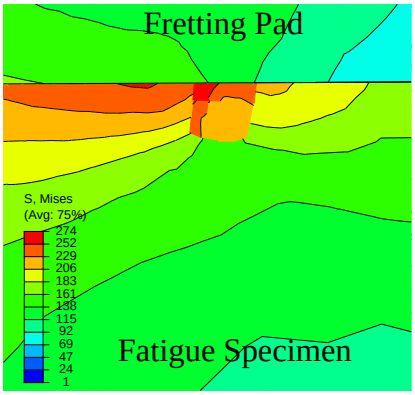

(b) Large (20 μm) SI

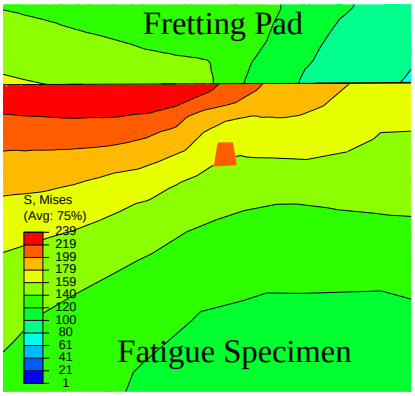

(c) Small (5 μm) SSI

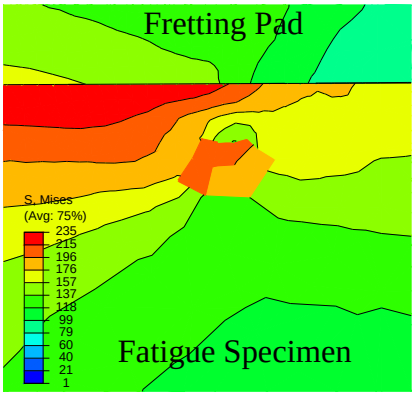

(d) Large (20 μm) SSI

Figure 8.17: von-Mises stress distribution at and near contact interface for stiff inclusions.

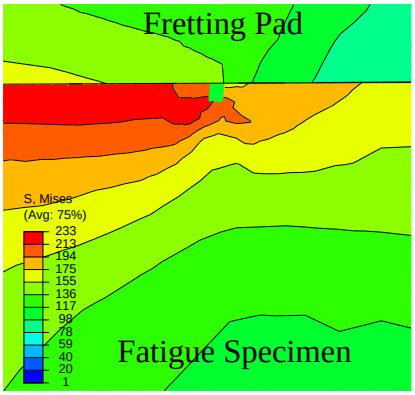

(a) Small (5 μm) SI

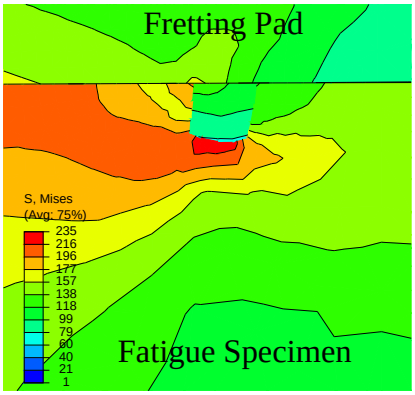

(b) Large (20 μm) SI

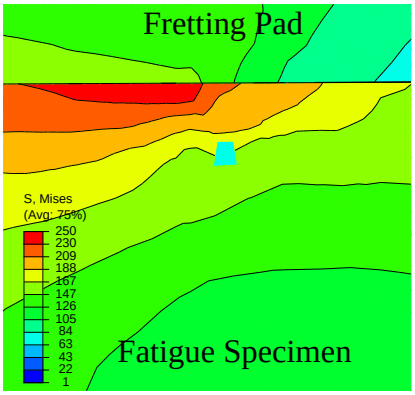

(c) Small (5 μm) SSI

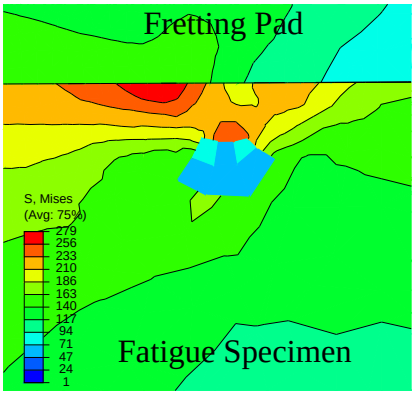

(d) Large (20 μm) SSI

Figure 8.18: von-Mises stress distribution at and near contact interface for soft inclusions.

Slip amplitude

Fretting slip amplitude is one the primary fretting fatigue parameters that has been used a lot by researchers to characterise its failure behaviour. Therefore, many attempts have been spend to distinguish between different fretting fatigue slip regimes. The fretting slip amplitude is affected by almost all of the primary variables. In this study the effect of different material inhomogeneities on fretting fatigue slip amplitude has been investigated. Figure 8.19 indicates the variation of slip amplitude for SMV and SSMV at maximum applied axial stress for all tests.

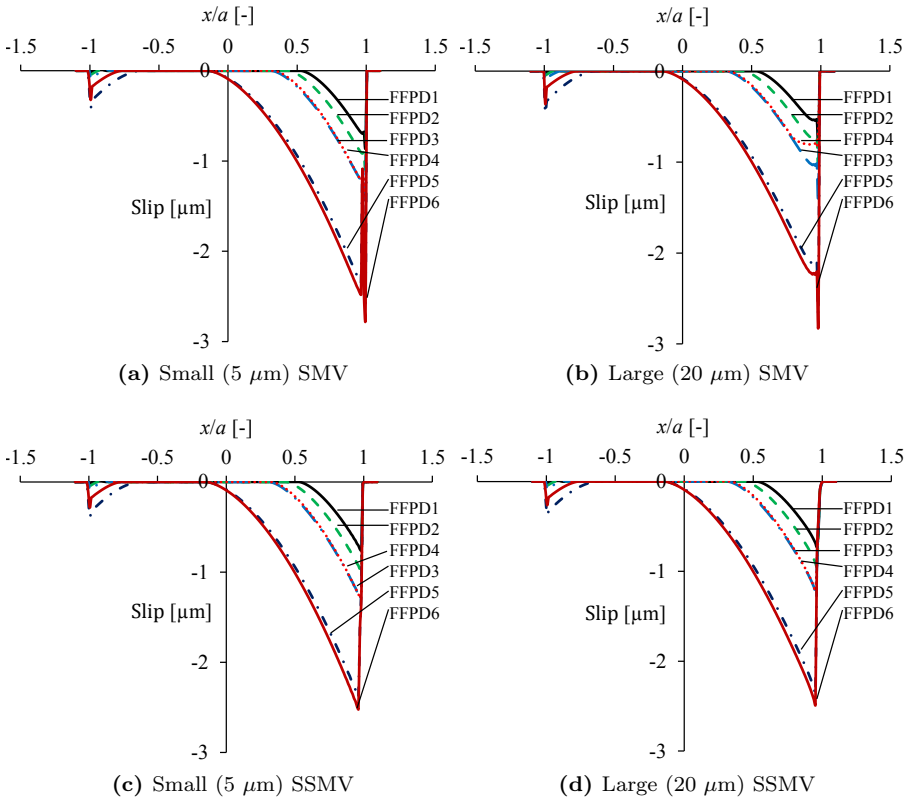

(a) Small (5 μm) SMV **(b)** Large (20 μm) SMV

(c) Small (5 μm) SSMV **(d)** Large (20 μm) SSMV

Figure 8.19: Fretting slip distribution at contact interface for different micro-voids.

From the Figures 8.19 (a)-(b) it can be noted that, the effect of small and large SMV are significant on slip distribution at contact edge. In contrast, for small and large SSMV models the effect of geometrical impurities are not crit-

ical. The same behaviour has been seen from the other types of impurities i.e. stiff and soft inclusions (SI and SSI) as shown in Figures 8.20 (a)-(d). Therefore it can be concluded that the variation of fretting fatigue slip amplitude at contact interface just can be affected by small and large SMV impurities.

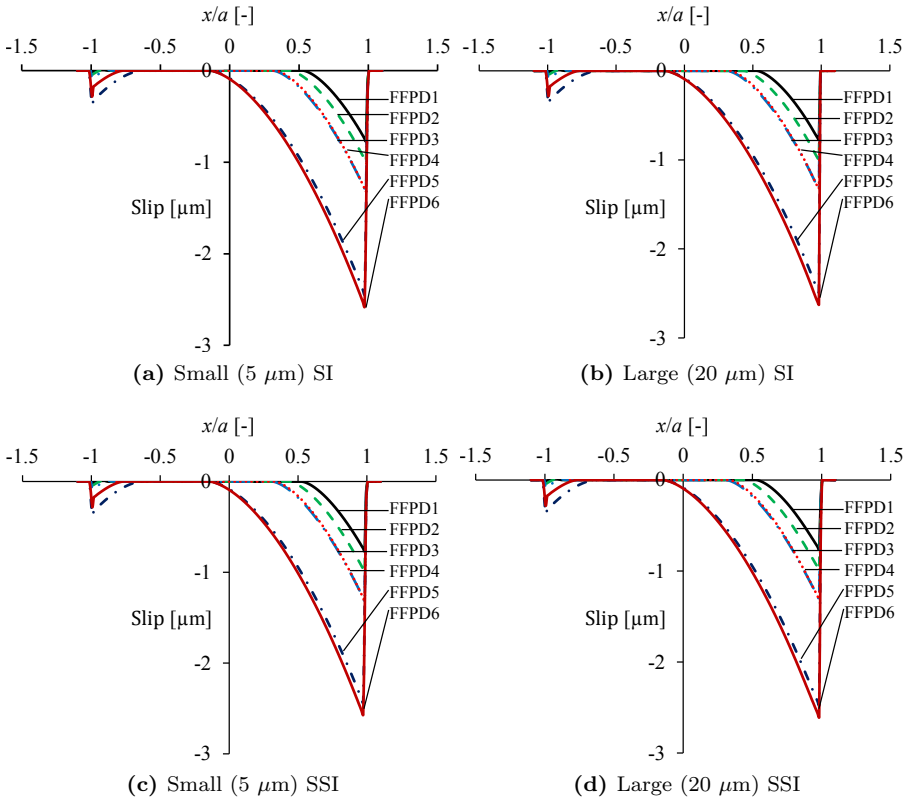

(a) Small (5 μm) SI **(b)** Large (20 μm) SI

(c) Small (5 μm) SSI **(d)** Large (20 μm) SSI

Figure 8.20: Fretting slip distribution at contact interface for different stiff inclusions.

These interesting results reveal that the fretting fatigue slip amplitude does not vary by geometrical impurities such as stiff and soft (both small and large) inclusions along with SSMV geometrical inhomogeneities. Moreover, these results show that the fretting fatigue lifetime can be affected at presence of geometrical impurities, which is elaborated later on, while the fretting slip amplitude does not vary.

Location of initial crack

In order to extract data from FE results, which are needed for calculating number of cycles to crack initiation from Equation 5.10, the potential location of fretting fatigue crack was calculated based on maximum location of dissipated energy at contact interface after one full cyclic loading condition. It has been shown earlier that the maximum location of dissipated energy is located near the contact edge, where the fretting fatigue cracking occurs based on experimental observation. Figures 8.21 (a)-(d) illustrate variation of dissipated energy versus normalized contact distance for all micro-voids models.

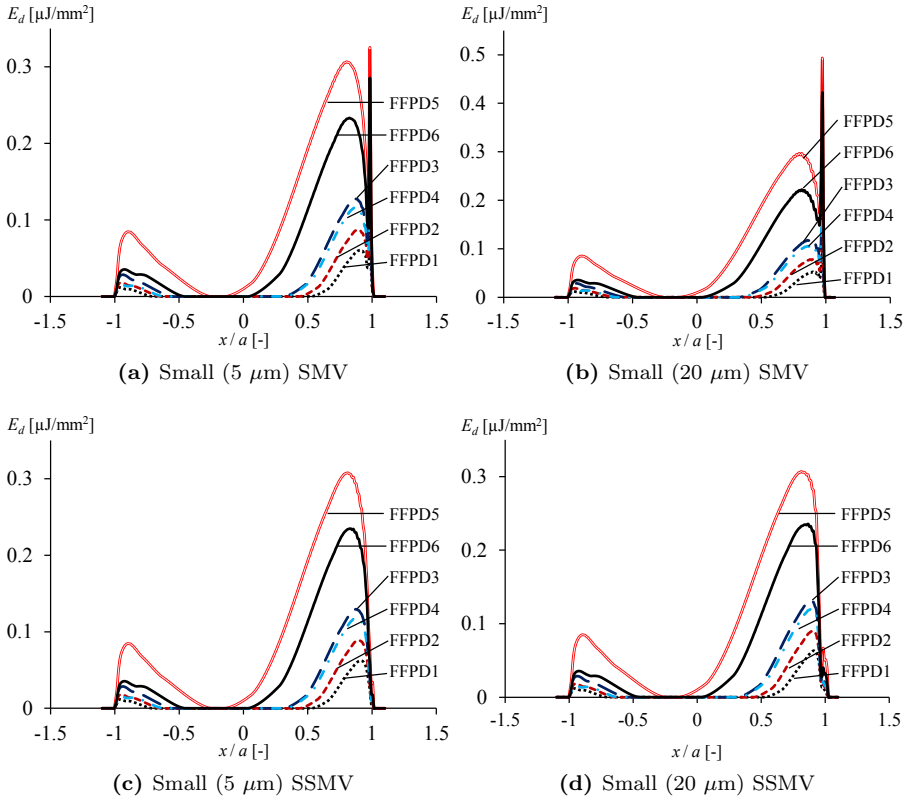

(a) Small (5 μm) SMV **(b)** Small (20 μm) SMV

(c) Small (5 μm) SSMV **(d)** Small (20 μm) SSMV

Figure 8.21: Dissipated energy at contact interface and estimated location of initial crack for different micro-voids.

As can be seen from the Figures 8.21 (a) and (b), the effect of surface micro-voids on dissipated energy is high and the estimated location of crack is

at edge of contact. In contrast, at presence of sub-surface micro-voids the used criterion does not show any change in the location of predicted initial crack as shown in Figures 8.21 (c) and (d). In case of stiff and soft inclusions the predicted location of initial crack were the same as estimated for homogeneous one.

All data related to estimated location of fretting fatigue initial crack are tabulated in Table 8.2. From the results, it can be concluded that the predicted location of initial crack by dissipated energy criterion just changes at presence of small and large SMV.

Table 8.2: Crack initiation location

Test No.	Homogeneous	x/a Micro-Voids		Stiff-Inclusions		Soft-Inclusions	
		5 μm	20 μm	5 μm	20 μm	5 μm	20 μm
Surface Inhomogeneities							
FFPD1	0.92	0.98	0.97	0.92	0.92	0.92	0.92
FFPD2	0.90	0.98	0.97	0.90	0.90	0.90	0.90
FFPD3	0.88	0.98	0.97	0.88	0.88	0.88	0.88
FFPD4	0.81	0.98	0.97	0.88	0.88	0.88	0.88
FFPD5	0.81	0.98	0.97	0.81	0.81	0.81	0.80
FFPD6	0.84	0.98	0.97	0.83	0.83	0.83	0.82
Sub-Surface Inhomogeneities							
FFPD1	0.91	0.91	0.91	0.91	0.91	0.91	0.91
FFPD2	0.90	0.90	0.91	0.90	0.90	0.90	0.90
FFPD3	0.88	0.88	0.89	0.88	0.88	0.88	0.88
FFPD4	0.81	0.88	0.89	0.88	0.88	0.88	0.89
FFPD5	0.81	0.81	0.81	0.81	0.81	0.81	0.81
FFPD6	0.84	0.83	0.87	0.83	0.83	0.83	0.83

Effect of geometrical impurities on initiation lifetime

Figures 8.22 (a)-(b) show comparison between estimated fretting fatigue crack initiation lifetime for different micro-voids, homogeneous models and calculated experimental results. Fretting fatigue crack initiation lifetime increases at presence of small SMV and declines by inserting large SMV specially at low axial applied stresses. However, inserting the same size micro-voids beneath the contact surface to the contact model, causes drop in fretting fatigue crack initiation lifetime.

The reason for rising the crack initiation lifetime at presence of small SMV can be related to shifting the stress concentration to the root of micro-voids from contact interface as illustrated in Figure 8.16 (b). It is worth to mention that the small SMV acts as the stress relief groove.

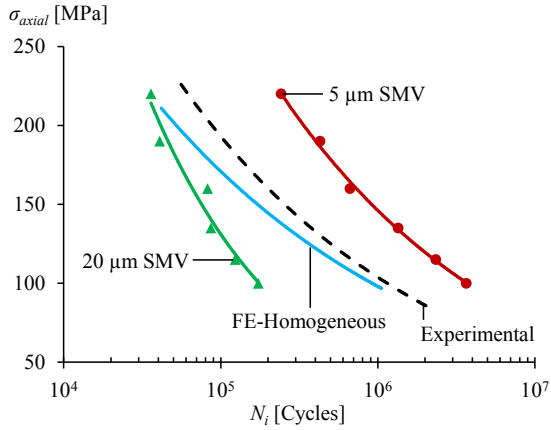

(a) SMV

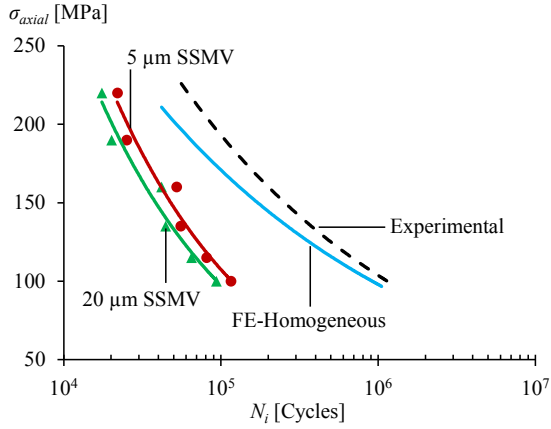

(b) SSMV

Figure 8.22: Comparing the predicted fretting fatigue initiation lifetime with homogeneous model and calculated experimental results for different types and sizes of micro-voids.

Figure 8.23 indicates that by shifting the stress concentration the average stress distribution extracted at process zone area decreases when compared with homogeneous model. This decline leads to drop of averaged equivalent multiaxial damage stress σ^*, which eventually causes the crack initiation lifetime to increase (see Equation 5.10). The remaining models consist of micro-voids and face crack initiation lifetime plummet due to rise of stress concentration at and near the location of micro-voids as shown in Figure 8.16.

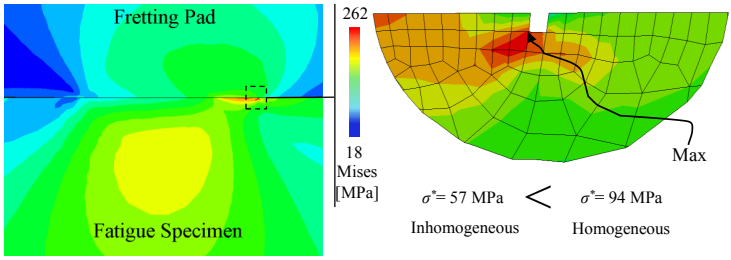

Figure 8.23: Averaged von-Mises stress inside the process zone at presence of 5 μm SMV.

Figures 8.24 (a) and (b) show that the fretting fatigue crack initiation lifetime declines for all models which include stiff inclusions. From the figures it can be seen that for both SI and SSI cases, the crack initiation lifetime decreases almost at the same rate. This decrease is because of increase in averaged equivalent multiaxial damage stress, similar to micro-void impurities cases. The same trend has been reported for Al 2024-T3 for plain fatigue test by Marines et al. [Marines et al., 2003]. They reported that when crack appears at location of inclusions the lifetime is less to compare with when crack nucleates at regular slip bands.

Figure 8.25 (a) illustrates that at high applied stress levels, the estimated fretting fatigue crack initiation lifetime at presence of 20 μm soft SI is closer to the calculated experimental one. This interesting results show that in real laboratory scale experiments there may be a soft inclusion, which is at contact interface near edge of contact causing the lifetime to decrease. The rest of results are the same as observed for stiff inclusion, i.e. by adding large soft SI and both size of SSI, the fretting fatigue crack initiation decreases due to rise of averaged equivalent multiaxial damage stress at location of impurities as demonstrated in Figure 8.25 (a) and (b).

Effect of location of crack on initiation lifetime

As mentioned above in Table 8.2 the predicted location of initial crack is not located where the impurities sited, except two types of impurities i.e. small and large SMV. All above predicted results were based on the assumption that the crack nucleates at or near the geometrical impurities. Since the location of initial crack was considered as centre of semi-circle (process zone), the stress

state that was extracted to substitute in Equation 5.10 may be affected by shifting the location of initial crack. For this purpose two sets of models e.g. small and large SSMV were selected to investigate, as shown in Table 8.2. The remaining models behave in the same manner.

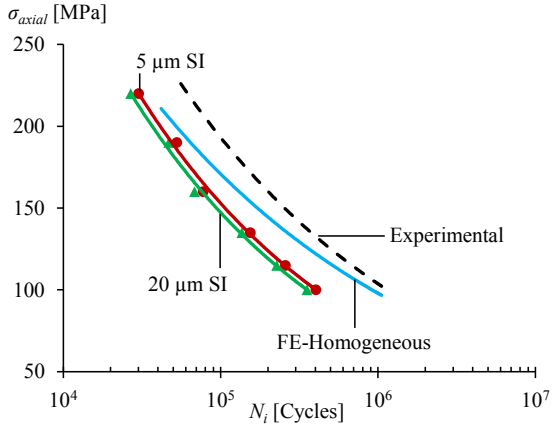

(a) SI

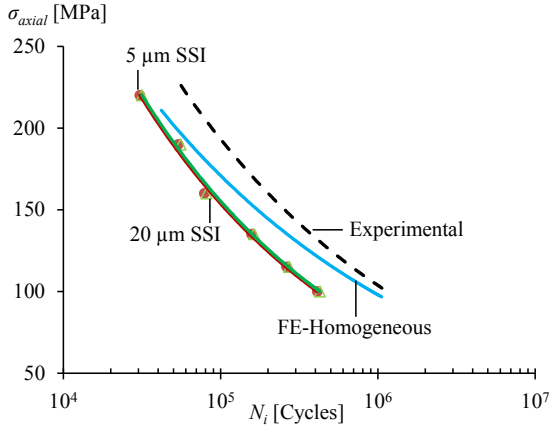

(b) SSI

Figure 8.24: Comparing the predicted fretting fatigue initiation lifetime with homogeneous model and calculated experimental results for different types and sizes of stiff inclusions.

Figure 8.26 compares the estimated initiation lifetime based on location of crack at impurities sites and contact interface. From the results, it can be concluded that shifting the location of initial crack does not affect the estimated fretting fatigue crack initiation lifetime significantly. However, the predicted

location of crack using the proposed dissipated energy is not capable of showing the effect of geometrical impurities as well as other available methods, which are based on stress or strain distribution at contact interface. The reason is that the dissipated energy at contact interface depends on slip amplitude and frictional shear stress.

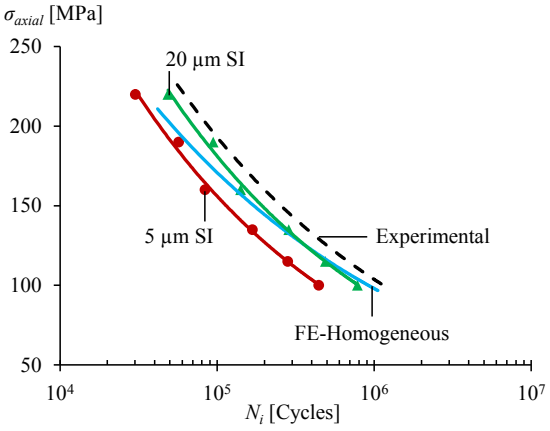

(a) SI

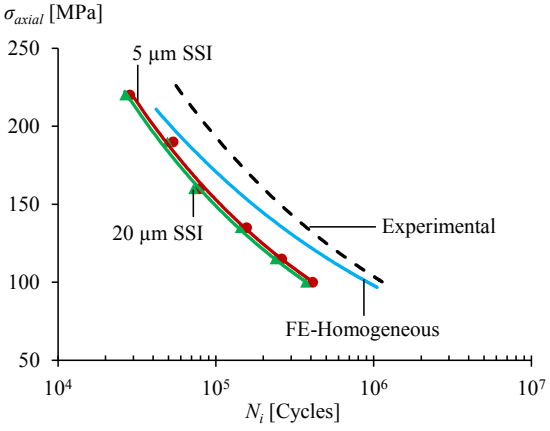

(b) SSI

Figure 8.25: Comparing the predicted fretting fatigue initiation lifetime with homogeneous model and calculated experimental results for different types and sizes of soft inclusions.

As shown above, in most cases the slip amplitude is not sensitive to presence of geometrical impurities. The same behaviour was found about the frictional shear stress distribution at contact interface. Therefore, the dissipated en-

ergy at contact interface does not change after inserting geometrical material inhomogeneities into the fretting fatigue contact model.

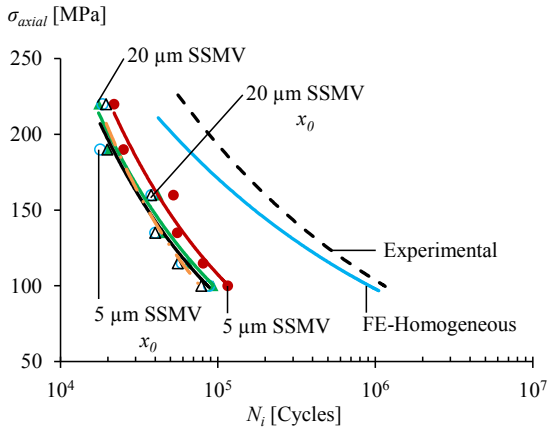

Figure 8.26: Effect of initial crack location shift on estimated lifetime for small and large SSMV.

8.4 Summary and conclusions

In this chapter firstly, the effect of phase difference between axial stress and tangential load on fretting fatigue behaviour has been investigated. Furthermore, the fretting fatigue response has been studied under cyclic contact loading condition. For monitoring the fretting fatigue response two parameters were monitored, namely tangential stress distribution and dissipated energy after one cycle. For this purpose fretting fatigue cylindrical configuration has been used. The following conclusions can be drawn based on the observed results in this study:

- For all models under phase difference PD= 90° and PD= 180°, the location of maximum dissipated energy always occurred at or near the left edge of contact, i.e. x/a= -1 when compared with the case of PD= 0° which is at or near x/a= 1. Based on these results the possible location of crack may be shifted to left edge of contact, i.e. x/a= -1.

- The stress distribution at contact interface was affected by all kinds of phase differences between axial stress and tangential load.

- At presence of cyclic contact loading condition the location of maximum dissipated energy was the same as constant contact load i.e at or near $x/a = 1$.

- For PD= 90° the estimated initiation lifetime increased when compared with PD= 0°, however, the estimated results lie within the scatter of ±75% upper and lower bound.

- In contrast, for PD= 180° the initiation lifetime declines considerably.

- At presence of cyclic contact loading condition the fretting fatigue lifetime decreases drastically.

Secondly, the effect of different geometrical impurities on fretting fatigue parameters and crack initiation lifetime has been investigated. The geometrical impurities defined as two sizes of small (5 μm) and large (20 μm). They were modelled in three different categories, namely surface and sub-surface micro-void, stiff and soft inclusions. Effect of these geometrical impurities were studied on different fretting fatigue primary variables such as different stress distributions at contact interface and fretting slip amplitude. It was assumed that the initial fretting fatigue crack nucleates at geometrical impurities sites, however their influence on location of initial crack was investigated using dissipated energy criterion. Finally, the predicted fretting fatigue lifetimes at presence of geometrical impurities were compared with the homogeneous model along with the calculated experimental results. The following conclusions can be drawn based on the observed results in this study:

- Presence of geometrical impurities affect the multiaxial stress distribution at or near contact interface, which leads to higher local stress concentration. In most cases the averaged stress at location of impurities was higher than averaged stress in homogeneous model and the stress concentration was shifted from contact surface to the location of impurity.

- The fretting slip distribution does not change by inserting geometrical impurities, except two cases of small and large SMV.

- The predicted location of fretting fatigue initial crack does not change when compared with the homogeneous model based on the dissipated energy criterion, except for two cases of small and large SMV.

- Fretting fatigue crack initiation lifetime plummets for the majority of modelled geometrical impurities. There was one case that the estimated crack initiation lifetime increased when compared with the calculated experimental results i.e. for small SMV. For large and soft SI, the estimated crack initiation lifetime was closer to the calculated experimental lifetime. One of the main conclusions of this work is that the high scatter observed experimental fretting fatigue lifetime can be related to presence of material inhomogeneities in particular geometrical impurities.
- The effect of initial crack site shift on estimated crack initiation lifetime is negligible.

Chapter 9

Conclusions, recommendations and future work

"In this chapter, the methodologies used in this study and the main conclusions are summarized"

9.1 Overview

By definition, fretting fatigue is a phenomenon, in which two contact surfaces undergo a small relative oscillatory motion due to cyclic loading. Literally, it can be defined as combination of tribological and fatigue behaviour of materials, which are in contact together. Due to fretting, fatigue lifetime is significantly reduced as compared to plane fatigue. This is because of the high stresses that are generated at the contact surfaces of the two bodies. Many failures in mechanical components due to fretting fatigue have been reported and investigated in literature, e.g. threaded pipe connections, riveted joints, blade-disk attachment in turbine, shrink-fitted shaft, aero-engine splined couplings and so on.

In general, fretting fatigue failure process is divided into two main phases, namely crack initiation and crack propagation. The fraction of fretting fatigue lifetime spent in crack initiation and in crack propagation depends on many factors, e.g. contact stresses, amount of slip, frequency, environmental conditions, etc., and varies from one application to another. Therefore, both crack initiation and propagation phases are important in analysing fretting fatigue. Although several studies on fretting fatigue have been reported in literature, most of the works were of experimental nature with a simple FE model to calculate contact stresses and strains. However, in fretting fatigue experiments, it is very difficult to detect the crack initiation phase; the onset of crack growth and the crack growth rate because damage and cracks are always hidden between the two contact surfaces. Therefore, numerical modelling techniques for analysing fretting fatigue crack initiation and propagation phases are very desirable. Furthermore, these numerical models could be used to predict the fatigue lifetime of components subjected to fretting conditions.

The main goal of this investigation was to develop generic numerical modelling techniques in order to predict the response of materials and the damage initiation and propagation under fatigue loading in fretting conditions. The individual objectives of the work are summarised as follows:

- Developing FE model for fretting fatigue crack initiation, which takes into account the accumulation of damage due to cyclic loading, the triaxiality nature of stress in the damaged materials, the oscillatory slip between the two contact surfaces.
- Developing FE model for fretting fatigue crack propagation, which takes

into account the effect of cyclic loading, the mode mixity and its effect on crack growth direction, fretting conditions and contact stresses.

- Combining the FE models for crack initiation and propagation to produce a fretting fatigue lifetime prediction tool.

9.2 Methodology used in this study

9.2.1 Experimental set-up

Some limited experimental tests were performed in order to validate the FE models and characterize fretting fatigue failure mechanisms for single clamp fretting fatigue set-up along with Single and Double Bolted Lap Joints (SBLJ and DBLJ). Digital Image Correlation (DIC) technique has been used in order to monitor fretting fatigue frictional properties. For this purpose, three different test configurations have been tested, i.e. single clamp fretting fatigue set-up, SBLJ and DBLJ. Moreover, the fretting fatigue failure mechanism was observed in automotive shock absorber's piston valve component i.e. washer-disc connection.

9.2.2 Numerical modelling approach

FE modelling approach has been used to simulate fretting fatigue behaviour, including contact, crack initiation and propagation models. To this end, in this investigation, a numerical approach has been used to predict fretting fatigue crack initiation and propagation lifetime. To do so, an uncoupled damage evolution law based on principles of CDM has been developed for modelling crack initiation. The conventional FEM and XFEM approaches have been used for calculating crack propagation lifetimes.

Different categories of fretting fatigue FE contact models have been simulated in different groups based on experimental test configurations. These groups were namely, FEA of fretting contact, fretting fatigue contact and practical applications including bolted lap joints (SBLJ and DBLJ) and washer-disc contact configuration of shock absorber.

For crack initiation, the uncoupled damage evolution law has been developed to model fretting fatigue crack initiation lifetime under elastic and elasto-plastic conditions. The developed damage model has been implemented to the

performed fretting fatigue experiments and results from literature. Damage parameters have been calibrated based on regression analysis to calculate the best least square fit between the estimated cycles to crack initiation and the experimental data. Eventually, using the developed damage model and the multiaxial stress state, which has been extracted using the concept of process zone, cycles to crack initiation have been calculated and compared with experimental data. Furthermore, in order to find the location of initial crack two different approaches, namely, stress and energy based methodologies have been introduced. In addition, the FE modelling approach has been used to monitor the effect of different fretting fatigue primary variables on localized plasticity in an Aluminium alloy (Al 2024-T3) test specimen. The effect of different fretting fatigue primary variables, such as axial stress, contact geometry and COF, on localized plasticity has been investigated. Subsequently, the relationship between the location of maximum localized plasticity and Ruiz fretting damage parameter with the crack initiation site has been discussed.

In terms of crack propagation, in the first step the general developed crack propagation model has been introduced using conventional FEM and XFEM approaches. In order to verify the developed codes, two different benchmark studies, namely, Double Edge Notch Tension (DENT) specimen and Double Cantilever Beam (DCB) specimen, have been modelled. Finally, to estimated the crack propagation lifetime, the developed codes i.e. both conventional FEM and XFEM approaches have been implemented to fretting fatigue crack propagation problem. In addition, crack propagation trajectory was modelled based on experimental observations and compared with some available criteria in literature, which are usually used for proportional loading problems i.e. MTS, MERR and KII=0.

To sum up, in order to predict fretting fatigue total lifetime the developed damage models can be used to calculate damage evolution up to macro crack initiation as function of stress and strain fields with time at each point of the specimen subjected to damage. Therefore, after calculating stress and strain using FE model, data required for damage model can be extracted from post processing analysis in order to estimate fretting fatigue crack initiation. The next step, for crack propagation the initial macro crack can be inserted in the contact model and propagated to final rupture of specimen subjected to fretting fatigue loading condition. Figure 9.1 demonstrates the flowchart of combined uncoupled damage and fracture mechanics approaches, which have been used

to predict fretting fatigue total lifetime.

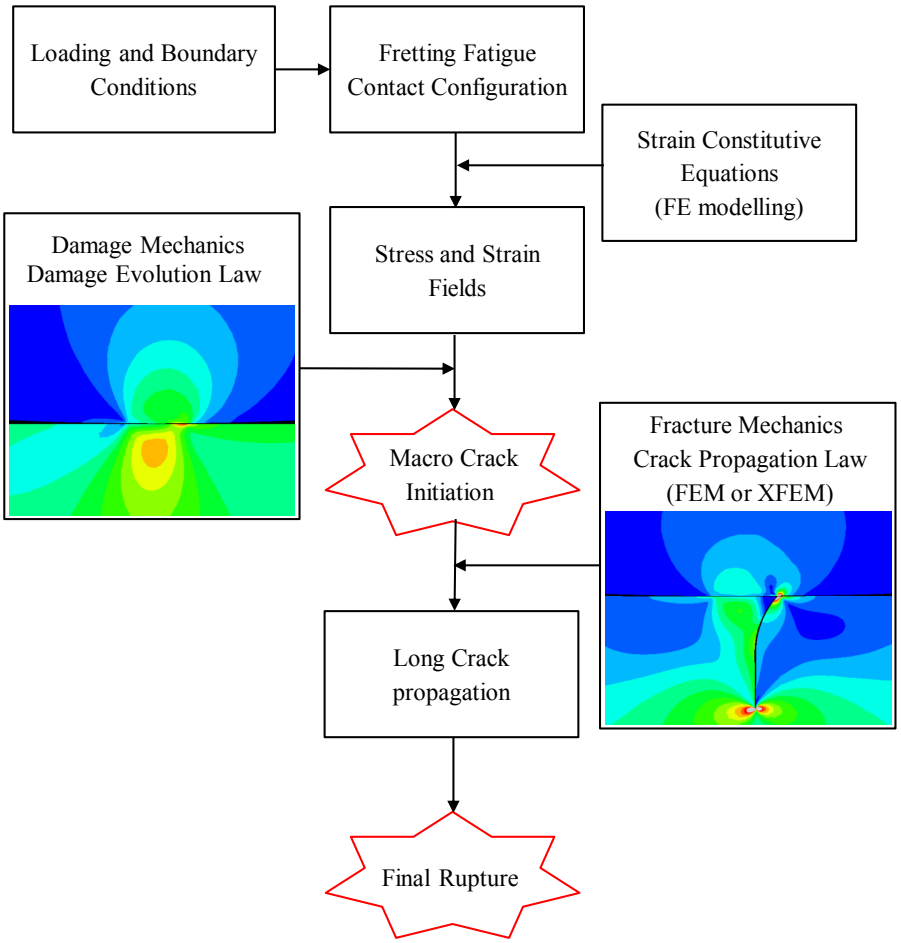

Figure 9.1: Flowchart view of fretting fatigue total lifetime prediction tool-kit.

9.3 Main conclusions

9.3.1 Fretting fatigue experiments

From DIC tests, it can be concluded that DIC technique is capable of determining the COF for contacts subjected to fretting fatigue loading condition. As expected the measured COF under static loading condition (i.e. SBLJ test)

was less than the COF obtained from fretting fatigue tests (i.e. fretting fatigue and DBLJ tests). The discrepancy between two obtained COF for fretting fatigue and DBLJ tests can be related to different test configuration that have been used for measuring COF and also to the well known scatter nature of COF. The fretting fatigue failure mechanism was observed in SBLJ, DBLJ and automotive shock absorber's piston valve component i.e. washer-disc connection. In case of washer-disc contact, the results showed that fretting damage appeared at contact interface between washer and disc causing the initial crack nucleation and advancing the crack up to the final rupture of valve disc.

9.3.2 Fretting fatigue contact model

It has been shown that, the use of finite element analysis is a convenient method to study the behaviour of structures or details of structures subjected to fretting fatigue loading condition. It has been revealed that using FE modelling approach gives extra information such as local relative slip and stress distributions at contact interface, which is not possible to be monitored using experimental approaches.

Using developed fretting fatigue contact models, effects of different loading conditions on fretting relative slip amplitude at contact interface have been investigated for single clamp flat and cylindrical contact configurations. Based on the FE models a parametric study has been performed to find the interaction effects of two primary variables namely, axial stress and contact force, on fretting fatigue FE slip amplitude. Using the FE modelling approach, a fretting fatigue FE slip map has been proposed that can be used for monitoring the local slip amplitude and subsequently, selecting right fretting fatigue parameters for performing experimental tests.

Eventually, fretting fatigue behaviour of SBLJ, DBLJ and washer-disc contact configuration has been investigated. It has been shown that FE modelling approach enhances the possibility to easily investigate more details compared to performed experimental tests in a laboratory and practical applications such as the distribution of relative slip amplitude, contact pressure or stresses at contact interfaces. It has been revealed that, once the FE model is calibrated with help of experimental test or other calculation methods such as analytical one, it even offers the great capability of performing large parametric studies to check the influence of different parameters on behaviour of different structures subjected to fretting fatigue loading condition.

9.3.3 Fretting fatigue crack initiation model

Results of predictor tool for fretting fatigue crack initiation lifetime, using CDM approach, have shown a good correlation with the experimental data. From the results, it can be noticed that the multiaxial nature of stress state at contact interface between fretting pad and fatigue specimen in fretting fatigue phenomena plays crucial role to predict the number of cycles to fretting fatigue crack initiation. In addition, these results prove that fretting fatigue's multiaxial behaviour can be modelled using CDM approach, which takes into account the effect of multiaxial state by means of considering the effect of stress triaxiality at the contact interface.

The same approach has been extended to investigate the effect of different fretting fatigue primary variables on the initiation lifetime. To this end, the effect of different phase difference between applied fretting fatigue loads and the effect of different geometrical impurities on fretting fatigue parameters and crack initiation lifetime have been investigated. The results have been discussed in Chapter 8.

9.3.4 Fretting fatigue crack propagation model

The results showed good correlation between FEM models using re-meshing technique and XFEM technique using single mesh approach. In addition, by comparing the numerical results with analytical solutions, it was concluded that the analytical values of SIFs were less than numerical values at earlier stage of crack propagation and converge far from the contact region.

In terms of crack propagation trajectory, it has been revealed that the average error of number of cycles to crack propagation was around 34% between predefined crack path based on experimental observation and predicted by MTS criterion for all simulated models. As discussed in Chapter 6, the main reason of observed discrepancy in estimation of crack growth trajectory can be related to non-proportional loading condition of fretting fatigue problem. One of the main points of this investigation was to show that, the available criteria for fretting fatigue crack propagation, which are used widely in literature, can not predict the right crack path. In spite of that finding a proper crack propagation criterion was not investigated further in this study, but it can be a start point to be investigated as will be explained later on in the recommendation section of this chapter.

9.4 Suggestion for future works

9.4.1 Experimental approach

As discussed earlier, both fretting fatigue crack initiation and propagation phases are important in analysing fretting fatigue. Although several studies on fretting fatigue have been reported in literature [Nowell, 1992, Szolwinski and Farris, 1996, Szolwinski and Farris, 1998, Farris et al., 2000, Jin and Mall, 2004a, Navarro et al., 2011, Majzoobi et al., 2011], most of the works were aimed to find the total lifetime or finding the cracks and damages using some experimental techniques such as electromagnetic technique (eddy current and potential drop techniques) or ultrasonic detection [Wagle and Kato, 2009]. All of available methods are applicable to detect relatively long cracks ($\approx$ 1 mm [Szolwinski and Farris, 1996, Szolwinski and Farris, 1998]) at contact interface and not damage threshold at micro level ($\leq$ 50 μm). Therefore, some new experimental techniques for analysing fretting fatigue crack initiation and propagation are very desirable.

The proposed DIC technique in this study, which has been used for monitoring frictional behaviour of contact, can be extended to detect onset of fretting fatigue crack initiation. The local strain at estimated location of initial crack changes due to degradation of material by forming micro-cracks and cavities. Using the concept of equivalent strain (see Chapter 2, section 2.3.2) and defining $\widetilde{E}$ as the elastic modulus of the damaged material, $\widetilde{E}$= (1-D)E. The damage variable is thus given by D=1-$E/\widetilde{E}$, which can be used to indirectly measure the damage variable D in a process known as the method of variation of elasticity modulus [Lemaitre and Lippmann, 1996]. On-line measuring of the local strain can be measured by the proposed DIC technique. The proposed method here utilizes features present on the surface of the test specimen (such as microstructure and material inhomogeneity) which provide useful contrast. This can be achieved by mounting a distance microscope and a DIC camera on a fretting fatigue test rig. This approach in strain measurement requires monitoring of the distance between two dark spots on the grayscale image. The change in length divided by the original length between the two spots provides the strain under the applied loads [Kartal et al., 2011]. In this way, by monitoring the strain variation during the cyclic loading, it is possible to measure D. Whenever, D is equal to $D_{critical}$, the damage threshold can be detected.

Furthermore, as elaborated in Chapter 5 the material constants (i.e. dam-

age variables A and β) were calibrated by subtracting calculated crack propagation life from total lifetime, due to lack of a concrete experimental approach to measure the initiation lifetime. In the proposed methodology for measuring the onset of initiation, for a given fretting fatigue test, the damage variable D can be measured as a function of fretting fatigue cycle N, generating an experimental D-N curve. Since the test specimen has undergone fatigue cycling, the material softens and the modulus measured is the damaged modulus of elasticity. Thus, by combination of developed numerical code and the experimental D-N curve, the damage parameters A and β can be obtained experimentally at onset of fretting fatigue crack initiation.

9.4.2 Numerical approach

From numerical point of view, by having the developed fretting fatigue crack initiation and propagation lifetime prediction in hand, there are plenty of parametric studies that can be performed. First of all, the proposed models for crack initiation and propagation can be extended to 3-D applications such as SBLJ, DBLJ and shock absorber's washer disc contact problems. Moreover, the effects of different fretting fatigue variables such as residual stress fields, coated layers, multiple geometrical impurities, different contact asperities, high and low temperatures on initiation and propagation lifetime can be investigated.

In particular for fretting fatigue crack initiation lifetime, the developed damage model can be extended to consider the effect of non-proportional loading condition in the model itself. The results can be compared with the developed model in this study to find the effect of non-proportionality on prediction of fretting fatigue lifetime.

In terms of crack propagation, the main issue is the right crack trajectory that can be in investigated further. To do so, the effect of non-proportionality on crack path should be investigated. This can be achieved by considering different factors that can affect crack propagation under non-proportional loading condition. As mentioned earlier most of these factors are not yet thoroughly understood. Some of these factors can be listed as: the material model, the degree of cyclic plastic deformation and its direction ahead of the crack tip, the crack closure phenomenon, the related mean stress effect, the components geometry in general and especially the variable mode-mixity along a crack front.

Appendix A

Guideline for FEA of fretting fatigue

As shown and also reviewed in Chapter 2 Finite Element Analysis (FEA) is a precious technique for evaluating performance of fretting and fretting fatigue phenomena. Development of complex numerical model of structures that are subjected to fretting and fretting fatigue condition is becoming pervasive. In this study in addition to achieve each evidential objective, it has been tried to provide a guideline for FEA of fretting and fretting fatigue. For this purpose, first in Chapter 2 some of the available models in literature have been reviewed. Subsequently, in this section some recommendations for reporting different FE modelling of fretting fatigue are put forward in order to find a reliable modelling approach.

A.1 Model identification

In order to be able to clarify the abilities and restrictions of simulated FE model, an overall description of the model should be provided in form of model identification, which can be consist of below information:

- Model name: A specific name that describes the model (e.g. FFTAL).
- Related practical application: Mentioning the target related practical application of the FE model (e.g. Titanium for dovetail joints or Al for aerospace industry).

- Version: Identifying the version of published model in case that the model is used with some changes.
- Mechanical domain: The mathematical equations that is used in the model (e.g. linear or no linear, static, dynamic and so on)
- Model utilities: The main objective that the model is used for (e.g. monitoring stress distribution at contact interface, calculating initiation lifetime or propagation lifetime).
- Highlights: What is innovative in the developed model (e.g. new friction formulation is defined)
- Restrictions: The significant limitation that can affect the model behaviour (e.g. modelling straight crack propagation under mode I)
- Reference to literature: In case that the model is not innovative, it can be referenced to other researchers' works.

A.2 Model structure

One of the main aims of this guideline is to help to provide appropriate data in order to reproducing the fretting or fretting fatigue model by other researchers. Therefore, the provided information should be enough for someone who is interested in detailed information from the model to reuse the model to perform simulations using same or similar inputs, or customize the model for their research needs.

- Geometrical design: Categorizing the FE model based on the different experimental configurations (e.g. Bridge type, Single clamp type or Practical applications).
- Constitutive representation: The material definition (e.g. linear elastic, elasto-plastic or user defined material behaviour)
- Loading and boundary conditions: Describing the model loading and boundary conditions based on the experimental test conditions.
- Contact algorithms: Defining the contact algorithms and if applicable the reason for selecting the particular algorithm (e.g. penalty function, normal Lagrange, augmented Lagrange or user defined algorithm)

- Contact properties: Specifying the type of contact (e.g node to node, node to surface, surface to surface, finite or small sliding and the COF)
- Contact status: The contact condition at the applied loading conditions (e.g. sticking, partial slip, gross or replicating sliding)
- Meshing: Because the performance of the simulation relies on the quality of mesh, the mesh convergence study should be performed for different fretting fatigue contact configurations. Thus, some details information regarding the FE mesh is needed (e.g. element type, element shape, element formulation or mesh density at contact interface).

A.3 Simulation structure

Th FE modelling approach normally consist of the mathematical equations that represent the mechanics. According to literature, the development of the fretting or fretting fatigue FE models, is tightly coupled to the simulation software capabilities. In this section the provided information identifies the underlying simulation structure to reproduce the results of the FE model.

- Name of software: Stating the software name (e.g. ABAQUS®, ANSYS®or in house software).
- Version of software: Stating the version of the FEA software used, because many aspects of FEA software are different between versions (e.g ABAQUS®6.11)
- Solution strategy: Identifying the solution strategy of the solver (e.g. implicit static or explicit) and its relevant settings (e.g. incremental)
- Convergence criteria: Providing the convergence tolerances used to determine the completion of simulation.
- Post-Processing: Providing the post-processing approach if the outputs are calculated from the raw simulation results or another software such as Matlab is used to do the post-processing.

A.4 Verification and validation

In the first step, the difference between *verification* and *validation* should be clarified. By definition, *verification* is about *solving the equations right*, whereas

validation is more related to *solving the right equations*.

A.4.1 Verification

Many researchers conduct their own *verification* based on verification tools provided by the simulation software package. In spite of this fact, it is important to explain the verification procedures. Some the *verification* items can be reported as:

- Comparison with analytical solutions: Specifying the analytical solution used for comprising purposes, if available.
- Methods of verification: Summarising the verification analyses conducted along with the verification procedure provided by FEA software (see Chapter 4 single clamp cylindrical contact configuration).
- Mesh convergence study (see Chapter 4).
- Sensitivity to simulation setting: Reporting the influence of different solutions techniques, numerical algorithms (e.g. contact statue or algorithm) on the FE model out put results.
- Repeatability: Reporting or referencing to literature, if any, of simulating the FE model with different software package with the same loading and boundary conditions lead to the same results.

A.4.2 Validation

As mentioned above, validating the model determines if the right equations are being solved to represent the fretting or fretting fatigue problem. Some the *validation* items can be reported as:

- Modelling hypotheses: Listing the main assumptions relevant to the simplification of the FE model of fretting or fretting fatigue configuration.
- Sensitivity analysis: Reporting any uncertainties in model inputs and parameters that can affect the reliability of the model (e.g. defining the COF based on some general knowledge (see Chapter 4 washer-disc contact model).
- Assumptions for applying loading and boundary conditions: Describing the assumptions and simplifications that are considered for applying the

loads and boundary conditions with respect to the real experimental set-up.

- Justification of parameters: Providing adequate justification to support the selection of the parameters for the FE model.
- Validation procedure: Describing the procedure that is used for validating the FE model. This procedure can be direct for instance comparing the performed experimental results with the FE model (see Chapter 4 SBLJ and DBLJ), or indirect validation based on data from literature.

To conclude, in short term, there is hope that these recommendations will encourage collaborative evolution and adoption by researchers, who are working in the field of fretting and fretting fatigue. These recommendations help to stablish confidants through model reproducibility, repeatability and accountability.

Appendix B

Publications

B.1 A1 - Peer reviewed journal publications included in Science Citation Index

1. Majzoobi, G.H., **Hojjati-Talemi, R.,** et al., (2010). A new device for fretting fatigue testing. *Transactions of the Indian institute of metals*, 63(2-3):493–497.

2. Majzoobi, G.H., **Hojjati-Talemi, R.,** Soori, M., (2011). Fretting fatigue behavior of Al7075-T6 at sub-zero temperature. *Tribology International*, 44(11):1443–1451.

3. **Hojjati-Talemi, R.,** Wahab, M.A., De Baets, P., (2012). Numerical investigation into effect of contact geometry on fretting fatigue crack propagation lifetime. *Tribology Transactions*, 55(3):365–375.

4. **Hojjati-Talemi, R.,** and Wahab, M.A., (2012). Finite Element Analysis of Localized Plasticity in Al 2024-T3 Subjected to Fretting Fatigue. *Tribology Transactions* 55(6):805–814.

5. **Hojjati-Talemi, R.,** and Wahab, M.A., (2013). Fretting fatigue crack initiation lifetime predictor tool: Using damage mechanics approach. *Tribology International*, 60(0):176–186.

6. **Hojjati-Talemi, R.,** and Wahab, M.A., Giner, E., Sabsabi M., (2013). Numerical estimation of fretting fatigue lifetime using damage and fracture mechanics. *Tribology Letters* 52(1):11–25.

7. **Hojjati-Talemi, R.,** Wahab, M.A., De Baets, P., (2014). Finite element simulation of phase difference effects on fretting fatigue crack nucleation behaviour. *Journal of Engineering Tribology* 228(4): 470-479.

8. **Hojjati-Talemi, R.,** Wahab, M.A., De Pauw J., De Baets, P., (2014). Prediction of fretting fatigue crack initiation and propagation lifetime in cylindrical contact configuration. *Tribology International* 76(0): 73-91.

9. De Pauw, J., De Waele, W., **Hojjati-Talemi, R.,** De Baets, P., (2014). On the use of digital image correlation for slip measurement during reciprocating sliding and fretting fatigue experiments. *International Journal of Solids and Structures* (In press).

10. **Hojjati-Talemi, R.,** Wahab, M.A., De Baets, P., (2014). Sensitivity of fretting fatigue parameters and crack initiation lifetime to different geometrical impurities. *Journal of Engineering Tribology* (Under review).

11. **Hojjati-Talemi, R.,** Wahab, M.A., Zahedi, A., (2014). On fretting fatigue failure mechanism: Application to automotive shock absorber valve. (Under preparation).

12. **Hojjati-Talemi, R.,** Wahab, M.A., De Baets, P., (2014). An experimental and numerical investigation on fretting fatigue behaviour of double bolted lap joint. (Under preparation).

13. **Hojjati-Talemi, R.,** Wahab, M.A., De Baets, P., (2014). Characterizing frictional behaviour of single and double bolted lap joints subjected to fretting fatigue. (Under preparation).

14. **Hojjati-Talemi, R.,** Wahab, M.A., De Baets, P., (2014). A practical guideline to reliable finite element modelling of fretting fatigue. (Under preparation).

B.2 A2 - Peer reviewed journal publications not included in Science Citation Index

1. **Hojjati-Talemi, R.,** Wahab, M.A., De Baets, P., De Pauw J., (2011). Effect of different fretting fatigue primary variables on relative slip amplitude. *Mechanical engineering letters* 5:57–67.

B.3 P1 - Peer reviewed Publications in conference proceedings included in Science Citation Index

1. **Hojjati-Talemi, R.,** Hojjati-Talemi, A., Wahab, M.A., De Baets, P., (2011). Finite element analysis of fretting fatigue using different pad's geometries and compression forces. *Journal of Key Engineering Materials* 452–453:9–12. Presented at the 9^{th} International conference on Fracture and Damage Mechanics. Nagasaki, Japan.

2. **Hojjati-Talemi, R.,** Hojjati-Talemi, A., Wahab, M.A., De Baets, P., (2011). Numerical modelling of fretting fatigue. *Journal of physics conference series*, 305. Presented at the 9^{th} International conference on Damage Assessment of Structures (DAMAS 2011), St Anne's College, University of Oxford, Oxford, UK.

3. Wahab, M.A., **Hojjati-Talemi, R.,** De Baets, P., (2012). FEA of fretting fatigue: a comparison between ANSYS and ABAQUS. *Journal of Key Engineering Materials*, 488–489:662–665. Presented at the 10^{th} International conference on Fracture and Damage Mechanics (FDM), Dubrovnik, Croatia.

4. Wahab, M.A., Hilmy, I,. **Hojjati-Talemi, R.,** (2013). On the use of low and high cycle fatigue damage models. *Journal of Key Engineering Materials*, 569–570:1029–1035. Presented at the 10^{th} International conference on Damage Assessment of Structures (DAMAS 2013), Dublin, Ireland.

B.4 C1 - Publications in conference proceedings

1. Majzoobi, G.H., **Hojjati-Talemi, R.,** et al., (2008). A new device for fretting fatigue testing. *Proceedings of* 5^{th} *international conference on creep, fatigue and creep-fatigue interaction.* Chennai, India.

2. **Hojjati-Talemi, R.,** Soori, M., Wahab, M.A., De Baets, P., (2011). Experimental and numerical investigation into effect of elevated temperature on fretting fatigue behavior. *Sustainable construction and design*, 2:2–

11. Presented at the Sustainable Construction and Design 2011 (SCAD), Ghent, Belgium: Ghent University, Laboratory Soete.

3. Wahab, M.A., Hilmy, I., Hafiz, T., **Hojjati-Talemi, R.,** (2012). Finite element modelling of damage fracture and fretting fatigue. 15^{th} *Proceedings of International Conference on Applied Mechanics and Mechanical Engineering*, AMME–15:D1–MD14.

4. De Pauw, J., De Waele, W., De Baets, P., **Hojjati-Talemi, R.,** (2012). Contact mechanics in fretting fatigue. *Sustainable construction and design*, 199–206. Presented at the Sustainable Construction and Design (SCAD2012), Ghent, Belgium: Ghent University, Laboratory Soete.

5. **Hojjati-Talemi, R.,** Wahab, M.A., De Pauw J., De Baets, P., (2012). On finite element analysis of fretting fatigue. *Sustainable construction and design*, 207–220. Presented at the Sustainable Construction and Design (SCAD2012), Ghent, Belgium: Ghent University, Laboratory Soete.

6. **Hojjati-Talemi, R.,** Wahab, M.A., (2012). XFEM for fretting fatigue: straight VS mixed mode crack propagation. *Proceedings of the* 4^{th} *International Conference on Crack Paths (CP2012)*, 351–358, Gaeta, Italy.

7. De Smedt, B., Wahab, M.A.,**Hojjati-Talemi, R.,** Hertschap, K., (2013). Survey on techniques to detect micro-cracks in steel after bending. *Sustainable construction and design.* Presented at the Sustainable Construction and Design (SCAD2013), Ghent, Belgium: Ghent University, Laboratory Soete.

8. Sadeghi, M., Wahab, M.A.,**Hojjati-Talemi, R.,** Yue, T., (2013). A review of FE on crack initiation in fretting fatigue. *Sustainable construction and design.* Presented at the Sustainable Construction and Design (SCAD2013), Ghent, Belgium: Ghent University, Laboratory Soete.

9. Yue, T., Wahab, M.A.,**Hojjati-Talemi, R.,** Sadeghi, M., (2013). Numerical modeling of fretting wear. *Sustainable construction and design.* Presented at the Sustainable Construction and Design (SCAD2013), Ghent, Belgium: Ghent University, Laboratory Soete.

10. **Hojjati-Talemi, R.,** Wahab, M.A.,Sadeghi, M., Yue, T., (2013). XFEM VS FEM: application to fretting fatigue 2D crack propagation. *Sustainable construction and design.* Presented at the Sustainable Construction

and Design (SCAD2013), Ghent, Belgium: Ghent University, Laboratory Soete.

11. **Hojjati-Talemi, R.,** Wahab, M.A., Yue, T., D'Alvise, L., (2014). On fretting fatigue behaviour of single bolted lap joint. 3^{rd} International Conference on Fracture Fatigue and Wear (FFW 2014), Kitakyushu, Japan.

B.5 C3 - Conference abstracts

1. Majzoobi, G.H., **Hojjati-Talemi, R.,** Soori, M., (2010). Fretting fatigue behavior of Al7075-T6 at sub-zero temperature. *Proceedings of the* 6^{th} *international symposium on fretting fatigue (ISFF6)* Chengdu, PR China.

2. **Hojjati-Talemi, R.,** (2011). Numerical modelling of fretting fatigue crack initiation and propagation. *Presented at the* 12^{th} *FEA PhD Symposium*, Ghent, Belgium: Ghent University. Faculty of Engineering and Architecture.

3. **Hojjati-Talemi, R.,** De Baets, P., Wahab, M.A., (2013). A fretting fatigue numerical lifetime prediction tool: combination of damage and fracture mechanics approaches. *Proceedings of the* 7^{th} *international symposium on fretting fatigue (ISFF7).* University Chengdu, University of Oxford, Oxford, UK. **Robert Waterhouse award, for the best paper presented by a young researcher in the eld of Fretting and Fretting fatigue**.

4. **Hojjati-Talemi, R.,** (2013). Numerical modeling techniques for fretting fatigue crack initiation and propagation. *Presented at the* 13^{th} *FEA PhD Symposium*, Ghent, Belgium: Ghent University. Faculty of Engineering and Architecture. **Laureate Poster Award, category 'Senior PhD researchers'**.

Bibliography

[Adibnazari and Hoeppner, 1994] Adibnazari, S. and Hoeppner, D. (1994). The role of normal pressure in modeling fretting fatigue. *Fretting fatigue, ESIS*, 18:125–133.

[Aggarwal et al., 2006] Aggarwal, M., Agrawal, V., and Khan, R. (2006). A stress approach model for predictions of fatigue life by shot peening of en45a spring steel. *International Journal of Fatigue*, 28(12):1845–1853.

[Aggarwal et al., 2005] Aggarwal, M., Khan, R., and Agrawal, V. (2005). Investigation into the effects of shot peening on the fretting fatigue behaviour of 65si7 spring steel leaf springs. *Proceedings of the Institution of Mechanical Engineers, Part L: Journal of Materials Design and Applications*, 219(3):139–147.

[Aghdam et al., 2012] Aghdam, A., Beheshti, A., and Khonsari, M. (2012). On the fretting crack nucleation with provision for size effect. *Tribology International*, 47:32–43.

[Alfredsson and Olsson, 2000] Alfredsson, B. and Olsson, M. (2000). Initiation and growth of standing contact fatigue cracks. *Engineering Fracture Mechanics*, 65(1):89–106.

[Almajali, 2006] Almajali, M. (2006). *Effects of Phase Difference Between Axial and Contact loads on Fretting Fatigue Behavior of Titanium Alloy.* PhD thesis, Air Force Institute of Technology.

[Anderson, 2005] Anderson, T. L. (2005). *Fracture mechanics: fundamentals and applications.* CRC press.

[AP, 2013] AP (2013). http://www.ap.org/. accessed: October 20, 2013.

[Araujo and Nowell, 2002] Araujo, J. and Nowell, D. (2002). The effect of rapidly varying contact stress fields on fretting fatigue. *International Journal of Fatigue*, 24(7):763–775.

[Arora et al., 2007] Arora, P. R., Jacob, M., Salit, M. S., Ahmed, E. M., Saleem, M., and Edi, P. (2007). Experimental evaluation of fretting fatigue test apparatus. *International journal of fatigue*, 29(5):941–952.

[Arrieta et al., 2004] Arrieta, H. V., Wackers, P., Van, K. D., Constantinescu, A., and Maitournam, H. (2004). Modelling attempts to predict fretting-fatigue life on turbine components. Technical report, DTIC Document.

[ASTM E2789-10, 2011] ASTM E2789-10 (2011). *Strandard guide for fretting fatigue testing*. American Society for Testing and Materials.

[ASTM-E8, 1997] ASTM-E8 (1997). Standard test methods for tensile testing of metallic materials. *Annual book of ASTM standards*, 3.

[Azevedo et al., 2009] Azevedo, C., Henriques, A., Pulino Filho, A., Ferreira, J., and Araújo, J. (2009). Fretting fatigue in overhead conductors: Rig design and failure analysis of a grosbeak aluminium cable steel reinforced conductor. *Engineering Failure Analysis*, 16(1):136–151.

[Baietto et al., 2013] Baietto, M., Pierres, E., Gravouil, A., Berthel, B., Fouvry, S., and Trolle, B. (2013). Fretting fatigue crack growth simulation based on a combined experimental and xfem strategy. *International Journal of Fatigue*, 47:31–43.

[Baietto et al., 2010] Baietto, M.-C., Pierres, E., and Gravouil, A. (2010). A multi-model x-fem strategy dedicated to frictional crack growth under cyclic fretting fatigue loadings. *International Journal of Solids and Structures*, 47(10):1405–1423.

[Barber and Ciavarella, 2000] Barber, J. and Ciavarella, M. (2000). Contact mechanics. *International Journal of Solids and Structures*, 37(1):29–43.

[Basquin, 1910] Basquin, O. (1910). *The exponential law of endurance tests*, volume 10. American Society for.Testing and Materials, ASTEA.

[Basseville et al., 2011] Basseville, S., Héripré, E., and Cailletaud, G. (2011). Numerical simulation of the third body in fretting problems. *Wear*, 270(11):876–887.

[Belytschko and Black, 1999] Belytschko, T. and Black, T. (1999). Elastic crack growth in finite elements with minimal remeshing. *International journal for numerical methods in engineering*, 45(5):601–620.

[Benhamena et al., 2010] Benhamena, A., Talha, A., Benseddiq, N., Amrouche, A., Mesmacque, G., and Benguediab, M. (2010). Effect of clamping force on fretting fatigue behaviour of bolted assemblies: Case of couple steel–aluminium. *Materials Science and Engineering: A*, 527(23):6413–6421.

[Bernardo et al., 2006] Bernardo, A., Araujo, J., and Mamiya, E. (2006). Proposition of a finite element-based approach to compute the size effect in fretting fatigue. *Tribology international*, 39(10):1123–1130.

[Bertini et al., 2008] Bertini, L., Beghini, M., Santus, C., and Baryshnikov, A. (2008). Resonant test rigs for fatigue full scale testing of oil drill string connections. *International Journal of Fatigue*, 30(6):978–988.

[Bhattacharya and Ellingwood, 1998] Bhattacharya, B. and Ellingwood, B. (1998). Continuum damage mechanics analysis of fatigue crack initiation. *International journal of fatigue*, 20(9):631–639.

[Bhattacharya and Ellingwood, 1999] Bhattacharya, B. and Ellingwood, B. (1999). A new cdm-based approach to structural deterioration. *International journal of solids and structures*, 36(12):1757–1779.

[Boddington et al., 1985] Boddington, P., Chen, K., and Ruiz, C. (1985). The numerical analysis of dovetail joints. *Computers & structures*, 20(4):731–735.

[BS EN 1090-3, 2008] BS EN 1090-3 (2008). Execution of steel structures and aluminium structures.

[Buciumeanu et al., 2007] Buciumeanu, M., Miranda, A., Pinho, A., and Silva, F. (2007). Design improvement of an automotive-formed suspension component subjected to fretting fatigue. *Engineering Failure Analysis*, 14(5):810–821.

[Cadario and Alfredsson, 2005] Cadario, A. and Alfredsson, B. (2005). Fretting fatigue crack growth for a spherical indenter with constant and cyclic bulk load. *Engineering fracture mechanics*, 72(11):1664–1690.

[Campbell, 2008] Campbell, F. C. (2008). *Elements of metallurgy and engineering alloys*. ASM International.

[Carter et al., 2012] Carter, B., Schenck, E., Wawrzynek, P., Ingraffea, A., and Barlow, K. (2012). Three-dimensional simulation of fretting crack nucleation and growth. *Engineering Fracture Mechanics*.

[Cattaneo, 1938] Cattaneo, C. (1938). Sul contatto di due corpi elastici: distribuzione locale degli sforzi. *Rendiconti dellAccademia nazionale dei Lincei*, 27(6):342–348.

[Chaboche and Lesne, 1988] Chaboche, J. and Lesne, P. (1988). A non-linear continuous fatigue damage model. *Fatigue & fracture of engineering materials & structures*, 11(1):1–17.

[Chakherlou and Abazadeh, 2012] Chakherlou, T. and Abazadeh, B. (2012). Investigating clamping force variations in Al2024-T3 interference fitted bolted joints under static and cyclic loading. *Materials & Design*, 37:128–136.

[Chakherlou et al., 2012] Chakherlou, T., Razavi, M., and Aghdam, A. (2012). On the variation of clamping force in bolted double lap joints subjected to longitudinal loading: A numerical and experimental investigation. *Strain*, 48(1):21–29.

[Chan et al., 2010] Chan, K. S., Enright, M. P., Moody, J. P., Golden, P. J., Chandra, R., and Pentz, A. C. (2010). Residual stress profiles for mitigating fretting fatigue in gas turbine engine disks. *International Journal of Fatigue*, 32(5):815–823.

[Colombie et al., 1984] Colombie, C., Berthier, Y., Floquet, A., Vincent, L., and Godet, M. (1984). Fretting: load carrying capacity of wear debris. *Journal of tribology*, 106(2):194–201.

[Cortez et al., 1999] Cortez, R., Mall, S., and Calcaterra, J. R. (1999). Investigation of variable amplitude loading on fretting fatigue behavior of ti–6al–4v. *International journal of fatigue*, 21(7):709–717.

[Cotterell and Rice, 1980] Cotterell, B. and Rice, J. (1980). Slightly curved or kinked cracks. *International Journal of Fracture*, 16(2):155–169.

[Crossland, 1956] Crossland, B. (1956). Effect of large hydrostatic pressures on the torsional fatigue strength of an alloy steel. In *Proc. Int. Conf. on Fatigue of Metals, Institution of Mechanical Engineers, London*, pages 138–149.

[Cruzado et al., 2013] Cruzado, A., Leen, S. B., Urchegui, M. A., and Gmez, X. (2013). Finite element simulation of fretting wear and fatigue in thin steel wires. *International Journal of Fatigue*, 55(0):7–21.

[Cruzado et al., 2012] Cruzado, A., Urchegui, M., and Gómez, X. (2012). Finite element modeling and experimental validation of fretting wear scars in thin steel wires. *Wear*, 289:26–38.

[De Pauw et al., 2013a] De Pauw, J., De Baets, P., De Waele, W., and Hojjati Talemi, R. (2013a). Design of a fretting fatigue test rig with compliant springs. In *Sustainable Construction and Design (SCAD-2013)*. Ghent University, Laboratory Soete.

[De Pauw et al., 2013b] De Pauw, J., De Waele, W., and De Baets, P. (2013b). On the influence of laser surface texture in fretting fatigue testing. *Mechanical Engineering Letters, Szent István University*, pages 104–111.

[Ding et al., 2011] Ding, J., Houghton, D., Williams, E., and Leen, S. (2011). Simple parameters to predict effect of surface damage on fretting fatigue. *International Journal of Fatigue*, 33(3):332–342.

[Ding et al., 2008] Ding, J., Leen, S., Williams, E., and Shipway, P. (2008). Finite element simulation of fretting wear-fatigue interaction in spline couplings. *Tribology-Materials, Surfaces & Interfaces*, 2(1):10–24.

[Ding et al., 2007a] Ding, J., Sum, W., Sabesan, R., Leen, S., McColl, I., and Williams, E. (2007a). Fretting fatigue predictions in a complex coupling. *International journal of fatigue*, 29(7):1229–1244.

[Ding et al., 2007b] Ding, J., Sum, W., Sabesan, R., Leen, S., McColl, I., and Williams, E. (2007b). Fretting fatigue predictions in a complex coupling. *International journal of fatigue*, 29(7):1229–1244.

[Dini and Nowell, 2003] Dini, D. and Nowell, D. (2003). Prediction of the slip zone friction coefficient in flat and rounded contact. *Wear*, 254(3):364–369.

[Dixon, 2007] Dixon, J. C. (2007). *The shock absorber handbook*. John Wiley & Sons, Ltd.

[Dobromirski, 1992] Dobromirski, J. (1992). Variables of fretting process: Are there 50 of them? *ASTM Special Technical Publication*, 1159:60–60.

[Dowling, 1971] Dowling, N. E. (1971). Fatigue failure predictions for complicated stress-strain histories. Technical report, DTIC Document.

[Edwards, 1981] Edwards, P. (1981). The application of fracture mechanics to predicting fretting fatigue. *Fretting Fatigue*, pages 67–97.

[El Haddad et al., 1980] El Haddad, M., Dowling, N., Topper, T., and Smith, K. (1980). J integral applications for short fatigue cracks at notches. *International Journal of Fracture*, 16(1):15–30.

[Endo and Goto, 1976] Endo, K. and Goto, H. (1976). Initiation and propagation of fretting fatigue cracks. *Wear*, 38(2):311–324.

[Endo et al., 1974] Endo, K., H, G., and Fukunaga, T. (1974). Effects of environment on fretting fatigue. *Bull. J.S.M.E*, 17(108):647–654.

[Erdogan and Sih, 1963] Erdogan, F. and Sih, G. (1963). On the crack extension in plates under plane loading and transverse shear. *Journal of basic engineering*, 85:519.

[Fadag et al., 2008] Fadag, H., Mall, S., and Jain, V. (2008). A finite element analysis of fretting fatigue crack growth behavior in ti–6al–4v. *Engineering Fracture Mechanics*, 75(6):1384–1399.

[Farrahi et al., 2005] Farrahi, G., Majzoobi, G., and Chinekesh, H. (2005). Effect of contact geometry on fretting fatigue life of aluminium alloy 2024-t3. *Indian Journal of Engineering and Materials Sciences*, 12(4):331.

[Farris et al., 2000] Farris, T. N., Harish, G., Tieche, C., Sakagami, T., and Szolwinski, M. P. (2000). Experimental tools for characterizing fretting contacts. *JSME international journal. Series A, Solid mechanics and material engineering*, 43(4):374–383.

[Fatemi and Socie, 1988] Fatemi, A. and Socie, D. F. (1988). A critical plane approach to multiaxial fatigue damage including out-of-phase loading. *Fatigue & Fracture of Engineering Materials & Structures*, 11(3):149–165.

[Findley, 1956] Findley, W. N. (1956). *Fatigue of metals under combinations of stresses*. Division of Engineering, Brown University.

[Fleming et al., 1997] Fleming, M., Chu, Y., Moran, B., Belytschko, T., Lu, Y., and Gu, L. (1997). Enriched element-free galerkin methods for crack

tip fields. *International Journal for Numerical Methods in Engineering*, 40(8):1483–1504.

[Forman et al., 2005] Forman, R. G., Shivakumar, V., Cardinal, J., Williams, L., and McKeighan, P. (2005). Fatigue crack growth database for damage tolerance analysis. Technical report, National Technical Information Service (NTIS).

[Fouvry et al., 2004] Fouvry, S., Duo, P., and Perruchaut, P. (2004). A quantitative approach of ti–6al–4v fretting damage: friction, wear and crack nucleation. *Wear*, 257(9):916–929.

[Fouvry et al., 2002] Fouvry, S., Elleuch, K., and Simeon, G. (2002). Prediction of crack nucleation under partial slip fretting conditions. *The Journal of Strain Analysis for Engineering Design*, 37(6):549–564.

[Fouvry et al., 1995] Fouvry, S., Kapsa, P., and Vincent, L. (1995). Analysis of sliding behaviour for fretting loadings: determination of transition criteria. *Wear*, 185(1):35–46.

[Fouvry et al., 2003] Fouvry, S., Kapsa, P., and Vincent, L. (2003). A global methodology to quantify fretting damages. *ASTM special technical publication*, 1425:17–32.

[Fouvry et al., 2007] Fouvry, S., Paulin, C., and Liskiewicz, T. (2007). Application of an energy wear approach to quantify fretting contact durability: introduction of a wear energy capacity concept. *Tribology International*, 40(10):1428–1440.

[FRANC2D/L, 2010] FRANC2D/L (2010). A crack propagation simulator for plane layered structures. School of Civil and Environmental Engineering, Cornell University, Ithaca, New York.

[Gall et al., 2001] Gall, K., Horstemeyer, M. F., Degner, B. W., McDowell, D. L., and Fan, J. (2001). On the driving force for fatigue crack formation from inclusions and voids in a cast A356 aluminum alloy. *International Journal of Fracture*, 108(3):207–233.

[Giannakopoulos and Suresh, 1998] Giannakopoulos, A. and Suresh, S. (1998). A three-dimensional analysis of fretting fatigue. *Acta materialia*, 46(1):177–192.

[Giner et al., 2005] Giner, E., Hills, D., and Fuenmayor, F. (2005). Complete elastic contact subject to cyclic shear in partial slip. *Journal of engineering mechanics*, 131(11):1146–1156.

[Giner et al., 2011a] Giner, E., Navarro, C., Sabsabi, M., Tur, M., Dominguez, J., and Fuenmayor, F. (2011a). Fretting fatigue life prediction using the extended finite element method. *International Journal of Mechanical Sciences*, 53(3):217–225.

[Giner et al., 2011b] Giner, E., Sabsabi, M., and Fuenmayor, F. (2011b). Calculation of K_{II} in crack face contacts using X-FEM. application to fretting fatigue. *Engineering Fracture Mechanics*, 78(2):428–445.

[Giner et al., 2013] Giner, E., Sabsabi, M., Ródenas, J. J., and Javier Fuenmayor, F. (2013). Direction of crack propagation in a complete contact fretting-fatigue problem. *International Journal of Fatigue*, 58:172–180.

[Giner et al., 2008] Giner, E., Sukumar, N., Denia, F., and Fuenmayor, F. (2008). Extended finite element method for fretting fatigue crack propagation. *International journal of solids and structures*, 45(22):5675–5687.

[Giner et al., 2009] Giner, E., Tur, M., Vercher, A., and Fuenmayor, F. (2009). Numerical modelling of crack–contact interaction in 2D incomplete fretting contacts using X-FEM. *Tribology International*, 42(9):1269–1275.

[Goh et al., 2006] Goh, C.-H., McDowell, D., and Neu, R. (2006). Plasticity in polycrystalline fretting fatigue contacts. *Journal of the Mechanics and Physics of Solids*, 54(2):340–367.

[Goh et al., 2001] Goh, C.-H., Wallace, J., Neu, R., and McDowell, D. (2001). Polycrystal plasticity simulations of fretting fatigue. *International Journal of Fatigue*, 23:423–435.

[Golden and Calcaterra, 2006] Golden, P. and Calcaterra, J. (2006). A fracture mechanics life prediction methodology applied to dovetail fretting. *Tribology International*, 39(10):1172–1180.

[Golden and Nicholas, 2005] Golden, P. J. and Nicholas, T. (2005). The effect of angle on dovetail fretting experiments in ti-6al-4v. *Fatigue & Fracture of Engineering Materials & Structures*, 28(12):1169–1175.

[Griffith, 1921] Griffith, A. A. (1921). The phenomena of rupture and flow in solids. *Philosophical transactions of the royal society of london. Series A, containing papers of a mathematical or physical character*, 221:163–198.

[Guo et al., 2008] Guo, R., Duan, R.-C., Mesmacque, G., Zhang, L., Amrouche, A., and Guo, R. (2008). Fretting fatigue behavior of riveted al 6xxx components. *Materials Science and Engineering: A*, 483:398–401.

[Gutkin and Alfredsson, 2008] Gutkin, R. and Alfredsson, B. (2008). Growth of fretting fatigue cracks in a shrink-fitted joint subjected to rotating bending. *Engineering Failure Analysis*, 15(5):582–596.

[H-Gangaraj et al., 2011] H-Gangaraj, S., Alvandi-Tabrizi, Y., Farrahi, G., Majzoobi, G., and Ghadbeigi, H. (2011). Finite element analysis of shot-peening effect on fretting fatigue parameters. *Tribology International*, 44(11):1583–1588.

[Hattori et al., 2003] Hattori, T., Nakamura, M., and Watanabe, T. (2003). Simulation of fretting-fatigue life by using stress-singularity parameters and fracture mechanics. *Tribology international*, 36(2):87–97.

[Hayashi and Nemat-Nasser, 1981] Hayashi, K. and Nemat-Nasser, S. (1981). Energy-release rate and crack kinking under combined loading. *Journal of Applied Mechanics*, 48:520.

[Heoppner et al., 1996] Heoppner, D. W., Elliot III, C. D., and Moesser, M. W. (1996). The role of fretting fatigue on aircraft rivet hole cracking. Technical report, DTIC Document.

[Hertz, 1881] Hertz, H. (1881). On the contact of elastic solids. *J. reine angew. Math*, 92(156-171):110.

[Hibbitt et al., 2011] Hibbitt, H., Karlsson, B., and Sorensen, P. (2011). Abaqus analysis user's manual version 6.10. *Dassault Systèmes Simulia Corp.: Providence, RI, USA*.

[Hills et al., 1988a] Hills, D., Nowell, D., and O'Connor, J. (1988a). On the mechanics of fretting fatigue. *Wear*, 125(1):129–146.

[Hills et al., 1988b] Hills, D., Nowell, D., and Sackfield, A. (1988b). Surface fatigue considerations in fretting. In *Interface Dynamics, Proceedings of the 14th Leeds-Lyon Symposium on Tribology, Elsevier, Amsterdam*, pages 35–40.

[Hills and Nowell, 1994] Hills, D. A. and Nowell, D. (1994). *Mechanics of fretting fatigue*. Solid mechanics and its applications vol. 30. Kluwer Academic Publishers.

[Hirsch and Neu, 2011] Hirsch, M. and Neu, R. (2011). Fretting damage in thin sheets: Analysis of an experimental configuration. *Tribology International*, 44(11):1503–1510.

[Hoeppner et al., 1994] Hoeppner, D., Adibnazari, S., and Moesser, M. W. (1994). Literature review and preliminary studies of fretting and fretting fatigue including special applications to aircraft joints. Technical report, DTIC Document.

[Hoeppner, 1981] Hoeppner, D. W. (1981). Environmental effects in fretting fatigue. *Fretting Fatigue*, pages 143–158.

[Hojjati Talemi, 2010] Hojjati Talemi, R. (2010). Fretting fatigue behaviour of AL 7075-T6 at subzero temperature. Master thesis, TIAU Univresity, Iran.

[Hornbach et al., 2006] Hornbach, D., Prevey, P., and Loftus, E. (2006). Application of low plasticity burnishing (lpb) to improve the fatigue performance of ti–6al–4v femoral hip stems. *J ASTM Int*, 3(5):45–55.

[Houghton et al., 2009] Houghton, D., Wavish, P., Williams, E., and Leen, S. (2009). Multiaxial fretting fatigue testing and prediction for splined couplings. *International Journal of Fatigue*, 31(11):1805–1815.

[Hyde et al., 2005] Hyde, T., Leen, S., and McColl, I. (2005). A simplified fretting test methodology for complex shaft couplings. *Fatigue & Fracture of Engineering Materials & Structures*, 28(11):1047–1067.

[Inglis, 1963] Inglis, C. E. (1963). *Applied mechanics for engineers*. Dover.

[Irwin, 1958] Irwin, G. (1958). Fracture encyclopedia of physics, vol. vi.

[Iyer and Mall, 2000] Iyer, K. and Mall, S. (2000). Effects of cyclic frequency and contact pressure on fretting fatigue under two-level block loading. *Fatigue and Fracture of Engineering Materials and Structures*, 23(4):335–346.

[Iyer and Mall, 2001] Iyer, K. and Mall, S. (2001). Analyses of contact pressure and stress amplitude effects on fretting fatigue life. *Journal of engineering materials and technology*, 123(1):85–93.

[Jayaprakash et al., 2010] Jayaprakash, M., Mutoh, Y., Asai, K., Ichikawa, K., and Sukarai, S. (2010). Effect of contact pad rigidity on fretting fatigue behavior of nicrmov turbine steel. *International Journal of Fatigue*, 32(11):1788–1794.

[Jayaprakash et al., 2011] Jayaprakash, M., Mutoh, Y., and Yoshii, K. (2011). Fretting fatigue behavior and life prediction of automotive steel bolted joint. *Materials & Design*, 32(7):3911–3919.

[Jin and Mall, 2000] Jin, O. and Mall, S. (2000). An investigation of friction force in fretting fatigue. *In Hoeppner, David W and Chandrasekaran, V and Elliott III, Charles B, Fretting fatigue: current technology and practices, ASTM STP 1367, American Society for Testing and Materials, West Conshohocken*, 1367:154–166.

[Jin and Mall, 2002] Jin, O. and Mall, S. (2002). Effects of independent pad displacement on fretting fatigue behavior of ti–6al–4v. *Wear*, 253(5):585–596.

[Jin and Mall, 2004a] Jin, O. and Mall, S. (2004a). Effects of slip on fretting behavior: experiments and analyses. *Wear*, 256(7):671–684.

[Jin and Mall, 2004b] Jin, O. and Mall, S. (2004b). Shear force effects on fretting fatigue behavior of ti-6al-4v. *Metallurgical and Materials Transactions A*, 35(1):131–138.

[Jin et al., 2007] Jin, O., Mall, S., and Hager, C. H. (2007). Fretting fatigue behavior of cu-al-coated ti-6ai-4v. *Tribology Transactions*, 50(4):497–506.

[Johnson and Johnson, 1987] Johnson, K. L. and Johnson, K. K. L. (1987). *Contact mechanics*. Cambridge university press.

[Jutte, 2004] Jutte, A. J. (2004). *Effect of a Variable Contact Load on Fretting Fatigue Behavior of Ti-6Al-4V*. PhD thesis, Air Force Institute of Technology.

[Kachanov, 1958] Kachanov, L. (1958). Time of the rupture process under creep conditions. *Isv. Akad. Nauk. SSR. Otd Tekh. Nauk*, 8:26–31.

[Kartal et al., 2011] Kartal, M., Mulvihill, D., Nowell, D., and Hills, D. (2011). Determination of the frictional properties of titanium and nickel alloys using the digital image correlation method. *Experimental mechanics*, 51(3):359–371.

[Kermanpur et al., 2008a] Kermanpur, A., Sepehri Amin, H., Ziaei-Rad, S., Nourbakhshnia, N., and Mosaddeghfar, M. (2008a). Failure analysis of ti-6al-4v gas turbine compressor blades. *Engineering Failure Analysis*, 15(8):1052–1064.

[Kermanpur et al., 2008b] Kermanpur, A., Sepehri Amin, H., Ziaei-Rad, S., Nourbakhshnia, N., and Mosaddeghfar, M. (2008b). Failure analysis of ti6al4v gas turbine compressor blades. *Engineering Failure Analysis*, 15(8):1052–1064.

[Kim and Mall, 2005] Kim, H. S. and Mall, S. (2005). Investigation into three-dimensional effects of finite contact width on fretting fatigue. *Finite elements in analysis and design*, 41(11):1140–1159.

[Kimura and Sato, 2003] Kimura, T. and Sato, K. (2003). Simplified method to determine contact stress distribution and stress intensity factors in fretting fatigue. *International journal of fatigue*, 25(7):633–640.

[Kindervater et al., 2000] Kindervater, C., Johnson, A., Kohlgrüber, D., and Lützenburger, M. (2000). Crash and high velocity impact simulation methodologies for aircraft structures. *Structural Failure and Plasticity (IMPLAST 2000)*, page 345.

[Kohnke, 2010] Kohnke, P. (2010). *ANSYS theory reference*. Ansys.

[Kondoh and Mutoh, 2000] Kondoh, K. and Mutoh, Y. (2000). Crack behavior in the early stage of fretting fatigue fracture. *ASTM Special technical publication*, 1367:282–294.

[Kovalevskii, 1981] Kovalevskii, V. (1981). The mechanism of fretting fatigue in metals. *Wear*, 67(3):271–285.

[Kubiak et al., 2010] Kubiak, K., Mathia, T., and Fouvry, S. (2010). Interface roughness effect on friction map under fretting contact conditions. *Tribology International*, 43(8):1500–1507.

[Kubota et al., 2003] Kubota, M., Niho, S., Sakae, C., and Kondo, Y. (2003). Effect of understress on fretting fatigue crack initiation of press-fitted axle. *JSME International Journal Series A*, 46(3):297–302.

[Lamacq et al., 1997] Lamacq, V., Dubourg, M.-C., and Vincent, L. (1997). A theoretical model for the prediction of initial growth angles and sites of fretting fatigue cracks. *Tribology international*, 30(6):391–400.

[Lanoue et al., 2009] Lanoue, F., Vadean, A., and Sanschagrin, B. (2009). Finite element analysis and contact modelling considerations of interference fits for fretting fatigue strength calculations. *Simulation Modelling Practice and Theory*, 17(10):1587–1602.

[Lee et al., 2004] Lee, H., Jin, O., and Mall, S. (2004). Fretting fatigue behavior of ti–6al–4v with dissimilar mating materials. *International journal of fatigue*, 26(4):393–402.

[Lee and Mall, 2004] Lee, H. and Mall, S. (2004). Some observations on frictional force during fretting fatigue. *Tribology Letters*, 17(3):491–499.

[Lee and Mall, 2006] Lee, H. and Mall, S. (2006). Investigation into tangential force and axial stress effects on fretting fatigue behavior. *Journal of engineering materials and technology*, 128(2):202–209.

[Lee et al., 2005] Lee, H., Mall, S., and Sathish, S. (2005). Investigation into effects of re-shot-peening on fretting fatigue behavior of ti–6al–4v. *Materials Science and Engineering: A*, 390(1):227–232.

[Leen et al., 2002] Leen, S., Hyde, T., Ratsimba, C. H., Williams, E., and McColl, I. (2002). An investigation of the fatigue and fretting performance of a representative aero-engine spline coupling. *The Journal of Strain Analysis for Engineering Design*, 37(6):565–583.

[Lemaitre, 1985] Lemaitre, J. (1985). Coupled elasto-plasticity and damage constitutive equations. *Computer Methods in Applied Mechanics and Engineering*, 51(1):31–49.

[Lemaitre, 1987] Lemaitre, J. (1987). Formulation and identification of damage kinetic constitutive equations. *Continuum Damage Mechanics, Theory and Application, edited by Krajcinovic et al., International Centre for Mechanical Sciences, CISM Courses and Lectures*, 295.

[Lemaitre, 1994] Lemaitre, J. (1994). *Mechanics of solid materials*. Cambridge university press.

[Lemaitre and Desmorat, 2005] Lemaitre, J. and Desmorat, R. (2005). *Engineering damage mechanics: ductile, creep, fatigue and brittle failures*. Springer.

[Lemaitre and Lippmann, 1996] Lemaitre, J. and Lippmann, H. (1996). *A course on damage mechanics*, volume 2. Springer Berlin.

[Leonard et al., 2011] Leonard, B. D., Patil, P., Slack, T. S., Sadeghi, F., Shinde, S., and Mittelbach, M. (2011). Fretting wear modeling of coated and uncoated surfaces using the combined finite-discrete element method. *Journal of tribology*, 133(2).

[Leonard et al., 2012] Leonard, B. D., Sadeghi, F., Shinde, S., and Mittelbach, M. (2012). A numerical and experimental investigation of fretting wear and a new procedure for fretting wear maps. *Tribology Transactions*, 55(3):313–324.

[Liang et al., 2012] Liang, L., Zhang, X., Peng, M., and Qin, G. (2012). Nonlinear characteristic simulation of hydraulic shock absorbers considering the contact of valves. In *The 2nd International Conference on Computer Application and System Modeling*, pages 1132–1134.

[Limess Messtechnik & Software GmbH, 2013] Limess Messtechnik & Software GmbH (Accessed: March 1, 2013). http://www.limess.com/.

[Liu and Hill, 2009] Liu, K. K. and Hill, M. R. (2009). The effects of laser peening and shot peening on fretting fatigue in ti–6al–4v coupons. *Tribology International*, 42(9):1250–1262.

[Lykins et al., 2001a] Lykins, C., Mall, S., and Jain, V. (2001a). A shear stress-based parameter for fretting fatigue crack initiation. *Fatigue & Fracture of Engineering Materials & Structures*, 24(7):461–473.

[Lykins et al., 2000] Lykins, C. D., Mall, S., and Jain, V. (2000). An evaluation of parameters for predicting fretting fatigue crack initiation. *International journal of fatigue*, 22(8):703–716.

[Lykins et al., 2001b] Lykins, C. D., Mall, S., and Jain, V. K. (2001b). Combined experimental–numerical investigation of fretting fatigue crack initiation. *International journal of fatigue*, 23(8):703–711.

[Madge et al., 2007] Madge, J., Leen, S., McColl, I., and Shipway, P. (2007). Contact-evolution based prediction of fretting fatigue life: Effect of slip amplitude. *Wear*, 262(9):1159–1170.

[Majzoobi et al., 2010] Majzoobi, G., Hojjati, R., Nematian, M., Zalnejad, E., Ahmadkhani, A., and Hanifepoor, E. (2010). A new device for fretting fatigue testing. *Transactions of The Indian Institute of Metals*, 63(2-3):493–497.

[Majzoobi et al., 2011] Majzoobi, G., Hojjati, R., and Soori, M. (2011). Fretting fatigue behavior of al7075-t6 at sub-zero temperature. *Tribology International*, 44(11):1443–1451.

[Maouche et al., 1997] Maouche, N., Maitournam, M., and Dang Van, K. (1997). On a new method of evaluation of the inelastic state due to moving contacts. *Wear*, 203:139–147.

[Marines et al., 2003] Marines, I., Bin, X., and Bathias, C. (2003). An understanding of very high cycle fatigue of metals. *International Journal of fatigue*, 25(9):1101–1107.

[Mary and Fouvry, 2007] Mary, C. and Fouvry, S. (2007). Numerical prediction of fretting contact durability using energy wear approach: Optimisation of finite-element model. *Wear*, 263(1):444–450.

[Massingham and Irving, 2006] Massingham, M. and Irving, P. (2006). The effect of variable amplitude loading on stress distribution within a cylindrical contact subjected to fretting fatigue. *Tribology international*, 39(10):1084–1091.

[McColl et al., 2004] McColl, I., Ding, J., and Leen, S. (2004). Finite element simulation and experimental validation of fretting wear. *Wear*, 256(11):1114–1127.

[McDiarmid, 1991] McDiarmid, D. (1991). A general criterion for high cycle multiaxial fatigue failure. *Fatigue & Fracture of Engineering Materials & Structures*, 14(4):429–453.

[Meguid et al., 2000] Meguid, S., Kanth, P., and Czekanski, A. (2000). Finite element analysis of fir-tree region in turbine discs. *Finite elements in analysis and design*, 35(4):305–317.

[Melenk and Babuška, 1996] Melenk, J. M. and Babuška, I. (1996). The partition of unity finite element method: basic theory and applications. *Computer methods in applied mechanics and engineering*, 139(1):289–314.

[Meriaux et al., 2010] Meriaux, J., Boinet, M., Fouvry, S., and Lenain, J. (2010). Identification of fretting fatigue crack propagation mechanisms using acoustic emission. *Tribology International*, 43(11):2166–2174.

[Milestone and Janeczko, 1971] Milestone, W. and Janeczko, J. (1971). Friction between steel surfaces during fretting. *Wear*, 18(1):29–40.

[Mindlin and Deresiewica, 1953] Mindlin, R. and Deresiewica, H. (1953). Elastic spheres in contact under varying oblique forces. *Journal of applied mechanics*, 20.

[Mirzaei, 2010] Mirzaei, M. (2010). *Fracture mechanics, theory and applications*. TMU University.

[Moës et al., 1999] Moës, N., Dolbow, J., and Belytschko, T. (1999). A finite element method for crack growth without remeshing. *International Journal for Numerical Methods in Engineering*, 46(1):131–150.

[Mohd Tobi et al., 2012] Mohd Tobi, A., Shipway, P., and Leen, S. (2012). Finite element modelling of brittle fracture of thick coatings under normal and tangential loading. *Tribology International*.

[Mohrbacher et al., 1995] Mohrbacher, H., Celis, J.-P., and Roos, J. (1995). Laboratory testing of displacement and load induced fretting. *Tribology International*, 28(5):269–278.

[Mugadu et al., 2002] Mugadu, A., Hills, D., and Nowell, D. (2002). Modifications to a fretting-fatigue testing apparatus based upon an analysis of contact stresses at complete and nearly complete contacts. *Wear*, 252(5):475–483.

[Munoz et al., 2007] Munoz, S., Navarro, C., and Dominguez, J. (2007). Application of fracture mechanics to estimate fretting fatigue endurance curves. *Engineering fracture mechanics*, 74(14):2168–2186.

[Murakami and Endo, 1994] Murakami, Y. and Endo, M. (1994). Effects of defects, inclusions and inhomogeneities on fatigue strength. *International Journal of Fatigue*, 16(3):163–182.

[Murthy et al., 2009] Murthy, H., Mseis, G., and Farris, T. (2009). Life estimation of ti–6al–4v specimens subjected to fretting fatigue and effect of surface treatments. *Tribology International*, 42(9):1304–1315.

[Mutoh and Jayaprakash, 2011] Mutoh, Y. and Jayaprakash, M. (2011). Tangential stress range–compressive stress range diagram for fretting fatigue design curve. *Tribology International*, 44(11):1394–1399.

[Mutoh and Xu, 2003] Mutoh, Y. and Xu, J.-Q. (2003). Fracture mechanics approach to fretting fatigue and problems to be solved. *Tribology international*, 36(2):99–107.

[Namjoshi et al., 2002] Namjoshi, S., Mall, S., Jain, V., and Jin, O. (2002). Fretting fatigue crack initiation mechanism in ti–6al–4v. *Fatigue & Fracture of Engineering Materials & Structures*, 25(10):955–964.

[Navarro and Domínguez, 2004] Navarro, C. and Domínguez, J. (2004). Initiation criteria in fretting fatigue with spherical contact. *International journal of fatigue*, 26(12):1253–1262.

[Navarro et al., 2003] Navarro, C., García, M., and Domínguez, J. (2003). A procedure for estimating the total life in fretting fatigue. *Fatigue & Fracture of Engineering Materials & Structures*, 26(5):459–468.

[Navarro et al., 2008] Navarro, C., Muñoz, S., and Domínguez, J. (2008). On the use of multiaxial fatigue criteria for fretting fatigue life assessment. *International Journal of Fatigue*, 30(1):32–44.

[Navarro et al., 2011] Navarro, C., Muñoz, S., and Domínguez, J. (2011). Influence of the initiation length in predictions of life in fretting fatigue. *Strain*, 47(s1):e283–e291.

[Nesládek et al., 2012] Nesládek, M., Španiel, M., Jurenka, J., Růžička, J., and Kuželka, J. (2012). Fretting fatigue–experimental and numerical approaches. *International Journal of Fatigue*, 44:61–73.

[Neu and Pape, 1998] Neu, R. W. and Pape, J. (1998). Methodologies for linking nucleation and propagation approaches for predicting life under fretting fatigue. In *Symposium on Fretting Fatigue: Current Technology and Practices, Salt Lake City*, pages 369–388.

[Nicholas et al., 2003] Nicholas, T., Hutson, A., John, R., and Olson, S. (2003). A fracture mechanics methodology assessment for fretting fatigue. *International journal of fatigue*, 25(9):1069–1077.

[Nishida et al., 2003] Nishida, T., Kondoh, K., Xu, J.-Q., and Mutoh, Y. (2003). Observations and analysis of relative slip in fretting fatigue. *ASTM Special technical publication*, 1425:33–43.

[Nix and Lindley, 1985] Nix, K. and Lindley, T. (1985). The application of fracture mechanics to fretting fatigue. *Fatigue & Fracture of Engineering Materials & Structures*, 8(2):143–160.

[Nix and Lindley, 1988] Nix, K. and Lindley, T. (1988). The influence of relative slip range and contact material on the fretting fatigue properties of 3.5 nicrmov rotor steel. *Wear*, 125(1):147–162.

[Nowell, 1992] Nowell, D. H. a. (1992). The development of a fretting fatigue experiment with well. defined characteristics. *Standardization of fretting fatigue test methods and equipment*, page 69.

[NSTB, 1989] NSTB (1989). Aircraft accident report. Technical Report NTSB/AAR-89/03, National Transportation Safety Board (NTSB).

[NSTB, 2013] NSTB (2013). Aircraft accident report. Technical Report NTSB/AAB-13/02, National Transportation Safety Board (NTSB).

[Papanikos et al., 1998] Papanikos, P., Meguid, S., and Stjepanovic, Z. (1998). Three-dimensional nonlinear finite element analysis of dovetail joints in aero-engine discs. *Finite elements in analysis and design*, 29(3):173–186.

[Pape and Neu, 1999] Pape, J. and Neu, R. (1999). Influence of contact configuration in fretting fatigue testing. *Wear*, 225:1205–1214.

[Pierres et al., 2011] Pierres, E., Baietto, M.-C., and Gravouil, A. (2011). Experimental and numerical analysis of fretting crack formation based on 3D X-FEM frictional contact fatigue crack model. *Comptes Rendus Mécanique*, 339(7):532–551.

[Quraishi et al., 2005] Quraishi, S., Khonsari, M., and Baek, D. (2005). A thermodynamic approach for predicting fretting fatigue life. *Tribology Letters*, 19(3):169–175.

[Radhakrishnan, 1992] Radhakrishnan, V. (1992). On bilinearity of manson-coffin low-cycle-fatigue relationship. *NASA STI/Recon Technical Report N*, 93:12739.

[Rammohan and Murthy, 2012] Rammohan, Y. and Murthy, H. (2012). Three dimensional finite element analysis of partial slip contacts subjected to combined loading. *Finite Elements in Analysis and Design*, 56:9–19.

[Rao et al., 2008] Rao, J., Kishore, C., and Mahadevappa, V. (2008). Weight optimization of turbine blades. In *Proceedings 12th International Symposium on Transport Phenomena and Dynamics of Rotating Machinery.*

[Ratsimba et al., 2004] Ratsimba, C., McColl, I., Williams, E., Leen, S., and Soh, H. (2004). Measurement, analysis and prediction of fretting wear damage in a representative aeroengine spline coupling. *Wear*, 257(11):1193–1206.

[Reeves and Hoeppner, 1976] Reeves, R. and Hoeppner, D. (1976). The effect of fretting on fatigue. *Wear*, 40(3):395–397.

[Rice and Rosengren, 1968] Rice, J. and Rosengren, G. (1968). Plane strain deformation near a crack tip in a power-law hardening material. *Journal of the Mechanics and Physics of Solids*, 16(1):1–12.

[Rooke and Jones, 1979] Rooke, D. and Jones, D. (1979). Stress intensity factors in fretting fatigue. *The Journal of Strain Analysis for Engineering Design*, 14(1):1–6.

[Ruiz et al., 1984] Ruiz, C., Boddington, P., and Chen, K. (1984). An investigation of fatigue and fretting in a dovetail joint. *Experimental Mechanics*, 24(3):208–217.

[Sabelkin and Mall, 2005] Sabelkin, V. and Mall, S. (2005). Investigation into relative slip during fretting fatigue under partial slip contact condition. *Fatigue & Fracture of Engineering Materials & Structures*, 28(9):809–824.

[Sabsabi et al., 2011] Sabsabi, M., Giner, E., and Fuenmayor, F. (2011). Experimental fatigue testing of a fretting complete contact and numerical life correlation using x-fem. *International Journal of Fatigue*, 33(6):811–822.

[Santus, 2008] Santus, C. (2008). Fretting fatigue of aluminum alloy in contact with steel in oil drill pipe connections, modeling to interpret test results. *International Journal of Fatigue*, 30(4):677–688.

[Sato, 1992] Sato, K. (1992). Determination and control of contact pressure distribution in fretting fatigue. *ASTM Special technical publication*, 1159:85–85.

[Sheikh et al., 1994] Sheikh, M., Fernando, U., Brown, M., and Miller, K. (1994). Elastic stress intensity factors for fretting cracks using the finite element method. *Fretting Fatigue, ESIS*, 18:83–101.

[Shin, 2009] Shin, K. S. (2009). Prediction of fretting fatigue behavior under elastic-plastic conditions. *Journal of mechanical science and technology*, 23(10):2714–2721.

[Sinclair et al., 2002] Sinclair, G., Cormier, N., Griffin, J., and Meda, G. (2002). Contact stresses in dovetail attachments: finite element modeling. *Journal of engineering for gas turbines and power*, 124(1):182–189.

[Smallman and Bishop, 1999] Smallman, R. E. and Bishop, R. J. (1999). *Modern physical metallurgy and materials engineering*. Butterworth-Heinemann.

[Smith et al., 1970] Smith, K., Topper, T., and Watson, P. (1970). A stress strain function for the fatigue of metal. *Journal of materials*, 5:767–778.

[Socie, 1987] Socie, D. (1987). Multiaxial fatigue damage models. *Journal of Engineering Materials and Technology*, 109(4):293–298.

[Song et al., 2002] Song, W., Keane, A., Rees, J., Bhaskar, A., and Bagnall, S. (2002). Turbine blade fir-tree root design optimisation using intelligent cad and finite element analysis. *Computers & structures*, 80(24):1853–1867.

[Stolarska et al., 2001] Stolarska, M., Chopp, D., Moës, N., and Belytschko, T. (2001). Modelling crack growth by level sets in the extended finite element method. *International journal for numerical methods in Engineering*, 51(8):943–960.

[Stover et al., 1985] Stover, R. J., Mabie, H., and Furey, M. (1985). A finite element investigation of a bearing/cartridge interface for a fretting corrosion study. *Journal of Tribology*, 107:157.

[Suter and Alkire, 2001] Suter, T. and Alkire, R. C. (2001). Microelectrochemical studies of pit initiation at single inclusions in al 2024-t3. *Journal of the Electrochemical Society*, 148(1):B36–B42.

[Sutton et al., 2009] Sutton, M. A., Orteu, J.-J., and Schreier, H. W. (2009). *Image correlation for shape, motion and deformation measurements: basic concepts, theory and applications*. Springer.

[Swalla and Neu, 2001] Swalla, D. and Neu, R. (2001). Influence of coefficient of friction on fretting fatigue crack nucleation prediction. *Tribology international*, 34(7):493–503.

[Szolwinski and Farris, 2000] Szolwinski, M. and Farris, T. (2000). Linking riveting process parameters to the fatigue performance of riveted aircraft structures. *Journal of aircraft*, 37(1):130–137.

[Szolwinski and Farris, 1996] Szolwinski, M. P. and Farris, T. N. (1996). Mechanics of fretting fatigue crack formation. *Wear*, 198(1):93–107.

[Szolwinski and Farris, 1998] Szolwinski, M. P. and Farris, T. N. (1998). Observation, analysis and prediction of fretting fatigue in 2024-t351 aluminum alloy. *Wear*, 221(1):24–36.

[Szolwinski et al., 1997] Szolwinski, M. P., Harish, G., and Farris, T. N. (1997). An experimental study of fretting fatigue crack nucleation in airframe alloys: A lifetime prediction and maintenance perspective. *in: First joint DOD/-FAA/NASA conference on aging aircraft, Ogden, Utah, USA*.

[Tada et al., 2000] Tada, H., Paris, P. C., Irwin, G. R., and Tada, H. (2000). *The stress analysis of cracks handbook*, volume 130. ASME press New York.

[Tanaka and Mura, 1982] Tanaka, K. and Mura, T. (1982). A theory of fatigue crack initiation at inclusions. *Metallurgical Transactions A*, 13(1):117–123.

[Tsai and Mall, 2000] Tsai, C. and Mall, S. (2000). Elasto-plastic finite element analysis of fretting stresses in pre-stressed strip in contact with cylindrical pad. *Finite elements in analysis and design*, 36(2):171–187.

[Van Beek, 2013] Van Beek, A. (2013). Tribology-ABC.

[Venkatesh et al., 2001] Venkatesh, T., Conner, B., Suresh, S., Giannakopoulos, A., Lindley, T., and Lee, C. (2001). An experimental investigation of fretting fatigue in ti-6al-4v: the role of contact conditions and microstructure. *Metallurgical and Materials Transactions A*, 32(5):1131–1146.

[Vethe, 2012] Vethe, S. (2012). *Numerical simulation of fatigue crack growth.* PhD thesis, Norwegian University of Science and Technology.

[Vic3D, 2013] Vic3D (2013). http://www.correlatedsolutions.com/.

[Vingsbo and Söderberg, 1988] Vingsbo, O. and Söderberg, S. (1988). On fretting maps. *Wear*, 126(2):131–147.

[Voisin et al., 1995] Voisin, J., Vannes, A., Vincent, L., Daviot, J., and Giraud, B. (1995). Analysis of a tube-grid oscillatory contact: methodology for the selection of superficial treatments. *Wear*, 181:826–832.

[Vormwald and Zerres, 2012] Vormwald, M. and Zerres, P. (2012). Review of fatigue crack growth under non-proportional loading. In *Proceedings of the 4th International Conference on Crack Paths (CP2012)*, pages 351–358.

[Wackers et al., 2010] Wackers, P., Arrieta, V., Alquezar-Getan, M., Constantinescu, A., and Maitournam, H. (2010). A modeling approach to predict fretting fatigue on highly loaded blade roots. *Journal of engineering for gas turbines and power*, 132(8).

[Wagle and Kato, 2009] Wagle, S. and Kato, H. (2009). Ultrasonic detection of fretting fatigue damage at bolt joints of aluminum alloy plates. *International Journal of Fatigue*, 31(8):1378–1385.

[Wagle and Kato, 2011] Wagle, S. and Kato, H. (2011). Size estimation of fatigue crack appearing at bolt joints of aluminum alloy plates by synchronized saw measurement. *Experimental mechanics*, 51(6):869–878.

[Walker, 1970] Walker, K. (1970). The effect of stress ratio during crack propagation and fatigue for 2024-t3 and 7075-t6 aluminum. *Effects of environment and complex load history on fatigue life, ASTM STP*, 462:1–14.

[Wang et al., 2013a] Wang, D., Zhang, D., and Ge, S. (2013a). Finite element analysis of fretting fatigue behavior of steel wires and crack initiation characteristics. *Engineering Failure Analysis*, 28(0):47–62.

[Wang et al., 2013b] Wang, D., Zhang, D., Wang, S., and Ge, S. (2013b). Finite element analysis of hoisting rope and fretting wear evolution and fatigue life estimation of steel wires. *Engineering Failure Analysis*, 27(0):173–193.

[Wang et al., 2007] Wang, R., Jain, V., and Mall, S. (2007). A non-uniform friction distribution model for partial slip fretting contact. *Wear*, 262(5):607–616.

[Waterhouse, 1981] Waterhouse, R. (1981). Theories of fretting processes. *Fretting Fatigue*, pages 203–219.

[Wawrzynek et al., 2012] Wawrzynek, P., Carter, B., and Ingraffea, A. (2012). Advances in simulation of arbitrary 3d crack growth using franc3d ng. In *ICF12, Ottawa 2009*.

[Wöhler, 1870] Wöhler, A. (1870). *Ueber die Festigkeits-versuche mit Eisen und Stahl*. Ernst & Korn, Berlin.

[Yan et al., 2006] Yan, C. L., Sun, G. Q., Shang, D. G., and Deng, J. (2006). Multiaxial fatigue damage models. *Key Engineering Materials*, 324:747–750.

[Zhang et al., 2013] Zhang, T., Harrison, N., McDonnell, P., McHugh, P., and Leen, S. (2013). A finite element methodology for wearfatigue analysis for modular hip implants. *Tribology International*, 65(0):113 – 127.

[Zhang et al., 2011] Zhang, T., McHugh, P., and Leen, S. (2011). Computational study on the effect of contact geometry on fretting behaviour. *Wear*, 271(9):1462–1480.

[Zhang et al., 2012] Zhang, T., McHugh, P., and Leen, S. (2012). Finite element implementation of multiaxial continuum damage mechanics for plain and fretting fatigue. *International Journal of Fatigue*, 44:260–272.